Development of Solid Oxide Fuel Cell cathodes for operation at 600 °C

Dissertation

Peter Ried

Montanuniversität Leoben
Januar 2009

Die vorliegende Arbeit wurde im Zeitraum von November 2004 bis Januar 2009 an der Montanuniversität Leoben unter der Leitung von Univ. Prof. Dipl.-Ing. Dr. techn. Werner Sitte im Rahmen des FWF Spezialforschungsbereichs “Elektroaktive Stoffe” und an der Empa, Swiss Federal Laboratories for Material Testing and Research, unter der Betreuung von Dr. Peter Holtappels im Rahmen der EU-Projekte “Real SOFC” und “SOFC600” durchgeführt.

Eidesstattliche Erklärung
Ich erkläre an Eides statt, dass ich diese Arbeit selbständig verfasst, andere als die angegebenen Quellen und Hilfsmittel nicht benutzt und mich auch sonst keiner unerlaubten Hilfsmittel bedient habe.

Affidavit:
I declare in lieu of oath, that I wrote this thesis and performed the associated research myself, using only literature cited in this volume.

Danksagung

Mein besonderer Dank gilt vor allem Univ. Prof. Dr. Werner Sitte und Dr. Peter Holtappels für die Begleitung durch die faszinierende Welt der Festkörperchemie und darin im Besonderen der Festelektrolytbrennstoffzellen und für alle Hilfestellungen bei Problemen.

Meinen Kollegen in Leoben danke ich herzlich!

- Dr. Edith Bucher für Ihre Hilfe in schwierigen technischen und wissenschaftlichen Fragen und für viel Geduld.
- George Caraman für seine Freundschaft, Unterstützung und perfekte Organisation in allen Lebenslagen.
- Dr. Wolfgang Preis für die umfassende Beratung bei kinetischen Messungen und für interessante Diskussionen.
- Dr. Jerzy Bugajski für Interesse, Ideen und Unterstützung bei vielen Experimenten und der polnischen Sprache.
- Peter Gsaxner für produktive und unterhaltsame Zusammenarbeit am Institut und an anderen Orten.
- Andreas Egger für Rat und Tat bei den letzten Erledigungen beim Einreichen.
- Dr. Norbert Stockinger für viele interessante Diskussionen und tiefgehende Fragen zur Festkörperchemie.
- Liliane Hackl für ihre umfassende Betreuung in administrativen Belangen.
- Karin Stanglauer für ihre Unterstützung bei der Synthese und interessante Gespräche und Einblicke in das Leben an der der Montanuniversität.
- Dietmar Eschedor für die Betreuung der Informatik und die Hilfe bei schweren Transporten.
- Dr. Peter Waldner für interessante Diskussionen zu späten Arbeitsstunden.
- Dr. Hermann Schranzhofer für seine Beratung in physikalischen und mathematischen Belangen.
- Dr. Andreas Bürgermeister für die Begleitung meiner ersten Schritte und für soziale Ein- und Ausblicke ins Institutsleben.

Mein Dank gilt auch besonders meinen Kollegen in Dübendorf!

- Dr. Thomas Graule für die herzliche Aufnahme an der Hochleistungskeramik, das Interesse an meiner Arbeit und die stetige Unterstützung.
- Meinen Bürokollegen Dr. Peter Holtappels, Dr. Artur Braun, Dr. Christian Soltmann und Daniel Wiedenmann für die inspirierende Arbeitsatmosphäre und Diskussionen zu wissenschaftlichen und lebenspraktischen Aspekten.
- Meinen Freuden- und Leidensgenossen bei der Dissertation Dr. Defne Bayraktar, Dr. Sophie Duval und Dr. Jörg Richter die die gute Freundschaft und Hilfe in allen Lebenslagen.
- Dariusz Burnat danke ich für die unglaublich produktive Zusammenarbeit, seinen Ideenreichtum und viele Fragen.

- Brigitte Schatzmann, Anke Brönstrup, Hansjürgen Schindler, Maik Thünemann und Roland Bächtold für die Unterstützung in vielfältigen technischen und administrativen Belangen und angenehme gemeinsame Pausen.
- Salvatore Fuso für die stetige Motivation am gemeinsamen Sprachenlernen und das Organisieren von unzähligen vielsprachigen und multikulturellen Mittagessen.
- Dr. Michel Prestat für wertvolle Tipps zu den Impedanzmessungen und zu der Französischen Aussprache.
- Dr. Andre Heel für wertvolle Diskussionen und produktive Zusammenarbeit unter oft schwierigen Bedingungen.
- Dr. Ulrich Vogt für seine Offenheit, interessante Gespräche und die Gastfreundschaft seiner Teeküche.
- Elisabeth Barna für die gegenseitige Unterstützung in schwierigen Zeiten und für das Teilen ihres enzyklopädischen Wissens in sozialen Fragen inner- und außerhalb der EMPA.
- Juliane Heiber für XRD-Messungen, technische Hilfestellungen und gemeinsame Essen, Sport und Spiel.
- Noemi van Gardenen für ihren Humor in schwierigen Lagen und für die Organisation gemeinsamer Unternehmungen nach der Arbeit.
- Dr. Gunnar Nurk für interessante Diskussionen zur Arbeit und seine Unterstützung beim Korrekturlesen.
- Selma Erat, Nikolaos Karageorgakis und viele andere, die mich auch nach meiner offiziellen Zeit an der EMPA immer noch herzlich aufgenommen haben.
- Dr. Andrea Ulrich und Adrian Wichser für die Elementanalytik mittels ICP-OES und angenehme Gespräche.

Ich bedanke mich bei den Mitarbeitern der Werkstätten und der Administration beider Institutionen, die durch ihre Unterstützung diese Arbeit erst möglich gemacht haben. Weiters möchte ich auch noch bei allen externen Kollegen Dank sagen, die mich in dieser Zeit unterstützt haben. Meinen Eltern danke ich für ihr stetige Unterstützung in allen Lebensbereichen und ihr grosses Interesse an meiner Arbeit. Susann Schneider danke ich abschliessend noch für die Hilfe bei der Verbesserung des Layouts.

Die Finanzierung meiner Arbeitskraft durch den FWF Spezialforschungsbereich Spezialforschungsbereichs “Elektroaktive Stoffe” (Projekt F915), sowie der EU-Projekte Real SOFC” (EC-Contract No.502612, SWISS contract SBF 03.170-2) und Project “SOFC600” (contract no. SES6-020089) sei hier dankend erwähnt.

List of contents

1 Introduction 1

1.1 Functioning principle behind Solid Oxide Fuel Cells 1

1.2 Thermodynamics of ideal and real SOFC systems 3

1.3 State-of-the-art Solid Oxide Fuel Cells and current development 6

1.4 Advantages of mixed conducting materials for the use as cathode materials 12

2 SOFC cathodes for operating temperatures between 550 °C and 650 °C 14

2.1 Oxygen reduction mechanisms 14

2.2 Models describing the influence of the kinetic parameters, the conductivity and the cathode microstructure on the cathode performance 15

2.2.1 Overview of different approaches 15

2.2.2 Adler model and concept of penetration depth 17

2.2.3 Three-dimensional model and model using segmented layers 19

2.3 Influence of cathode engineering on performance 22

2.3.1 LSCF 22

2.3.2 Composites 23

2.3.3 Thin layers 24

2.4 Material systems for SOFC cathodes at reduced operating temperature 25

2.5 Review on the state of art cathode materials from the (Ba, La, Sr)(Co, Fe)$O_{3-\delta}$ system 26

2.6 Influence of micro structural changes on cathode performance 27

2.6.1 Adhesion to the electrolyte, triple phase boundary length, porosity and thickness 27

2.6.2 Conventional approach with µ and sub-µ particles 28

2.6.3 Perspectives of sub micro and nano powders and mixtures in development of SOFC cathodes 29

2.7 Approach to cathode operating between 550 °C and 650 °C 30

3 $La_{0.6}Sr_{0.4}Co_{0.2}Fe_{0.8}O_{3-\delta}$ and $Ba_{0.5}Sr_{0.5}Co_{0.8}Fe_{0.2}O_{3-\delta}$ synthesis and characterization 32

3.1 Synthesis 32

3.1.1 Synthesis by spray pyrolysis 32

3.1.2 Flame spray synthesis 34

3.2 Characterization 36

3.2.1 Characterization techniques 36

3.2.2 Results: Powder characterization of $La_{0.6}Sr_{0.4}Co_{0.2}Fe_{0.8}O_{3-\delta}$ and $Ba_{0.5}Sr_{0.5}Co_{0.8}Fe_{0.2}O_{3-\delta}$, $La_{0.6}Sr_{0.4}FeO_{3-\delta}$ and $(La_{0.8}Sr_{0.2})_{0.95}FeO_{3-\delta}$ 38

3.2.3 Overview of most important results for LSCF and BSCF 55

3.3 Discussion 56

3.3.1 Structure and chemical composition (of LSCF and BSCF) 56

3.3.2 Compatibility of LSCF and BSCF with YSZ and CGO 56

3.3.3 Coefficients of thermal expansion 58

3.4 Statement about the quality of material synthesis 58

4 Electrical conductivity and kinetic parameters of selected compounds from the (Ba, La, Sr)(Fe,Co)$O_{3-\delta}$ system 60

4.1 Aspects of transport properties of mixed ionic/electronic conductors 60

4.1.1 Oxygen non-stoichiometry and electrical conductivity of mixed conductors 60

4.1.2 Oxygen exchange kinetics and chemical diffusion 67

4.1.3 Assessment of conductivity relaxation curves 68

4.2 Experimental techniques 71

4.2.1 Measurement of the electrical conductivity by the van der Pauw method ... 71

4.2.2 Setup for conductivity relaxation experiment 72

4.2.3 Analysis of conductivity relaxation curves 73

4.3 Results: Electrical conductivity as function of temperature and oxygen partial pressure 76

4.3.1 Electrical conductivity of LSCF: isobars and isotherms 76

4.3.2 Electrical conductivity of BSCF: isobars and isotherms 79

4.3.3 Electrical conductivity of LSF82: Isobars and isotherms 80

4.4 Discussion: Comparison of electrical conductivity (isotherms) of $La_{0.6}Sr_{0.4}Co_{0.2}Fe_{0.8}O_{3-\delta}$ and $Ba_{0.5}Sr_{0.5}Co_{0.8}Fe_{0.2}O_{3-\delta}$, $La_{0.6}Sr_{0.4}FeO_{3-\delta}$ and $(La_{0.8}Sr_{0.2})_{0.95}FeO_{3-\delta}$ 82

4.4.1 Temperature dependence of the electrical conductivity 82

4.4.2 Comparison of oxygen partial pressure dependence of the electrical conductivity 86

4.4.3 General comparison of conductivities ... 88

4.5 Results: surface exchange and oxygen ion transport in LSCF, BSCF, LSF82 and LSF64 ... 89

4.5.1 Chemical surface exchange coefficient of LSCF ... 89

4.5.2 Chemical diffusion coefficient of LSCF ... 90

4.5.3 Chemical surface exchange coefficient of BSCF ... 90

4.5.4 Chemical diffusion coefficient of BSCF ... 91

4.5.5 Chemical surface exchange coefficient of LSF82 ... 92

4.5.6 Chemical diffusion coefficient of LSF82 ... 93

4.6 DISCUSSION: Comparison of oxygen exchange and diffusion kinetics ... 94

4.6.1 Chemical surface exchange of LSCF, BSCF, LSF82 and LSF64 ... 94

4.6.2 Chemical diffusion coefficients of LSCF, BSCF, LSF82 and LSF64 ... 97

4.7 Conclusions ... 100

5 Electrochemical properties of LSCF//CGO//LSCF cells ... 101

5.1 Experimental: Preparation of symmetrical cells with $La_{0.6}Sr_{0.4}Co_{0.2}Fe_{0.8}O_{3-\delta}$ cathode layers on $Ce_{0.9}Gd_{0.1}O_{1.95}$ electrolyte substrates by screen printing ... 101

5.2 Experimental: Impedance spectroscopy as a tool to examine ionic/electronic transport properties ... 105

5.2.1 Impedance as perturbation function of an alternating current (AC) signal ... 105

5.2.2 Experimental setup and sample preparation ... 107

5.3 Results: influence of the powder composition and the sintering temperature on the cathode microstructure ... 110

5.3.1 Influence of the powder composition ... 110

5.3.2 Temperature dependence of the microstructure comparing N25 and C25 ... 112

5.3.3 Influence of the solid loading on the microstructure ... 115

5.3.4 Temperature dependence of the microstructure comparing C11N22, CNE33 and CNE46 ... 116

5.4 Discussion: influence of the starting powders and the solid loading on the microstructure ... 119

5.5 Results: Impedance Response of LSCF//CGO//LSCF cells ... 121

5.5.1 Temperature dependence of impedance response ... 121

5.5.2 Partial pressure dependence of the impedance response ... 122

5.5.3 Influence of paste composition on the impedance ... 124

5.6 Discussion : Oxygen partial pressure dependence of the impedance response ... 125

5.7 Results: Influence of the paste composition on the cathode polarization resistance ... 128

5.7.1 Influence of the sintering temperature on the polarisation resistance of cathodes produced from C25 and N25 ... 128

5.7.2 Influence of the sintering temperature on single and multi phase cathodes ... 130

5.7.3 Influence of the layer thickness on the polarisation resistance of C25 cathodes ... 132

5.8 Discussion: Comparison of lowest measured polarization resistances for all starting powders ... 134

5.8.1 Microstructure and cathode polarization resistance – influence of the layer thickness and the grain size on R_{pol} applying C25 and N25 ... 134

5.8.2 Comparison of cathodes prepared with the highest heat treatment temperatures ... 137

5.8.3 Microstructure and cathode polarization resistance – influence of the grain size on R_{pol} applying C11N22 and NE46 and CNE46 ... 138

5.9 Assessment of the obtained results ... 142

5.9.1 Assessment of processing, thermal treatment and obtained polarization resistance at 600 °C ... 142

5.9.2 Assessment of the polarization resistance at 600 °C and 800 °C with modelled values ... 142

5.10 Discussion: correction of the polarization resistance ... 144

5.11 Conclusions regarding the corrected values of the polarization resistance ... 150

6 Final Discussion and Conclusions ... 151

7 Summary ... 154

Development of Solid Oxide Fuel Cell cathodes for operation at 600 °C

1 Introduction

This chapter illustrates the principles of Solid Oxide Fuel Cells, their advantages in converting hydrocarbon fuels into electrical energy and the reasoning behind reducing the SOFC operation temperature down to 600°C. Advantages of mixed conducting materials, which are the preconditions for high cathode performance at 600 °C, are listed.

1.1 Functioning principle behind Solid Oxide Fuel Cells

Solid oxide fuel cells (SOFCs) are highly efficient devices for the direct conversion of chemical energy into electrical energy and the conversion of the fuels into carbon dioxide and water. The basic ideas and materials were already proposed by Nernst at the end of the 19th century. However, during the past 100 years, considerable progress in its theory has been made, and many experiments are still ongoing ever since Nest's breakthrough [1]. Especially since the 1960s, an increase in development is being undertaken.

The component in the SOFC, from which the name is derived, is the solid electrolyte, which is the oxygen ion conductor, such as yttria-stabilized zirconia ($Y_{0.16}Zr_{0.84}O_{1.92}$, YSZ), which serves both to separate the two gas atmospheres and to transport the oxygen ions without significant losses from the cathode to the anode via oxygen vacancies in the oxygen sub lattice. Its ionic conducting properties were first found in 1899 by Nernst [2], and Schottky suggested it in 1935 as electrolyte material for a fuel cell. The first demonstration using YSZ in an operating cell was presented by Baur and Preis in 1937 [3]. In 1943 Wagner recognised the existence of vacancies in the anion sub lattice of mixed oxide solid solutions and hence explained the conduction mechanism of the Nernst glowers, namely that they are oxide ion conductors [4]. At operating temperatures between 650 °C and 1000 °C the electrode reactions are usually fast allowing the use of non-noble electro-catalysts as electrodes. The electrodes together with the electrolyte form an all-solid-state system. Fuel and oxygen are present in the gas phase [5], and the reacting species form in contact to the electrodes.

The oxygen is absorbed, dissociated and reduced on the cathode surface and converted into oxygen ions, transported through the solid electrolyte to the fuel electrode (anode) where the oxygen ions can react with the fuel. During this reaction, the oxygen ion is releasing two electrons to an external circuit. The principle is shown in Figure 1.

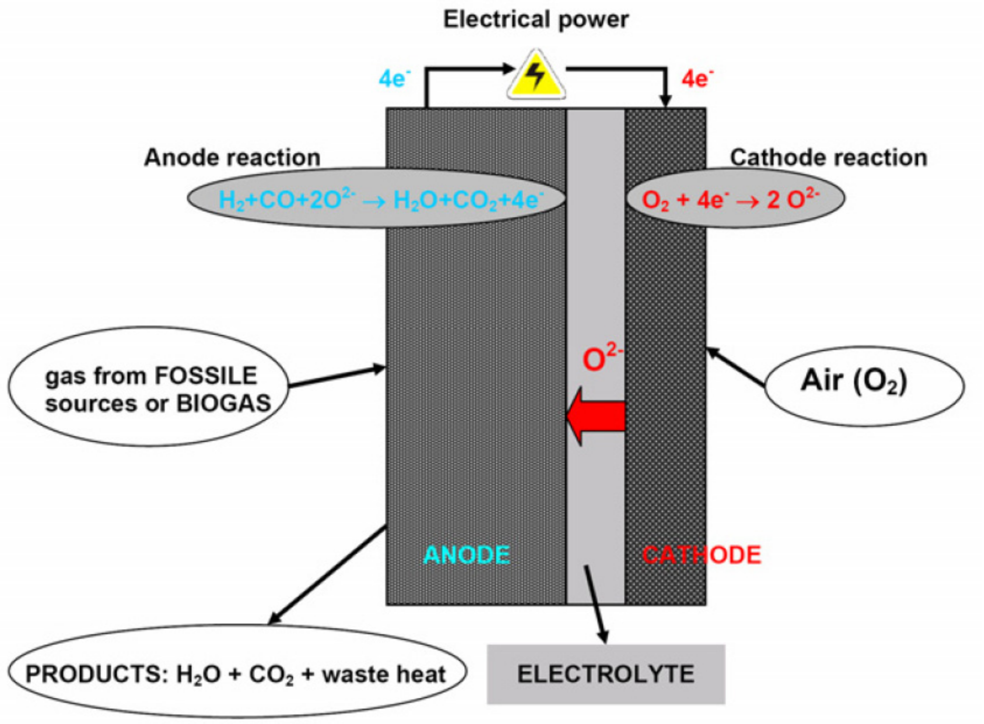

Figure 1: The principle operating mode of a Solid Oxide Fuel Cell.

The advantage of fuel cells is to provide a highly efficient fuel conversion into H_2O and CO_2 as clearly defined reaction products. The solid oxygen ion conducting electrolyte is the name giving the characteristic of the SOFC. The fuel cell consists of two separate chambers divided by the solid and gas tight oxygen-ion conducting electrolyte. As shown above in Figure 1, in the air chamber, at the cathode, oxygen is reduced to oxygen ions which are incorporated into the solid electrolyte.

$$\frac{1}{2} O_2 + 2e^- \rightarrow O^{2-}$$

At the anode chamber the fuel, for example hydrogen, is oxidized

$$H_2 + O^{2-} \rightarrow H_2O + 2e^-$$

The electrochemical potential, created by the difference in the oxygen partial pressure between cathode and anode, is the driving force for an electrical current in an outer circuit.

The overall reaction corresponds to the combustion of the fuel:

$$H_2 + \frac{1}{2}O_2 \rightarrow H_2O$$

1.2 Thermodynamics of ideal and real SOFC systems

The fuels considered for SOFCs are reformates consisting of mostly hydrogen and carbon monoxide. The fuels are oxidized in the presence of oxygen ions in the fuel chamber, whereas water and carbon dioxide are formed at the anode as reaction products.

The thermodynamic aspects are described below as e.g. by Holtappels and Stimming [5]. The air and the fuel electrode being present in separated chambers possess different electrochemical potentials that create a potential difference across the cell. The potential difference can be calculated with the Gibb's Free Enthalpy $\Delta G_{f,x,T}$ for the oxidation reaction of both H_2 and CO as shown in Equations 1-4.

$$H_2 + \frac{1}{2} O_2 \rightarrow H_2O \qquad \text{Equation 1}$$

$$U_0 = -\frac{\Delta G^0_{f,H2O,T}}{2F} + \frac{RT}{2F}\ln\left(\frac{\sqrt{p(O_2)_{cathode}}\,p(H_2)_{anode}}{p(H_2O)_{anode}}\right)$$ Equation 2

$$CO + \frac{1}{2}O_2 \rightarrow CO_2$$ Equation 3

$$U_0 = -\frac{\Delta G^0_{f,CO2,T}}{2F} + \frac{RT}{2F}\ln\left(\frac{\sqrt{p(O_2)_{cathode}}\,p(CO)_{anode}}{p(H_2O)_{anode}}\right)$$ Equation 4

The maximum available voltage (U_0) that can be reached from one single cell and is dependend of the fuel type, the partial pressure of the reacting species, the ratio of hydrogen to carbon monoxide, and the operating temperature. R is the gas constant, and F is the Faraday constant. $\Delta G_{f,x}$ in Equation 2 and 4 depends on the respective temperatures according to the following Equation 5 and 6.

$$\Delta G_{f,H20}(T) = -247.4 + 0.0541T$$ Equation 5

$$\Delta G^0_{CO2}(T) = -282.5 + 0.0866T$$ Equation 6

The potential difference U_0 decreases with increasing temperature. The reason is the considerable contribution of the reaction entropy to the Gibbs Free Energy of the reactions. The entropy contribution to $\Delta G_{f,x}$ is also the basis for the existence of thermodynamic efficiency,

$$\eta_{th} = \frac{\Delta G}{\Delta H}$$ Equation 7

being below 1 (0.7-0.9), and its further decrease with increasing temperature, as displayed for the reaction between H_2 and O_2 in Figure 2. ΔH is the reaction enthalpy.

The effective efficiency of SOFCs producing electrical energy theoretically increases with the decrease in temperature (refer to the red curve in Figure 2). A very basic example for an empirical efficiency is the Carnot efficiency (Equation 8) for an engine model, in which the higher the temperature difference of the fluid is, the higher the efficiency will be. For example, the efficiency for conventional steam turbine machines with temperatures at around 800 K is considerably lower than for fuel cells.

$$\eta_{th} = \frac{Tw - Tk}{Tw} (Tk = 320K) \qquad \text{Equation 8}$$

Tw and Tk are the temperatures of the hot fluid at the inlet and the exhaust of the engine, respectively.

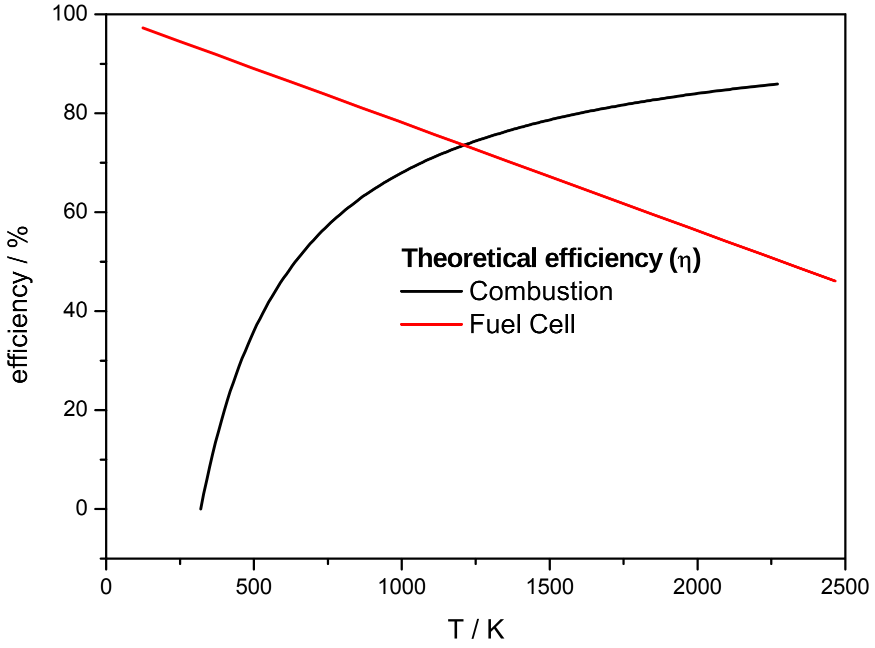

Thermodynamic efficiency of fuel cells compared with Carnot efficiency of combustion engines

Figure 2: Comparison between theoretical Carnot (black) and thermodynamic (red) efficiency.

However, the efficiency of real SOFC systems is lower than the theoretical values above. The electrolyte resistance and the polarization losses at cathode and anode contribute to the losses of the fuel cell. Additionally, heat losses, limited fuel utilization at the anode side and the resistances of cell interconnects reduce the electrical efficiency to approximately 60 %. If heat recovery is applied, overall system efficiencies can reach values between 80-90 %.

1.3 State-of-the-art Solid Oxide Fuel Cells and current development

Presently, the basic differences between the various SOFC systems are in their designs. Although a number of different materials have been investigated, yttria or scandia substituted zirconia, Ni-YSZ cermets and Sr-doped lanthanum manganite are the modern materials used as electrolyte, anode and cathode, respectively [5]. These materials are applied in various designs, within operating temperatures between 750 and 1000 °C.

Already in the 1960ies first tubular cells (Figure 3) were tested by Siemens-Westinghouse showing a high performance for operating temperatures above 950 °C. However, the costs, due to relatively expensive fabrication methods, and low volumetric power densities are drawbacks of this system. Micro tubes, several millimetres in diameter have an increased volumetric power density (increasing surface to volume ratio with decreasing diameter) and their design is the highly focused subject of interest that is currently being researched [6]. However, mass production of high performing cells at tolerable costs is needed.

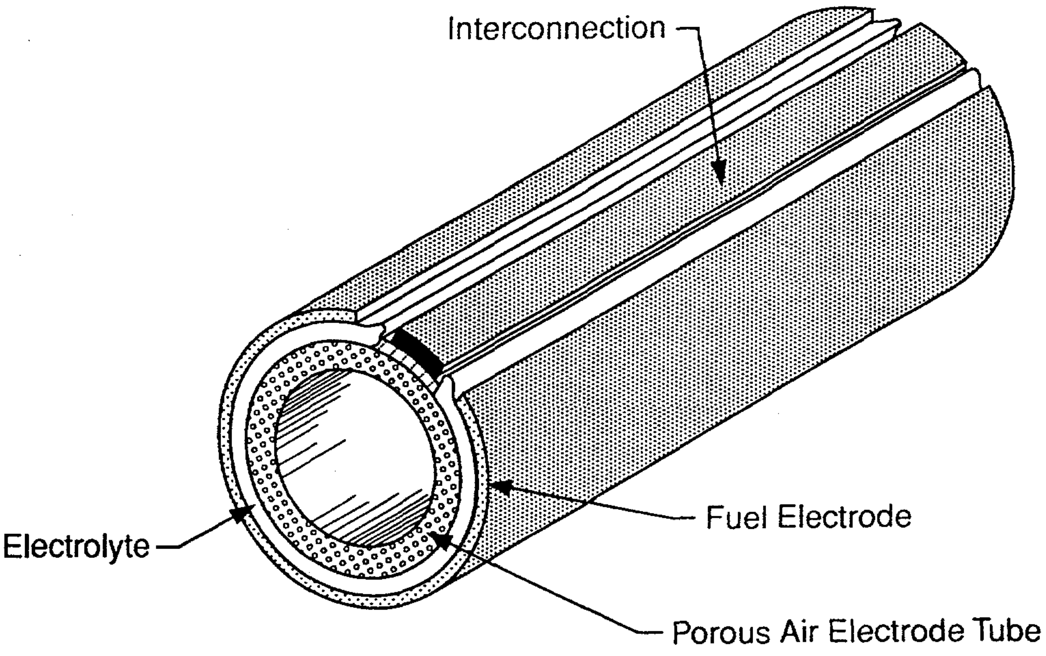

Figure 3: Tubular design of the solid oxide fuel cell from Siemens Westinghouse
from Singhal [7].

The flat plate design shows promise for mass production, because of the use of cheap fabrication techniques and its high volumetric power densities. Planar flat electrolyte supported cells and stacks, operating at 930-950 °C, have been developed worldwide, by companies such as Siemens [8] and Ceramic Fuel Cells Limited [9]. Interconnection materials are typically Cr-alloys. Stacks with both internal and external mani folding presently widely produced.

Today cells with operating temperatures lower than 850 °C are already on the market. As an example a cell made from the electrolyte applied by Ceramic Fuel Cells Limited (CFCL) is shown in Figure 4a. The cells are typically 160 to 200 μm thick and operate at T > 800 °C. However, due to problems related to the high operating temperatures, electrolyte supported cells are losing its attraction to be produced. Recently, there is a clear trend that anode-supported flat plate cells will become dominant Figure 4b.

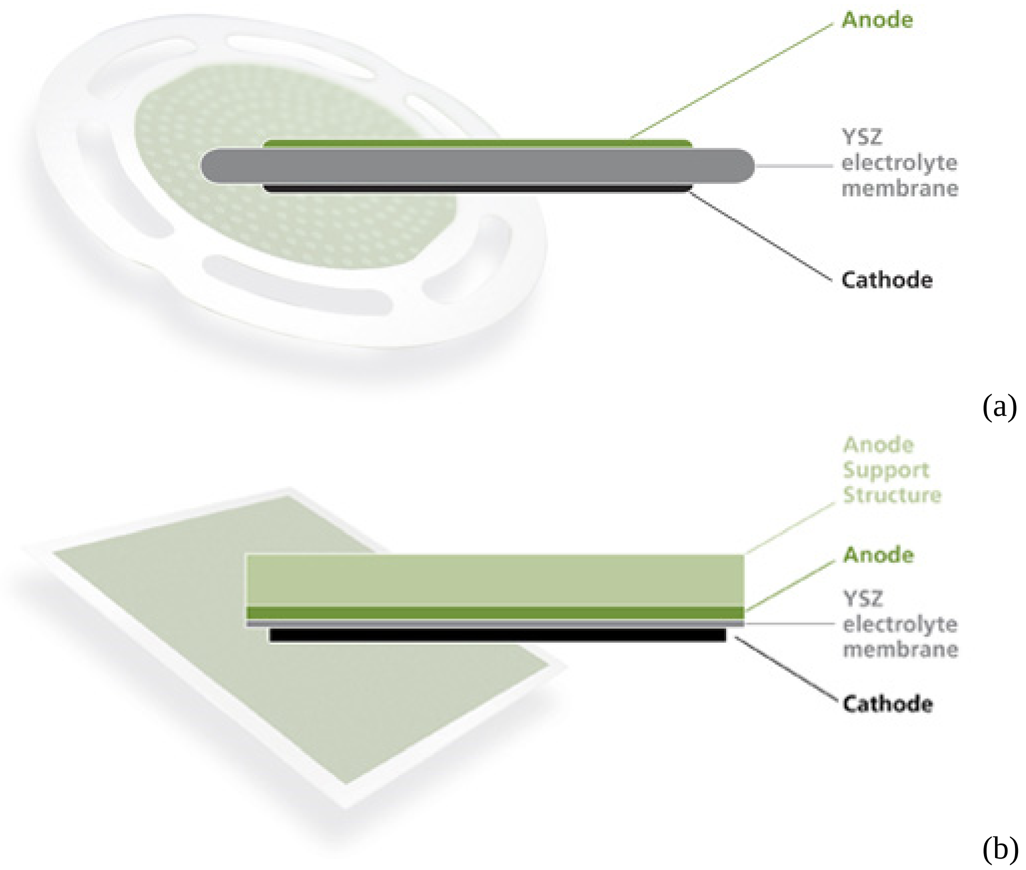

Figure 4: Electrolyte supported (a) and anode supported (b) fuel cells (from Ceramic Fuel Cells Limited [10]).

After Jülich demonstrated the feasibility of the anode supported electrolyte design, [11] most SOFC developers worldwide have started their own development line of anode supported electrolyte cells. Anode supported fuel cells from CFCL's and Haldar Topsoe [12] are typically around 300 microns thick and operate at < 780 °C with a much higher power density compared to electrolyte supported fuel cells. The anode-supported electrolyte cells have attracted high interest in recent years.

Solid oxide fuel cells at operating conditions produce an electromotive force between 0.7-0.9 V, depending on the fuel usage. Therefore, the single cells are connected in series in order to achieve larger electrical power. Bipolar plates is an example for connecting elements between cells, stacked on top of each other. These fuel cell stacks are consisting of bipolar plates and electrode-electrolyte units. The anode supported design offers the possibility to reduce the operating temperature so that cheap and easy to handle alloys, such as ferritic steels, can be used to construct stacks. The reduction in the operating temperature is supposed to reduce material stress and degradation for many SOFC components. Current research and development have the aim to find the proper material systems for an operating temperature of 600 °C.

Particularly, the problem of chromium evaporation from steel interconnects is present at high operating temperatures. Normally, long-term stability of interconnects at such temperatures is achieved using chromium alloys. Chromium also limits the thermal expansion of the alloy, giving it a similar coefficient of expansion to the surrounding ceramic electrolytes. However, at operating temperatures of 800 °C, the chromium is released and destroys the electrode/electrolyte interface [13]. The reduction of the operating temperature allows the usage of ferritic steals instead of chromium alloys and so decreases the degradation of the fuel cell performance and the costs [5].

The material properties have to fit to the special preconditions at operating temperatures lower than the state-of-the-art SOFC. The main requirements of SOFC materials are sufficiently high conductivity and catalytic activity of the electrodes, chemical stability and durability. The state-of-the-art electrolyte, anode and cathode materials are shortly presented here. Furthermore, new materials, considered to work effectively at lower operating temperatures are briefly discussed.

The most commonly used electrolyte material today is zirconia, stabilized in the conductive cubic phase with up to 10 mol% yttria or scandia. Alternative electrolyte materials with higher conductivity at temperatures around 600 °C are substituted $LaGaO_3$ and substituted ceria (e.g. $Gd_{0.1}Ce_{0.9}O_{1.95}$) that was chosen as electrolyte for the present study.

The solid electrolyte is the key component and has to fulfil the following criteria for the effective operation of the SOFC [14]:

- High ionic conductivity, negligible electronic conductivity at operating temperature. Low resistance regarding the passage of oxygen ions is the precondition for a high performance, while the electronic conductivity has to be as low as possible to avoid parasitic losses due to short cuts that reduce the cell performance. These preconditions have to be fulfilled in both anodic (reducing) and cathodic (oxidizing) atmospheres.

- Gas tightness: the electrolyte must not show any porosity or cracks.
- Stability: the electrolyte has to be chemically and mechanically stable in oxidizing and reducing atmosphere. No phase transitions between room and operating temperature should occur, because in most cases they are connected with volume changes inducing mechanical stress.
- Compatibility: the electrolyte has to be chemically compatible to the other cell components with a fitting coefficient of thermal expansion. However, the above mentioned condition limits the number of applicable electrolyte materials and therefore, in most cases the anode and cathode materials are fit to the electrolyte.

First stage SOFCs used single-phase materials as anodes (e.g. graphite, iron oxide, Pt-metal or transition metals). However, this approach contained a lot of drawbacks such as corrosion, degradation processes, the mismatch of the thermal expansion between the anode and the zirconia electrolyte, and the limitation of the fuel oxidation process only to a triple phase boundary between gas – electrode – electrolyte.

The anode and the anode substrate have to fulfil the following criteria [14]:

- High mechanical and chemical stability: the mechanical stability of the cell has to be mainly fulfilled by the anode substrate, which has to be stable under water vapour in highly reducing atmospheres.
- High electronic conductivity.
- Chemical compatibility with the electrolyte.
- Coefficient of thermal expansion fitting to the electrolyte.
- Sufficient open porosity: the gas transport to the electrochemically active area close to the electrolyte should be fast to avoid losses due to diffusion over potentials.
- High catalytic activity for the oxidation of the fuel gas and preferably catalytic activity and selectivity for the reforming of hydrocarbons.

These requirements are almost entirely fulfilled by cermets (ceramic-metal) consisting of nickel (Ni) and yttria stabilized zirconia (YSZ). The cermet (Ni/YSZ) therefore has been used now for more than 30 years as an anode material providing mixed conducting features. YSZ provides ionic conductivity resulting from oxygen ion transport via vacancy mechanism, Ni as excellent catalyst for hydrogen reduction ensures the electronic conductivity. However, this system also contains several drawbacks requiring an optimization of the microstructure to enlarge the efficiency of the fuel oxidation. The directed electric current through the cell leads also to nickel agglomeration and the ability of nickel to crack higher hydrocarbons leads to carbon deposition. Both these features reduce the effectiveness of the anode process in the cell. Further potential anode materials (belonging to the perovskite system) as $La_{1-x}Sr_xCrO_{3-\delta}$, so far used as interconnectors for SOFC or modified aiming a maximized electronic conductivity and chemical stability in reducing atmospheres $La_{1-x}Sr_xCr_{1-y}M_yO_{3-\delta}$ (M = Mn, Fe, Co, Ni) are topics of ongoing research [15].

The main requirements for the cathode material [14] are:

- High electronic conductivity.
- Chemical compatibility with the electrolyte material, as well as chemical and structural stability in air at operating temperature.
- Coefficient of thermal expansion close to the electrolyte and anode substrate.
- Sufficiently high surface exchange coefficient for the oxygen exchange including high catalytical activity for the dissociation and reduction of oxygen molecules.

High performing cathode materials especially for lower operating temperatures furthermore, should have a high conductivity for oxygen ions (as further described in Chapter 1.4).

Commonly used cathode materials for the temperature range between 800 °C and 1000 °C are $(La,Sr)MnO_{3-\delta}$ (LSM) as cathode materials Current research and development focuses on alternative materials for temperatures around 600 °C with comparable performance and longer life time. The two major groups of candidates for an operation temperature between 600 °C and 700 °C belong to the $Ln_{1-x}Sr_xCo_{1-y}Fe_yO_{3-\delta}$ (LSCF, where Ln – e.g. La, Sm, Nd, Gd, Dy) $Ln_{1-x}A_xM_{1-y}Mn_yO_{3-\delta}$ (LSCM, where Ln – e.g. La, Nd, Pr; A – Ca, Sr; M – a 3d metal different from Mn) systems. Furthermore, the compounds $La_{1-x}Sr_xNi_{1-y}Fe_yO_{3-\delta}$ and $LaNi_{1-y}Co_yO_{3-\delta}$ are systems of current interest [15]. These compositions have been described in the literature as materials with better electrochemical properties than the manganese containing compositions [16-24]. However, they are more problematic regarding the chemical compatibility [23, 25-28] with the electrolyte and the CTE [29].

However, materials for fuel cell components need to be modified in order to reduce the losses at lower operating temperatures. All cell components from the anode and electrolyte to the cathode and the current collector contribute to the losses of the SOFC reducing the efficiency. The activation energy of the cathode (oxygen reduction electrode) is significantly higher (110 – 140 kJ mol^{-1}) than the activation energy for the anode (80 – 90 kJ mol^{-1}) and the one of the YSZ electrolyte (80 - 90 kJ mol^{-1}). Thus at lower temperatures the largest part of the overall fuel cell resistance originates from the polarization resistance of the cathode [30].

Due to a large variety of materials and approaches to achieve a well performing microstructure, particularly the cathode has a potential to be improved. Therefore, the development of cathodes especially for lower operating temperatures is still in progress. Reducing the operating temperature to the level of 600 °C will have a large impact on lifetime and costs of SOFC system, thereby facilitating the commercial introduction of clean and efficient SOFC technology for combined heat and power generation in society, as well as auxiliary power for transport applications.

1.4 Advantages of mixed conducting materials for the use as cathode materials

Mixed ionic and electronic conductors (MIECs) are candidates for the application as cathodes in the temperature range between 550 °C and 650 °C. The advantage is the ability to transport the oxygen ions trough the material to the electrolyte. Due to this fact the reaction zone can be extended from the triple phase boundary (gas, cathode and electrolyte) to a remarkably larger area of the cathode as illustrated in Figure 5. The comparison with an exclusively electronic conducting material shows schematically the extended reaction zones of molecular oxygen (marked in red) that is reduced into oxygen ions that can be incorporated into the electrolyte after reduction. Appropriate cathode materials for low operating temperatures should provide a high electrical conductivity, high catalytic activity for the oxygen reduction reaction and preferably ionic conductivity.

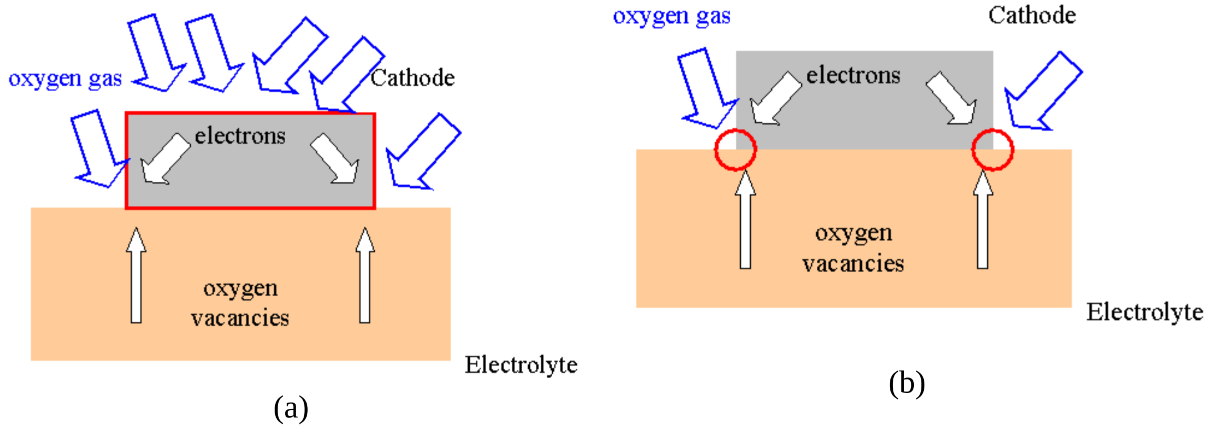

Figure 5: Comparison between electronic (a) and mixed conducting (b) cathode materials for SOFC.

Powders of four mixed conducting materials were synthesised to be compared regarding the suitability as cathodes for operation at 600 °C. The approach to develop a well performing cathode for the above temperature comprises the evaluation of the material properties, the selection of one suitable material and therewith the application as a cathode by screen printing of dispersed powders and subsequent firing. The quality of the layers is evaluated by scanning electron microscopy and impedance spectroscopy. The microstructures and the obtained polarization resistances of the layers are compared to literature values and models to evaluate the chosen approach to well performing cathodes for 600 °C operating temperature.

The thesis first addresses the assessment of material properties of four different cathode materials for SOFC cathodes from the (Ba,La,Sr)(Co,Fe)$O_{3-\delta}$ system. First of all the phase purity, the chemical compatibility with the electrolyte, the shrinkage behaviour and the CTE of dense specimen are evaluated. The selection of one material for the development of screen printing slurries to be applied as SOFC cathode is addressed in chapter 3 and 4. These two chapters are regarding the material synthesis and characterization as well as the evaluation of the electrical conductivity and the kinetic parameters regarding the oxygen exchange and transport properties of the materials. The different screen printing slurries were used for the development of cathodes with diverse microstructures. Chapter 5 discusses the polarization resistance of cathodes as a function of the microstructure and the precursor powders. Finally, the connection between microstructure, electrical properties, oxygen exchange kinetics as material properties and the polarization resistance as performance parameter for SOFC cathodes are being discussed.

2 SOFC cathodes for operating temperatures between 550 °C and 650 °C

Suitable cathode materials have to show mechanical and chemical stability at high temperatures as well as high electronic conductivity and catalytic activity for the oxygen reduction reaction. The thermal expansion of the cathode has to be matched with the electrolyte and the current collector requiring a coefficient of thermal expansion similar like the used solid electrolyte. Furthermore, long term stability under operation conditions is desirable. BSCF, for example, is an upcoming cathode material, that shows a high performance in the interesting temperature range between 550 °C and 650 °C.

Parameters of interest consequently are: electronic and ionic conductivity, surface exchange and diffusion coefficient, coefficient of thermal expansion and furthermore, thermodynamic stability of cathode materials in combination with the above mentioned impurities and neighbouring materials. The polarization resistance and the area specific resistance obtained from electrochemical measurements can be modelled from the kinetic parameters, the conductivity (σ) and the cathode microstructure as shown by Adler et al. [31], Søgaard et al. [32] and Rüger et al. [33].

2.1 Oxygen reduction mechanisms

The most important mechanisms thought to cover the oxygen reduction in SOFC cathodes are described in more detail by Adler et al. [34] and are displayed in Figure 6. α,β and γ refer to the electronically conducting phase, the gas phase, and the ionically conducting phase, respectively:

(a) Incorporation of oxygen into the bulk of mixed conductors

(b) Adsorption and/or partial surface reduction of oxygen on the α-phase

(c) Transport of O^{2-} in the bulk of the mixed conductor or

(d) Transport of O^{2-} or O^{n-} on the surface to the α/γ interface

(e) Charge transfer of O^{2-} (electrochemically) or

(f) Charge combinations of O^{n-} and e^-, respectively, occurring through the β/γ interface

(g) One or more of these mechanisms can be rate determining, the electrolyte acts generating and transporting oxygen ions.

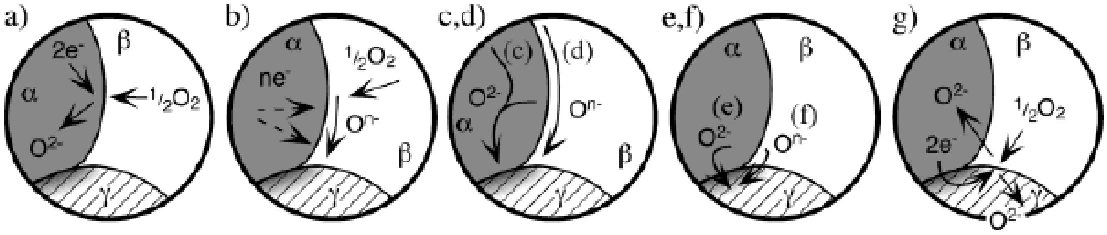

Figure 6: Different mechanism concerning the oxygen reduction reaction in SOFC cathodes from Adler et al. [34].

The overall cathode reaction can be expressed in the Kröger-Vink-notation

$$O_{2,g} + 2V_{O,electrolyte}^{\bullet\bullet} + 4e^{-}_{cathode} \Leftrightarrow 2O^{x}_{O,electrolyte} \qquad \text{Equation 9}$$

where molecular oxygen of the gas phase is reduced in several steps. Finally the oxygen ions are incorporated into the electrolyte via vacancies and transported to the anode side of the fuel cell. An appropriate model to characterize the catalytic activity of the SOFC cathode is based on the cathode microstructure. Furthermore, the electrical conductivity, and the oxygen exchange and transport properties of the cathode material have to be considerd.

2.2 Models describing the influence of the kinetic parameters, the conductivity and the cathode microstructure on the cathode performance

2.2.1 Overview of different approaches

Different models are available in the literature to estimate the polarization resistance of a SOFC cathode at a given temperature from the kinetic parameter and the conductivity.

Prestat et al. give an overview [35, 36] regarding the development of $La_xSr_{1-x}Co_yFe_{1-y}O_{3-\delta}$ (LSCF) cathodes starting with the Adler model considering the defect chemistry and the impact of the mixed conductivity on dense and porous cathodes. Strontium- and iron-substituted lanthanum cobaltites (LSCF) have become interesting as suitable materials for intermediate temperature SOFCs since 1995 [18, 37]. The electro catalytic activity of LSCF is higher than that of $La_xSr_{1-x}MnO_{3-\delta}$ (LSM) regarding the reduction of oxygen. Having similar electronic conductivity as LSM, LSCF exhibits better bulk transport properties of oxygen. Adler et al. [31] described one of the first models for mixed conducting cathode materials. The impedance spectra of symmetrical cells were compared with the modelled results and are the proof for the quality of this model.

The importance of the charge transfer at the electrode/electrolyte interface is concerned by Liu and Wu [38], measuring the impedance of porous $La_{0.7}Sr_{0.3}Co_{0.2}Fe_{0.8}O_{3-\delta}$ electrodes at equilibrium with various electrolyte materials. They observe a remarkable effect of the electrolyte materials on the area specific resistance (ASR) of the cathode reaction. The impedance of porous and dense LSCF electrodes was the topic of a comparison of Sirman et al. [39]. The dense electrode of 1 µm thickness showed a significantly larger polarization resistance than the porous one. Steele and Bae [40] additionally measured the influence of a dense LSCF layer (1 µm thick) placed between a porous LSCF film and a CGO electrolyte. The area specific resistance of single layer porous cathodes was interpreted by the use of oxygen surface exchange coefficients, available in the literature. The ASR was reduced by a factor of 2-3 by introducing a thin (1 µm) dense layer of $La_{0.6}Sr_{0.4}Co_{0.2}Fe_{0.8}O_{3-\delta}$ (LSCF) in contact to the gadolinium-doped cerium oxide (CGO) electrolyte. This effect could be explained by the increase of the effective interfacial contact area between LSCF and CGO. The calculations [40] using data for oxygen self diffusion coefficients resulted in much higher ASR values than determined experimentally for these duplex layer cathode structures possibly due to rapid diffusion via grain boundaries.

Esquirol et al. [41] pointed out the importance of oxygen non-stoichiometry. Their studies cover the properties of the interface between porous LSCF and CGO. Above 600 °C LSCF is supposed to be oxygen-non-stoichiometric and shows mixed ionic-electronic properties enhancing the contribution of the bulk pathway. Below this temperature the surface pathway is favoured due to the absence of oxygen vacancies for bulk diffusion.

2.2.2 Adler model and concept of penetration depth

The mechanism of the oxygen reduction is still discussed for mixed ionic-electronic electrodes [34]. Adler et al. suggested a mechanism for oxygen reduction at porous $La_{0.6}Ca_{0.4}Co_{0.2}Fe_{0.8}O_{3-\delta}$ and LSCF cathodes [31]. The authors assumed the oxygen surface exchange as well as solid-state diffusion to be rate-determining, while the charge transfer step at the electrode/electrolyte to be almost negligible. The total cell impedance (Equation 10) is mathematically equivalent to the Gerischer impedance.

$$Z = R_{chem}\sqrt{\frac{1}{1-j\omega t_{chem}}} \qquad \text{Equation 10}$$

The characteristic resistance ($R_{chem,}$ Equation 11) describes the chemical contribution to the cell impedance at a defined temperature (T), j the imaginary unit, ω the frequency of the perturbation and t_{chem} the characteristic time constant.

$$R_{chem} = \frac{RT}{2F^2}\sqrt{\frac{\tau}{(1-\in)c_v D_v a r_0(\alpha_f + \alpha_b)}} \qquad \text{Equation 11}$$

R is the gas constant, F the Faraday constant, and (α_f and α_b) are constants depending on the specific mechanism of the exchange reaction. The parameters are the porosity ($\in$) of the cathode, the vacancy concentration (c_v), the vacancy diffusion coefficient (D_v), the internal surface area (a) and the tortuosity (τ), the exchange neutral flux density $r_{0.}$ They have to be evaluated or assumed and put into the model. Furthermore, the gas diffusion and the charge transfer between the cathode and the electrolyte play a role. The modelling and experiments [31] were carried out with symmetrical cells in the equilibrium state. The surface pathway was not considered in the reaction mechanism. The "chemical capacitance" (C_{chem}), defined in Equation 12, can be obtained dividing the characteristic time constant (t_{chem}) by the characteristic resistance (R_{chem}),

$$C_{chem} = \frac{t_{chem}}{R_{chem}} = \frac{2F^2(1-\in)c_v\delta}{ART} \qquad \text{Equation 12}$$

where δ is the penetration depth that corresponds to the extension of the reaction zone beyond the three-phase boundary due to mixed conduction in the porous electrode. δ is obtained by the normalization of the critical length (L_c= D/k) with structural parameters (Equation 13).

$$\delta = \sqrt{\frac{(1-\in)}{\tau}\frac{L_c}{a}}\ .$$ Equation 13

For large values of δ (≥ 1 μm), this extension results in a large chemical capacitance, which allows to distinguishing the chemical contributions to the cell impedance because of the different characteristic time constant. However, for large values of δ the chemical capacitance will be on the same order as the interfacial capacitances (between cathode/electrolyte and cathode/current collector) in the system. Chemical processes cannot be distinguished from other processes that dominate near the three-phase boundary under these conditions. Figure 7 shows a qualitative picture of the vacancy concentration profiles in the cross section of an electrode particle. The reduction reaction can take place over the entire surface of the particle when the penetration depth is much larger than the average particle size (d_p) and the entire particle is reduced (a). However, when δ is much smaller than d_p only a small part of the mixed conductor close to the electrolyte is reduced (b), leading to a reduction reaction restricted to a region close to the three-phase boundary [31]. Thus average particle sizes smaller than δ are supposed to increase the catalytical activity for the oxygen exchange reaction.

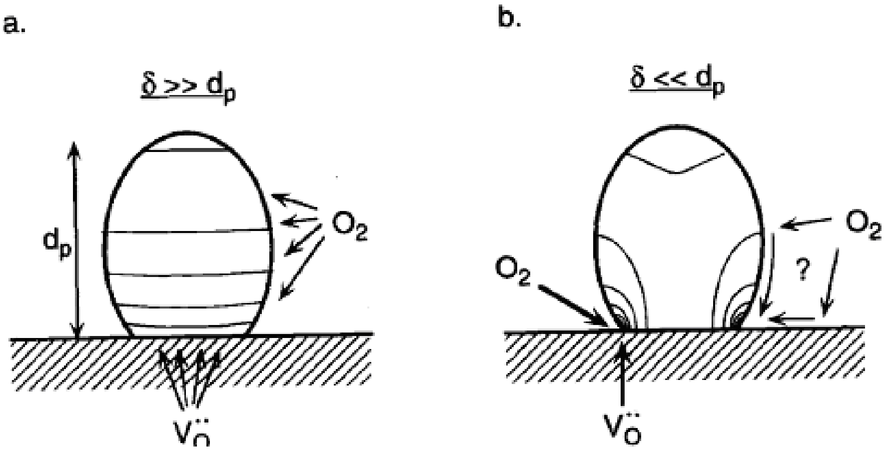

Figure 7: Illustration of the penetration depth according to Adler et al. [31] and the influence of the particle size.

2.2.3 Three-dimensional model and model using segmented layers

A three-dimensional model and the performance evaluation by the ASR of LSCF cathodes was presented recently by Rüger et al. [33]. This model will be used for the comparison of the cathode microstructures and the R_{pol} of the cathodes in Chapter 5. The model takes into account the processes (i) gas diffusion, (ii) surface exchange, (iii) bulk diffusion and (iv) charge transfer as illustrated in Figure 8 at constant temperature and constant pressure.

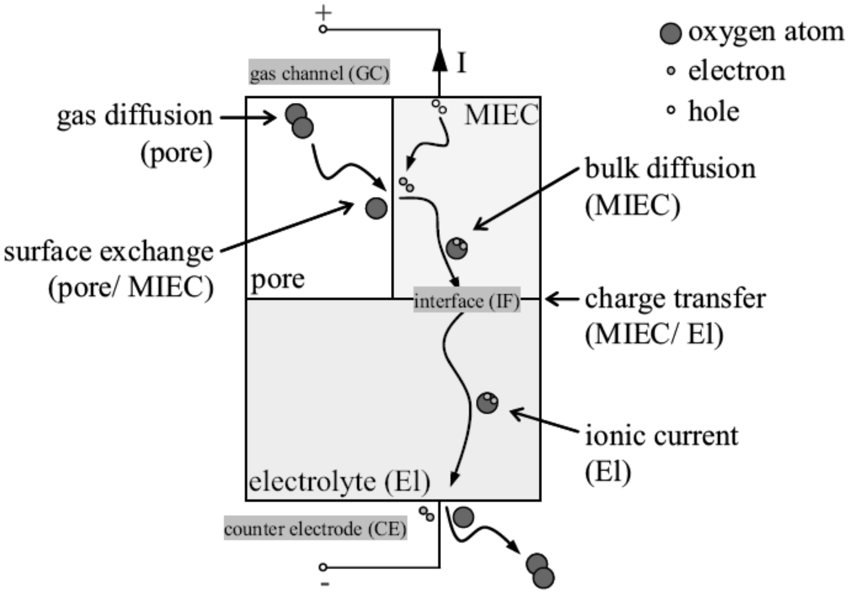

Figure 8: Illustration of the processes in a cathode/electrolyte interface after Rüger et al. [33].

The oxygen partial pressures on the anode and cathode side (p_{GC}, p_{CE}) as well as the potentials of the electrodes (Φ_{MIEC}, Φ_{CE}) are defined as the four boundary conditions. The electrode potential of the cathode (Φ_{MIEC} , Equation 14) contains all voltage losses (η_{Model}) attributed to the model. At η_{Model} = 0 V the current I = 0 A, whereas with increasing η_{Model} values the current I in the model is created.

$$\Phi_{MIEC} = U_{Nernst}(p_{GC}, p_{CE}) + \Phi_{CE} + \eta_{Model} \qquad \text{Equation 14}$$

The area specific resistance of the cathode is calculated by Rüger et al. [33] as a characteristic measure for the MIEC cathode performance ($ASR_{Model} = \eta_{Model} / I\ A$), where A is the corresponding area of the cathode. The current density is integrated in order to obtain the current (I). The electrolyte resistance ($ASR_{El} = l_{el} / \sigma_{El}$) can be substracted, because the electrolyte length l_{el} and the ionic conductivity σ_{El} of the electrolyte are known. Resulting from the above formula the area specific resistance of the cathode ($ASR_{cat} = ASR_{Model} - ASR_{El}$) can be calculated. Rüger et al. [33] take the influence of current constriction in the electrolyte into account, which is in contrast to one-dimensional models. This additional loss contributes to the ASR_{cat}, which can be compared with the measured values.

Figure 9 shows the simulated area specific cathode resistance (ASR_{cat}) at 800 °C. A, B, C, and D denote different combinations of kinetic parameter (k_O, D_O). The calculated characteristic map of the ASR_{cat} can be divided into three regions:

(i) Surface controlled ASR_{cat} occurs in case of small k_O-values, if the diffusion of oxygen ions within the material is rather fast. The ASR_{cat} is exclusively determined by the value of k_O (right of the dotted line).

(ii) Left to the dotted line, both surface exchange k_O and diffusion coefficient D_O determine the ASR_{cat} equally and increases with decreasing k_O and D_O values.

(iii) Small D_O-values in contrast to large k_O-values lead incorporation of oxygen favourably at the triple phase boundary (= short diffusion length, because diffusion becomes negligible).

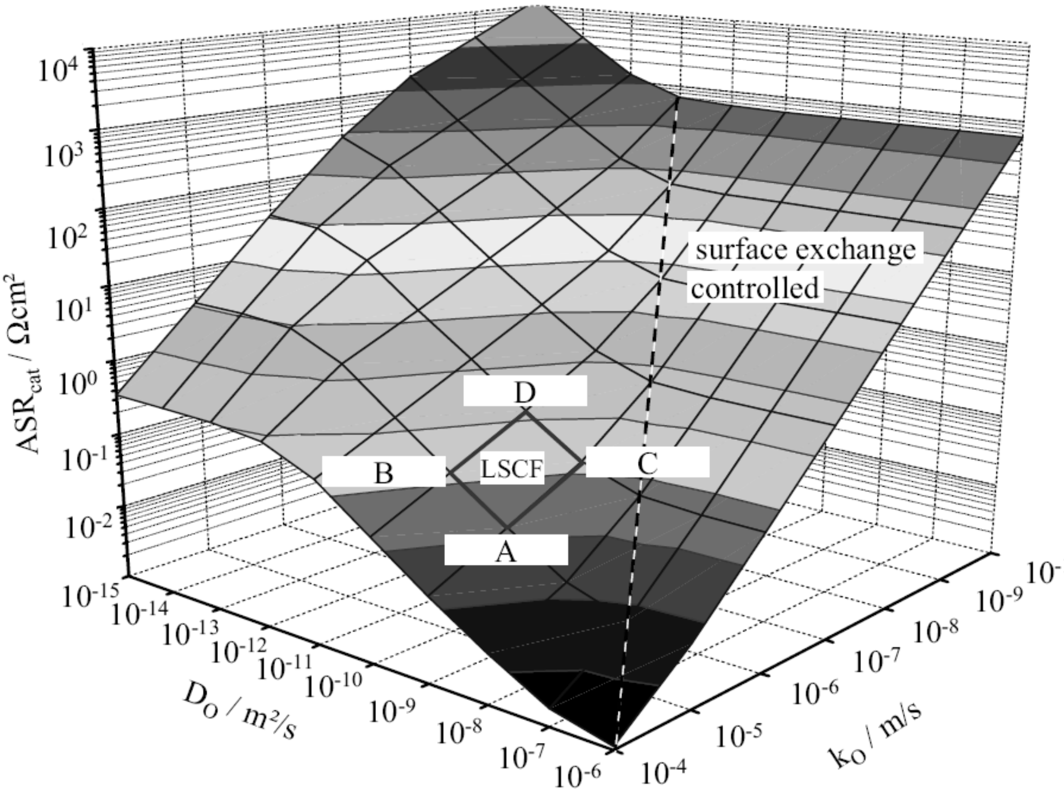

Figure 9: The modelled area specific cathode resistance ASRcat at 800 °C, from Rüger et al. [33].

The Rüger model [33] allows to calculate the ASR_{cat} as a function of the particle size, (cube length in the model). The four different combinations of the kinetic parameters (A, B, C, D) with a constant cathode thickness of 12 µm show an improvement (= decrease) of the ASR_{cat} by a factor of ~ 2 decreasing the particle size from 1 µm to 250 nm.

The ASR_{cat} was simulated for cathode thicknesses (l_{cat}) of 12 and 30 µm and is displayed in Table I (taken from [33]). The parameter combinations (A, B, C and D) represent a "typical" LSCF ($La_{0.6}Sr_{0.4}Co_{0.2}Fe_{0.8}O_{3-\delta}$) cathode at a temperature of 800 °C with exchange coefficients k_O between 10^{-6} m/s and 10^{-5} m/s and with bulk diffusion coefficients D_O between 10^{-10} m^2/s and 10^{-9} m^2/s, according to literature data [32, 42]. The ASR_{cat} of an LSCF cathode should vary between 38 mΩcm^2 and 385 mΩcm^2 related to that when its thickness is between 12 and 30 µm. The penetration depth (δ) is additionally given as an important measure for cathode structures. If δ amounts in a large fraction of the cathode thickness, a decrease of the ASR_{cat} is possible by an increase of the cathode thickness according to Adler et al. [31].

Table I: The area specific cathode resistance ASR_{cat} and the penetration depth δ at 800 °C as a function of different parameter combinations (from Rüger et al. [33]).

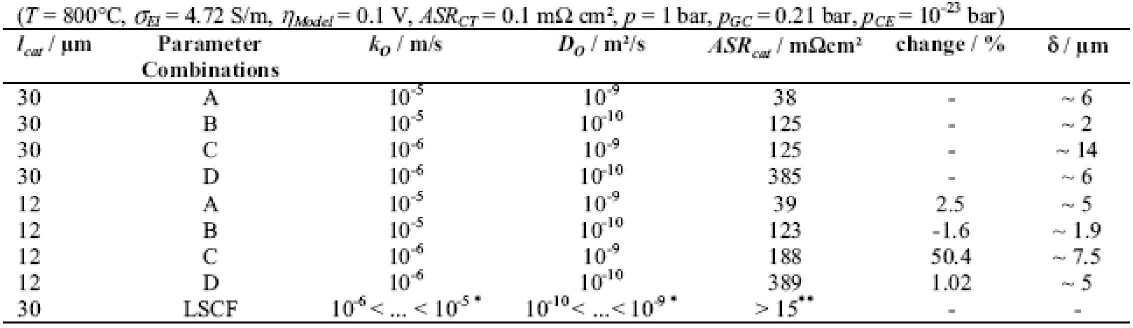

($T = 800°C$, $\sigma_{El} = 4.72$ S/m, $\eta_{Model} = 0.1$ V, $ASR_{CT} = 0.1$ mΩ cm², $p = 1$ bar, $p_{GC} = 0.21$ bar, $p_{CE} = 10^{-23}$ bar)

l_{cat} / µm	Parameter Combinations	k_O / m/s	D_O / m²/s	ASR_{cat} / mΩcm²	change / %	δ / µm
30	A	10^{-5}	10^{-9}	38	-	~ 6
30	B	10^{-5}	10^{-10}	125	-	~ 2
30	C	10^{-6}	10^{-9}	125	-	~ 14
30	D	10^{-6}	10^{-10}	385	-	~ 6
12	A	10^{-5}	10^{-9}	39	2.5	~ 5
12	B	10^{-5}	10^{-10}	123	-1.6	~ 1.9
12	C	10^{-6}	10^{-9}	188	50.4	~ 7.5
12	D	10^{-6}	10^{-10}	389	1.02	~ 5
30	LSCF	$10^{-6} < ... < 10^{-5}$ *	$10^{-10} < ... < 10^{-9}$ *	> 15**	-	-

An entire cathode thickness l_{cat} of 12 µm would be sufficient for parameter combination B with $k_O = 10^{-5}$ m/s and $D_O = 10^{-10}$ m^2/s and δ ~ 2 µm. However, for parameter combination C with $k_O = 10^{-6}$ m/s and $D_O = 10^{-9}$ m^2/s and δ ~ 14 µm the cathode thickness l_{cat} of 30 µm is still insufficient. The three-dimensional model of Rüger et al. [33] hence provides information required for the selection of the "optimum" thickness l_{cat} of a MIEC cathode as a function of k_O and D_O.

Søgaard et al. [32] presented a model for composite cathodes using an approach dividing the cathode into segments. The percolation of the phases and the estimated contact area with the electrolyte were taken into account modelling the polarization resistance of cathodes as a function of the different grain sizes of a mixed electronic/ionic cathode material and CGO as ionic conducting part, cathode film thickness and porosity. They showed that the measured results of the polarization resistance of two cathodes with different grain sizes and porosity could be successfully approximated by the model. The results of measurements and the corresponding models show that a decrease in the porosity from 50 to 30 per cent as well as a decrease in the particle size lead to a decrease in the polarization resistance from approximately 1 Ωcm^2 to 0.2 Ωcm^2 at 600 °C and from 0.03 Ωcm^2 to 0.01 Ωcm^2 at 800 °C.

2.3 Influence of cathode engineering on performance

2.3.1 LSCF

In the literature various approaches to obtain well performing cathode microstructures are proposed. Differences in the performance of the layers are supposed to be not only dependent on the microstructure but also on the preparation of the cathode.

Jiang et al. [43] investigated O_2 reduction reactions on $(La,Sr)MnO_{3-\delta}$ (LSM) and $(La,Sr)(Co,Fe)O_{3-\delta}$ (LSCF) electrodes at temperatures between 700 and 900 °C. They devided the reduction of O_2 on the LSM electrode in three reaction steps: first surface dissociative adsorption and diffusion, then charge transfer and oxygen ion migration into the electrolyte. Dissociative adsorption and diffusion are rate determining at low temperatures while the oxygen ion migration/diffusion into the zirconia electrolyte becomes dominant at high temperatures. Regarding the results of the LSCF cathode of Jiang et al. [43], this study indicates that both surface and bulk diffusion processes are essential for the overall O_2 reduction kinetics. The lowest total resistance of the LSCF electrodes measured therinwas between 0.32 Ωcm^2 at zero polarization and 0.2 Ωcm^2 at 28 mV polarization and 700 °C.

Lei et al. [44] investigated cathodes from nano crystalline $La_{0.6}Sr_{0.4}Co_{0.2}Fe_{0.8}O_{3-\delta}$ (LSCF) powder with a specific surface area of 22.9 m^2 g^{-1} and an average particle size of 175 nm as prepared by a glycine-nitrate solution combustion method and subsequent ball-milling. The single cell Ni–YSZ/YSZ/LSCF with the cathode sintered at 750 °C demonstrates the lowest polarization resistance. As a drawback of the low sintering temperature the instable cathode microstructure is mentioned. Polarization resistances as low as 0.2 Ωcm^2 are reported at 650 °C for the sum of cathode and anode electrodes for cells with LSCF cathodes sintered at 800 °C.

2.3.2 Composites

Zhao et al. [45] present $La_{0.6}Sr_{0.4}Co_{0.2}Fe_{0.8}O_{3-\delta}$ /$Ce_{0.7}Bi_{0.3}O_2$ (LSCF–CBO) electrodes, prepared by the polymer–gel method. and report a good contact between the composite electrode and the $Ce_{0.9}Gd_{0.1}O_{1.95}$ (CGO) electrolyte after sintering at 900 °C for 2 h. The oxygen adsorption/desorption process was identified as the rate limiting step, indicated by the dependence of the polarization resistance $R_{pol} \propto p(O_2)^{1/2}$ on the oxygen partial pressure. The area specific resistivity resulted in 0.16 Ωcm^2 and activation energies around 1.4 eV at 706 °C in air with an optimum additon of 35 vol% CBO in LSCF.

Dusastre et al. [46] investigated the properties of $La_{0.6}Sr_{0.4}Co_{0.2}Fe_{0.8}O_{3-\delta}$ /$Ce_{0.9}Gd_{0.1}O_{1.95}$ composite cathodes. A four times lower area specific resistivity could be reached by the addition of 36 vol% $Ce_{0.9}Gd_{0.1}O_{1.95}$ to $La_{0.6}Sr_{0.4}Co_{0.2}Fe_{0.8}O_{3-\delta}$ in comparison with pour LSCF. The authors point out the consistence with the effective medium percolation theory. At 590 °C pour faces of LSCF typically amount to 4 Ωcm^2 and composites to values lower than 1 Ωcm^2 (best cathode 0.6 Ωcm^2 at 590 °C) with activation energies between 0.95 and 1.5 eV.

Hwang et al. [47] tested symmetrical electrochemical cells with various electrodes, namely $La_{0.6}Sr_{0.4}Co_{0.2}Fe_{0.8}O_{3-\delta}$, (LSCF), LSCF–($Ce_{0.9}Gd_{0.1}O_{1.95}$) CGO 40 vol%, LSCF–platinum (Pt) and LSCF–CGO–Pt 1 vol%. Impedance spectroscopy was used to investigate the relationship between the electro catalytic properties and electrode microstructure of the electrochemical cells. They concluded that Pt might accelerate the oxygen adsorption at high temperature, CGO at lower temperatures (500-600 °C) seemed to serve as path for fast oxygen ion diffusion. CGO/LSCF at 600 °C showed lower R_{pol} (4 Ωcm^2) than the pure LSCF cathode (12 Ωcm^2). The decrease of the activation energy from 1.47 eV to 1.26 eV was attributed to the CGO addition.

Murray et al. [48] studied $La_{0.6}Sr_{0.4}Co_{0.2}Fe_{0.8}O_{3-\delta}$ (LSCF) and LSCF–$Ce_{0.8}Gd_{0.2}O_{1.9}$ (CGO20) composite cathodes on YSZ electrolytes for potential applications in low-temperature solid oxide fuel cells (SOFCs). The impedance was measured over a temperature range from 500 °C to 750 °C at $p(O_2)$ between 10^{-3} and 1 atm. The LSCF electrodes exhibit by a factor of 10 lower low-current interfacial resistance than observed for $(La,Sr)MnO_3$ cathodes. The polarization resistance could be lowered further by a factor of 10 by the addition of 50 vol% CGO20 to LSCF. Values for the LSCF–CGO20 cathodes were as low as 0.01 Ωcm^2 at 750 °C and 0.33 Ωcm^2 at 600 °C.

Mai et al. [49] studied various ferrite-based cobalt-containing perovskites as cathode materials. Differently to Murray et al. [48] and Lei et al. [44] they placed an interlayer of the composition $Ce_{0.8}Gd_{0.2}O_{1.9}$ between the electrolyte and the cathode to prevent undesired chemical reactions between the materials. Different compositions of $La_{1-x-y}Sr_xCo_{0.2}Fe_{0.8}O_{3-\delta}$ (x =0.2 and 0.4; y = 0-0.05) were tested. The cathodes resulted in a factor two higher current densities (1.76 Acm^{-2} at 800 °C and 0.7 V) than the state-of-the-art manganite-based cathodes. Addtionally the A-site deficiency (denoted with y) and high strontium content were found to have a positive effect on the cell performance. The area specific resistance for whole cells in operation was reported to be between 0.2 and 1 Ωcm^2 measured at 650 °C.

2.3.3 Thin layers

Baumann et al. [50] studied dense thin film microelectrodes of $La_{0.6}Sr_{0.4}Co_{0.2}Fe_{0.8}O_{3-\delta}$ prepared by pulsed laser deposition and standard photolithographic techniques on YSZ substrates. The oxygen exchange reaction at the surface of the electrode was identified to be the largest part of the electrochemical resistance (5 Ωcm^2 at 750 °C) under zero or small dc bias.The chemical capacitance of this main process is associated with oxygen stoichiometry changes in the bulk of the electrode. Furthermore, an additional capacitance of the interface between the electrode and the electrolyte is present.

Beckel et al. [51] showed the fabrication of $La_{0.6}Sr_{0.4}Co_{0.2}Fe_{0.8}O_{3-\delta}$ (LSCF) based thin film cathodes by spray pyrolysis with a maximum processing temperature of 650 °C. The study shows that it is possible to reach comparable ASR (<1 Ωcm^2 at 650 °C) with 500 nm thick cathodes as with thick film LSCF cathodes (10–100 µm) by reducing the grain size or introducing a thin dense cathode layer between the porous cathode and the electrolyte. The activation energy was reduced from 1.55 eV to 1.18 eV.

2.4 Material systems for SOFC cathodes at reduced operating temperature

The compounds of LSC group are based on strontium-substituted $LaCoO_{3-\delta}$, which shows a quite high ionic–electronic conductivity up to 650 Scm^{-1} at 800 °C. However, this material exhibits a relatively high coefficient of thermal expansion [29], much higher than the electrolyte materials suitable for the application in SOFC (i.e. GDC, LSGM, YSZ). Coefficients of thermal expansion of the materials from the $La_{1-x}Sr_xFeO_{3-\delta}$ (LSF) group are considerably low and close to those of the electrolytes; still, their conductivity is not satisfying. Nevertheless, it is possible to combine the benefits of these materials applying mixed perovskites like LSCF.

The high metallic conductivity of the $LaNi_{1-y}Co_yO_{3-\delta}$ type compounds with suitably low thermal expansion coefficient seems to be promising [15]. However, these materials show notably lower thermal stabilities and the influence of Ni on the ionic conductivity is not fully understood so far.

Several materials of interest mostly from the $(La,Sr)(Co,Fe)O_{3-\delta}$ system for the application as cathode for SOFCs were compared regarding the CTE by Petric et al. [29]. Most mixed conducting materials have a large mismatch in the CTE compared to the electrolyte materials in contrast to the almost pure electronic conductor $(La,Sr)MnO_{3-\delta}$ (LSM).

Ullmann et al. [52] show the correlation between the CTE and the ionic conductivity. High ionic conductivity seems to be always connected with a high CTE in comparison with the electrolyte material. This difference limits the applicability of the cathode material due to mechanical stress especially when the fuel cell is thermally cycled.

Regarding the $(Ba,Sr)(Co,Fe)O_{3-\delta}$ system that is of recent interest, Wei et al. [53] discuss the crystal structure thermal expansion. Li et al. [54] studied $(Ba_{0.5}Sr_{0.5})_{1-x}La_xCo_{0.8}Fe_{0.2}O_{3-\delta}$ (BSLCF; 0.05<x<0.20) in relation to their potential use as intermediate temperature solid oxide fuel cell cathode. The CTE of BSLCF is increasing slightly with the increasing content of La, and all the compounds showed an increasingly high expansion at high temperature. Proved by TG, it was associated with the loss of lattice oxygen.

2.5 Review on the state of art cathode materials from the (Ba, La, Sr)(Co, Fe)$O_{3-\delta}$ system

$(La_{0.8}Sr_{0.2})_{0.95}FeO_{3-\delta}$ (LSF82), $La_{0.6}Sr_{0.4}FeO_{3-\delta}$ (LSF64), $La_{0.6}Sr_{0.4}Co_{0.2}Fe_{0.8}O_{3-\delta}$ (LSCF) and $Ba_{0.5}Sr_{0.5}Co_{0.8}Fe_{0.2}O_{3-\delta}$ (BSCF) were investigated within this study. The $(Ba,La, Sr)(Co,Fe)O_{3-\delta}$ material system is therefore described in more detail in the following chapter.

Materials from the $(La,Ba,Sr)(Fe,Co)O_{3-\delta}$ like the investigated $(La_{0.8}Sr_{0.2})_{0.95}FeO_{3-\delta}$ (LSF82), $La_{0.6}Sr_{0.4}FeO_{3-\delta}$ (LSF64), $La_{0.6}Sr_{0.4}Co_{0.2}Fe_{0.8}O_{3-\delta}$ (LSCF) and $Ba_{0.5}Sr_{0.5}Co_{0.8}Fe_{0.2}O_{3-\delta}$ (BSCF) are frequently proposed [16, 44, 48, 55, 56] for SOFC cathodes at intermediate temperatures. BSCF, which was initially developed for oxygen separation membranes [57] has later been tested in fuel cells with a partially substituted $Ce_{1-x}(Me^{3+})_xO_{2-x/2}$ electrolyte and presented as a high-performance cathode for the next generation of solid-oxide fuel cells [58] but studies on the kinetics and conductivity as e.g. [59] are scarce. A conductivity relaxation study of different compositions of $La_{0.6}Sr_{0.4}(Co,Fe)O_{3-\delta}$ is available in the literature [60], which can serve for the validation of the reliability of the evaluated parameters of this thesis. The composition of $(La_{0.8}Sr_{0.2})_{0.95}FeO_{3-\delta}$ (LSF82) in difference to $La_{0.8}Sr_{0.2}FeO_{3-\delta}$ [61] is slightly non stoichiometric on the A-site, aiming to reduce the incorporation of zirconia into the B-site of the perovskite which blocks the electrical conduction at the interface

YSZ/LSF82 [62]. A ceria interlayer can also reduce this effect of dissolution of Zr cations in the A-site of the perovskite. Suitable candidates should show high catalytic activity for the oxygen exchange reaction and a sufficiently high electronic conductivity for current pick-up.

A comprehensive study about different $La_xSr_{1-x}FeO_{3-\delta}$ materials regarding the structure, electrical and kinetic properties especially in reducing atmospheres is already available in the literature [63] and can serve as a comparison for the A-site deficient material discussed here. It is shown for several perovskites (e.g. LSF [25] and LSCF [64] that they react with yttria stabilized zirconia (YSZ) forming $LaZrO_3$. Alternative electrolyte materials as CGO or $LaGaO_3$ have to be applied when using these materials. Preferably dense interlayers between cathode and YSZ electrolyte can also overcome this problem.

Qiu et al. [65] showed that no reaction between LSCF and CGO occurs being annealed at 1200 °C for 36 hours. However, BSCF is claimed to react with CGO20 and YSZ [26].

The properties of the four materials compared in the present study were tested under equal experimental conditions. The characterisation of their electrical properties, oxygen exchange and transport is performed and discussed in terms of the fuel cell cathode application.

2.6 Influence of micro structural changes on cathode performance

2.6.1 Adhesion to the electrolyte, triple phase boundary length, porosity and thickness

The cathode microstructure is supposed to have a major influence on the catalytic activity and performance. The adhesion to the electrolyte is an important requirement for a suitable cathode in order to ensure an appropriate transfer of oxygen ions either via the triple phase boundary or from the bulk of the cathode into the electrolyte material. Good contact between cathode and electrolyte is the first precondition for a good electrochemical performance of the cathode. Steele et al. [40] found that a dense thin interlayer of LSCF between the electrolyte and the porous LSCF cathode could increase the performance by the factor 2-3. Furthermore, the authors discuss the influence of the kinetic parameters and the conductivity on the cathode performance in another publication [66].

The length of the triple phase boundary seems to be especially important for prevalently electronically conducting cathode materials such as (La,Sr)MnO$_{3-\delta}$ (LSM). The oxygen reduction is limited to areas close to the triple phase boundary. Composite mixtures with cathode and electrolyte powders increase the triple phase boundary and the performance of LSM cathodes. Mixed conductors (BSCF, LS(C)F) with sufficiently high ionic conductivity have the advantage to offer larger reaction areas for the oxygen reduction reaction thus extending the reaction zone several μm into the cathode.

The porosity of the cathode is important to allow fast gas diffusion to the reactive zone or to the triple phase line. Furthermore, the mechanical stability of the cathode, the resulting active surface area and a good connection between the grains to ensure the electrical conductivity of the cathode layer are factors that have to be considered in the fabrication of the cathode. Regarding the particle size, two different approaches can in principle be found in the literature: cathode microstructures with an average particle size in the micro and sub micro range and pastes with nano particles. These two aspects are described in the following two sub-chapters.

2.6.2 Conventional approach with μ and sub-μ particles

As an example among a large number of publications Murata et al. [67] prepared La$_{0.6}$Sr$_{0.4}$Co$_{0.2}$Fe$_{0.8}$O$_{3-\delta}$ (LSCF) powder through a citric synthesis route with average particle sizes of 0.66 and 0.53 μm after subsequent ball milling for 1.5 and 3 h, respectively. They showed that the cathode performance was strongly influenced by the starting particle size and the sintering temperature. The smaller cathode polarization for both 700 and 800 °C operating temperature was obtained with the cathode prepared from the finer powder (0.53 μm) and sintering at 850 °C as shown in Figure 10. The trend to reduce the polarization resistance lowering the particle size is clearly visible.

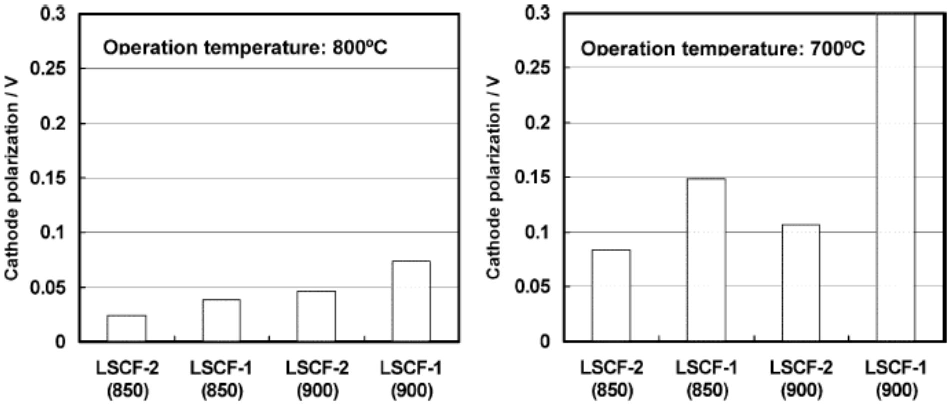

Figure 10: Polarization of cathodes prepared from sub-micro powders of different average particle sizes (LSCF-1 = 0.66 μm) and (LSCF-2 = 0.53 μm) at sintering temperature (°C, indicated below); as published by Murata et al. [67].

Starting from this approach the reduction of the primary particle size and therefore, the use of nano powders is supposed to further reduce the polarization resistance. This is in agreement with the model of Rüger et al. [33] and Søgaard et al. [32] that predict a decrease of the polarization resistance with the decrease of the particle size in the cathode layer.

2.6.3 Perspectives of sub micro and nano powders and mixtures in development of SOFC cathodes

Lei et al. [44] prepared nano crystalline $La_{0.6}Sr_{0.4}Co_{0.2}Fe_{0.8}O_{3-\delta}$ (LSCF) powder with a specific surface area of 22.9 m^2 g^{-1} and an average particle size of 175 nm. They used a nitrate-glycine solution combustion method and subsequent ball-milling. The authors point out the low polarization resistance of the electrodes and good adhesion of the cathode layer sintered as low as 750 °C. However, poor micro structural stability could be reached with this low sintering temperature. They could overcome this problem by pre-calcining the LSCF powder at 900 °C. The optimum sintering temperatue is increased to 850 °C with the benefit of improved maximum power density of > 1 Wcm^{-2} and 0.8 Wcm^{-2} at 0.7 V and 700 °C. The low temperature processing makes it possible to produce interlayer-free LSCF cathodes on YSZ with simplifyed microstructure while improving the cell performance providing a high surface area for the oxygen reduction reaction.

Søgaard et al. [30] and Mogensen et al. [68] recently reported the effect of infiltrated nano particles lowering the polarization resistance of SOFC cathodes and anodes by a factor between 3-10 times. The reasons are not totally clear and the authors suggest that the effect of impregnation with nano-particles occurs due to the nano-particles' ability to change the surface of the original electrodes in particular with respect to the triple phase boundary. However, after annealing at 980 °C this effect disappears.

2.7 Approach to cathode operating between 550 °C and 650 °C

Mixed conductors and small grain sizes, as can been seen in the previous literature review, seem to be the best approach for high performance cathodes at lower temperatures. The optimization of the cathode for operation at 600 °C is essential to reduce the parasitic losses and be able to produce highly efficient SOFCs with an enhanced life time. The reduction of the state-of-the-art operating temperature down to 600 °C requires the application of adequate materials and approaches like the application of nano powders being used for the production of cathodes in this work. The goal of the thesis is the selection of the most suitable cathode material selected out of four promising candidates.

The assessment of the powder quality is described in Chapter 3. The materials, namely LSCF, LSF64, LSF82 and BSCF were assessed regarding their material properties. After lab production by flame spray synthesis (nano powders) and spray pyrolysis (sub-μ powder) the powder properties were evaluated. Although the powders are partly commercially available, this approach was chosen for all materials in order to ensure the reproducibility of the synthesis. Additionally, flame spray synthesis was applied, because a one step synthesis of nano powders was possible in favourable cases.

Chapter 4 describes the evaluation of electrical conductivity and chemical surface exchange and diffusion coefficients (= oxygen exchange and transport) that were determined on dense bulk samples. Together with the above mentioned powder properties they served as selection criteria for the appropriate material. The described literature models ascribe a direct influence on the cathode performance to these properties. Together with the powder quality these properties served as selection criteria for one out of the four materials.

Chapter 5 describes the production of cathodes by screen printing [69, 70] and the ‘Proof of Concept’ of the material selection according to chapter 3 and 4 by the evaluation of the cathode polarization resistance as a fingerprint for the performance. The processing of nano powders requires special attention due to high shrinkage during drying and sintering. The cathode polarization is finally discussed in light of the material properties.

3 $La_{0.6}Sr_{0.4}Co_{0.2}Fe_{0.8}O_{3-\delta}$ and $Ba_{0.5}Sr_{0.5}Co_{0.8}Fe_{0.2}O_{3-\delta}$ synthesis and characterization

This chapter addresses the techniques used for powder synthesis and the characterization of powder properties. The powders were synthesized by two methods: spray pyrolysis and flame spray synthesis. The X-ray diffraction pattern was taken in order to check the phase purity of the powder, inductive coupled plasma - optical emission spectroscopy (ICP-AES) to analyse the elemental ratios in BSCF and LSCF. The sintering behaviour and the coefficient of thermal expansion were evaluated by dilatometry and the density of sintered pellets was checked with the Archimedes method.

3.1 Synthesis

3.1.1 Synthesis by spray pyrolysis

The spray pyrolysis is an important technique to synthesise powder batches in quantities between 500 g and 5 kg. The precursor that consists conventionally of nitrate solutions in water is sprayed into a preheated oven (540 °C) in order to evaporate the water, and subsequently to precipitate the raw ceramic powders. The subsequent calcination step at 700 °C serves to decompose most of the remaining nitrates and carbonates.

The spray pyrolysis device consists of a peristaltic pump in order to define the flow rate of the precursor suspension, a spray nozzle that is screwed leak proof to the faceplate of the oven with a gas outlet for the gases containing H_2O, CO_2 and NO_x. The schematic view of the oven is shown in Figure 11 on the left and with the steps from the precursor solution to a pure product on the right side.

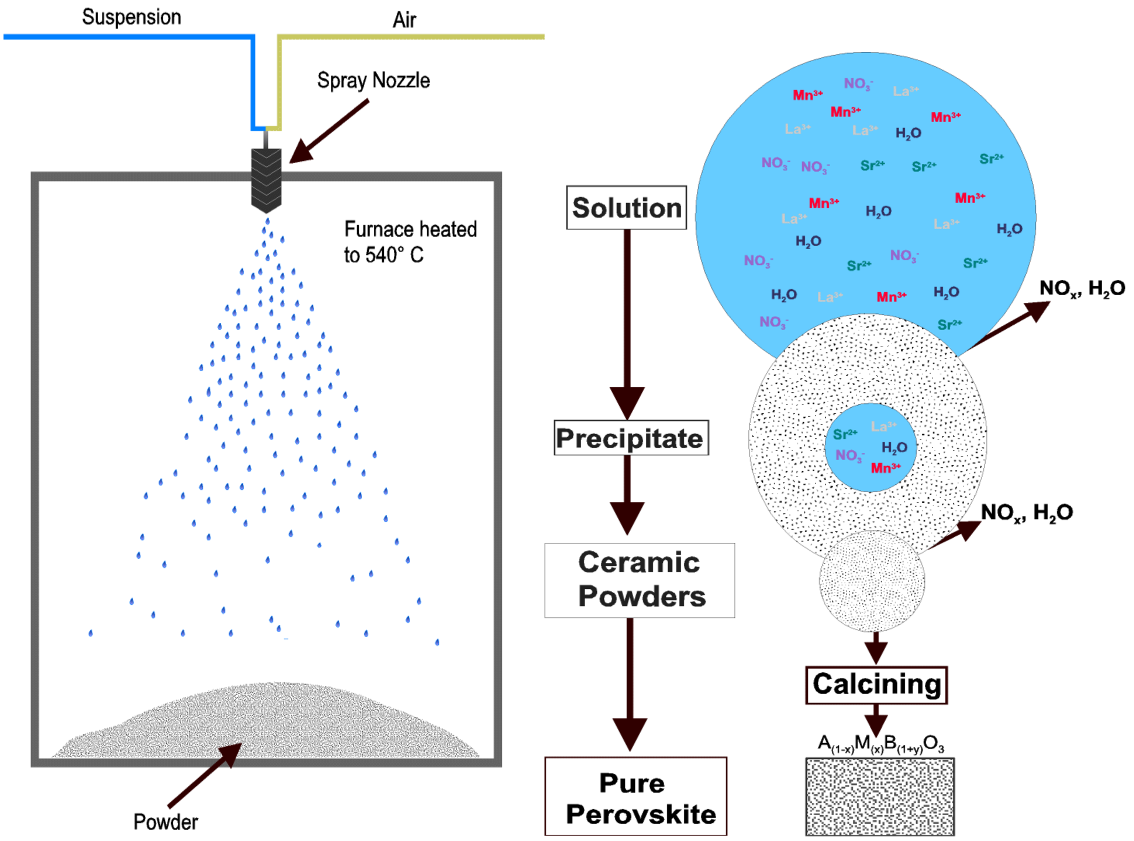

Figure 11: Spray pyrolysis: schematic view of the oven and the steps from the precursor solution to the phase pure product according to Holtappels et al. [71].

The nitrates of Ba, La, Sr, Co and Fe were dissolved first in water in the appropriate molar ratio to obtain $La_{0.6}Sr_{0.4}Co_{0.2}Fe_{0.8}O_{3-\delta}$ and $Ba_{0.5}Sr_{0.5}Co_{0.8}Fe_{0.2}O_{3-\delta}$ respectively (Table I). The appropriate amount of chemicals was weighted into a 10 L beaker and dissolved in deionised water. The adequate amount of cellulose (50 g/L) was added and stirred by a magnetic stirrer until the solution became transparent.

Table II: Initial weights of chemicals for BSCF and LSCF.

	$La(NO_3)_3.6H_2O$	$Ba(NO_3)_2$	$Sr(NO_3)_2$	$Fe(NO_3)_3.9H_2O$	$Co(NO_3)_2.6H_2O$
BSCF	--	597.26 g	483.67 g	369.41 g	1063.95 g
LSCF	3497.40 g	--	1140.20 g	4014.1 g	785.00 g
Flow rel. to maximum:	Air	10-15 %			
Peristaltic pump		12-15 RPM			

The solution is pumped through a nozzle by compressed air into a reaction compartment that is heated to 550 °C in order to atomize and pyrolyse in one step. The cellulose is acting as a fuel and combusted by the nitrates from the precursor solutions. In addition, a peristaltic pump is used in order to regulate the flux of the nitrate solutions. After spraying the solution the resulting powder is heated to 700 °C for two hours in order to eliminate most of the nitrates and carbonates, which are decomposing to a major part at this temperature. The obtained raw powders are still not phase pure and need calcining at temperatures between 900 °C and 1100 °C prior to further processing. The theoretical yield of 1000 g BSCF and 3000 g LSCF correspond to the initial weight of the raw chemicals. The yield of BSCF was 850 g and that of LSCF in 2800 g raw powder (85 and 93 % of relative to the theoretical yield).

3.1.2 Flame spray synthesis

The flame spray synthesis is a suitable technique to produce particles with a very high surface area. The temperatures in the flame are very high and under certain conditions it's possible to produce cristallographically phase pure powders directly in one step reaction [72]. The precursor solutions were prepared by dissolving stoichiometric amounts of the chemicals as can be seen in Table II. As solvent, a mixture of distilled water and dimethylformamide (DMF) in a ratio of 3:1 was used.

A special flame-spray unit was used for the synthesis with a cutting nozzle (red, Pangas, Switzerland) with a centered capillary, surrounded by a circular gap for the dispersion gas. And 6 supporting flamelets, positioned at a distance of 3.5 mm from the centre (Figure 12). A continuous double syringe pump (PN1610, Postnova Analytics, Germany) was used to control the flow rate of the precursor solution and pump it through a capillary tube. The precursor solution was dispersed at the exit by the oxygen (99.95%, Carbagas, Switzerland) supplied through the centre gas outlet. The carrier flamelets consist of a mixture of oxygen (17 l min^{-1}) and acetylene (13 l min^{-1}, both >99.5%, Carbagas, Switzerland) that was kept constant for all series of experiments. The gas flow rates were set by mass flow controllers (MFC, Bronkhorst, the Netherlands). The produced powder was collected in a baghouse filter (Friedli AG, Switzerland).

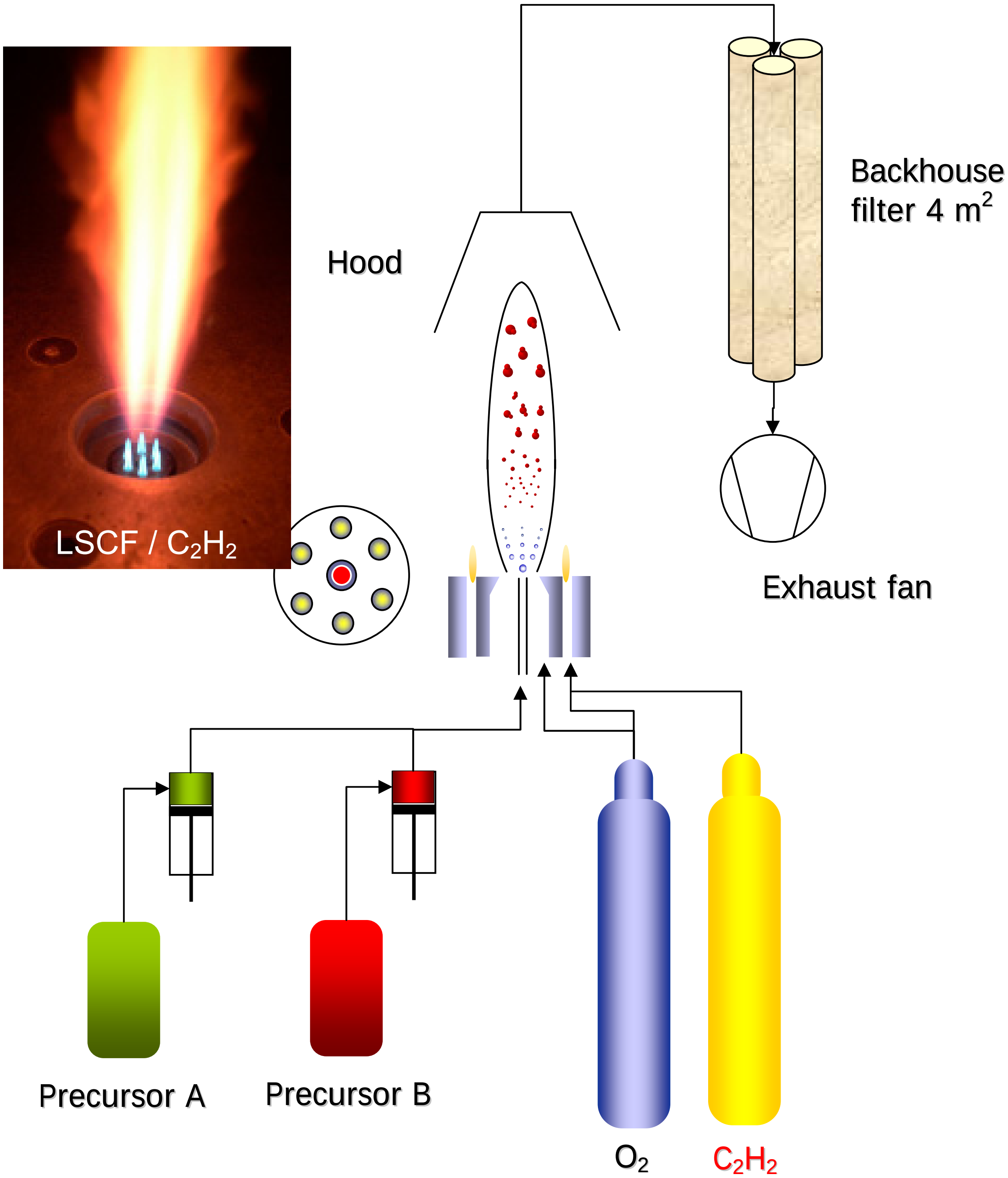

Figure 12: Schematic view of the flame spray synthesis device with gas and precursor feed, spray nozzle geometry and backhouse filter (with kind permission of Andre Heel [73]).

3.2 Characterization

3.2.1 Characterization techniques

X-ray diffraction

The powder diffraction pattern was recorded after putting an appropriate amount of roughly 1 g into the sample holder and pressing the powder into the mold inside the holder in order to ensure a flat homogeneous surface of the investigated powder. The crystal structure was analysed by X-ray diffraction (PANalytical X'Pert Pro MPD, Netherlands) with Cu-Kα (λ = 1.5405 Å) radiation. Scanning was carried out over a 2 θ range of 10–80° with a step size of 0.0167° within a scan time of 18 min.

Specific surface area according to Brunauer, Emmet, Teller (BET)

Quantities of approximately 1 g of sub-μ sized powder and 0.2 g nano powder were used to determine the specific surface area (SSA) of the powders after drying the powders for 12 hours at 180 °C under N_2 flow. The SSA was determined by a five-point nitrogen adsorption isotherm at 77 K (SA 3100, Coulter Electronics, USA). The BET equivalent particle diameter ($d_{BET} = 6/(\rho.SSA)$) for the nano powders was approximated by assuming monodisperse, spherical and non-aggregated particles, where ρ is defined as the density of the corresponding phase pure composition [74].

Shrinkage behaviour and thermal expansion by dilatometer measurement

The loose sub-micron LSCF powder was calcined at 1050 °C and ball milled, the BSCF powder was pressed into a pellet, calcined at 950 °C and ball milled to obtain the sufficient phase purity for the sintering. These powders were pressed isostatically with 2000 bar into rods and placed into the dilatometer. Shrinkage behaviour of the as-produced powders and the coefficient of thermal expansion (CTE) of sintered samples were determined by dilatometry (Baehr Thermoanalyse DIL802, Germany). Experiments for the shrinkage behaviour were made in air between 25 °C and 1350 °C with a heating rate of 5 K min^{-1} by using an alumina sample holder. The determination of the CTE was carried out in air with a sapphire system in the temperature range of 100–980 °C.

Particle size distribution

The particle size distribution was evaluated using a Particle Sizer LS230 (Beckmann Coulter, USA) after suspending the powder in water. The working range of the LS230 is between 0.04 µm to 2000 µm. The mean particle size (d50) of the nano powders was estimated from BET results as already described before, because the mean particle size was out of this range. The particle sizer uses the Polarization Intensity Differential Scattering (PIDS) method. A precise characterization of small particle sizes in the sub-µ range is achieved using three wavelengths of light (450 nm, 600 nm and 900 nm, obtained by filtering light from an incandescent bulb) at two polarizations directions and detectors placed in different scattering angles up to 45°.

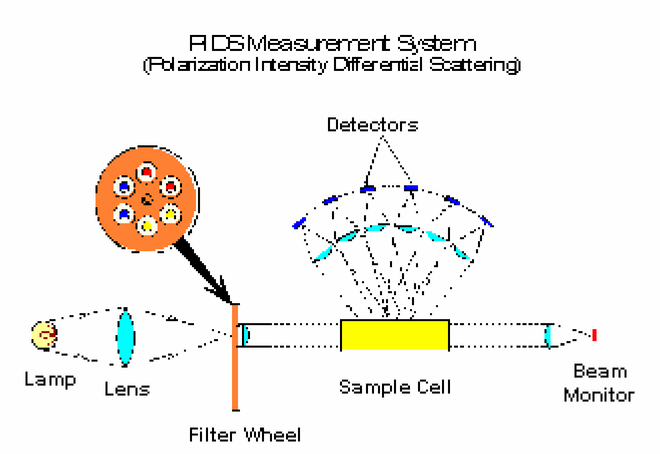

Figure 13: Scheme of the PIDS-assembly in the Coulter counter LS230.

Inductively coupled plasma – optimal emission spectroscopy (ICP-OES)

This method was used in order to determine the exact element ratios of the calcined powders in comparison to the targeted stoichiometry. Sample amounts of 29.9 mg (LSCF) and 32 mg (BSCF) were completely dissolved in diluted nitrohydrochloric acid prepared from hydrochloric and nitric acid using Merck concentrated acids in suprapur quality in a 3:1

ratio and 10-times diluted using high–purity water (18.2 MΩ cm), prepared by a Milli-Q Gradient A10 System (Millipore). The solution was finally filled to an end volume of 10 ml. All calibration and quality standards were prepared from single and multi-element standards in ICP-quality (Merck and Alfa Aesar). The analyses were performed under standard hot plasma conditions. Operation conditions are summarized in Table III.

Table III: Operating conditions for ICP-OES analysis*.

Parameter	**VARIAN VistaPro**
Power [W]	1200
Plasma gas flow [L/min]	15
RF generator [MHz]	40.86 (free-running)
Aux. gas flow [L/min]	1.00
Nebulizer gas flow [L/min]	0.75
Nebulizer	Meinhard concentric nebulizer
Spray chamber	cyclonic quartz chamber
Resolution	about 10 pm (at 267,7 nm)
Dynamic range	10^6 (CCD, 70000 pixels)
Wavelength range	167 – 785 nm

*with kind permission of A. Wichser and A. Ulrich [75].

The following elements and wavelengths were used for quantification with ICP-OES [75]: La 333.749 nm, 379.082 nm, 408.871 nm Sr 216.596 nm, 407.771 nm, 421.552 nm, Co 230.786 nm, 237.863 nm, 238.892 nm, Fe 259.940 nm 234.350 nm, 238.204 nm, 239.563 nm, Ba 233.957 nm, 455,403 nm, 493.408 nm.

3.2.2 Results: Powder characterization of $La_{0.6}Sr_{0.4}Co_{0.2}Fe_{0.8}O_{3-\delta}$ and $Ba_{0.5}Sr_{0.5}Co_{0.8}Fe_{0.2}O_{3-\delta}$, $La_{0.6}Sr_{0.4}FeO_{3-\delta}$ and $(La_{0.8}Sr_{0.2})_{0.95}FeO_{3-\delta}$

Structural properties of different powders from the (La,Ba,Sr)(Co,Fe)$O_{3-\delta}$ system

Powder diffractograms of as pyrolysed and calcined LSCF and BSCF are displayed in the following figures. Figure 14 shows the diffraction pattern of LSCF as pyrolysed and after subsequent heat treatment. Heat treatment at 1100 °C for 10 hours resulted in a sufficiently phase pure powder with an orthorhombic microstructure with a (Å) = 5.532, b (Å) = 5.553, c (Å) = 7.835 and the corresponding cell volume of 240.68 $Å^3$ (10^6 pm^3). After ball milling of the calcined powder resulted in a sub-µ (d_{50}=0.42 µm) particle size with a specific surface area 4.9 m^2 / g.

The raw powders of LSCF fired at a maximum temperature of 700 °C shows already the peaks that correspond to the perovskite microstructure, but also a large number of smaller peaks from impurities. After calcining at 900 °C most of the additional peaks become smaller than the background noise and the peaks corresponding to the orthorhombic microstructure become more pronounced. The impurities can be attributed to the oxides of La, Sr and Fe.

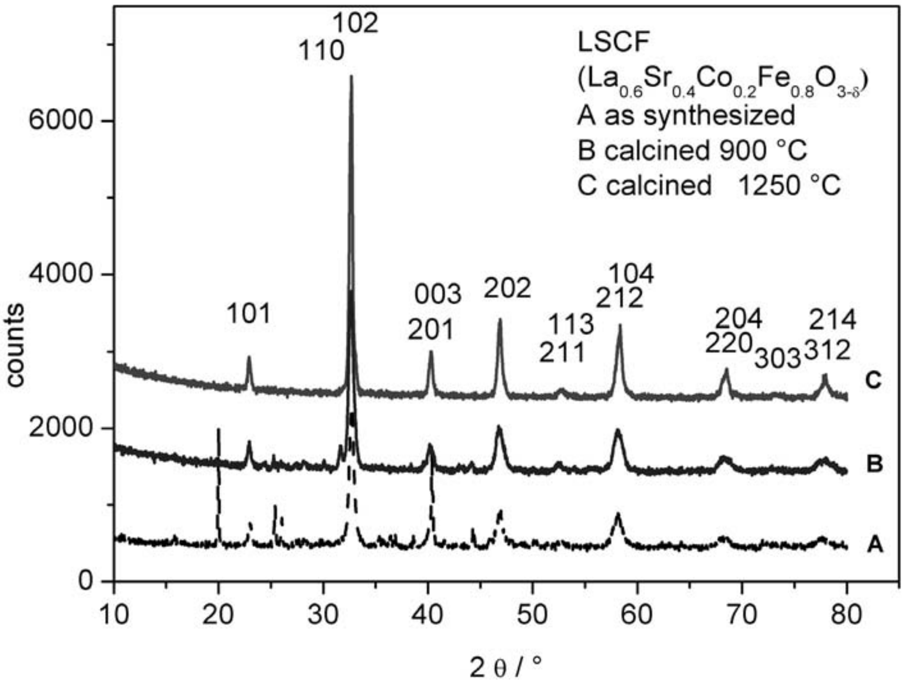

Figure 14: XRD diffraction pattern of raw (broken line) and calcined (solid lines) LSCF powders.

Resulting from the ICP-OES analysis, the stoichiometry of LSCF ($La_{0.58}Sr_{0.42}Co_{0.21}Fe_{0.79}O_{3-\delta}$) is close to the targeted one ($La_{0.6}Sr_{0.4}Co_{0.2}Fe_{0.8}O_{3-\delta}$). The hexagonal perovskite structure is in agreement with results from the literature [18]. Figure 15 shows the comparison between LSCF nano powder, directly obtained from flame spray synthesis together with the spray pyrolysed powder that was heat treated additionally at 1250 °C. The diffraction pattern of the nano powder shows a smaller height of the peaks and slightly more background noise. The peak positions correspond to that of the spray pyrolysed powder with an orthorhombic microstructure.

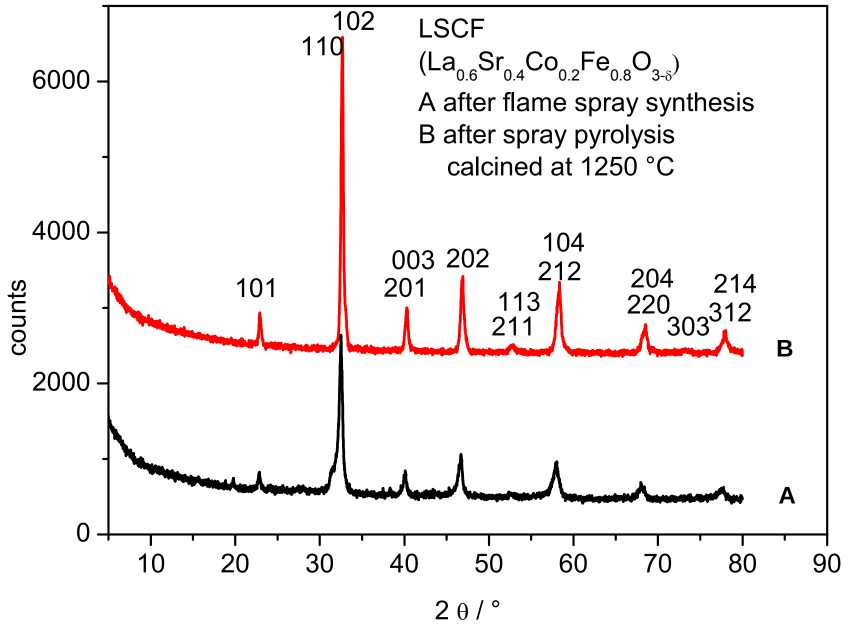

Figure 15: Comparison of powder diffraction pattern from flame spray synthesis (A) and from spray pyrolysis and subsequent calcination (B).

The diffraction pattern for a BSCF powder is shown in Figure 16 directly after production (highest temperature was 700 °C), after calcination at 800 °C, at 950 °C for a pressed and calcined powder pellet and at 1100 °C for loose powder. Phase purity of BSCF was achieved only after calcination at 1100 °C and the XRD analysis yielded into a tetragonal symmetry with the lattice parameters (a=b=3.983 Å, c = 3.982 Å).

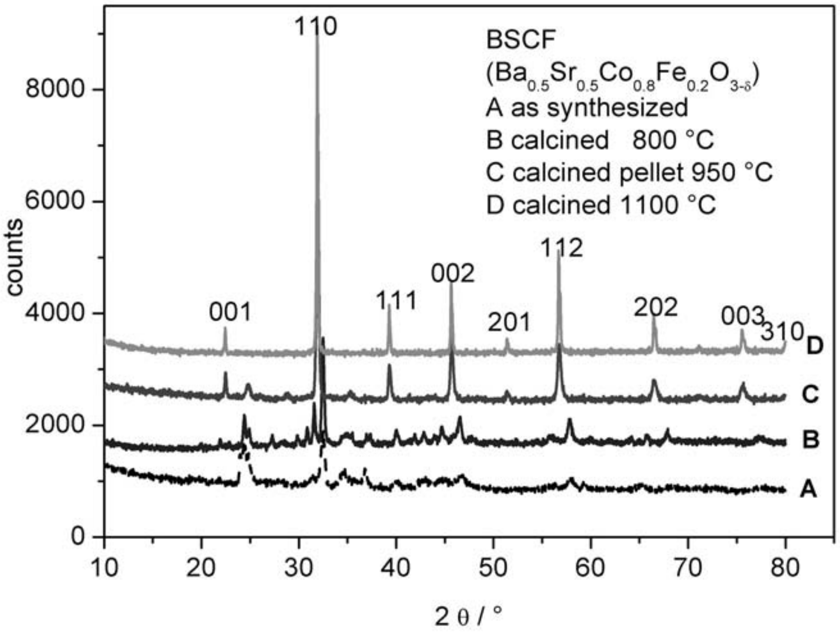

Figure 16: XRD spectra of as synthesized (broken line) and calcined (solid lines) powders of BSCF.

The ICP results reveals only a slight A-site excess (2% Ba excess) leading to the stoichiometry $Ba_{0.52}Sr_{0.50}Co_{0.80}Fe_{0.20}O_{3-\delta}$. The c axis is only slightly smaller then the (a = b) axis, indicating a slight tetragonal distortion in comparison to literature (11, 16) where a cubic microstructure for BSCF is proposed and might be attributed to the A-site excess.

The X-ray diffraction pattern of the LSF82 raw powder as obtained by spray pyrolyis and after calcination of the powder at 1100 °C for 10 h is displayed in Figure 17. The heat treatment at 1100 °C for 10 h resulted in a sufficiently phase pure powder with an orthorhombic microstructure with a (Å) = 5.532, b (Å) = 5.553, c (Å) = 7.835 and the corresponding cell volume of 240.68 Å^3 (10^6 pm^3). After ball milling of the calcined powder sub-μ (d_{50}=0.42 μm) particle size with a specific surface area 4.9 m^2 / g were obtained.

The raw powder shows already the peaks that are attributed to the orthorhombic structure. However, additional peaks, attributed to the oxides of La, Sr and Fe, indicate the as pyrolysed powder is not phase pure.

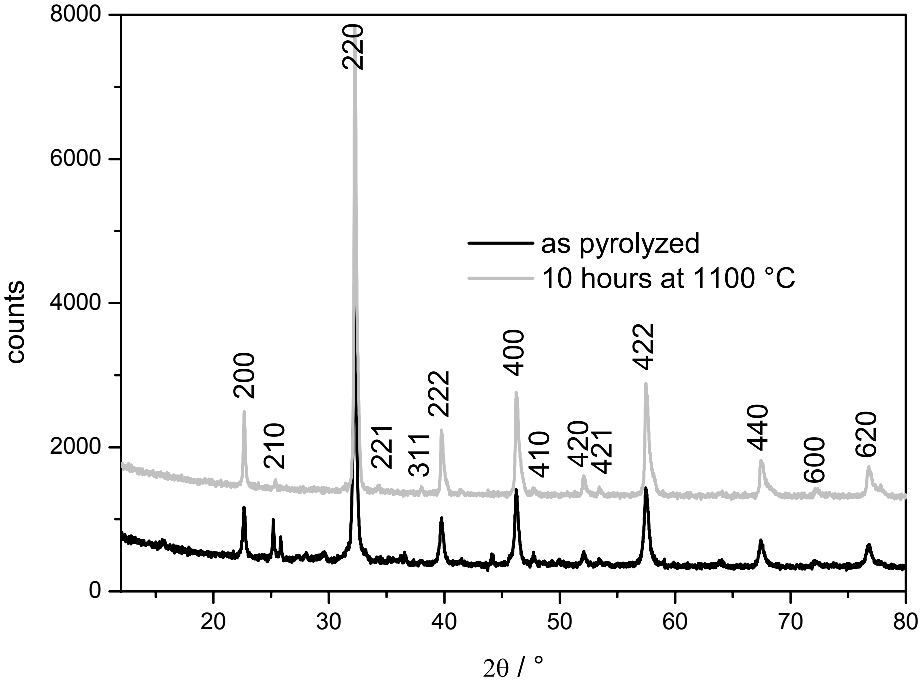

Figure 17: LSF82 X-ray diffraction pattern of as pyrolysed and heat treated powder.

The X-ray diffraction pattern of a LSF64 powder directly after flame spray synthesis and after calcination of the powder at 1200 °C for 10 h is displayed in Figure 18. The heat treatment at 1200 °C for 4 h resulted in a sufficiently phase pure powder with a cubic microstructure with a (Å) = 3.8862 and the corresponding cell volume of 58.69 Å^3 (10^6 pm^3). The powder as pyrolysed is not phase pure with additional peaks attributed to the oxides of La, Sr and Fe.

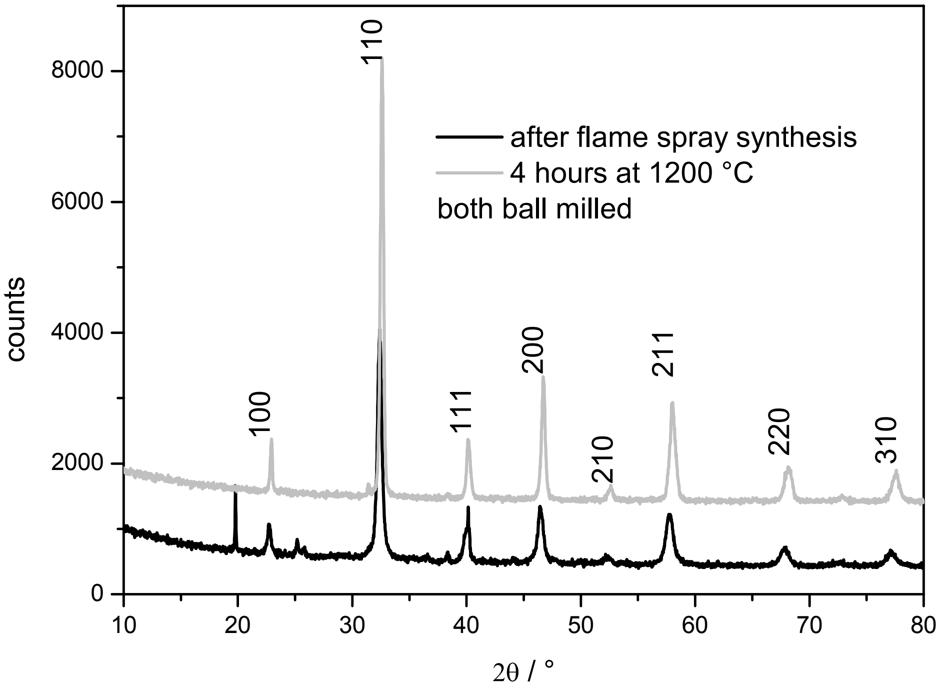

Figure 18: LSF64 X-ray diffraction pattern of as pyrolysed and heat treated powder.

Compatibility between cathode and electrolyte materials

LSCF sub-µ or nano powder were mixed with CGO (HC Starck) und YSZ (Tosoh YSZ 8YS) powder respectively in the weight ratio 1:1 in an agate mortar. The resulting powder was then pressed uni-axially into a pellet and heat treated. The mixture was examined before and after heat treatment for 300 hours at 800 °C and 2 hours at 1000 °C by XRD. The same procedure was applied to sub-µ BSCF and the results should show, if there was any reaction between the cathode and electrolyte material.

The suitability of $Ce_{0.9}Gd_{0.1}O_{3-\delta}$ (CGO) and $Y_{0.16}Zr_{0.84}O_{3-\delta}$ (YSZ) as electrolytes with LSCF and BSCF materials were tested. XRD spectra of powder mixtures were checked before and after calcination. In comparison to already available studies in the literature [23, 25-27, 76, 77] it was important for the processing if the smaller particle size of the LSCF nano powder would increase the reactivity with the electrolyte material as well.

Figure 19 shows the XRD pattern of a mixture between YSZ and sub-µ BSCF before and after heat treatment in comparison with the pure materials. The mixture shows a significant change of the peaks especially visible with two peaks at about 30° and 32°. The BSCF peak (32°) seems to vanish completely or merge into a duplet peak at around 30°. Additional peaks and the peak shift of other peaks between 32° and 65° clearly indicate reactions between BSCF and YSZ.

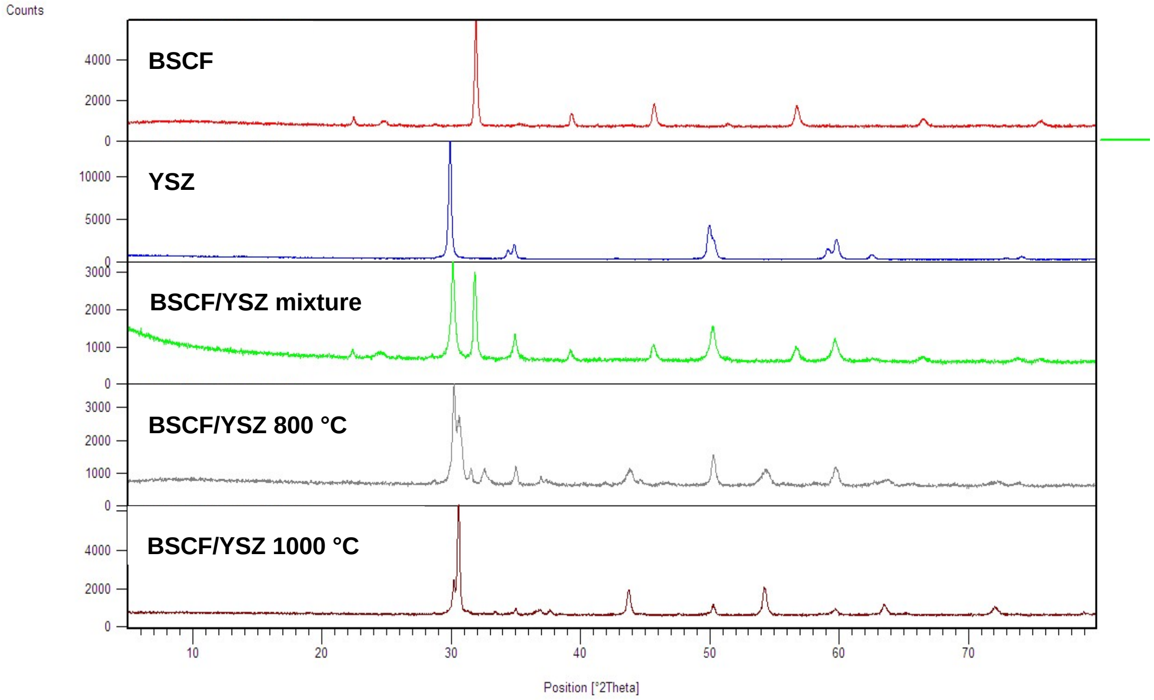

Figure 19: Reactivity of YSZ/BSCF sub-µ powder heated at 800 °C for 300h and at 1000 °C for 2h.

Figure 20 shows the XRD of a mixture between CGO10 and BSCF before and after heat treatment in comparison with the pure materials. The materials shows only little change in the spectra, the peak at 32°, however, shows a shoulder when heat treated at 800 °C, however, almost no change at 1000 °C. The peak at 57° has a shoulder at 800 °C, which is not visible for the untreated mixture (green) and becomes a visible peak, when heat treated at 1000 °C.

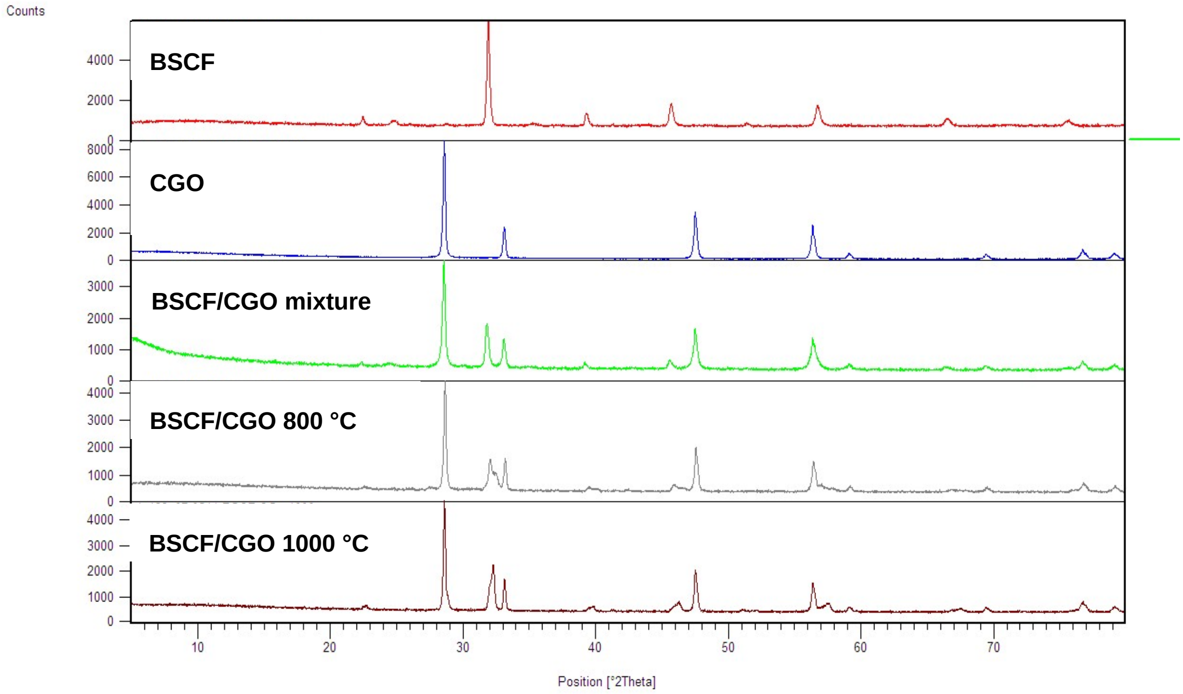

Figure 20: Reactivity of CGO/BSCF sub-µ powder heated at 800 °C for 300h and at 1000°C for 2h.

Figure 21 shows the XRD of a mixture between YSZ and LSCF sub-µ powder before and after heat treatment in comparison with the pure materials. After the heat treatment at 800 °C, there are only minor changes visible in the spectra. The relative intensity of the peaks at 30° and 33° changes, another intensity change can be observed at 47° and 50° in respect to a slight change at 58° and 60°. At 31° an additional peak becomes visible and another one at 29° is fading. Additionally a lot of small peaks appear at diffraction angles between 30° and 70°. The changes in the spectra are more pronounced at 1000 °C than at 800 °C. The peak at 29° is fading out, the peak at 30° is now changed to be more intensive than the one at 33° and there is a new peak in between, which is clearly visible.

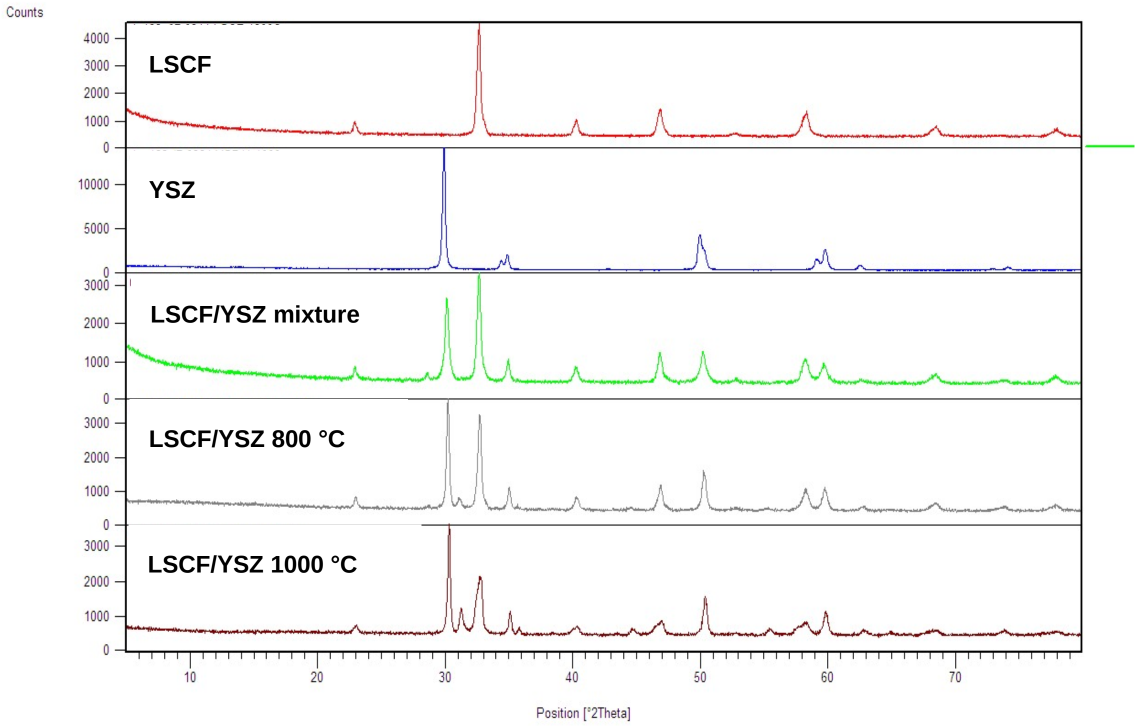

Figure 21: Reactivity of YSZ/LSCFsub-µ powder heated at 800 °C for 300h and at 1000 °C for 2h.

Figure 22 shows the XRD of a mixture between YSZ and LSCF nano powder before and after heat treatment in comparison to the pure materials. Additionally to the broadened peaks of the untreated material, the reactions are already visible in the XRD spectra after heat treatment at 800 °C.

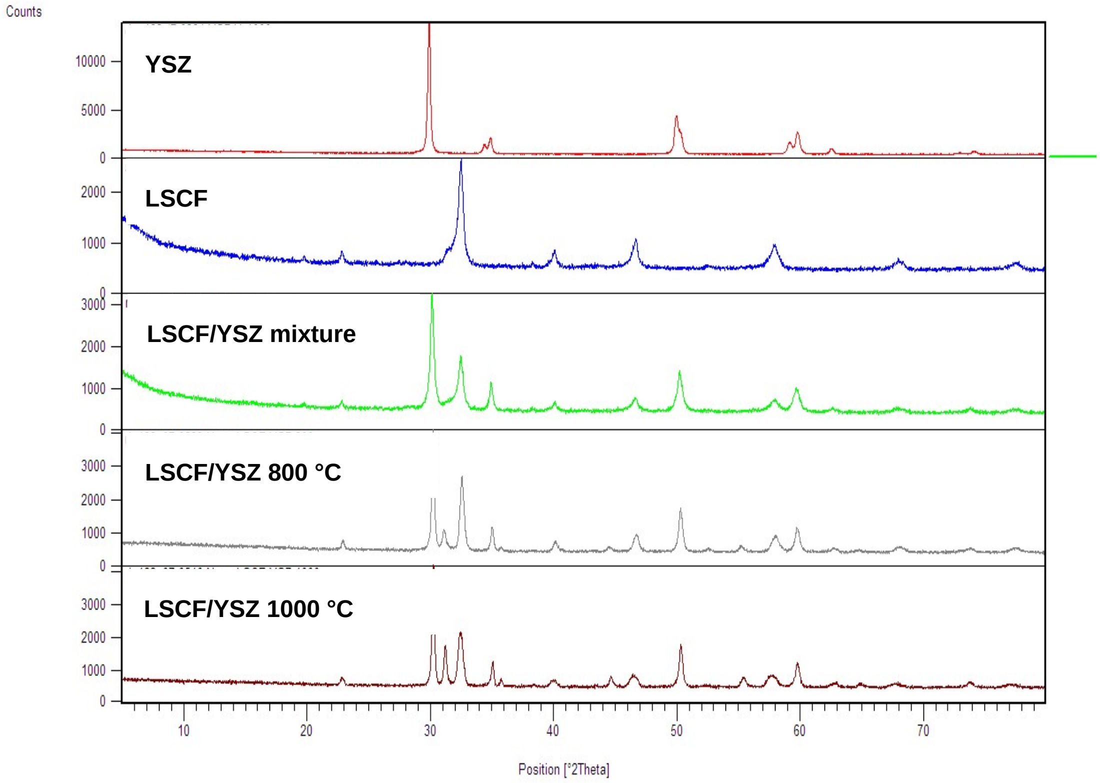

Figure 22: Reactivity of YSZ/LSCF nano powder heated at 800 °C for 300h and at 1000 °C for 2h.

The reactivity between sub-μ LSCF and CGO are displayed in Figure 23. There are no major changes in the spectra, only the duplets at around 33° and 47° change the relative intensity of the peaks. There is no significant change in the amorphous fraction of the spectrum (gently inclining part of the spectrum at diffraction angles < 15°) after 300 hours at 800 °C compared to the mixture before heat treatment. After 2 hours at 1000 °C the amorphous part becomes smaller and the left peaks of the two duplets attributed to LSCF both decrease.

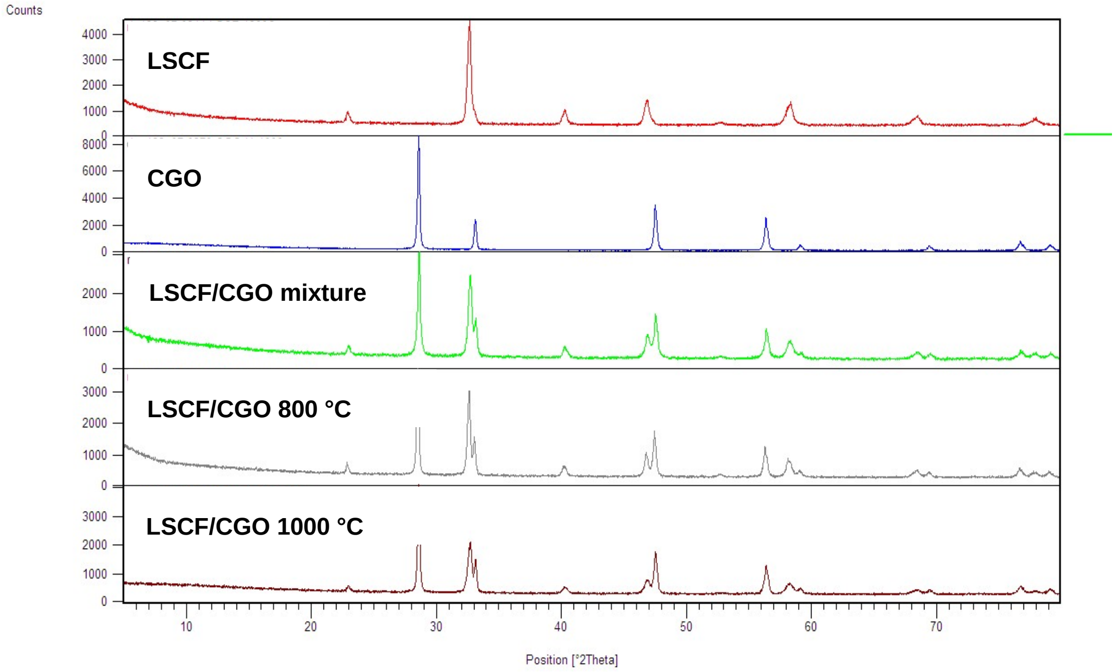

Figure 23: Reactivity of CGO/LSCF sub-μ powder heated at 800 °C for 300h and at 1000 °C for 2h.

The reactivity between nano LSCF and CGO10 are displayed in Figure 24. There are no major changes in the spectra, only the relative intensities of the peaks in the duplets at around 33° and 47° change.

In contrast to the mixture CGO/sub-μ LSCF the left peaks of the duplets corresponding to the LSCF powder increases significantly. At the same time the amorphous fraction (= gently inclining part of the spectrum at diffraction angles < 15°) of the nano powder becomes smaller. In contrast to the sub-μ LSCF the left peaks of the duplets are increased after the heat treatment.

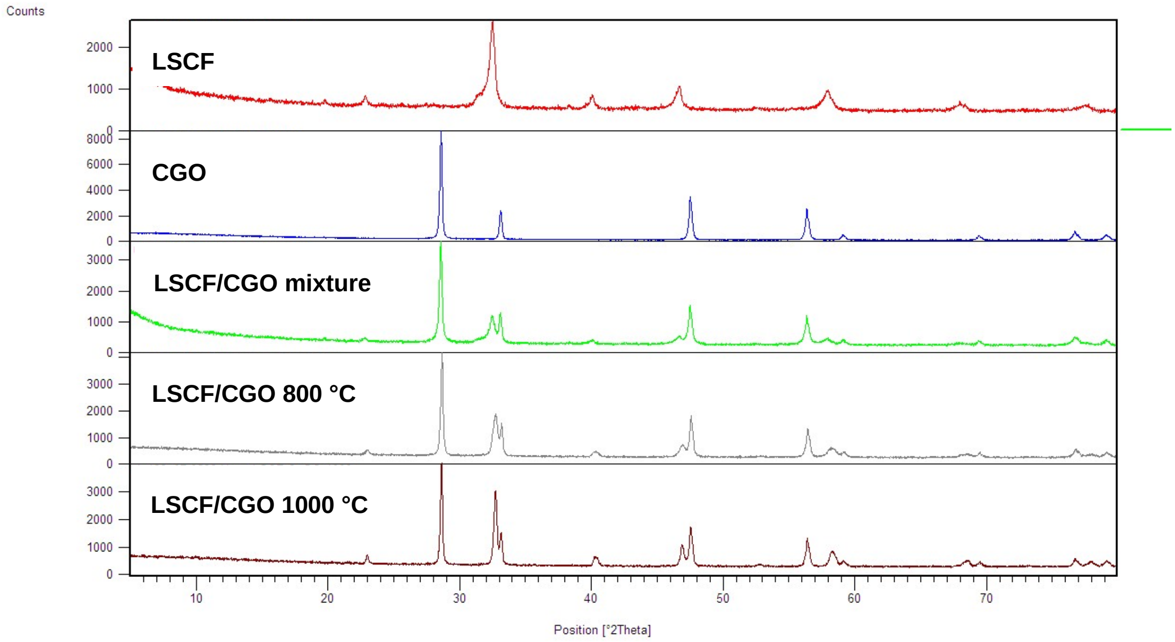

Figure 24: Reactivity of CGO/LSCF nano powder heated at 800 °C for 300h and at 1000 °C for 2h.

Sintering behaviour of $La_{0.6}Sr_{0.4}Co_{0.2}Fe_{0.8}O_{3-\delta}$ and $Ba_{0.5}Sr_{0.5}Co_{0.8}Fe_{0.2}O_{3-\delta}$ powders

The investigated shrinkage of pressed powder specimen can give important hints for further processing of the powders. The coefficient of thermal expansion characterizes a cathode if suitable in combination with an electrolyte material. The shrinkage behaviour of calcined powders was investigated in order to find out the adequate sintering program to sinter dense specimen crack free specimen for further investigations. The shrinkage indicated by the length change (ΔL in %) begins at temperatures around 1000 °C for LSCF (Figure 25) and 850 °C for BSCF (Figure 26). In order to avoid cracks due to a fast sintering process the temperature program is adapted by slower heating rates after reaching these temperatures. Peaks in the shrinkage rate curve ($\Delta L/\Delta t$) indicate temperatures, where fast shrinkage occurs.

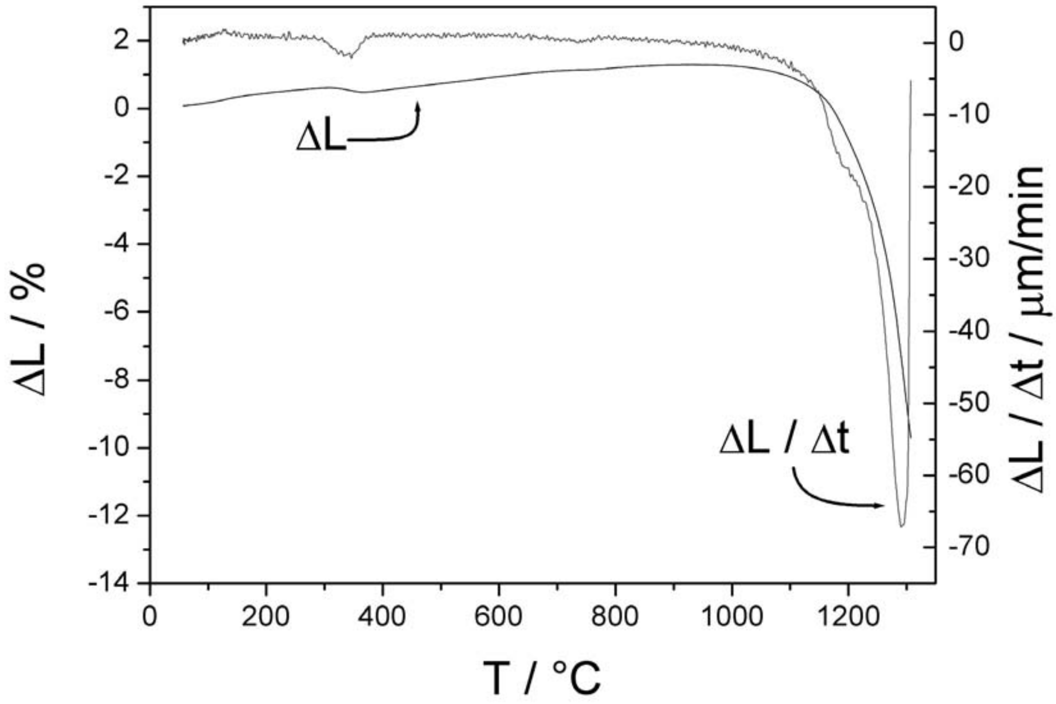

Figure 25: Dilatometer curve from calcined LSCF powder at a constant heating rate of 5 K/min

The length change of the BSCF (Figure 26) sub-micron powder sample seems to increase constantly in the lower temperature range. This increase is most probably attributed to the thermal expansion of the material. The small peaks in the shrinkage rate (ΔL/Δt) at around 300 °C and 700 °C might be attributed to the loss of water and carbonates rather than to phase changes in the material.

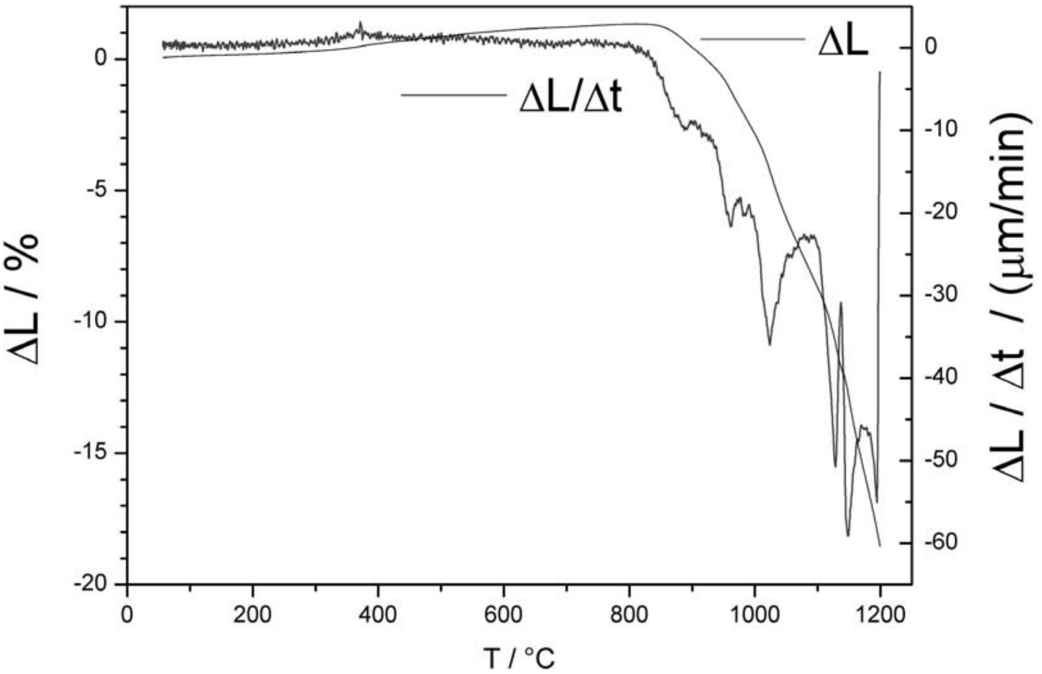

Figure 26: Dilatometer curves from calcined BSCF powder at a constant heating rate of 5 K/min

Starting from 800 °C, the shrinkage rate becomes zero and at higher temperatures several superposing peaks occur. Peaks between 800 °C and 900 °C might be attributed to the decomposition of carbonates, a very narrow one at 1120 °C might be attributed to the optimum sintering temperature and the two peaks at higher temperatures might be attributed to liquid phase sintering or ever partial decomposition of the material.

The sintering profiles displayed in Figure 27 were applied taking the temperature difference between the oven and the sample into account. Lower heating rates (2 K/min instead of 5 K/min) were applied for both materials at T > 800 °C. The beginning shrinkage of BSCF and the possible release of CO_2 from BSCF might be the reasons, why this procedure lead to an increase of the sample density compared to samples only heated with a simple ramp and dwelling time. Dwelling times were introduced in order to allow the material to finish the corresponding sintering processes or phase changes. The sintering of LSCF required only a slower ramp (2K/min) between 800 and 1300 °C and 4 hours dwelling time at the maximum temperature. BSCF needed to be dwelled additionally at 1050 °C for 30 min and heated to 1150 °C which involves probably liquid phase sintering of the material. Dense samples were obtained after dwelling finally for 4 hours at 1130 °C. The liquid phase sintering or even partial melting for BSCF is also suggested in the literature [57], possibly indicated by two pronounced peaks in the temperature range between 1150 °C and 1200 °C. However, a dwell time at 1150 °C led to samples with 2 – 3 % lower densities. At higher temperatures even small holes were visible when breaking the samples, that are most likely attributed to decomposition of the BSCF material.

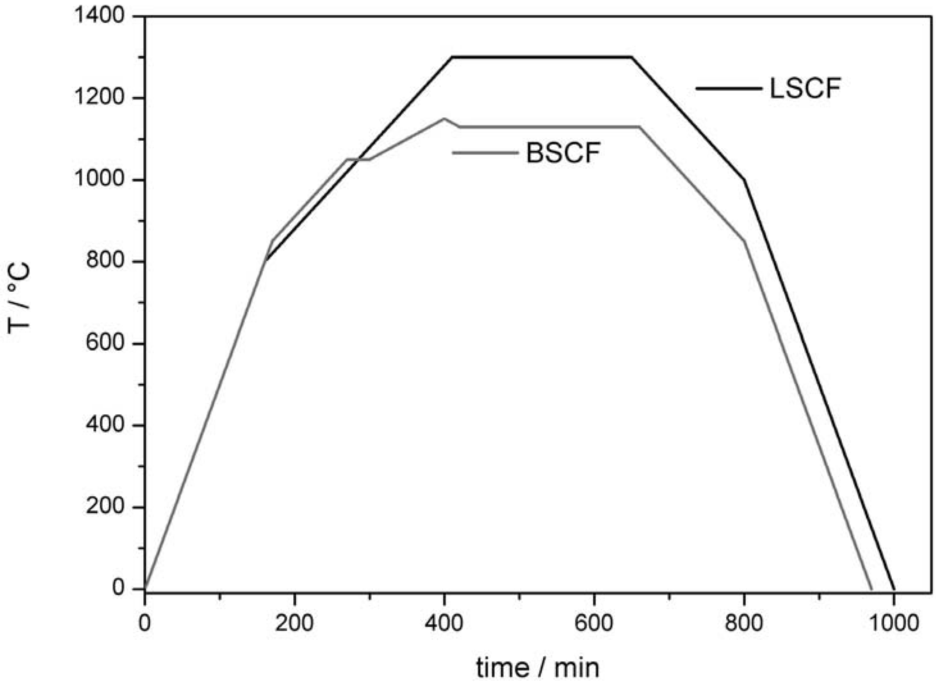

Figure 27: Optimized temperature profiles to sinter LSCF and BSCF samples.

The resulting microstructure of the sintered LSCF samples is presented in Figure 28. Both samples show dense sintered bodies as required for the subsequent conductivity relaxation measurements. The granularity of the LSCF sample is nicely visible for the unpolished LSCF sample. The grains on the sample surface have a size between 2 μm and 10 μm and the grain boundaries show no cracks and holes. This is a clear indication for a dense sintered sample.

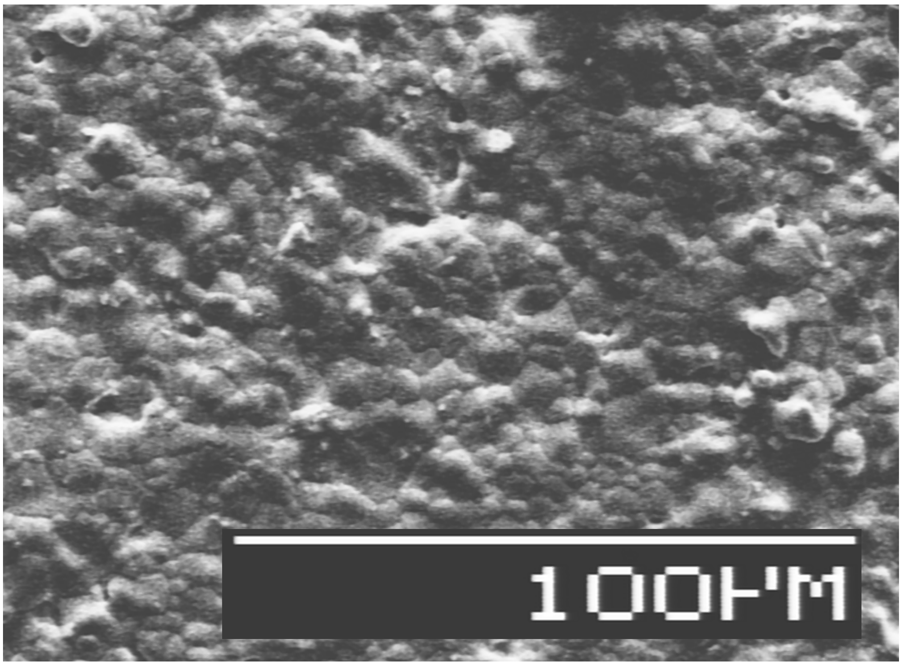

Figure 28: Electron micrographs of sintered (1300 °C) LSCF sample (unpolished).

The BSCF (Figure 29) sample was polished and subsequently thermally etched for 2 hours at 950 °C. Despite etching, no grains visible and the grain boundaries are only visible in some of the cavities attributed to grain pull-out due to the polishing. The grain boundaries are most probably blurred during the polishing of this relatively soft material.

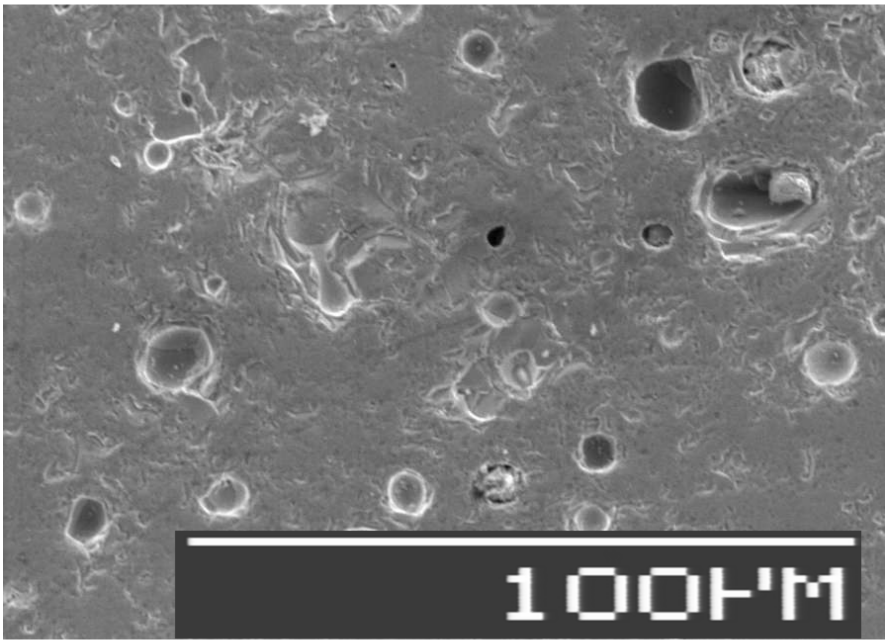

Figure 29: Electron micrographs of sintered (1130 °C) BSCF sample (polished and thermally etched).

Thermal expansion of dense $La_{0.6}Sr_{0.4}Co_{0.2}Fe_{0.8}O_{3-\delta}$ and $Ba_{0.5}Sr_{0.5}Co_{0.8}Fe_{0.2}O_{3-\delta}$ bars

Having obtained dense specimen with the described sintering program dilatometer measurements were used to determine the expansion of the BSCF and LSCF as a function of the temperature. The length change of BSCF and LSCF is compared in Figure 30 The corresponding CTE for BSCF was 12.6 ppm/K between 200 °C and 400 °C and 27.3 ppm/K between 425 °C and 980 °C compared to LSCF with 16.2 ppm/K between 200-700 °C and 28.0 ppm/K 800 °C and 980 °C.

The present measurement shows that thermal expansion occurs in the lower temperature intervals, while chemical expansion adds up at higher temperatures and leads to much higher apparent CTE values. The thermal expansion of the material is observed in the temperature interval when the stoichiometry of the material is constant. An additional ‘chemical expansion’ is attributed to the partial reduction of the oxide leading to an increase of oxygen vacancies (increasing oxygen non- stoichiometry) at higher temperatures.

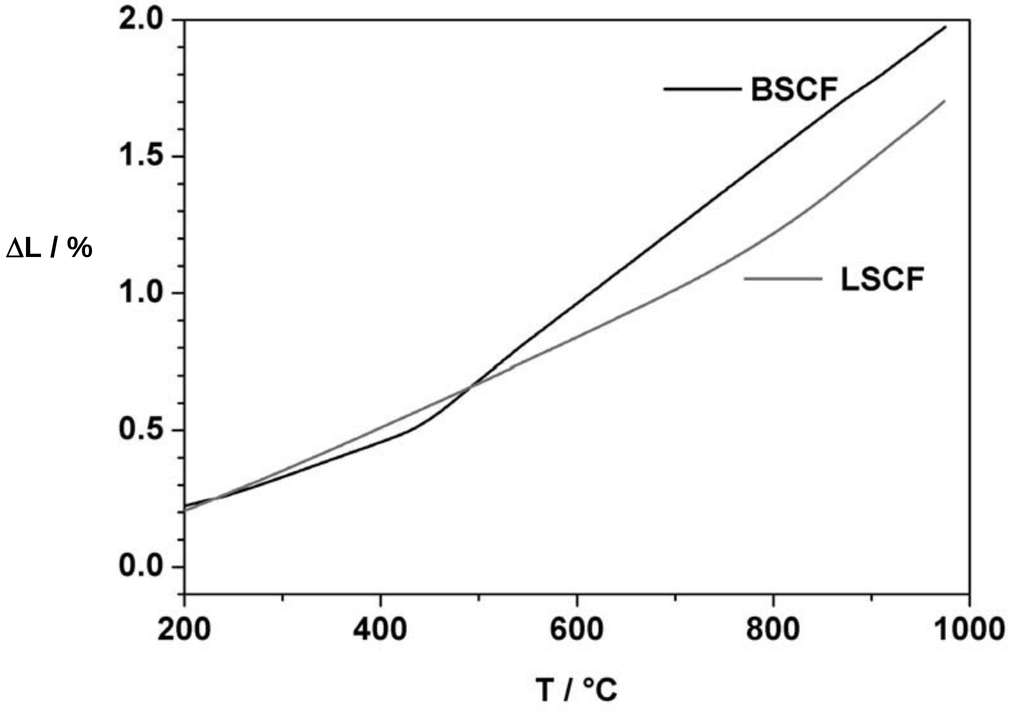

Figure 30: Relative length change of LSCF and BSCF measured in air.

The CTEs of LSF64 and LSF82 were not measured in the course of the present study. Literature data [29] for LSF64 show similar values as for BSCF and LSCF. LSF82 according to the literature [37] has a CTE of 12.6 ppm/K between 300 °C and 900 °C and is therefore supposed to be the material with expansion most similar to the electrolyte materials investigated in this study.

3.2.3 Overview of most important results for LSCF and BSCF

The result of the ICP-OES analysis, the results of XRD, the specific surface areas of the powders, the density of the pellets and the CTEs of BSCF and LSCF are summarized in Table III.

Table IV: Powder properties of LSCF and BSCF powder including results from ICP-OES analysis.

	BSCF	**LSCF**
nominal composition	$Ba_{0.5}Sr_{0.5}Co_{0.8}Fe_{0.2}O_{3-\delta}$	$La_{0.6}Sr_{0.4}Co_{0.2}Fe_{0.8}O_{3-\delta}$
cation ratio (by ICP-AES)	$Ba_{0.50}Sr_{0.52}Co_{0.80}Fe_{0.20}O_{3-\delta}$	$La_{0.58}Sr_{0.42}Co_{0.21}Fe_{0.79}O_{3-\delta}$
crystallographic phase	tetragonal (a=b=3.983, c = 3.982 Å)	hexagonal (a = b = 5.499, c = 6.690 Å)
BET spec. surface area	3.60 m^2/g (as produced) 1.90 m^2/g (calcined 950 °C, no further treatment) 5.20 m^2/g (after ball milling)	9.37 m^2/g (as produced) 2.27 m^2/g (calcined 1050 °C, no further treatment) 4.70 m^2/g (after ball milling)
XRD density (ρ_{XRD})	5.73 g cm^{-3}	6.23 g cm^{-3}
Density (ρ_{spec})	5.47 g cm^{-3}	5.86 g cm^{-3}
% of XRD density	94.1	95.5
CTE fitted to expansion curves for dense specimen	12.6 ± 0.1 ppm (200 °C – 400 °C) 27.3 ± 0.1 ppm(425 °C – 980 °C)	16.2 ± 0.1 (200-700 °C) 28.0 ± 0.1 (800-980 °C)

Phase pure powders with similar CTE were also produced by EMPA in the compositions $La_{0.6}Sr_{0.4}FeO_{3-\delta}$ and $(La_{0.8}Sr_{0.2})_{0.95}FeO_{3-\delta}$ but not characterized in detail as BSCF and LSCF.

3.3 Discussion

3.3.1 Structure and chemical composition (of LSCF and BSCF)

Phase pure materials of LSCF and BSCF could be achieved by spray pyrolysis after calcination, and of LSCF prepared directly with flame spray synthesis without the need of further heat treatment. However, no phase pure BSCF nano powders could be synthesised by flame spray synthesis. The most probably reason is the sensitivity even to a low CO_2 content [78] as present in air. Carbonates (e.g. $BaCO_3$, $SrCO_3$) are formed during synthesis [79] and do not decompose at the conditions being present at flame spray synthesis.

The structure of LSCF - despite at small deviation to the targeted stoichiometry - corresponds to the literature [18], while BSCF shows a slight tetragonal distortion in comparison to the cubic microstructure that can be found in the literature [57, 80].

The orthorhombic microstructure with a (Å) = 5.532, b (Å) = 5.553, c (Å) = 7.835 of LSF82 is close to values from literature for $La_{0.8}Sr_{0.2}FeO_{3-\delta}$ [63] a (Å) = 5.523(1), b (Å) = 5.550(1), c (Å) = 7.817(2). LSF64 could be indexed by a cubic in contrast to a rhombohedral microstructure found by Patrakeev et al. [63]. Water and carbon dioxide content in the raw materials and the experimental error, which is estimated to be 0.5 %, are the most likely causes for the slight deviation from the target stoichiometry as summarized in Table III. The small tetragonal distortion of BSCF is tentatively attributed to the 2% A-site excess.

3.3.2 Compatibility of LSCF and BSCF with YSZ and CGO

YSZ shows a reaction with both BSCF and LSCF already after heat treatment at 800 °C. Compared with YSZ, CGO seems to be the better compatible material in respect to both tested cathode materials. However, BSCF after heat treatment at 1000 °C shows additional peaks in the XRD spectra of the powder mixtures indicating additional phases of reaction products. The reactivity of LSCF nano powder and sub-μ LSCF seems to be slightly different, indicated by different intensity of the reaction products. BSCF/YSZ mixtures show the appearance of additional phases indicated by new peaks already after annealing at 800

°C. In the literature [26] similar tests (using YSZ and $Gd_{0.2}Ce_{0.8}O_{1.9}$) were already presented, and show similar reactions as observed in the present study. In course of the investigations at 800 °C here presented, no additional peaks in the XRD pattern are visible for BSCF/CGO. After heat treatment at 1000 °C the peaks indicate the formation of $BaCeO_3$ and $SrCoO_3$.

Additional peaks indicate the reaction between LSCF and YSZ and the formation of additional phases. The changes at 1000 °C indicate that similar reaction products and phases are formed during the heat treatment independently from the used sub-µ and nano powders. In the literature [25] the secondary phases are identified as $La_2Zr_2O_7$, $SrZr0_3$ and $CoFe_2O_4$ after substantially longer heat treatment. This slightly different ratio of the peaks observed for the nano powder compared to the coarse powders can be most probably attributed to two factors: the reaction of the nano powder already occurs at lower temperatures, because the surface energy of the material is higher, and due to a higher part of the powder, that seems to be still amorphous and having an increased reactivity.

The present investigations of the compatibility between LSCF and CGO show only a change of the relative intensity of the peaks duplets at around 33° and 47° (Figure 23 and 24). This result might correspond to small changes in the lattice. The change of the relative intensity is different for the coarse and the nano powder possibly due to the increased reactivity due to the small particle size and an amorphous part of the powder. The present investigation of the compatibility with the electrolyte powder is in agreement with the literature, where no reaction with the CGO electrolyte [65] for a wide range of LnSCF cathode materials (Ln = lanthanides) is reported. A more recent study [23], including the compatibility $La_{0.8}Sr_{0.2}Co_{0.2}Fe_{0.8}O_{3-\delta}$, points out changes in the lattice parameters of the cathode material in contact with $Gd_{0.2}Ce_{0.8}O_{1.9}$ after heat treatment between at 800 °C, 1000 °C, and 1200 °C for 100 h. Despite the difference in the composition this result implies doubts about the long time compatibility of LSCF and CGO.

3.3.3 Coefficients of thermal expansion

The chemical expansion of BSCF seems to contribute to the CTE already at lower temperatures compared to LSCF. The change in the slope is attributed to the start of the oxygen exchange of the material. However, due to slow oxygen exchange kinetics, the samples might not be fully equilibrated during the measurement, because of a rapid heating rate of 300 °C/h. Therefore, the temperature attributed to the beginning of the oxygen exchange might be higher than observed by thermo gravimetric measurements [81]. Furthermore, the apparent CTE in the high temperature region might appear higher than under equilibrium conditions. CTE values, that are found in the literature [52], give in most cases the mean values in a certain temperature range. The value for LSCF (21.4 ppm/K) is between the measured value for the low temperature and the high temperature interval for LSCF. Wang et al. [82] reports a value of 18.53 ppm/K in the temperature interval between 30 °C and 850 °C, but the measurement curve is bending at a much higher temperature (around 700 °C compared to 410 °C in the present measurement).

Compared to common electrolyte materials as stabilized zirconia and substituted ceria with a CTE around 10 ppm/K at 600 °C and 12 ppm/K in the higher temperature range LSCF and BSCF materials show a mismatch in the thermal expansion already in the low temperature region, where the oxygen loss is considered negligible.

3.4 Statement about the quality of material synthesis

Phase pure powders of all four materials were obtained after heat treatment of the materials. The analysed composition of BSCF and LSCF correspond to the cation ratio of the nominal composition within an experimental error of maximally 5 per cent.

The compatibility of BSCF and LSCF with YSZ is neither given at 800 °C after treatment for 300 hours nor after heat treatment at 1000 °C for 2 hours. Only LSCF is fully compatible to CGO at both temperatures, BSCF show reactions at 1000 °C which can be a disadvantage for the firing after screen printing of the cathodes. Due to the favourable fact, that

LSCF shows no visible reaction products in the XRD spectra and only minor reactions with BSCF, CGO10 was chosen as electrolyte material for symmetrical test cells.

The single-step-synthesis of phase pure nano powder was only possible for LSCF. BSCF shows secondary phases after flame spray synthesis [79] and needs subsequent heat treatment to obtain phase pure powders . Phase pure powders of LSF82 and LSF64 could be produced by spray pyrolysis with a mean particle size in the sub-μ range after subsequent heat treatment and ball milling.

The phase purity of BSCF, LSCF, LSF82 and LSF64 powders was the precondition for the subsequent evaluation of the electrical and electro catalytical properties which is fulfilled for all powders.

4 Electrical conductivity and kinetic parameters of selected compounds from the (Ba, La, Sr)(Fe,Co)$O_{3-\delta}$ system

The literature review in chapter 2 shows, that the electrical conductivity and the kinetic parameter are strongly related to the cathode performance. The intention of the conductivity relaxation experiments was to evaluate the mixed ionic electronic transport properties and the chemical surface exchange coefficient in order to compare the catalytic activity of four materials from the (Ba,La,Sr)(Fe,Co)$O_{3-\delta}$ system, namely $La_{0.6}Sr_{0.4}Co_{0.2}Fe_{0.8}O_{3-\delta}$ and $Ba_{0.5}Sr_{0.5}Co_{0.8}Fe_{0.2}O_{3-\delta}$, $La_{0.6}Sr_{0.4}FeO_{3-\delta}$ and $(La_{0.8}Sr_{0.2})_{0.95}FeO_{3-\delta}$. The quality criteria of the powders as phase purity and the particle size as described in chapter 3, the kinetic parameter, and the electrical conductivity were taken as criteria for the selection of one of the four cathode materials for the production of screen printing pastes. The results as a function of the temperature and the oxygen partial pressure are addressed and discussed for the application as SOFC cathodes.

4.1 Aspects of transport properties of mixed ionic/electronic conductors

4.1.1 Oxygen non-stoichiometry and electrical conductivity of mixed conductors

The dependence of the electrical conductivity on the temperature and the oxygen non-stoichiometry can be explained by the defect chemistry of the materials. The conductivity is modelled for several cases by Bucher et al. and Sitte et al. [83-89]. The perovskite-type oxides $La_{0.4}Sr_{0.6}CoO_{3-\delta}$ (LSC46) and $La_{0.4}Sr_{0.6}FeO_{3-\delta}$ (LSF46), which exhibit high electronic and ionic conductivities, are taken as examples [88] out of it. Oxygen vacancies and/or electron holes are able to compensate negative effective charges caused by Sr-doping of $LaBO_{3-\delta}$ (B = Co, Fe). The number of holes ($h^{\bullet}$) and oxygen vacancies ($V_O^{\bullet\bullet}$) has a contrary influence on the conductivity. An increase of the oxygen content in the lattice of the material leads to an increase of the p-type charge carriers (B^{4+}-ions, respectively electron holes). Oxygen release from the sample, on the other hand, leads to the formation of vacancies, while decreasing the number of holes. A decrease of the electronic conductivity together with an increase of the ionic conductivity can be observed. The equilibrium can be expressed in the Kröger-Vink notation ($\mathrm{M_S^C}$)

$$\frac{1}{2}O_2 + V_O^{\bullet\bullet} + 2B_B^x \Leftrightarrow O_O^x + 2B_B^{\bullet}, \qquad \text{Equation 15}$$

where M corresponds to the species, S is the lattice site that the species occupies and C corresponds to the electronic charge of the species relative to the site that is occupied. Zero charge is indicated by x, a single positive charge by •, and a negative charge by ‘. The double positively charged vacancies are denoted by $\mathrm{V_O^{\bullet\bullet}}$, neutral Fe^{3+} and Co^{3+} on Fe- and Co-sites by $\mathrm{B_B^x}$. Oxygen on oxygen sites is written as $\mathrm{O_O^x}$, and the positively charged Fe^{4+} and Co^{4+} as $\mathrm{B_B^{\bullet}}$. The corresponding equilibrium constant according to the mass action law is expressed in Equation 16.

$$K_{ox} = \frac{[O_O^x][B_B^{\bullet}]}{p(O_2)^{1/2}[V_O^{\bullet\bullet}][B_B^x]^2}. \qquad \text{Equation 16}$$

The charge disproportionation of $\mathrm{B_B^x}$ into $\mathrm{B_B^{\bullet}}$ and $\mathrm{B_B^{'}}$ accordingly writes as

$$\mathrm{2B_B^x \Leftrightarrow 2B_B^{'} + 2B_B^{\bullet}}, \qquad \text{Equation 17}$$

with the equilibrium constant

$$\mathrm{K_i = \frac{[B_B^{'}][B_B^{\bullet}]}{[B_B^x]^2}}. \qquad \text{Equation 18}$$

Bucher et al. [88] in their point defect model ascribe electrons and holes to be localized on the specific B-site ions. They obtain 3 additional Equations (19-21) from the electro neutrality condition and the site conservation requirements for the O-site respectively B-site species.

$$[Sr_{La}^{'}]+[B_B^{'}]=[B_B^{\bullet}]+2[V_O^{\bullet\bullet}], \qquad \text{Equation 19}$$

$$[V_O^{\bullet\bullet}]+[O_O^{x}]=3, \qquad \text{Equation 20}$$

$$[B_B^{x}]+[B_B^{'}]+[B_B^{\bullet}]=1. \qquad \text{Equation 21}$$

The equilibrium constants K_i and K_{ox} can be determined by nonlinear least square fits after solving the set of 5 Equations represented by Equation 16 and Equation 18-21 [88]. The corresponding expression represents the oxygen partial pressure $p(O_2) = f(K_i,K_{ox}, x, \delta)$, where x stands for the Sr-content and the oxygen vacancy concentration is given by δ. The simple point defect model (no dependence of the mobility of charge carriers on the oxygen content) predicts a plateau of δ at values of $\delta \approx x/2$ (dashed line in figure 31). The measured values of δ don't show this picture, which is attributed to the decreasing ratio K_{ox}/K_i.

Figure 31 shows an example according to Bucher et al. [88] fitting the non-stoichiometry of $La_{0.4}Sr_{0.6}CoO_{3-\delta}$ as a function of the $p(O_2)$ at 750 °C and 825 °C. The fitting of the experimental data was done with the described point defect model, the simplified point defect model and the itinerant electron model [90].

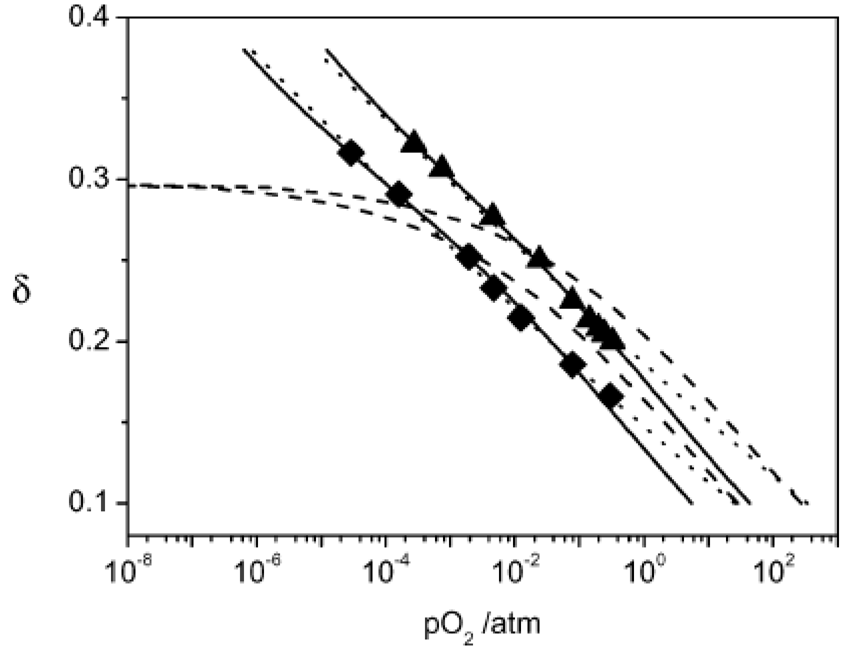

Figure 31: Experimental data from Bucher et al. [88] of the oxygen non-stoichiometry of $La_{0.4}Sr_{0.6}CoO_{3-\delta}$ at 750 °C (♦) and 825 °C (▲). Lines correspond to nonlinear least squares fits to the point defect model (solid), the simple point defect model (dashed), and the itinerant electron model [90],dotted).

Ionic and electronic defect concentrations can be also calculated from experimental data of the oxygen non-stoichiometry. It can be seen looking at Equation 22 that the conductivity is a function of the number and the mobility of charge carriers (mobilities of electrons and holes (μ_n and μ_p) are.

$$\sigma = e\frac{N_A}{V_m}(p\mu_p + n\mu_n) \qquad \text{Equation 22}$$

N_A is Avogadro's number, V_m is the molar volume, e is the elementary charge, and the p- and n- type charge carriers are molar fractions of $[B_B^{\bullet}]$ and $[B_B^{'}]$, respectively.

The point defect model allows the modelling of the electrical conductivity (σ) as a function of δ. The equilibrium constants K_i and K_{ox} are used to determine the number of p-type charge carriers at defined δ. The mobility of holes subsequently can be estimated from the electronic conductivity and the calculated charge carrier concentrations as a function of oxygen non-stoichiometry [87].

Bucher et al. [87] present three models for σ(δ). The simplest one sets the mobility of the charge carriers as independent of the oxygen content and σ therefore is regarded as a linear function of the site fractions ($y_{2,3} = [B_B^{'}]/([B_B^{x}]+[B_B^{'}])$, $y_{4,3} = [B_B^{\bullet}]/([B_B^{x}]+[B_B^{\bullet}])$). However, this simple model doesn't fit to the conductivity data from $La_{0.4}Sr_{0.6}FeO_{3-\delta}$ taken from Bucher et al. [87] as displayed in Figure 32.

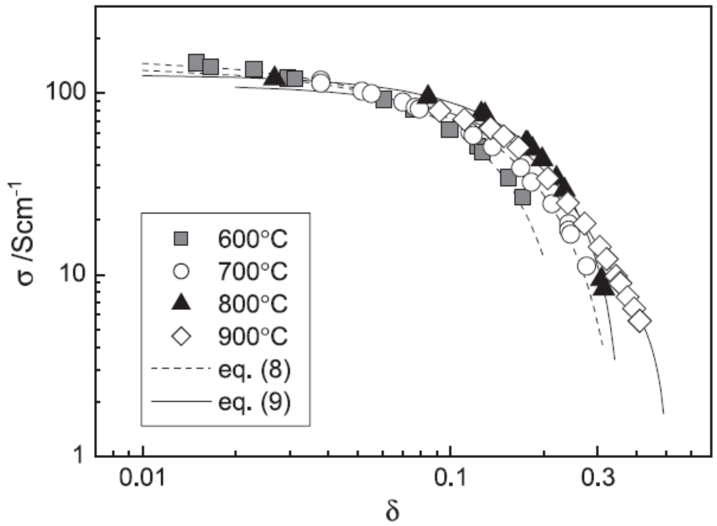

Figure 32: The electronic conductivity of LSF46 as a function of the oxygen non-stoichiometry. Dashed lines correspond to fits of the first term of Equation 23 at 600 °C and 700 °C. Solid lines represent fits to Equation 24 at 800 °C and 900 °C as published by Bucher et al. [87].

Two other models were applied successfully by Bucher et al. [87] that could describe the significant decrease of σ with increasing δ. The mobility of charge carriers was modelled as a function of the available site fractions $y_{3,2} = [B_B^{x}]/([B_B^{'}]+[B_B^{x}])$ and $y_{3,4} = [B_B^{x}]/([B_B^{\bullet'}]+[B_B^{x}])$, taking the fraction of vacant oxygen sites into account. The increase of the conductivity with increasing oxygen content (3 - δ) is expressed in Equation 23 and 24.

$$\sigma(\delta) = C[y_{4,3}(1-A\delta) + y_{2,3}(1-B\delta)], \qquad \text{Equation 23}$$

$$\sigma(\delta) = C[y_{4,3}\, y_{3,4}\,(1-A\delta) + y_{2,3}\, y_{3,2}\,(1-B\delta)], \qquad \text{Equation 24}$$

with the parameters A and B for the dependences of μ_p and μ_n on the oxygen vacancy concentration and C as a scaling factor. The dependence on the fraction of available sites ($y_{3,2}$ and $y_{3,4}$) is included in Equation 24, but not in Equation 23.

Equation 23 results in a better fit at 600 °C and 700 °C even when the second term (corresponds to the contribution of n-type conductivity) is neglected, Equation 24 is more appropriate fitting $\sigma(\delta)$ at 800 °C and 900 °C. This fact might correspond to the increasing importance of the n-type conductivity at higher temperatures.

Temperature dependence of the electronic conductivity at constant oxygen partial pressure

The temperature dependence of the electronic conductivity of LSF46 and the oxygen nonstoichiometry are compared in Figure 33 as taken from Bucher et al. [87]. The maximum of the conductivity appears to correspond to the same temperature where δ begins to increase. As described before, the formation of oxygen vacancies leads to a decrease of p-type charge carriers. Bucher et al. [87] showed by the analysis of σ vs. δ at 600-900 °C that the decreasing number of holes leads to a decrease of the conductivity because the impact is stronger than the increasing mobility of the charge carriers with increasing temperature.

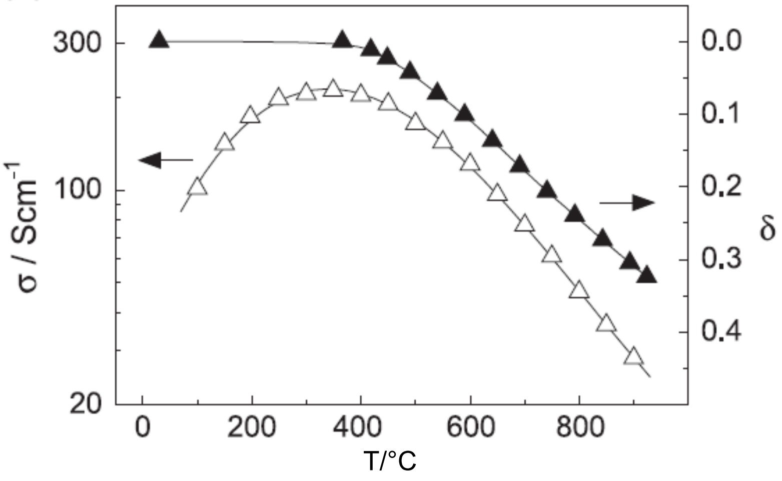

Figure 33: Temperature dependences of the electronic conductivity and the oxygen nonstoichiometry of LSF46 at 1.0 10^{-2} bar (from [87]).

Temperature dependence of the iso-stoichiometric electronic conductivity

Knowing the temperature dependence of σ and δ at different oxygen partial pressures, the conductivities at constant values of δ can be evaluated. Figure 34 shows a comparison of the conductivity at isobar and iso-stoichiometric (δ = constant) conditions as published by Bucher et al. [83] and Sitte et al. [86].

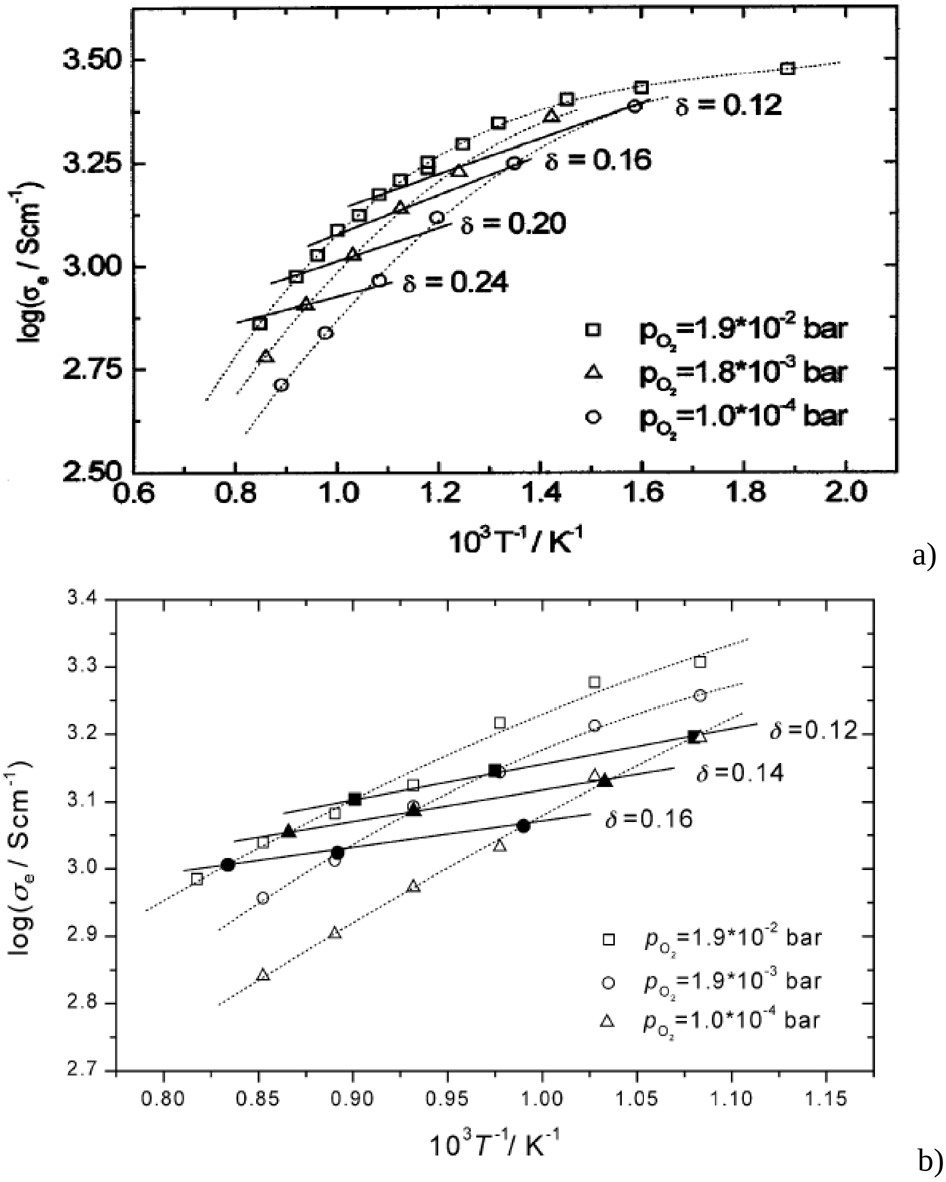

Figure 34: Electronic conductivities of La$_{0.4}$Sr0$_{.6}$CoO$_{3-\delta}$ (a) and La$_{0.6}$Sr0$_{.4}$CoO$_{3-\delta}$ (b) as a function of T^{-1} at constant p(O$_2$), solid lines respresent the iso-stoichiometric conductivities (from [83] (a) and [86](b)).

Sitte et al. [86] suggest a thermally activated (activation energy between 0.2-0.5 eV) polaron hopping conduction mechanism for $La_{0.6}Sr_{0.4}CoO_{3-\delta}$ because of a linear dependency of $\ln(\sigma_e T)$ vs. T^{-1} and an increase of the activation energy with increasing oxygen deficiency. Similar as for LSF46 a decrease of σ most probably coincides with the decrease of the concentration of free electrons holes [91]. This is equivalent to the decrease of tetravalent Co ions as already described for the modelling of σ. Furthermore, the conduction mechanism has been interpreted by the itinerant electron model [92] in the temperature range of 650-900 °C which is in agreement with the modelling of Bucher et al. [87] for higher temperatures. As visible in Figure 34 the conductivity at a constant temperature is changing as a function of the $p(O_2)$. Using this fact, the oxygen exchange of the material can be monitored by the conductivity, if the difference in the conductivity of a sample in two different atmospheres is large enough.

4.1.2 Oxygen exchange kinetics and chemical diffusion

The performance of mixed conducting cathode materials can be closely related to the oxygen exchange processes between the oxide ceramics and the surrounding atmosphere. Both the surface exchange of oxygen as well as the chemical diffusion through the bulk of the non-stoichiometric oxides are important factors [93]. Among different methods that can be found in the literature as coulometric titration [94-97], impedance spectroscopy [98, 99], carrier gas coulometry [100], electrochemical polarization experiments [101], Isotope Exchange Depth Profiling [102], and thermogravimetry [77, 103], conductivity relaxation [81, 89, 104-108] was chosen in order to evaluate the chemical surface exchange and diffusion coefficients as a function of the temperature and oxygen partial pressure.

The so called conductivity relaxation method applying the van der Pauw method as described by Preis et al. [109] was used in the present study to determine simultaneously the chemical diffusion and surface exchange coefficient. Conductivity relaxation is an adequate method because the electrical conductivity in the case of the investigated materials is is a very sensitive number in order to detect changes in the oxygen chemical potential in the surrounding atmosphere of the sample. Even small $p(O_2)$ steps result in considerable changes in the electrical conductivity that can be attributed to small changes in the oxygen content of the specimen [110].

4.1.3 Assessment of conductivity relaxation curves

The calculations presented in [110] correspond to the total amount of diffusing species (oxygen) exchanged between the ceramics and the gas phase (diffusion source) as expressed in Equation 25.

$$\frac{m(t)}{m(\infty)} = \frac{1}{V}\int_V \frac{c - c_0}{c_\infty - c_0} dV' \qquad \text{Equation 25}$$

The change in the electrical conductivity, used in the conductivity relaxation method, is proportional to the mass exchange of the sample. The normalized conductivity (σ_n) can be calculated by dividing the differences between the conductivity of the sample at a certain time (t) after the $p(O_2)$ change in the reactor σ_t and at the equilibrium before the $p(O_2)$ change σ_o by the conductivity of the sample in equilibrium a long time after the $p(O_2)$ change (σ_{inf}) minus σ_o (Equation 26).

$$1 - \sigma_n = 1 - \frac{\sigma_t - \sigma_0}{\sigma_{inf} - \sigma_0} = 1 - \frac{m_t}{m_\infty} \qquad \text{Equation 26}$$

After normalizing the conductivity, the linear fit of $\ln(1-\sigma_n)$ vs. t(ime) can be evaluated.

Criterion 1: Intercept with ordinate $-0.21 \leq A \leq 0$

According to Crank [111] a mixed controlled behaviour of the sample can be assumed, when the intercept of the fit through the long term interval of $\ln(1-\sigma_n)$ fulfils criterion 1. Figure 35 shows an exemplary curve with an intercept of the ordinate (A) amounting in -0.13. The curve meets criterion 1 which reflects the domain between $D \to \infty$ and $k \to \infty$.

Therefore, the simultaneous evaluation of both, the surface exchange and the diffusion coefficient can be performed.

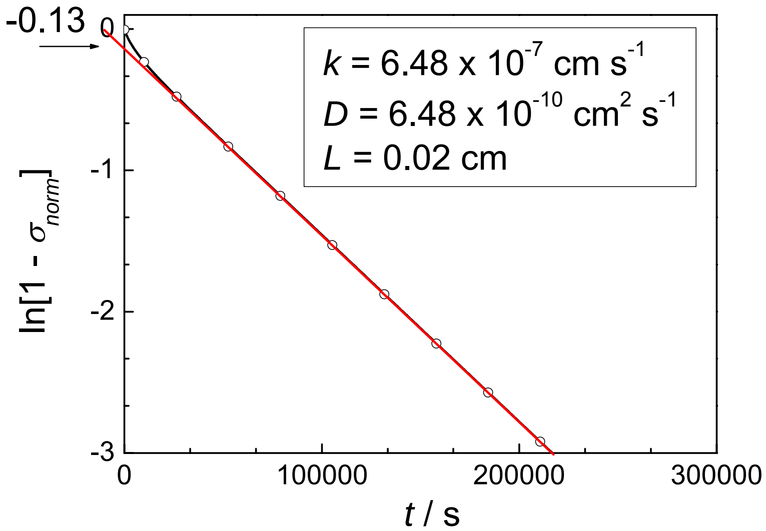

Figure 35: Example of surface exchange and diffusion (= mixed) controlled behaviour and the corresponding Equation to fit the kinetic parameter (with kind permission of W. Preis [112]).

The kinetic parameters $\tilde{D}$ and $\tilde{k}$ can be obtained by fitting to the long time approximation (Equation 27) according to Preis et al. [112, 113]. The critical length (L_c) of the sample is defined as the quotient of $\tilde{D}/\tilde{k}$ as also used by Lane et al. [106]. The sample thickness (L) should not deviate more than a factor of 100 (reflected in criterion 2) from the critical length to allow a meaningful evaluation of both $\tilde{D}$ and $\tilde{k}$.

$$\ln(1-\sigma_n) = \ln\left(\frac{2\tilde{k}^2}{\tilde{D}^2\gamma^2\left[(\tilde{k}L/\tilde{D})^2/4+\gamma^2L^2/4+\tilde{k}L/(2\tilde{D})\right]}\right) - \tilde{D}\gamma^2 t$$

Equation 27

with

$\tilde{k}/\tilde{D} = \gamma\tan(\gamma L/2)$

Criterion 2: 1 < kL/D < 1000

If the intercept of the linear fit (A) with the ordinate does not fulfil criterion 2, diffusion or surface exchange ($\tilde{k}$) controlled behaviour of the sample is indicated. $\tilde{D}$ or $\tilde{k}$ can be evaluated by linear models presented for both cases. The appearance of the data for both cases is displayed in Figure 36.

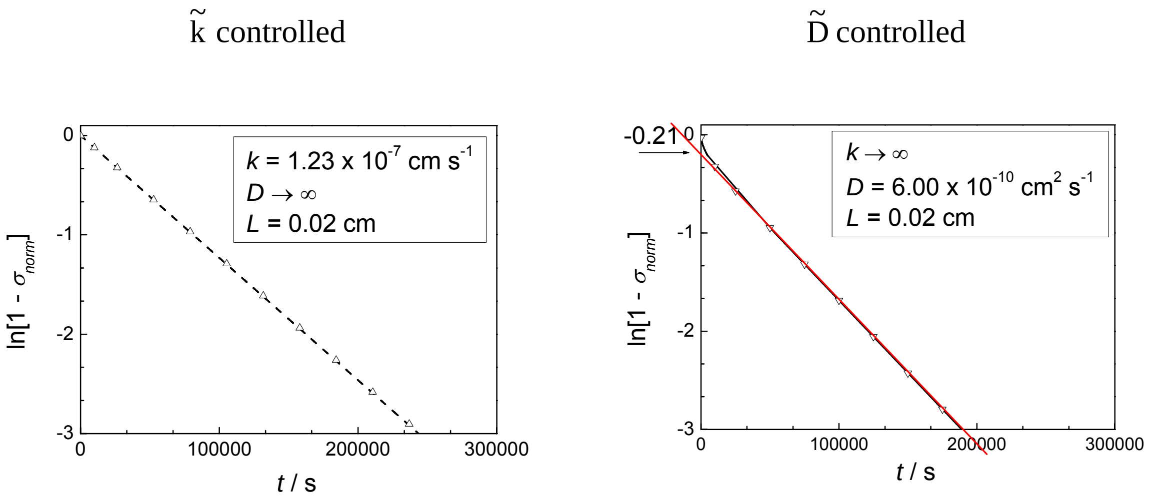

$\tilde{k}$ controlled

$\tilde{D}$ controlled

Figure 36: Appearance of data points for $\tilde{D}$ and $\tilde{k}$ controlled behaviour of the conductivity relaxation curves (with kind permission of W. Preis [112]).

In case A >> 0 and ln(1- σ_n) vs. t in the short time interval is linear $\tilde{k}$-controlled kinetics can be fit with an alternative linear model according to Equation 28.

$$\ln(1-\sigma_n) = 0 - \frac{2\tilde{k}}{L}t \qquad \text{Equation 28}$$

In case A = -0.21 und ln(1- σ_n) vs. t is bended downwards in the short time interval, then only an evaluation of $\tilde{D}$ is meaningful and can be fitted with Equation 29.

$$\ln(1-\sigma_n) = \ln\left(\frac{8}{\pi^2}\right) - \frac{\tilde{D}\pi^2}{L^2}t \qquad \text{Equation 29}$$

In the case of small deviations from criterion 1, a mixed controlled evaluation might be possible, but criterion 2 has to be fulfilled to obtain meaningful results.

4.2 Experimental techniques

4.2.1 Measurement of the electrical conductivity by the van der Pauw method

The van der Pauw [114] method was applied in order to obtain accurate values of the electrical conductivity of the samples. The method is based upon a theorem which can be applied for a flat sample of arbitrary shape. The contacts have to be sufficiently small and located at the circumference of the sample. Furthermore, the sample must be singly connected, hence not show pores, holes, cracks. The error of the presented measurements according to Grientschnig et al. [115] is at most 5 per cent, while the use of a linear geometry is causing much larger errors.

The contacts are placed on the edge of the sample in approximately 90° distance. After applying a constant current between contact R and S measuring the voltage between P and Q, the contacts are changed and the current is applied between R and Q and the voltage is measured between P and S. The resistances $R_{PQ,RS}$ and $R_{PS,RQ}$ are calculated as the quotient between the measured voltage divided by the applied current. Knowing the thickness of the sample the specific conductivity (σ) can be evaluated iterating Equation 30.

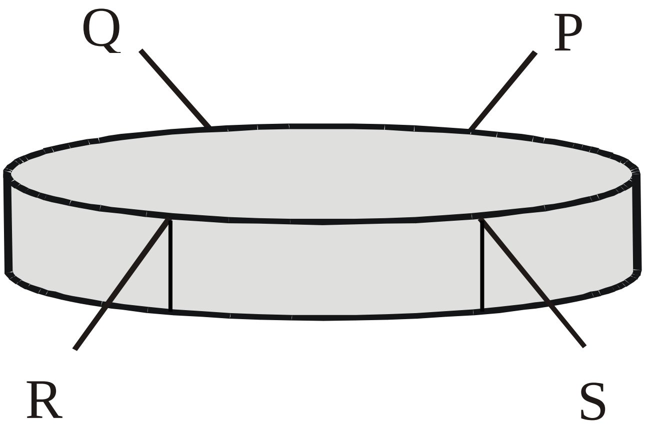

Figure 37: Pellet shaped sample equipped with contacts in the van der Pauw geometry.

$$\exp(-\pi R_{PQ,RS} d \sigma) + \exp(-\pi R_{PS,RQ} d \sigma) = 1 \qquad \text{Equation 30}$$

The major advantage of the van der Pauw geometry is that only the thickness of the sample pellet has to be known exactly.

4.2.2 Setup for conductivity relaxation experiment

Conductivity relaxation curves for LSF82 were obtained between 626 °C and 841 °C in a $p(O_2)$ range between 10^{-4} to 0.2 bar oxygen partial pressure. Data were obtained for BSCF and LSCF between 600 °C and 800 °C and for LSF64 at 700 °C. The principal setup for the conductivity relaxation experiments is shown schematically in Figure 38. Similar set-ups for conductivity relaxation experiments can be found in the literature [19, 116].

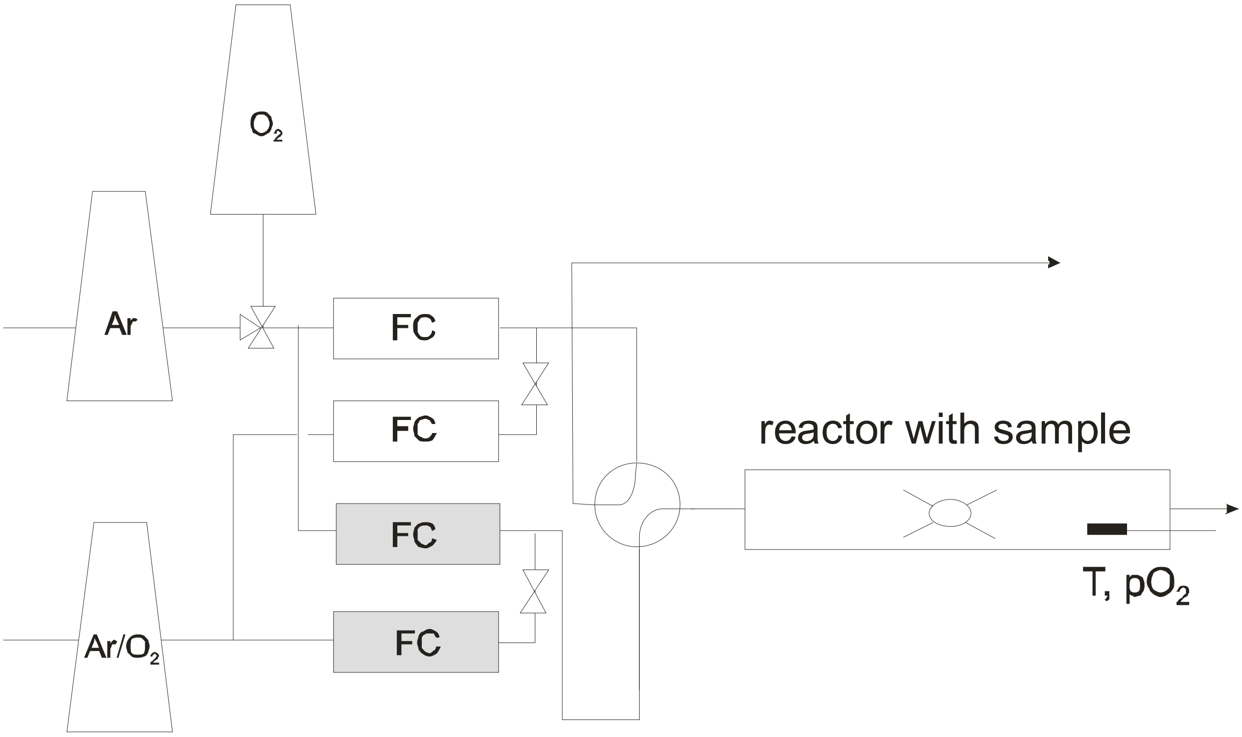

Figure 38: Experimental setup for the conductivity relaxation experiments (with kind permission of E. Bucher [117]).

The sample is placed in a reactor made from quartz glass, with a temperature and $p(O_2)$ sensor (Setnag France) in the direct vicinity of the sample. Applying a constant current, the voltage of the sample at a constant temperature was recorded continuously to detect the sample's response when switching between two gas mixtures with different $p(O_2)$ values by a 4-way-valve. Flow controllers (Mycrolis, FC2700) were used to set a constant flow of the gas mixture. The $p(O_2)$ was thus changed stepwise by a constant factor (typically 2).

4.2.3 Analysis of conductivity relaxation curves

Prior to the conductivity relaxation experiments the relaxtion time of the empty reactor (τ) is evaluated. It has to be small in comparison with the relaxation time of the sample as further described in [113, 118]. The oxygen partial pressure of the empty reactor is measured applying a stepwise change of the oxygen partial pressure to the reactor and τ is obtained fitting to

$$c_t = c_0 + (c_{inf} - c_0)\left[1 - exp\left(-\frac{t}{\tau}\right)\right] \qquad \text{Equation 31}$$

knowing the partial pressure at a certain time (t) after the change is fitted (c_t) before (c_0), and at infinite time (c_{inf}) after the $p(O_2)$ change (c_{inf}) as a function of time. Further details about the flush time correction can be found in the literature [113, 118]. In course of the presented measurements the relaxation time of the sample was at least 100 times larger than τ.

A typical experiment is shown in Figure 39 including the in-situ detection of the $p(O_2)$ during the measurement. The black curve shows the change of the $p(O_2)$ in the direct vicinity of the sample. The red curve displays the temperature of the gas atmosphere during the measurement and the blue curve the conductivity of the sample in arbitrary units.

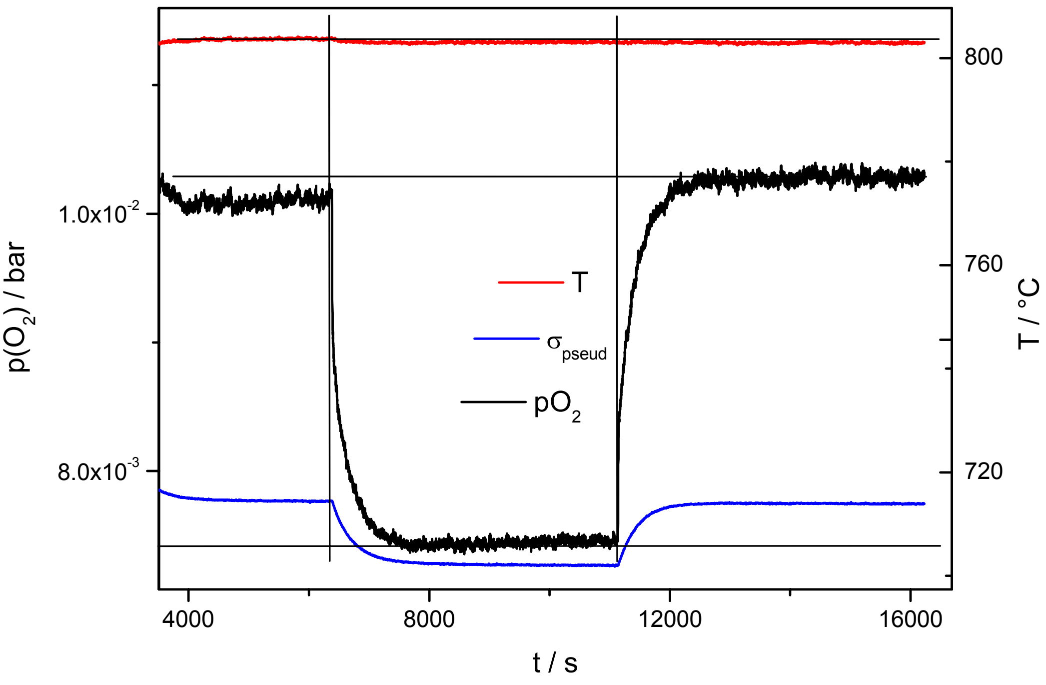

Figure 39: Conductivity relaxation experiment showing the conductivity as a function of the p(O_2) change between two constant atmospheres. The conductivity (blue curve, arbitrary units) of the sample, and the temperature (red) and the p(O_2) in the direct vicinity of the sample are displayed.

The p(O_2) in the direct vicinity of the sample is changing gradually to a constant value during about 2000 s, while the atmosphere of the empty reactor changes quickly in about 5 s as described further in detail elsewhere [81]. The recorded electrical conductivity clearly indicates that the conductivity changes when the sample changes its oxygen content. In the present case, the conductivity decreases, when the sample looses oxygen. The stepwise change of the p(O_2) from 0.01 bar to 0.007 bar at the inlet of the reactor provokes an oxygen release of the sample, indicated by the slow decay of the measured p(O_2) in the direct vicinity of the sample. After reaching a constant value of the p(O_2) in the reactor the conductivity becomes constant. The stepwise change of the gas atmosphere from 0.007 bar back to 0.01 bar analogically provokes a slow increase of the conductivity, corresponding to a slow increase of the p(O_2) in the direct vicinity of the sample until both parameters reach a constant value.

The measured conductivity relaxation curves were normalized and the chemical diffusion and surface exchange coefficients were obtained by fitting of the appropriate solution of the diffusion Equation 32. Details are described in the literature [100]):

$$(1-\sigma_{\mathrm{norm}}) = 2h^2 \sum_{n=0}^{\infty} \frac{1/\tau}{1/\tau - \alpha_n^2 \tilde{D}} \times \frac{\exp(-\alpha_n^2 \tilde{D} t) - \alpha_n^2 \tilde{D} \tau \exp(-t/\tau)}{\alpha_n^2 (h^2 L^2/4 + hL/2 + L^2 \alpha_n^2/4)} \qquad \text{Equation 32}$$

σ_{norm} is the normalized conductivity of the sample, L is the thickness of the disk-shaped sample, $\tilde{k}$ the chemical surface exchange and $\tilde{D}$ the chemical diffusion coefficient respectively, and α_n is given by the roots of $\alpha_n \tan(\alpha_n L/2) = h$ with h = $\tilde{k}/\tilde{D}$. The non-ideal step response of the quartz reactor containing the sample is taken into account by the time constant (τ) needed to flush the empty reactor. The time constant was determined prior to the conductivity relaxation experiments and was found to be lower than 10 s for the whole $p(O_2)$ range [81] which is at least one order of magnitude lower than the relaxation time of the samples.

An example of a normalized conductivity relaxation curve and the fit of the appropriate solution of the diffusion Equation (Equation 32) to the experimental values are given in Figure 40.

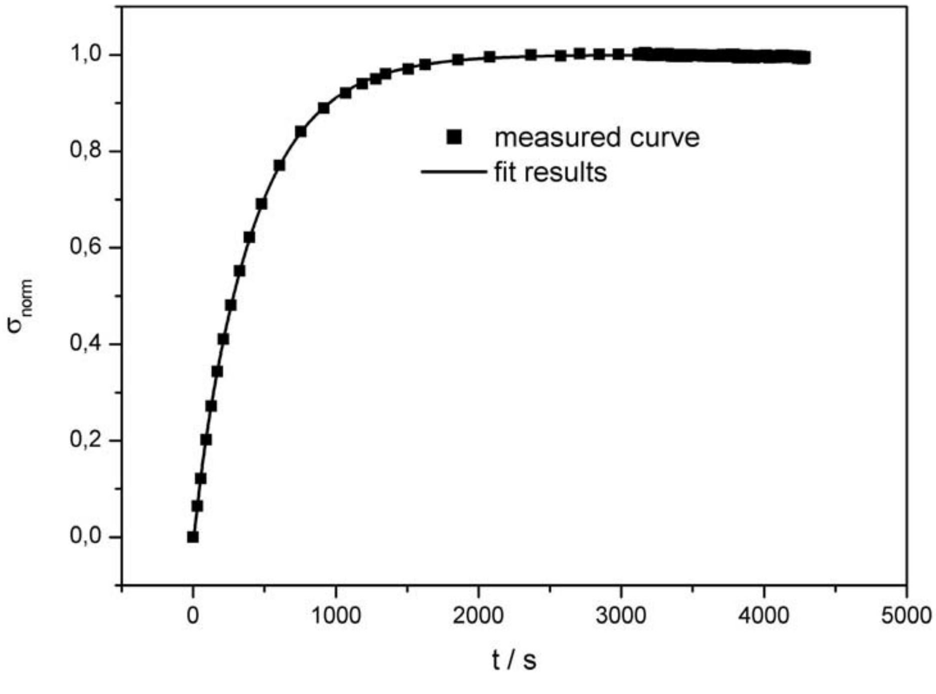

Figure 40: Normalized conductivity relaxation curve (BSCF, 600 °C, 0.033 bar ≤ $p(O_2)$ ≤ 0.086 bar) and the corresponding fit.

Good agreement between measured and simulated data is obtained. Both $\tilde{k}$ and $\tilde{D}$ could be evaluated, when the critical length ($L_c = \tilde{D}/\tilde{k}$) of the sample was not deviating more than a factor of approximately 50 from the thickness of the sample. In several cases only $\tilde{k}$ could be evaluated (when L_c was much higher than the sample's thickness) and only $\tilde{D}$ when L_c was much lower than the sample thickness. $\tilde{D}$ and $\tilde{k}$ values were plotted versus the mean $p(O_2)$ for both oxidation and reduction experiments.

The temperature and $p(O_2)$ dependence of the conductivity was measured in the same setup in course of the conductivity relaxation experiments as well as in separate experiments respectively. After time between 30 min and more than 12 h (depending on the temperature) the conductivity in the thermodynamic equilibrium was measured.

4.3 Results: Electrical conductivity as function of temperature and oxygen partial pressure

4.3.1 Electrical conductivity of LSCF: isobars and isotherms

The temperature dependence of the electrical conductivity of LSCF is displayed in Figure 41 in air and pure oxygen atmosphere. The conductivity of LSCF is increasing with temperature to a maximum of 418 S/cm in air and 412 S/cm in pure oxygen at approximately 550 °C. The conductivity slowly decreases at higher temperatures, which is slightly less pronounced in the pure oxygen atmosphere.

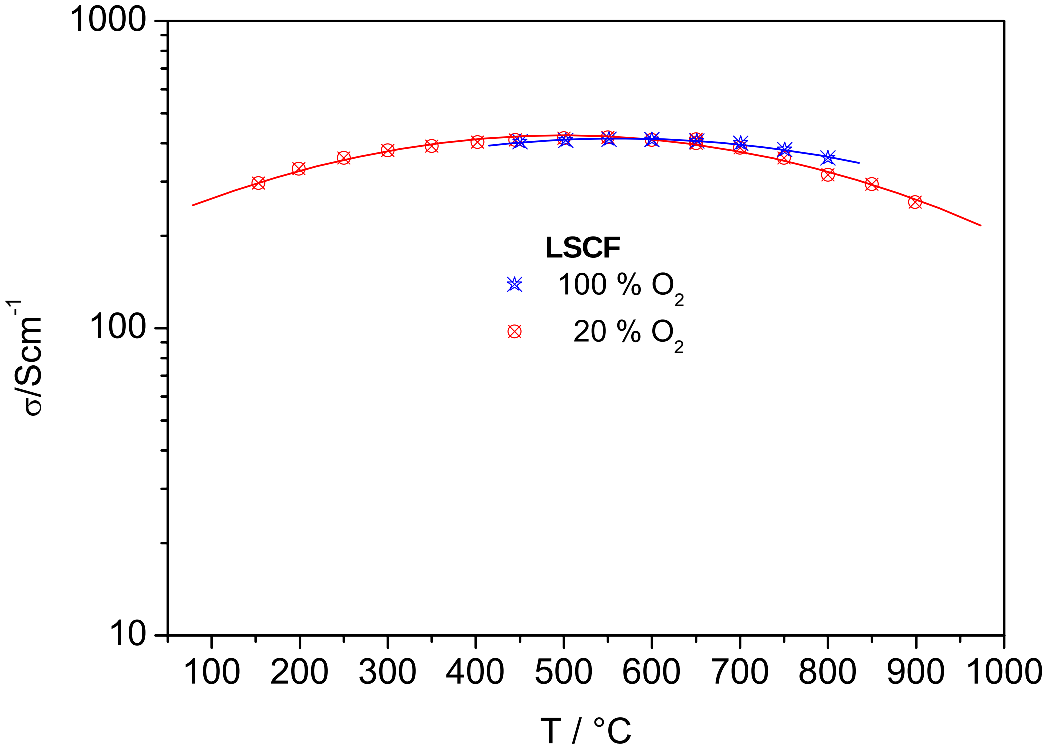

Figure 41: Temperature dependence of the electrical conductivity of LSCF in pure oxygen and 20 % O_2 with lines to guide the eye.

Figure 42 shows the Arrhenius plot of the conductivities measured at p(O_2) = 0.01 bar, 0.2 bar and in pure oxygen atmosphere. The part of the data was selected, where the slope shows a linear dependence and the activation energies (E_A = 0.67-0.73 eV) were calculated from the slope.

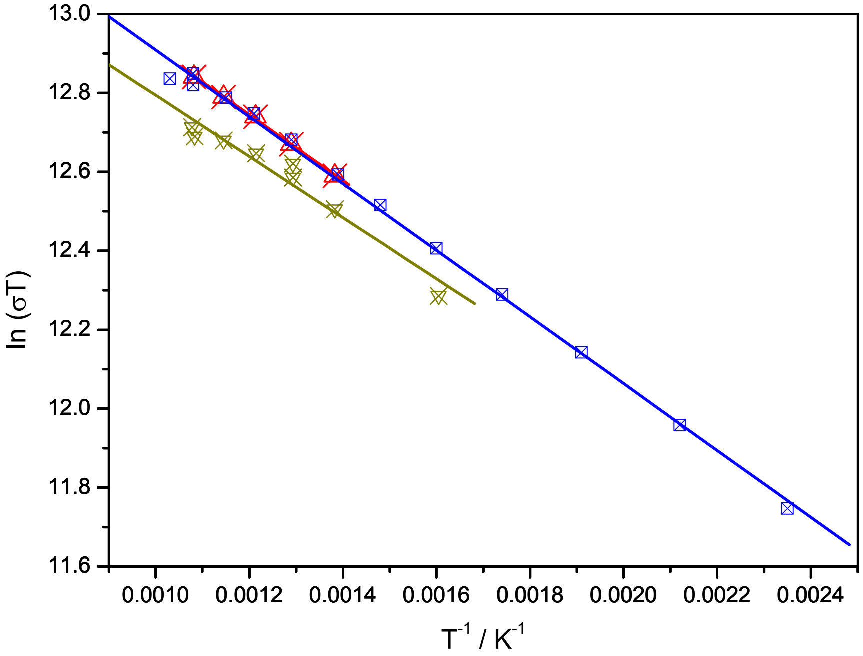

Figure 42: Arrhenius plot of LSCF: temperature dependence the electrical conductivity at $p(O_2)$ = 1 bar (red, E_a = 0.072 eV), $p(O_2)$ = 0.2 bar (blue, E_a = 0.070 eV), and $p(O_2)$ = 0.01 bar (green, E_a = 0.067 eV).

The oxygen partial pressure dependence of the conductivity of LSCF is displayed in Figure 43. The slope is lower in the $p(O_2)$ interval between 0.01-1 bar and increases when the oxygen partial pressure is further reduced.

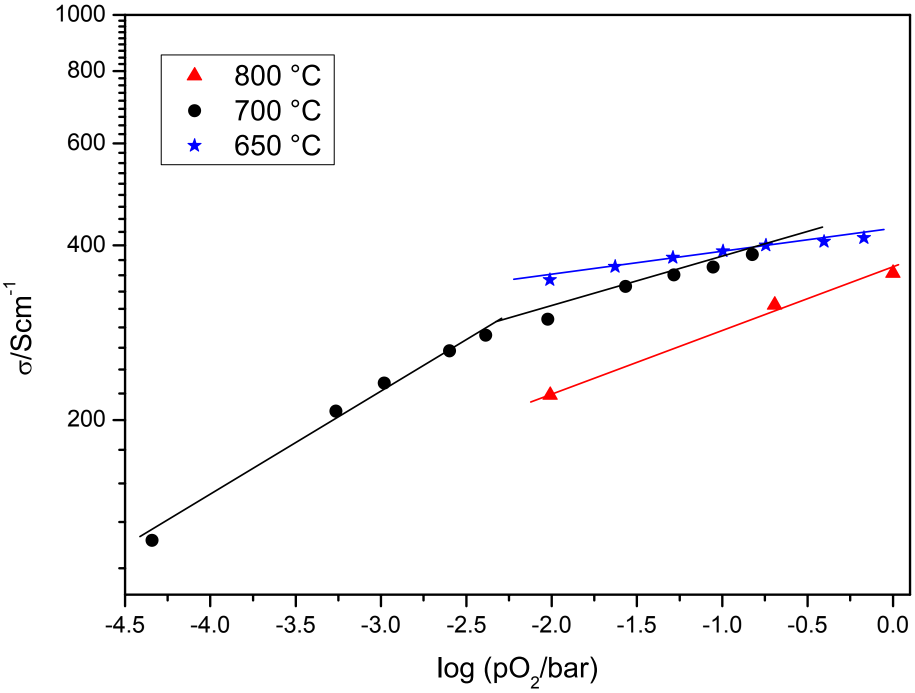

Figure 43: Oxygen partial pressure dependence of the electrical conductivity at 650 °C, 700 °C and 800 °C of LSCF6428 (lines to guide the eye).

4.3.2 Electrical conductivity of BSCF: isobars and isotherms

The temperature dependence of the electrical conductivity in the thermodynamic equilibrium of BSCF is displayed in Figure 44 for atmospheres with different oxygen partial pressure. The maximum in the conductivity in air (54 Scm^{-1}) and pure oxygen (84 Scm^{-1}) is reached at approximately 350 °C. At temperatures between 400 °C and 900 °C only a slight decrease in the conductivity is visible.

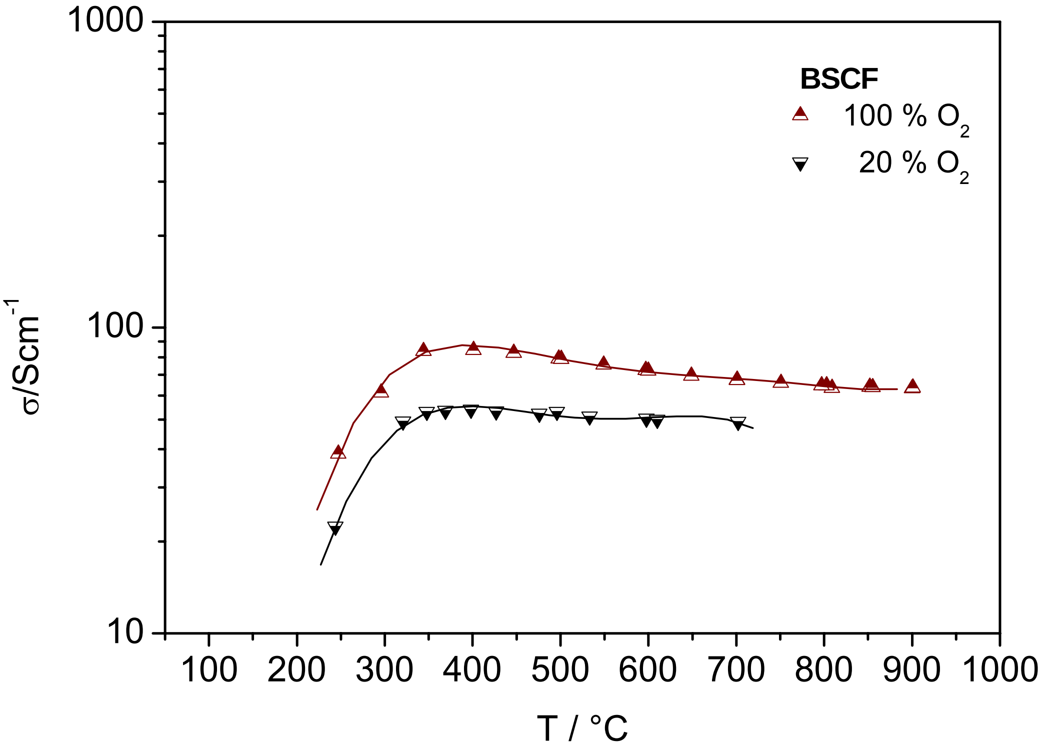

Figure 44: Temperature dependence of the electrical conductivity of BSCF in pure oxygen and 20 % O_2 atmosphere (lines to guide the eye).

The oxygen partial pressure dependence of the conductivity of BSCF is displayed in Figure 45. A change in the slope of the curves can be observed at $p(O_2)$ around 0.01 bar. The oxygen partial pressure dependence of the conductivity is more pronounced at $p(O_2)$ higher than 0.01 bar than at lower partial pressures.

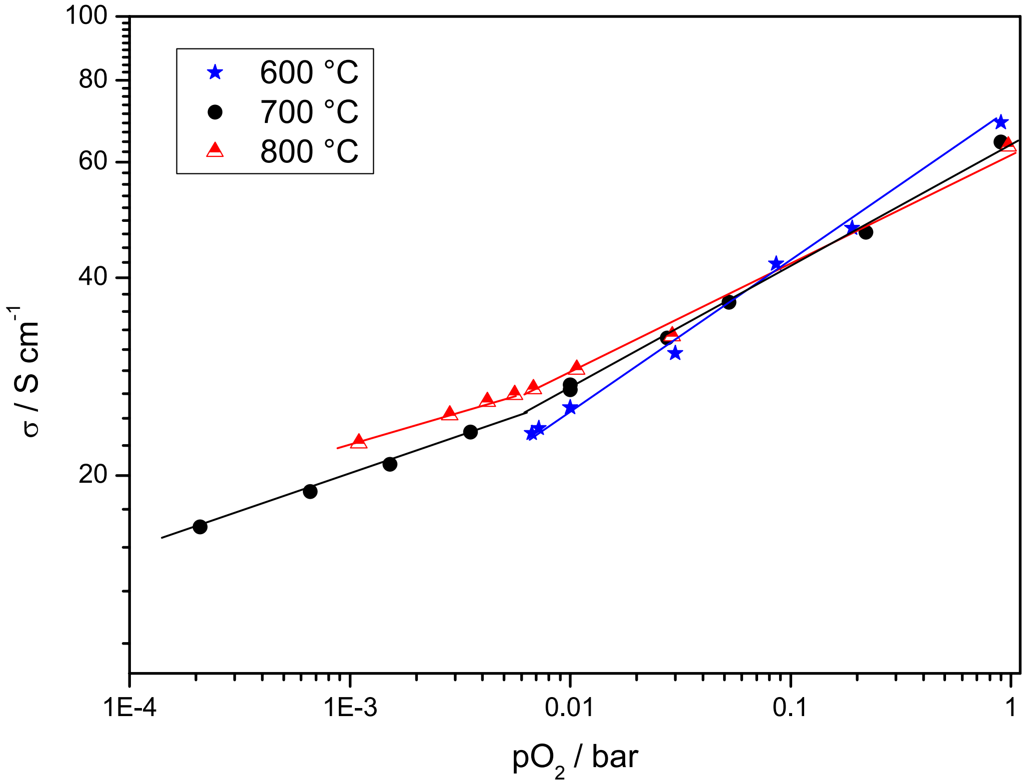

Figure 45: Oxygen partial pressure dependence of the electrical conductivity at 600 °C, 700 °C and 800 °C of BSCF (lines to guide the eye).

4.3.3 Electrical conductivity of LSF82: Isobars and isotherms

The temperature dependence of the electrical conductivity at a p(O_2) of 0.175 bar is displayed in Figure 46. The maximum conductivity in air is 91.7 Scm^{-1} at 686 °C with the corresponding activation energy of 0.12 eV.

The oxygen partial pressure dependence of the total electrical conductivity of LSF82 is displayed in Figure 47 at 626 °C, 736 °C and 841 °C. Generally, the conductivity increases with decreasing temperature between 841 °C and 626 °C. At a p(O_2) of 0.175 bar (log(p(O_2) = -0.75) the conductivity at 736 °C is higher than at 626 °C (Figure 46). Generally, the conductivity at higher p(O_2) is almost temperature independent between 626 °C and 841 °C.

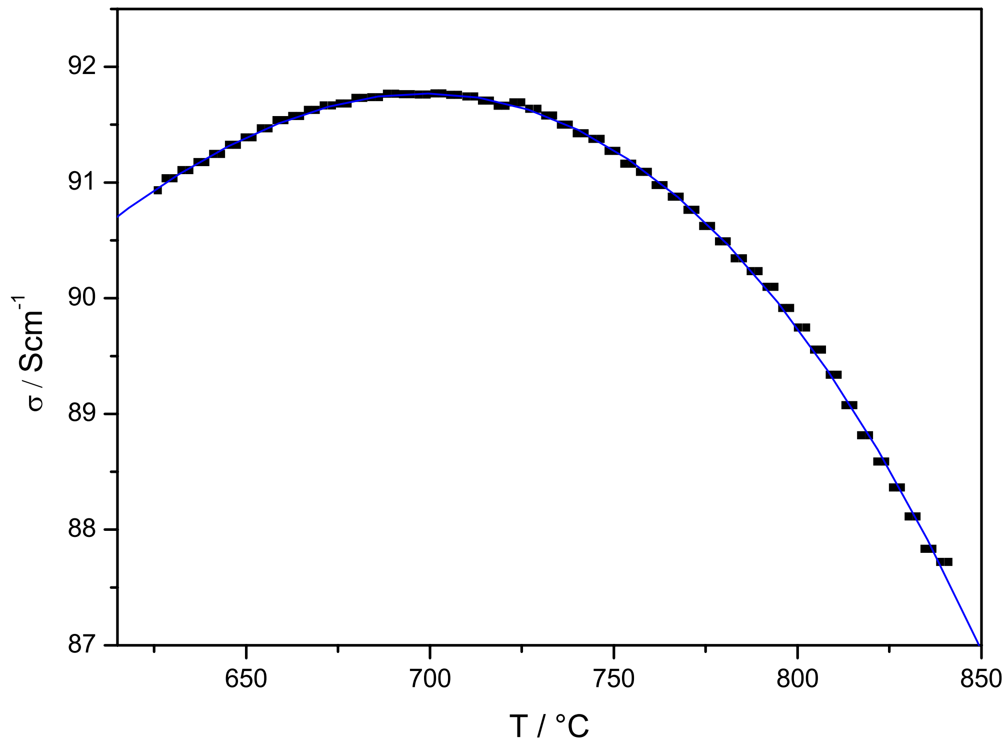

Figure 46: Electrical conductivity measured during cooling (0.2 K/min) at 0.175 bar oxygen partial pressure (line to guide the eye).

The slope at 626 °C is similar to LSCF at 650 °C in the higher p(O_2) interval between 1 mbar and 1 bar increases when the oxygen partial pressure is further reduced. The increase in the slope with the temperature is less pronounced at p(O_2) $\geq$ 1 mbar than for LSCF. This can be seen also in Figure 46. Generally, these two materials show similar trends in the partial pressure dependence with temperature between 626 °C and 841 °C at higher as well as lower partial pressures.

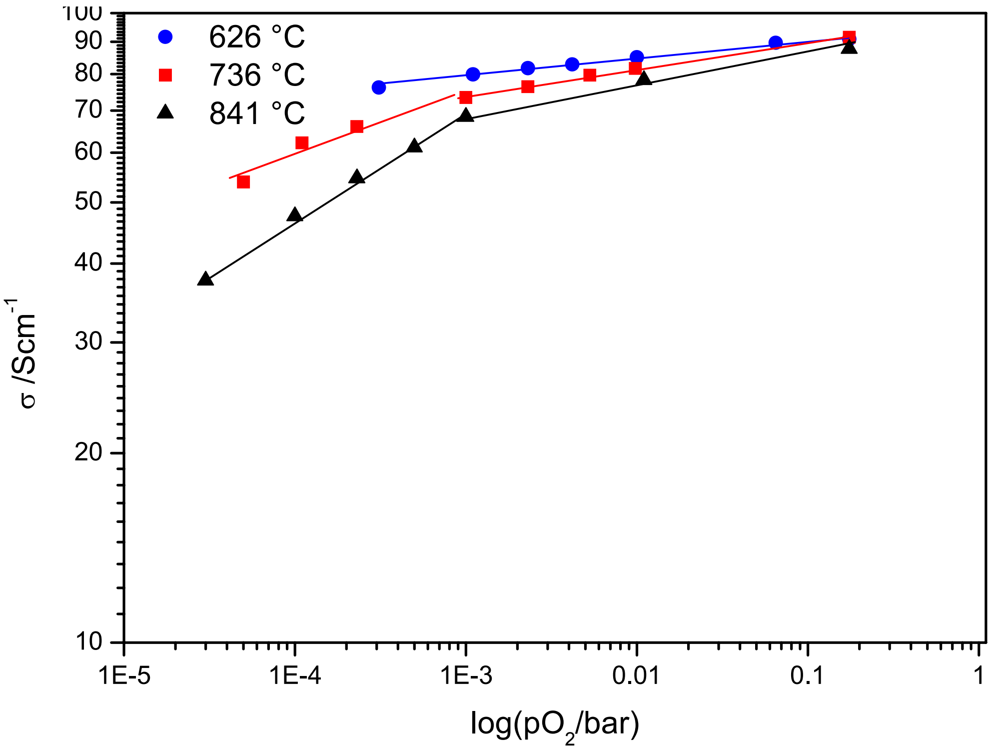

Figure 47: The p(O_2) dependence of the electrical conductivity of LSF82 at 626 °C, 736 °C and 841 °C (lines to guide the eye).

4.4 Discussion: Comparison of electrical conductivity (isotherms) of $La_{0.6}Sr_{0.4}Co_{0.2}Fe_{0.8}O_{3-\delta}$ and $Ba_{0.5}Sr_{0.5}Co_{0.8}Fe_{0.2}O_{3-\delta}$, $La_{0.6}Sr_{0.4}FeO_{3-\delta}$ and $(La_{0.8}Sr_{0.2})_{0.95}FeO_{3-\delta}$

4.4.1 Temperature dependence of the electrical conductivity

LSCF shows the highest conductivity and lowest activation energy among the tested materials. The values are in agreement with the literature [18, 52]. The activation energy was calculated from the slope of the Arrhenius plot in the linear regions and is summarized in Table V. The low activation energies of the materials suggest predominantly electronic conductivity. The activation energies of the ionic conductivities of SOFC cathode materials according to an evaluation of Ullmann et al. [52] are in the order of 0.7-1.4 eV. Hole conduction is presumed for all the four materials, because it is only slightly affected by the oxygen partial pressure. As pointed out in chapter 4.1.1 the conductivity maxima can be attributed to the temperatures where progressive oxygen exchange starts to take place and the increasing mobility of the holes is suppressed by the decreasing number of holes as charge carriers. Electrons as charge carriers seem to become more important at higher temperatures (≥ 800 °C) or lower oxygen partial pressures (< 10^{-4} bar) as can be seen from modelling the electronic conductivity by Bucher et al. [88]. The itinerant electron model fits better to the experimental data at higher T and lower p(O_2) which corresponds to considerations by Mizusaki [119]. Thus, electrons as charge carriers are present and the conductivity is decreasing with temperature as in metals. Table V summarizes the activation energies of the different materials in air and oxygen for different temperature ranges. The low activation energies correspond to an almost temperature independent conductivity of all tested materials.

Table V: Activation energy of the electrical conductivity of BSCF, LSCF, LSF64 and LSF82 (SD stands for standard deviation).

Conditions **T-range**	E_A / eV	SD / eV
BSCF air 250-350 °C	0.270	0.011
BSCF O_2 350-700 °C	0.052	0.002
LSCF air 150-550 °C	0.075	0.001
LSCF O_2 400-800 °C	0.072	0.001
LSF64 air (Mosley et al. [120])	0.31	-
LSF82 air 626-780 °C	0.116	0.001

The conductivity of LSCF is increasing with increasing temperature to a maximum of 418 S/cm in air and 412 S/cm in pure oxygen at approximately 550 °C, (E_A = 0.067-0.073 eV) in the p(O_2) range between 0.01 and 1 bar. The maximum conductivity is slightly higher and the activation energy is slightly lower as found by Tai et al. [18] who suggest small polaron conduction at temperatures below the conductivity maximum. At higher temperatures they speculate that the oxygen loss and the oxygen vacancy formation might be responsible for the decrease in the electrical conductivity. The decrease in the mobility of the charge carriers with increasing oxygen vacancy formation was later shown by Bucher and Sitte [87] for $La_{0.4}Sr_{0.6}FeO_{3-\delta}$. A similar behaviour is assumed to be present also for the four materials composition compared here.

The conductivity of BSCF generally is higher as evaluated by Wei et al. [54] and the activation energy (30.8 kJ/mol (= 0.270 eV) vs. 35.5 kJ/mol) in the lower temperature region is slightly lower than this literature values. Wei et al. [54] also suggest hopping of p-type small polaron as conduction mechanism. The activation energy at T > 350 °C amounts to 0.051 eV which is even lower than for LSCF and reflects the almost temperature independent behaviour of BSCF at temperatures higher than the conductivity maximum. The maximum conductivity of LSF82 is 91.7 Scm^{-1} in air at 686 °C. The evaluated activation energy for LSF82 similarly as for LSCF is 0.12 eV. In the literature [37] a slightly lower activation energy (= 0.09 eV) as well as a conductivity maximum at higher temperatures (800 °C vs. 736 °C) for $La_{0.8}Sr_{0.2}FeO_{3-\delta}$ are reported. The conductivity of LSF64 at 700 °C is 190 Scm^{-1} in pure oxygen and of 168 Scm^{-1} in air measured. The temperature dependence wasn’t evaluated. According to the literature [120] the activation energy of LSF64 is 0.31 eV and close to the value of BSCF below 350 °C, as illustrated with the triangle in the Arrhenius plot of the four materials displayed in Figure 48. The slope of BSCF at T > 350 °C is similar to LSCF and LSF82 that all show almost temperature independent behaviour of the conductivity.

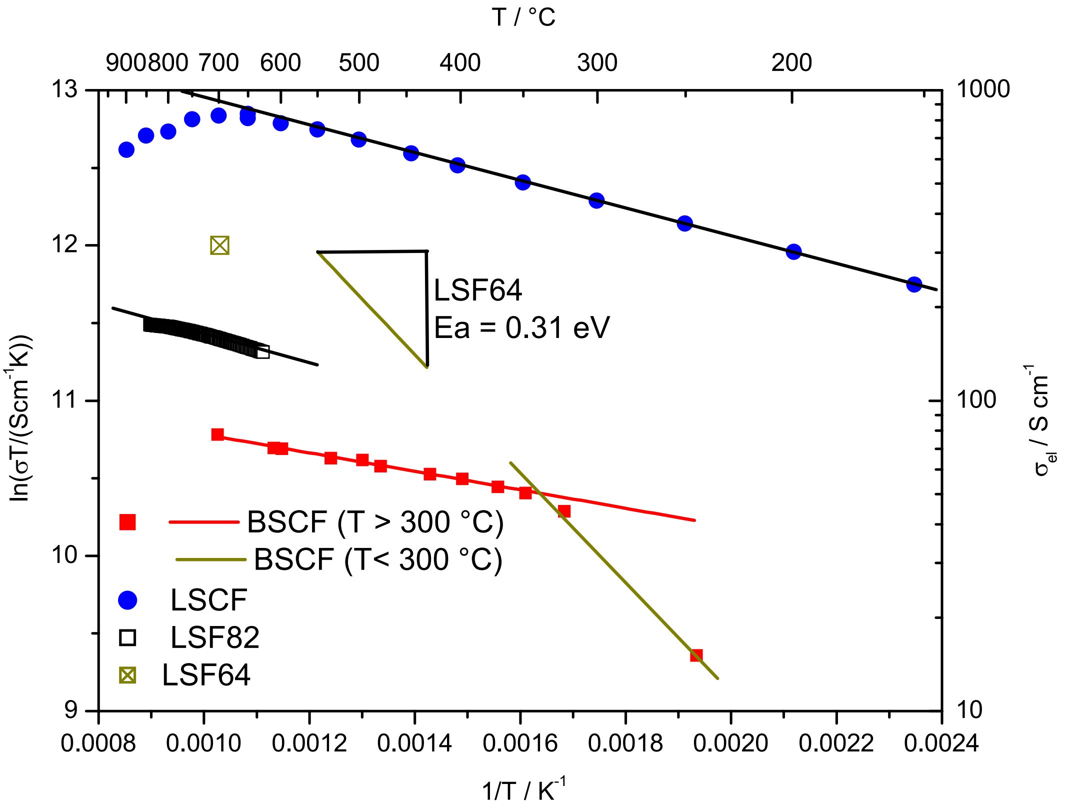

Figure 48: Electrical conductivity in air: Arrhenius plots of BSCF, LSCF of LSF82 and the illustration of the activation energy of LSF64 (lines to guide the eye).

Tai et al. [37] additionally to small polaron conduction also propose 3 more mechanism to explain the unique electrical conducting behaviour of oxides with similar composition like LSCF: (a) thermally activated charge disproportionation of Co ions; (b) ionic compensation by the formation of oxygen vacancies at higher temperatures; (c) preferential electronic compensation to form Fe^{4+} rather than Co^{4+}. At temperatures higher than the conductivity maximum a decrease, which is attributed to the temperatures, where the oxygen exchange of the materials starts to create an increasing number of vacancies thus competing with the electron holes [63, 86] that are supposed to be mostly responsible for the conductivity under the present conditions. This effect is less pronounced in the pure oxygen atmosphere, most probably due to the fact, that less oxygen vacancies are created and therefore, more holes as charge carriers are present as in air.

The reduction of LSCF is supposed to start at slightly lower temperatures than the conductivity maximum around 550 °C. The CTE in (chapter 3.2.2) seems to increase at T > 600 °C due to chemical expansion. Since the oxygen content influences both, electrical conductivity and thermal expansion, the large increase in the apparent CTE (up to 28 ppm/K) indicates a high polarizability of the material and thus a stronger dependence of the conductivity on $p(O_2)$ might be expected. In order to check if the oxygen non stoichiometry changes are in agreement with the observed $p(O_2)$ dependent conductivity the following analysis is made for LSCF based on literature data for the oxygen non stoichiometry and the results in Figure 43.

The change in the $p(O_2)$ from 1 bar to 0.2 bar at 800 °C corresponds to a change in $\Delta\delta$ from approximately 0.03 mol to 0.05 mol [22]. Similarly at 700 °C, $\Delta\delta$ is increasing from 0.015 mol to 0.03 mol. In this temperature range the increase in the temperature by 100 K has a similar impact on the non-stoichiometry as the change in the oxygen partial pressure from 1 bar to 0.2 bar. The changes in the conductivity are following the same pattern and have similar values at 700 °C at 0.2 bar (386 Scm^{-1}) and 800 °C 1 bar (358 Scm^{-1}) and lower ones at 800 °C and 0.2 bar oxygen partial pressure (316 Scm^{-1}). Therefore, the $p(O_2)$ dependence and temperature dependence of the electrical conductivity are in agreement with the oxygen non stoichiomety of LSCF. The high CTE values (chapter 3) might result from the heating rate of 5 K/min, because no equilibrium between the dense sample and the gas atmosphere could be reached. It further indicates that the oxygen release is thermally activated rather than p(O_2) dependent. This makes sense, because the redox potentials of Co and Fe at a given temperature are quite close and thus the relative oxidation states between $Fe^{3+/4+}$ and $Co^{3+/4+}$ might vary without any influence on the average oxidation states and thus the oxygen content. LSCF contains already a higher amount of B^{3+} and thus can "buffer" a reduction in p(O_2).

BSCF shows only a low temperature dependence of the electrical conductivity between 350 °C and 800 °C, however the p(O_2) dependence is much more pronounced. The almost temperature independent behaviour of the conductivity at T > 400 °C might be explained by a plateau of $\Delta\delta/\Delta T$ [81] at higher temperatures after reaching a maximum at approximately 400 °C . The number of additional vacancies relative to the temperature increase becomes constant and might be compensated by the increasing mobility of the charge carriers. An additional effect might be the formation of Co^{4+} due to the thermally activated charge disproportionation as mentioned before.

4.4.2 Comparison of oxygen partial pressure dependence of the electrical conductivity

The p(O_2) dependence of the electrical conductivity of LSCF, LSF64 and LSF82 is similarly low at p(O_2) > 0.01 bar and becomes more pronounced when decreasing the p(O_2) and increasing the temperature. BSCF shows a significantly lower p(O_2) dependence in the lower p(O_2) region but a larger dependence in the higher p(O_2) region than the other materials.

The p(O_2) dependence of the electrical conductivity is summarized in Table VI. The exponent (x) in the Equation $\sigma \sim p(O_2)^x$ represents the slope in the plot log σ vs. log p(O_2) and is ranging from 0.038 to 0.103 for LSCF between 650 °C and 800 °C and from 0.177 to 0.224 for BSCF between 600 °C and 800 °C in the p(O_2) range between 0.01 bar and 1 bar. The slope changes at lower p(O_2) and is increasing for LSCF but decreasing for BSCF. LSF82 shows a slope between 0.028 and 0.048 at temperatures ranging from 626 °C to 841 °C and LSF64 a slope of 0.092 at 700 °C.

Table VI: Oxygen partial pressure dependence of the electrical conductivity for BSCF, LSCF, LSF82 and LSF64.

Conditions **$p(O_2)$ range**	Exponent $p(O_2)^x$	SD of x	Conditions **$p(O_2)$ range**	Exponent $p(O_2)^x$	SD of x
BSCF 600 °C 0.007-1 bar	0.224	0.006	LSF82 626 °C 0.001 – 0.2 bar	0.028	0.001
BSCF 700 °C 0.01-1 bar	0.177	0.007	LSF82 736 °C 0.001 – 0.2 bar	0.042	0.001
BSCF 700 °C 2E-4–0.01 bar	0.127	0.005	< 0.001 bar	0.098	0.017
BSCF 800 °C 0.01-1 bar	0.180	0.010	LSF82 841 °C 0.001 – 0.2 bar	0.048	0.004
BSCF 800 °C 0.001–0.01 bar	0.112	0.005	< 0.001 bar	0.169	0.006
LSCF 650 °C 0.01–1 bar	0.038	0.003	LSF64 700 °C 0.001 – 0.78 bar	0.092	0.008
LSCF 700 °C 0.01–1 bar	0.088	0.008	LSF64 700 °C < 0.001 bar	0.191	0.005
LSCF 700 °C 5E-5–4E-3 bar	0.180	0.010			
LSCF 800 °C 0.01–1 bar	0.103	0.012			

Figure 49 illustrates the differences between BSCF and the LS(C)F materials regarding the $p(O_2)$ dependence of the electrical conductivity at T ≥ 700 °C. As already mentioned, the temperature dependence of the electrical conductivity as regards LSF82 is relatively low. Therefore, a comparison with the other materials that were measured at 700 °C seems to be justified despite the temperature difference of 36 °C.

An explanation for the pronounced $p(O_2)$ dependence of BSCF is possibly the low number of 3-valent B-ions being present that could act as a reduction buffer, because in contrast to LSCF only A^{2+} are present with Ba^{2+} and Sr^{2+}. In fact BSCF shows a larger $p(O_2)$ dependence than LSCF. The conductivity maxima of BSCF in accordance to LSCF seem to correspond to the change of the coefficient of thermal expansion. Bucher et al. [81] assume that the low temperature maximum in the conductivity of BSCF at approximately 350 °C coincides with a change in the CTE as published in [121]. The lower $p(O_2)$ dependence in the low $p(O_2)$ region (< 0.01 bar) might be explained by a stabilizing effect of Ba [57]as A-site cation.

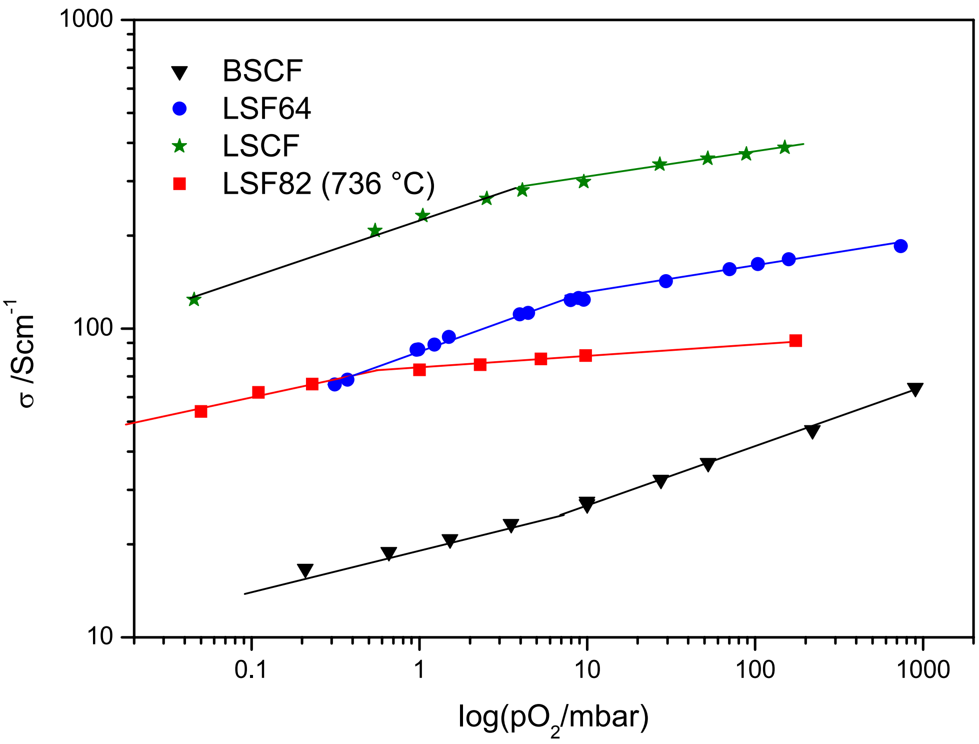

Figure 49: Electrical conductivity: oxygen partial pressure dependence at T ≥ 700 °C of BSCF, LSCF, LSF82 and LSF64 (lines to guide the eye).

LSF64 shows a similar dependency on the oxygen partial pressure as LSCF with an increase of the slope at $p(O_2) < 0.01$ bar. The reason is most probably the same cation ratio on the A-site. The conductivity of LSF64 is lower than for LSCF, most probably due to the absence of Co-ions that lead to an increase of the mobility of p-type carriers [18]. The low $p(O_2)$ dependence of LSF82 might be attributed to the larger redox capacity due to a higher amount of La^{3+} ($La_{0.8}$ vs. $La_{0.6}$) on the A-site.

4.4.3 General comparison of conductivities

LSCF and LSF64 show the highest electrical conductivity at the working conditions of an SOFC at approximately 0.2 bar oxygen partial pressure and are therefore considered as the favourable materials in terms of conductivity. LSF82 and BSCF in contrast have by factor 5 to 8 lower electrical conductivities than LSCF. The $p(O_2)$ dependence of the electrical conductivity is generally low and less pronounced for LSCF, LSF82 and LSF64 compared to BSCF. All four materials have low activation energies and show most probably hole conduction at temperatures below the conductivity maximum. LSCF and LSF64 seem to be the favourable materials in terms of the electrical conductivity for the application as SOFC cathodes at 600 °C among the four tested.

4.5 Results: surface exchange and oxygen ion transport in LSCF, BSCF, LSF82 and LSF64

4.5.1 Chemical surface exchange coefficient of LSCF

The chemical surface exchange coefficients ($\tilde{k}$) for LSCF are displayed in Figure 50 in the $p(O_2)$ range between 0.4 mbar and 1 bar at 700 °C and 800 °C with values between 1E-5 and 4E-3 $cm.s^{-1}$. The increase of $\tilde{k}$ is apparently linear at 700 °C in the $p(O_2)$ intervals from 0.4 mbar to 10 mbar and above 10 mbar. The slopes from the double logarithmic plot are 0.89 at 700 °C in the lower $p(O_2 < 0.01$ bar) interval and 0.76 in the higher $p(O_2 > 0.01$ bar) interval. The data points in Figure 50 regarding LSCF at 700 °C are compared with fits to literature data of the surface exchange coefficient [60].

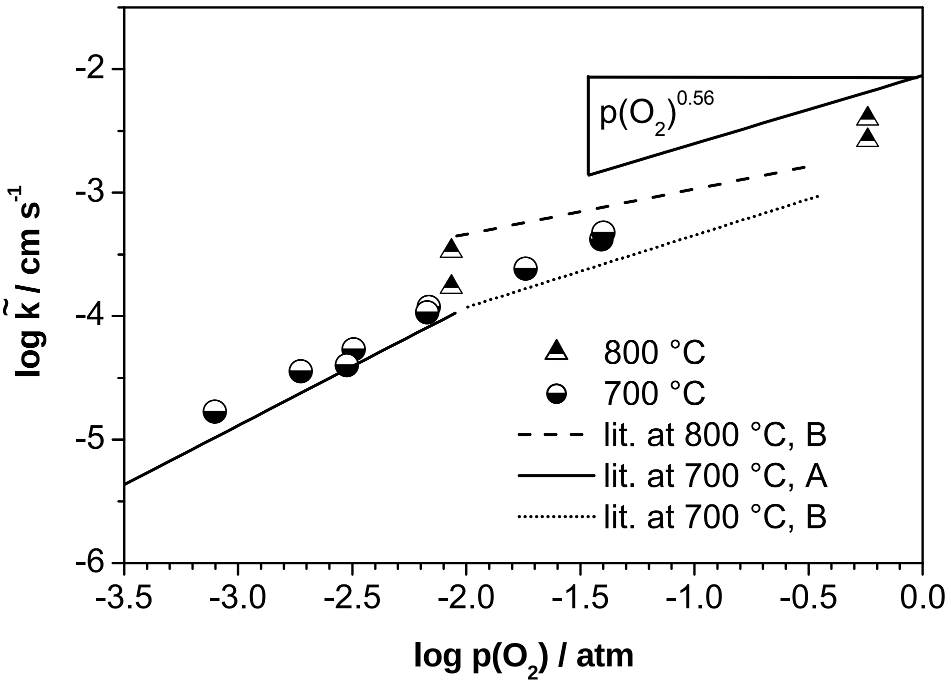

Figure 50: Chemical surface exchange coefficients ($\tilde{k}$) of LSCF as a function of the oxygen partial pressure compared with fits to literature data from Bouwmeester et al. [60] at $p(O_2)$ lower than 0.01 atm (A) and ≥ 0.01 atm (B) and the slope of 0.56 according to Lane et al. [106] at 800 °C as a comparison.

4.5.2 Chemical diffusion coefficient of LSCF

The diffusion coefficients of LSCF displayed in Figure 51 as a function of $p(O_2)$ show values between 4E-6 and E-5 $cm^2\ s^{-1}$. LSCF shows only a slight increase in $\tilde{D}$ (slope = 0.2 at 800 °C and 0.09 at 700 °C) of the diffusion coefficient with increasing $p(O_2)$.

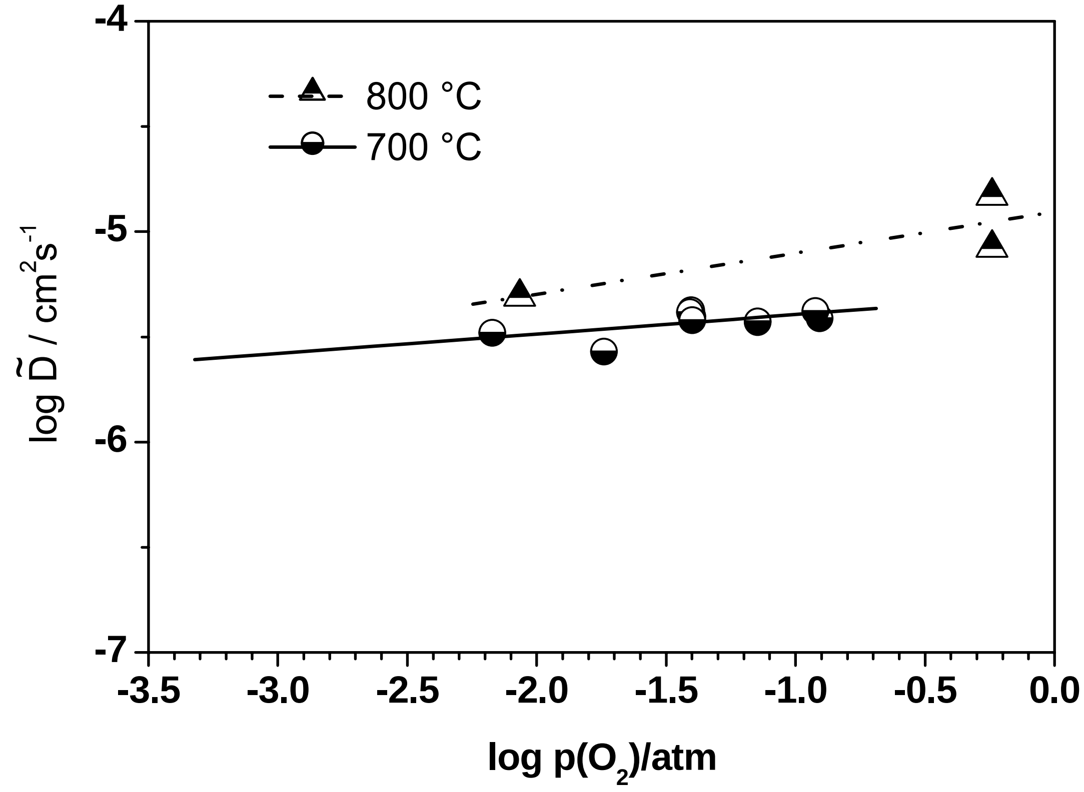

Figure 51: Chemical diffusion coefficients ($\tilde{D}$) of LSCF as a function of the oxygen partial pressure.

4.5.3 Chemical surface exchange coefficient of BSCF

The oxygen partial pressure dependence of the chemical surface exchange coefficient ($\tilde{k}$) is shown in Figure 52 for BSCF in the $p(O_2)$ range between 0.4 mbar and 1 bar at 600 °C and 700 °C with values between 4E-5 and 7E-3 cm s^{-1}. The increase of $\tilde{k}$ is apparently linear at 600 °C and 700 °C in the $p(O_2)$ intervals from 0.4 mbar to 1 bar. The linear dependence yields a slope of 0.53 at 600 °C and 0.64 at 700 °C.

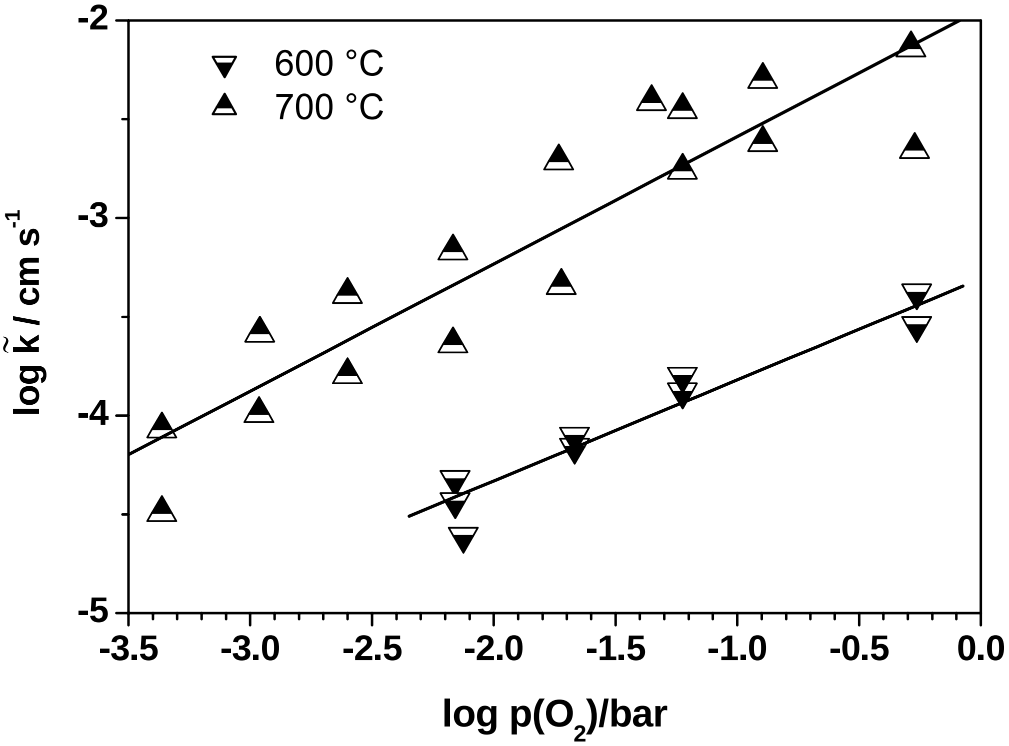

Figure 52: Chemical surface exchange coefficients ($\tilde{k}$) of BSCF as a function of the oxygen partial pressure.

4.5.4 Chemical diffusion coefficient of BSCF

The diffusion coefficients of BSCF are displayed in Figure 53 as a function of the p(O_2) and show values between 4E-7 and 4E-5 cm^2.s^{-1}. LSCF shows only a slight increase in $\tilde{D}$ (slope = 0.2 at 800 °C and 0.09 at 700 °C) with increasing p(O_2). BSCF has a pronounced p(O_2) dependence increasing from 0.42 at 600 °C to 0.61 at 700 °C and 0.63 at 800 °C.

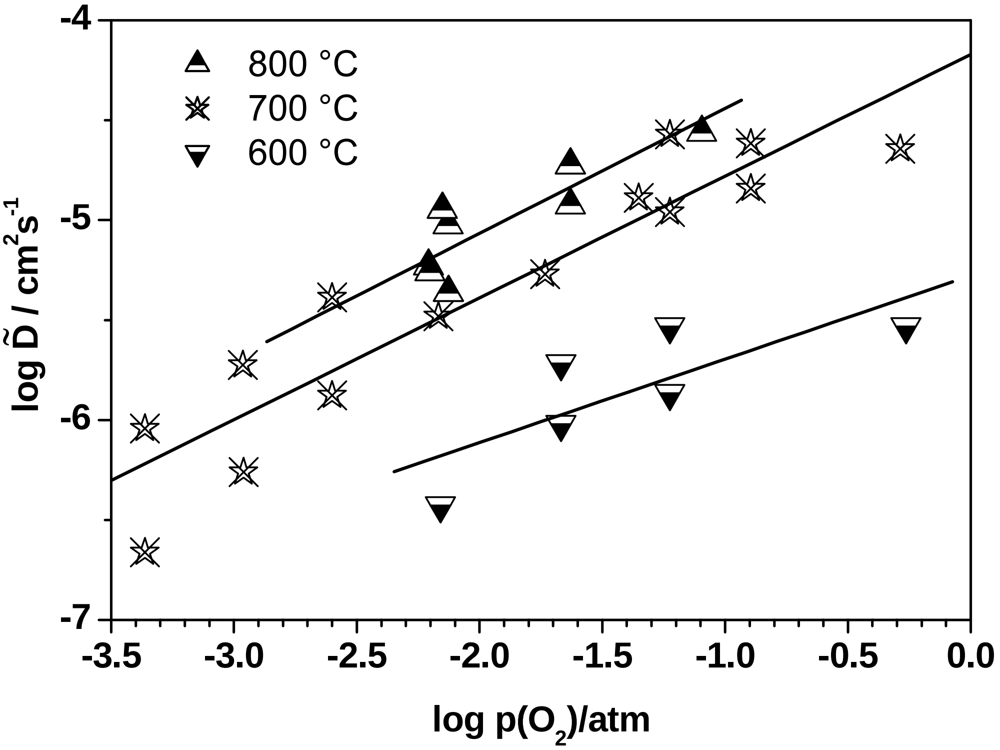

Figure 53: Chemical diffusion coefficients ($\tilde{D}$) of BSCF as a function of the oxygen partial pressure.

4.5.5 Chemical surface exchange coefficient of LSF82

The chemical surface exchange coefficients ($\tilde{k}$) of LSF82 are displayed in Figure 54 in the p(O$_2$) range between 0.4 mbar and 0.2 bar at 626, 736 °C and 841 °C with values between 4E-6 and 4E-2 cm s^{-1}. The slope of $\tilde{k}$ is increasing with decreasing temperature, so the p(O$_2$) dependence and values of $\tilde{k}$ are more pronounced at 626 °C than at 841 °C. The slope at 626 °C is 1.25, at 736 °C 1.07 and 0.96 at 626 °C.

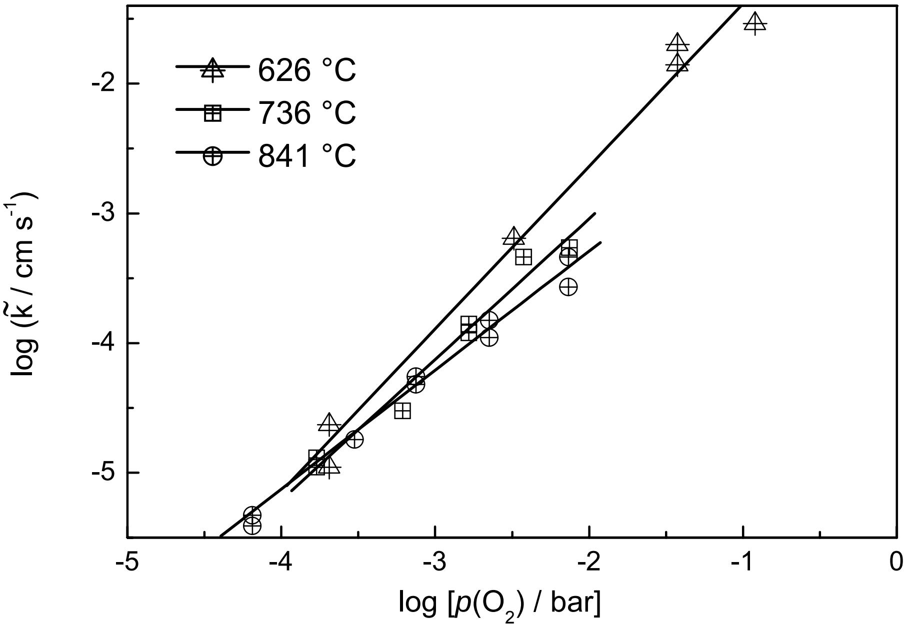

Figure 54: Chemical surface exchange coefficients ($\tilde{k}$) of LSF82.

4.5.6 Chemical diffusion coefficient of LSF82

The diffusion coefficients of the LSF82 are displayed in Figure 55 as a function of the p(O_2) and show values between 4E-8 and 8E-6 cm^2 s^{-1}. The p(O_2) dependence of LSF82 is increasing with increasing temperature. The increasing slope yields 0.25 at 626 °C, 0.5 at 736 °C, and 0.8 at 841 °C with increasing temperature.

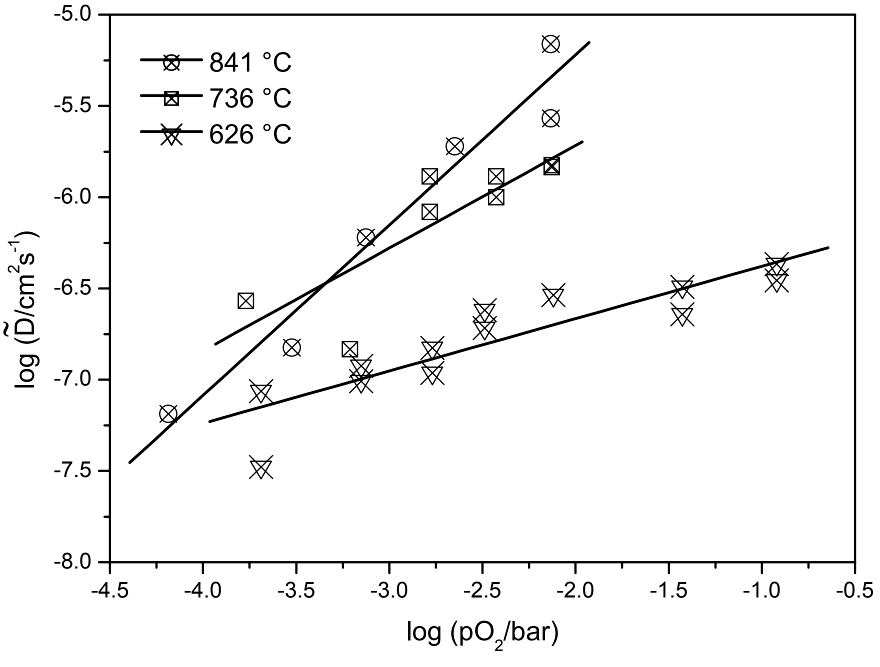

Figure 55: Chemical diffusion coefficients (D_{chem}) of LSF82; dependence on the p(O_2).

4.6 DISCUSSION: Comparison of oxygen exchange and diffusion kinetics

4.6.1 Chemical surface exchange of LSCF, BSCF, LSF82 and LSF64

The linear fits of the chemical surface exchange coefficients of LSCF, LSF64 and BSCF are displayed in Figure 56 as a function of the $p(O_2)$ at 700 °C and at 736 °C for LSF82. LSF64 and BSCF are exceeding the values for LSCF by about one order of magnitude at a $p(O_2)$ around 1 mbar. LSF82 shows values in between but was only evaluated up to a $p(O_2)$ of 10 mbar. The error bars in the figures indicate the experimental uncertainty. At SOFC relevant $p(O_2)$ around 0.2 bar LSF64, BSCF and LSCF show similar values due to the profound increase of $\tilde{k}_{LSCF}$ with increasing $p(O_2)$. The slopes of $\tilde{k} \propto p(O_2)^x$ are displayed in Table VII.

Table VII. Dependence of the chemical oxygen surface exchange coefficient on the oxygen partial pressure ($\tilde{k} \propto p(O_2)^x$)

$p(O_2)$ range A < 0.01 bar < B T /°C	x_{LSCF}	x_{BSCF}	x_{LSF82}*	x_{LSF64}
A + B 600 °C (626 °C*)	-	0.53	1.25 (A + B)*	-
A, B 700 °C (736 °C*)	0.89 (A) 0.76 (B)	0.64 (A + B)	1.07 (A)*	0.76 (A + B)
A, B 800 °C (841 °C*)	0.5 (B)	-	0.96 (A)*	-

The slope of $\log(\tilde{k})$ versus $\log(p(O_2))$ can be related to the reaction order of the surface exchange reaction. Different mechanisms are suggested in the literature for the oxygen exchange mechanism by ten Elshof et al. [19], and Merkle and Maier [122] involving i.a. molecular ($\tilde{k} \propto p(O_2)^1$) and atomic oxygen ($\tilde{k} \propto p(O_2)^{0.5}$) in the rate determining step. A value of $\tilde{k} \propto p(O_2)^{0.76}$ is ascribed to the transfer of one electron to the adsorbed molecular oxygen as the rate determining step of the oxygen reduction. The fits of

BSCF show slopes close to 0.5 suggesting atomic oxygen to be involved in the rate determining step [122]. The values of $\tilde{k}_{LSF64} \propto 0.75$ at 700 °C could correspond to the transfer of one electron to the adsorbed molecular oxygen. The slopes of LSCF and LSF82 especially at $p(O_2) < 10$ mbar at 700 °C and 736 °C, respectively, are close to 1 and therefore, molecular oxygen is supposed to be involved in the rate determining step for the oxygen exchange reaction. At 700 °C and $p(O_2) > 0.01$ bar LSCF has a slope of 0.76 which is attributed to the same mechanism as LSF64. As the other materials LSCF at 800 °C shows a value close to 0.5 at $p(O_2) \geq 10$ mbar suggests atomic oxygen thus at SOFC relevant oxygen partial pressure.

The temperature dependence of $\tilde{k}$ is more pronounced for BSCF than for LSCF and LSF82. At 800 °C the oxygen diffusion for BSCF is rate determining at the given dimensions of the sample (L_c is much lower than the sample dimensions) and therefore, $\tilde{k}$ couldn't be reliably evaluated from conductivity relaxation curves.

The data points in Figure 50 regarding LSCF at 700 °C are compared with fits through literature data from Bouwmester et al. [60] of the surface exchange coefficient. Sahibzada et al. [123]et al. at 700 °C and $p(O_2) < 30$ mbar obtained a value of $\tilde{k}$ that are about one order of magnitude higher than the presented. The slopes of the literature plots amount to 0.96 ± 0.08 between 0.01 bar and 2E-4 bar but only to 0.58 ± 0.03 between 0.01 and 0.4 atm. At 800 °C the presented data points deviate from the fit through these literature data (0.37 ± 0.07) from. However, the slope of the fit through the data points at 800 °C (0.62 ± 0.09) is close to the dependence presented by Lane et al ([106], $p(O_2)^{0.56}$). Also Søgaard et al. [32] found dependencies $\tilde{k} \propto p(O_2)^{0.5}$ at 800 °C and values close to the presented data of this study.

LSF64 was also investigated by conductivity relaxation by ten Elshof et al. [19] and Søgaard et al. [124]and show significantly lower values of $\tilde{k}$ at 725 °C and 700 °C with slopes of 0.75 and 0.62, respectively. Slight differences in the samples (e.g. grain size, polishing of the sample surface) and the experimental procedure (e.g. step width of the $p(O_2)$ in the experiment) are possible reasons. The slope found in this study is 0.76, which is closer to the values of ten Elshof et al. [19].

The results from Petitjean et al. [61] show clearly that $La_{0.8}Sr_{0.2}FeO_{3-\delta}$ has oxygen tracer diffusion and surface exchange coefficients superior to both $La_{0.8}Sr_{0.2}MnO_{3-\delta}$ and $La_{0.8}Sr_{0.2}CoO_{3-\delta}$ which justifies the selection of as a candidate for SOFC cathodes. A comparison between the results obtained in course of this study would require additional data from thermogravimetry to convert the literature data into the chemical diffusion and surface exchange coefficient as done for BSCF [81].

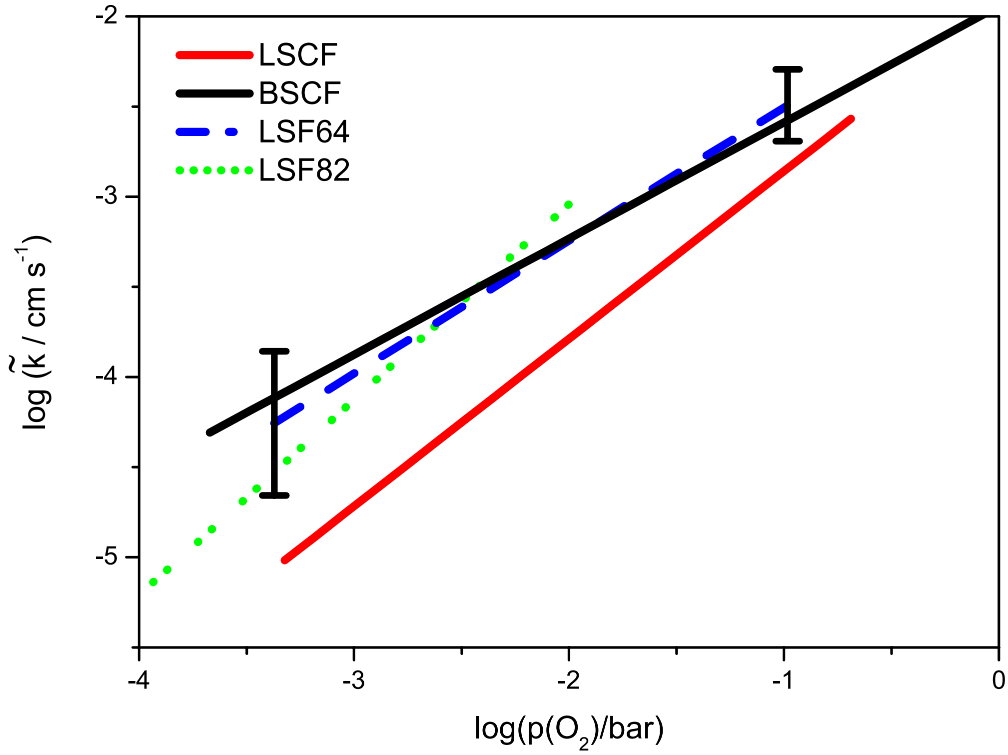

Figure 56: Surface exchange coefficient: oxygen partial pressure dependence at ≥ 700 °C.

Generally the values of $\tilde{k}$ were found to be higher performing oxidation experiments than for reduction when changing the atmosphere between two fixed $p(O_2)$ values during the present study. Similar discrepancies for conductivity relaxation experiments on $La_{0.5}Sr_{0.5}CoO_{3-\delta}$, $La_{0.6}Sr_{0.4}Co_{1-y}Fe_yO_{3-\delta}$, and $La_{0.5}Sr_{0.5}Fe_{0.8}Ga_{0.2}O_{3-\delta}$ were attributed to the determining influence of the target $p(O_2)$and limitations of the experimental setup [60, 125-127]. Bucher et al. [81] suggest the pronounced positive $p(O_2)$ dependences of the parameters, e.g. $\tilde{D} \infty p(O_2)^{(0.6 \pm 0.1)}$ and $\tilde{k} \infty p(O_2)^{(0.6 \pm 0.1)}$ at 700 °C [121] to be the cause of systematically higher $\tilde{D}_{[ox]}$ than $\tilde{D}_{[red]}$ and mostly higher $\tilde{k}_{[ox]}$ than $\tilde{k}_{[red]}$ of BSCF. Extrapolating $\tilde{k}$ at 700 °C to $p(O_2)$ of 0.2 bar of all tested materials show values $\geq 10^{-3}$ cm s^{-1}.

4.6.2 Chemical diffusion coefficients of LSCF, BSCF, LSF82 and LSF64

The values of the diffusion coefficient of LSCF at 700 °C and 800 °C are in agreement with the literature data [19, 60, 106] including comparable compositions e.g. $La_{0.6}Sr_{0.4}Co_{0.4}Fe_{0.6}O_{3-\delta}$. The diffusion coefficient of LSCF shows only a weak dependence (≤ 0.19) on the $p(O_2)$ while BSCF has a pronounced $p(O_2)$ dependence (0.6 ± 0.1) at all $T \geq 700$ °C. Due to the stronger increase of $\tilde{D}$ with increasing $p(O_2)$, the diffusion coefficients of BSCF exceed those of LSCF at $p(O_2) > 0.2$ bar.

The strong decrease of the oxygen diffusion coefficient of BSCF with decreasing $p(O_2)$ was not expected, because in general the ionic conduction increases with increasing of the oxygen deficiency. Vacancy ordering might be the competing effect that occurs due to the already very high oxygen deficit in the material [63, 84]. The same assumption can be made also for LSF64 and LSF82 that show similarly high p (O2) dependence. The slopes of the dependence $\tilde{D} \propto p(O_2)^x$ are summarized in Table VIII.

Table VIII: Dependence of the chemical oxygen diffusion coefficient on the oxygen partial pressure ($\propto p(O_2)^x$)

T/°C	x_{LSCF}	x_{BSCF}	x_{LSF82}*	x_{LSF64}
600 °C (626 °C*)	-	0.42	0.25	-
700 °C (736 °C*)	0.2	0.61	0.50	0.76
800 °C (841 °C*)	0.09	0.63	0.80	-

Compared to literature data from Søgaard et al. [32] LSCF shows similar values at 800 °C and the slope ($\tilde{D} \propto p(O_2)^{0.2}$ in the range $10^{-3} < p(O_2)/\text{bar} < 10^{-1}$) is in agreement with own results that shows rather $p(O_2)$ independent behaviour. The magnitude of $\tilde{D}$ and the $p(O_2)$ dependence Bouwmeester et al. [60] is also corresponding to the obtained values in the above mentioned range, but shows a higher dependence at $p(O_2) < 10^{-3}$ bar, which is attributed to vacancy ordering. However, Lane et al. [106] found values of $\tilde{D} \propto p(O_2)^{0.37}$ at $0.05 < p(O_2)/\text{bar} < 1$ and 800 °C.

The oxygen self diffusion coefficient is estimated from data of $\tilde{D}_{BSCF}$ via the thermodynamic factor by Bucher et al. [81] obtained from thermogravimetric data. Between 600 °C and 700 °C at a $p(O_2)$ of approximately 10 mbar the oxygen self diffusion coefficient is about one order of magnitude lower than the chemical diffusion coefficient. The estimated values correspond closely both in the magnitude and the temperature dependence to the data of Berenov et al. [102]who determined the oxygen tracer diffusion coefficient between 370 °C and 550 °C at 0.21 atm.

Søgaard et al. [124] found values for $\tilde{D}$ of $(La_{0.6}Sr_{0.4})_{0.99}FeO_{3-\delta}$ at 700 °C that are about one order of magnitude lower than the presented for LSF64. The value of $\tilde{D}$ is also decreasing with decreasing $p(O_2)$ similarly to LSF64. The slope is also not compared with the presented data because only two data points are shown in that study.

Data from Petitjan et al. [61] show that the oxygen tracer diffusion coefficient of $La_{0.8}Sr_{0.2}FeO_{3-\delta}$ is equally high as for $La_{0.8}Sr_{0.2}CoO_{3-\delta}$. A direct comparison between the data of the present study would require additional TG data to calculate the thermodynamic factor.

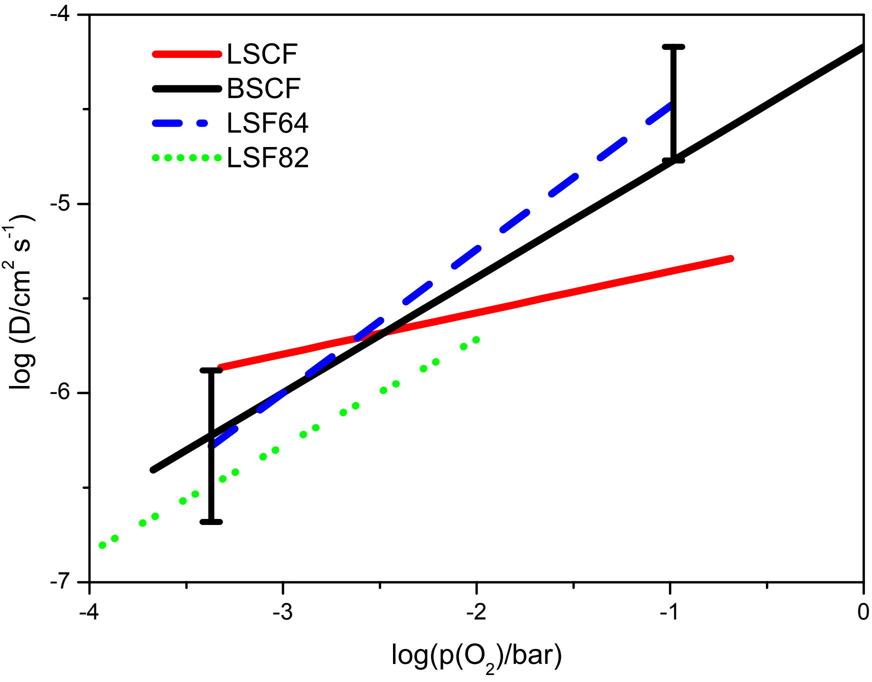

Figure 57: Dependence on the oxygen partial pressure at 700 °C: chemical diffusion coefficients of different cathode materials (LSF82 at 736 °C).

Regarding the oxygen exchange and diffusion BSCF and LSF64 are the kinetically “fastest” materials at SOFC relevant conditions. LSF82 shows surface exchange coefficients in a similar range than BSCF and LSF64 but significantly lower diffusion over entire measured $p(O_2)$ range. LSCF shows similar oxygen exchange kinetics as BSCF and LSF64 at SOFC relevant conditions but lower values in the low $p(O_2)$ range. In contrast to the other materials LSCF shows only a small dependency of the diffusion coefficient on the $p(O_2)$ but lower values at SOFC relevant conditions.

The diffusion coefficients of LSF64 and BSCF are exceeding the values of LSCF by about one order of magnitude at a $p(O_2)$ around 0.2 bar. LSF82 shows values in between but was only evaluated up to a $p(O_2)$ of 10 mbar. Regarding $\tilde{D}$, LSF82 at 626 °C has a rather low $p(O_2)$ dependence such as LSCF while at $T \geq 736$ °C the temperature dependence becomes more pronounced similar to BSCF. The pronounced decrease of the diffusion coefficient can be explained by oxygen vacancy ordering occurring at a $p(O_2)$ below 10^{-2} bar [60]. A lower tendency to vacancy formation at 700 °C might be ascribed to LSCF. The lower $p(O_2)$ dependency of LSF82 at 626 °C seems to agree with this assumption, because less oxygen vacancies are assumed to be present. At high polarization currents in fuel cells the $p(O_2)$ can virtual shift to lower values. Due to the pronounced $p(O_2)$ dependence of $\tilde{D}$ of LSF82, LSF64 and BSCF this effect can lead to lower oxygen diffusion in these materials. LSCF has the lower $\Delta\delta$ than BSCF in the temperature range between 600 °C and 800 °C [26, 128-130]. Both high oxygen vacancy concentration and high chemical diffusion coefficients suggest that the oxygen ion conductivity in BSCF is higher at the SOFC relevant conditions. However, the pronounced dependence of the diffusion coefficient of BSCF on the $p(O_2)$ might become critical at high cell polarisation, which virtually shifts the $p(O_2)$ to lower values and thus lowers the ionic transport rate.

4.7 Conclusions

The comparison with literature data shows that the values of the kinetic parameter can deviate up to one order of magnitude for the same material. This is attributed to differences in the sample preparation rather than the measurement method. As described in chapter 4.1 the assessed values correspond to effective media diffusion, because the samples are polycrystalline dense pellets. The grain size of the polycrystalline samples and different surface properties are two possible parameters that might responsible.

Diffusion controlled behaviour (e.g. for LSCF at 800 °C and $p(O_2) > 0.05$ bar and BSCF at 800 °C) as well as surface exchange controlled (e.g. for LSCF at 700 °C and $p(O_2) <$ 0.01 bar) behaviour of the samples was observed. It can be clearly observed that the sample thicknesses of approximately limit the temperature and $p(O_2)$ range where $\tilde{D}$ and $\tilde{k}$ can be determined simultaneously.

The selection of a cathode material is a compromise between different factors. LSCF finally was chosen because of a significantly higher electrical conductivity. LSCF shows a high surface exchange coefficient at SOFC relevant conditions. Furthermore, the diffusion coefficient shows low $p(O_2)$ dependence, possibly a favourable material property at high cathode polarization. Considering the electrical conductivity and oxygen exchange, the powder properties and the compatibility with the electrolyte material discussed in Chapter 3, LSCF turns out to be the most promising candidate. As mentioned already in Chapter 3, the production of phase pure nano powders [72, 79] was a further precondition for the study of the powder as a cathode. Therefore, LSCF was chosen for the processing of screen printing pastes including sub-µ and nano powders to be applied as cathodes on CGO electrolyte substrates.

5 Electrochemical properties of LSCF//CGO//LSCF cells

LSCF turned out to be a promising candidate materials for the air electrode in SOFCs as shown in the material evaluation regarding powder properties (chapter 3) due to phase pure production of nano powder and compatibility with $Gd_{0.1}Ce_{0.9}O_{1.95}$ as well as high electrical conductivity and oxygen exchange kinetics (chapter 4). The literature review in chapter 2 shows the advantage of smaller particle sizes of the precursor for the electrochemical performance. Modelling of the cathode polarization resistance [32] and area specific resistance [33] confirm these considerations. Following this approach the implementation of nano powders was regarded as promising way to cathodes with a high performance. However, there are some drawbacks in the processing of screen printing pastes containing nano powders [69, 70]. The small particle sizes lead to higher sintering activity and shrinking during heat treatment. The high surface area of the powders requires a larger amount of dispersing chemicals and the particle size limits the maximum solid loading of the screen printing pastes. Slow drying and burnout of the chemicals are required in order to ensure good layer quality.

5.1 Experimental: Preparation of symmetrical cells with $La_{0.6}Sr_{0.4}Co_{0.2}Fe_{0.8}O_{3-\delta}$ cathode layers on $Ce_{0.9}Gd_{0.1}O_{1.95}$ electrolyte substrates by screen printing

Symmetrical cells were produced by screen printing of LSCF pastes on both sides of a dense $Ce_{0.9}Gd_{0.1}O_{1.95}$ pellet (HC-Starck) and subsequent heat treatment. The preparation of screen printing pastes for the application as cathode layers is described in detail by Burnat [70]. Table IX shows the IDs of the samples produced in course of the present investigations, the corresponding firing temperatures, and the performed investigations.

The pastes were produced from LSCF sub-μ (coarse = C) and nano powder (=N), $Ce_{0.9}Gd_{0.1}O_{1.95}$ electrolyte (=E) powder, terpineol as liquid medium, Solsperse3000

(Clariant) as a dispersant and polyvinylbutyral (PVB) as a binder. After printing and heat treatment, the samples were investigated by light microscopy (LM), scanning electron microscopy (SEM) and electrochemical impedance spectroscopy (EIS). The detailed paste recipes can be found elsewhere [70, 131].

Table IX: Sample IDs with firing temperatures and investigation methods.

Sample ID	Powder content/ powder morphology	Firing T / °C	Investigations
C25 C40	25 vol% sub-μ (coarse) 40 vol% (only at 1000 °C, SEM)	900 950 1000 1100	SEM, EIS SEM, EIS SEM, EIS EIS
N25 N20* N40°	25 vol% nano powder (20 vol%, only at 1050 °C, SEM) (40 vol %, only at 1000 °C, SEM)	950 1000 1050	SEM, EIS LM, SEM SEM
NE46	33 vol% (46 wt% electrolyte powder)	1000 1100	EIS EIS
C11N22	33 vol% (11 vol% sub-μ + 22 vol% nano)	950 1000 1200	SEM, EIS LM, SEM, EIS SEM, EIS
CNE46	33 vol% (46 wt% electrolyte powder, rest C:N=1:2 mix)	950 1000	SEM, EIS LM, SEM, EIS

The paste rheology was investigated with Rheolab MC120 (Physica Messtechnik GmbH, Germany) equipped with thermostat system VT100 (Physica). According to earlier investigations [132, 133] regarding YSZ screen printing pastes, ideal screen printing pastes should show a thixotropic behaviour. The visicosity at low shear rates should be high enough to prevent the paste from dropping down from the sieve under the force of gravity. Secondly, the paste favourably should become more fluid under applied shear stress in order to be able to fill the screen and print subsequently.

The rheology of applicable pastes is displayed in Figure 58, showing partly different rheological behaviour. Paste NE46 shows the desired thixotropic behaviour, but C25 behaves almost like a Newtonian liquid.

The shear thinning of this paste is very low, thus the viscosity is only decreasing very slowly with increasing shear rate or applied shear stress during printing. Especially C25 with 6 % binder addition resulted in smooth cathodes layers after printing similar to the other pastes. N25 and C11N22 show shear thinning behaviour, but a Newtonian plateau at shear rates lower than 10 s^{-1}.

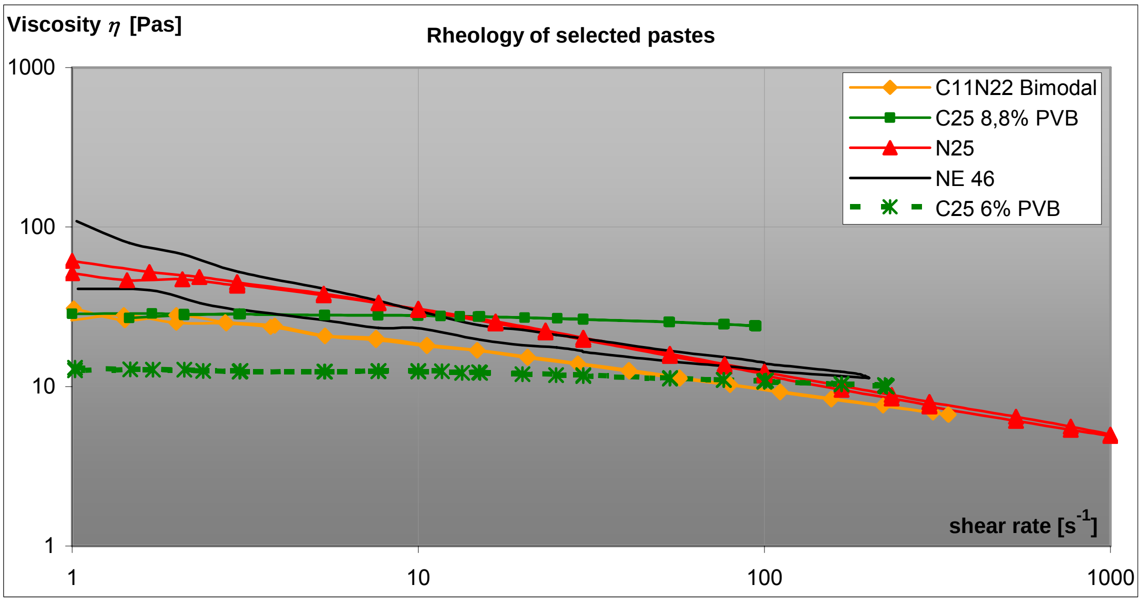

Figure 58: Rheological behaviour of selected pastes.

The heat treatment of nano powders and the corresponding pastes required adapted heating ramps of 1 K/min instead of 5 K/min and additional dwell times. Additionally all pastes required a burnout of the organic binder system to reduce the delamination of the layers.

The burnout of terpineol is attributed to a temperature around 200 °C and therefore, the dwell time D_1 was introduced. The dispersant and binder are supposed to burn out at 300 °C and after slow heating (R_2) the dwell time (D_2) was introduced. After heating up to 800 °C with the standard heating rate (R_3) of 5 K the samples were heated to the target temperature with 1 K/min (R_4) because the sintering activity of the powders starts exceeding this temperature. The samples were dwelled for 4 hours at the target temperature (D_3, 900-1200 °C) and subsequently cooled with 2 K/min to room temperature.

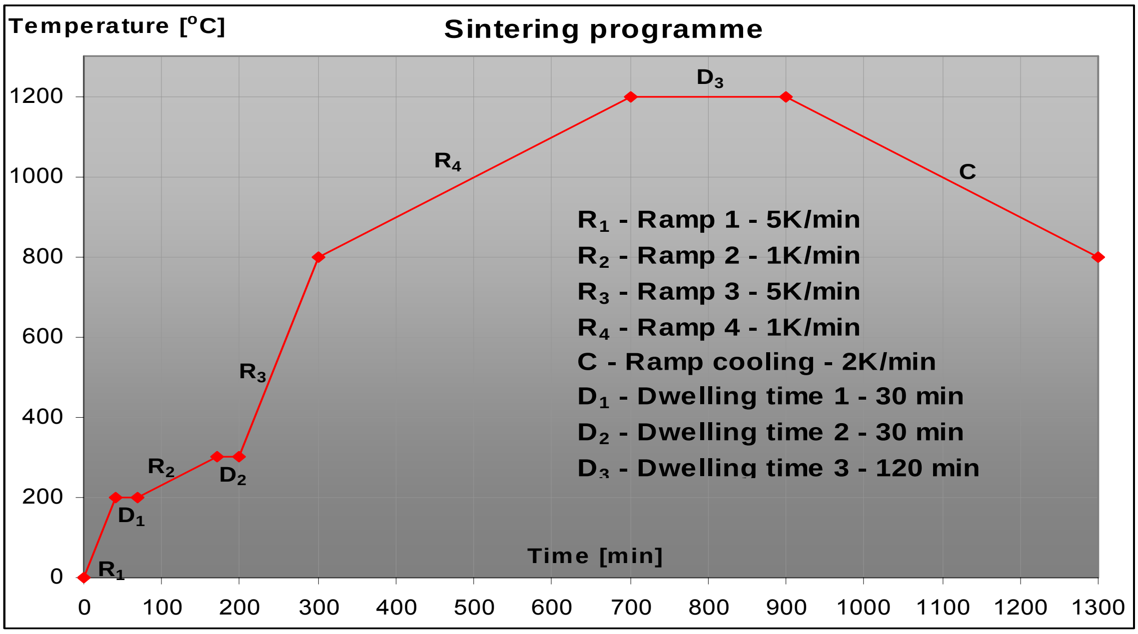

Figure 59: Optimized temperature profile according to the TG and dilatometer curves of the LSCF pastes

The stability after sintering was checked with the tape test by applying an adhesive tape on the cathode layer and checking the adhesion of the layer by fast removing the tape [70]. Samples with sufficient adhesion on the electrolyte were examined further by light microscopy (LM) and scanning electron microscopy (SEM). The surface of the layers after the heat treatment was examined with respect to cracks by LM. The cross section of the samples was examined with the SEM (Tescan Vega 5130-SB) after breaking the samples and sputtering with Pd/Au (Cressington Sputter Coater 108auto). The samples were additionally contacted with conducting carbon paste (Leit-C nach Göcke, Plano GMBH) to ensure a good electrical contact between the examined cross section and the sample holder.

5.2 Experimental: Impedance spectroscopy as a tool to examine ionic/electronic transport properties

5.2.1 Impedance as perturbation function of an alternating current (AC) signal

The principle of the impedance spectroscopy (IS) is to obtain the frequency dependent sample's response to the change of the electrical field, which is an exactly defined perturbation function. The most important advantage is the possibility to separate processes with different time constants. The precondition is that they have to occur in different frequency domains – in other words the difference between the relaxation times of the processes has to be large enough.

In course of this study EIS is used for the evaluation of the polarization resistance which reflects the sum of charge transport in the electrodes, for the ohmic resistance of the electrolyte, involving bulk and the grain boundary resistivities, charge transfer processes between different phases, double layer capacitance, surface adsorption, redox-reactions and in some cases also corrosion and passivating processes.

The resistance (R) is a measure for the voltage losses in the various reactions steps at a given current. The capacitance (C) of a reaction step has no impact on the active resistance, but causes a time delay between current and potential in sinus signal. The product RC results in the characteristic time constant ($\tau = 1/\omega$) of a process, where ω is the characteristic frequency of the reaction step. Usually, the capacitance values differ by orders of magnitudes between double layer, grain boundaries, surface adsorbates, while the resistances often can be present in similar values. The differences in the capacitance result in different time constants thus allow to distinguishing the various reaction steps of the system.

Applying a sinusoidal alternating voltage of a defined frequency to a linear responding system, an AC current with the same frequency with an amplitude (I_0) and a phase shift (θ) can be measured. The impedance is defined in analogy to ohmic law in the case of directed current (Equation 33).

$$Z = \left(\frac{E_0 \sin(\omega t)}{I_0 \sin(\omega t + \theta)} \right) \qquad \text{Equation 33}$$

The amplitude E_0/I_0 is written as Z_0. The impedance can be displayed as a complex number ($Z(\omega)=Z_0 e^{j\theta}$) using $E = E_0 e^{j\omega t}$ and $I = I_0\ e^{j(\omega t-\theta)}$. The real part of the impedance is $Z' = Z_0 \cos \theta$ and the imaginary part $Z'' = Z_0 \ \ I \sin \theta$, while the magnitude of $|Z| = (Z'^2 + Z''^2)^{1/2} = Z_0$.

Systems with frequency dependent impedance characteristics result in different values in the impedance at different frequencies. Different opportunities to display the spectra exist. The so called Nyquist plot displays the real part (Z') as x-axis and the imaginary part (Z") as y-axis. The frequency dependent representation of impedance values is the so called Bode plot. The magnitude of Z, the real (Z') and imaginary (Z") part, the phase angle or the capacitance e. g. can be displayed as a function of the frequency. The Bode plot (Z" vs. frequency) can give hints about the speed of some processes expressed by the inverse time constant ($1/\tau = 1/(RC) = \omega$) of the corresponding processes.

The different time constants (= C and/or R values) help to distinguish the contributions of CGO electrolyte and the LSCF cathode to the total cell resistance. Furthermore, different processes as the oxygen exchange, oxygen gas phase and bulk diffusion as well as oxygen ion transfer between cathode and electrolyte could be distinguished within the cathode [41, 134]. This, however, requires knowledge about the detailed mechanism or extensive kinetic analysis, which is not the scope of this work.

The EIS of symmetrical cells prepared within this study were investigated at elevated temperatures between 485 °C and 800 °C. A special experimental setup is needed to ensure constant measuring conditions regarding the temperature and the oxygen partial pressure and a separation of the sensitive electronic parts from the hot environment. The test rig used is described in the following chapter

5.2.2 Experimental setup and sample preparation

The entire test rig (Figure 60) includes a furnace (Carbolite VST 12/200) with a control unit (Eurotherm 2416), the measuring cell (Probostat A^{TM}, NorECS AS) and a gas mixing device with gas flow controllers (QFlow 140, computer controlled by Red-y smart software). The cell test housing was floated with a constant stream (controlled by gas flow controllers, QFlow 140 + Red-y smart, Vögtlin) of a N_2/O_2 80:20-mixture of 100 mL/min. The temperature in the direct vicinity of the sample was measured with an S-type (Pt/Pt-Rh10%) thermocouple.

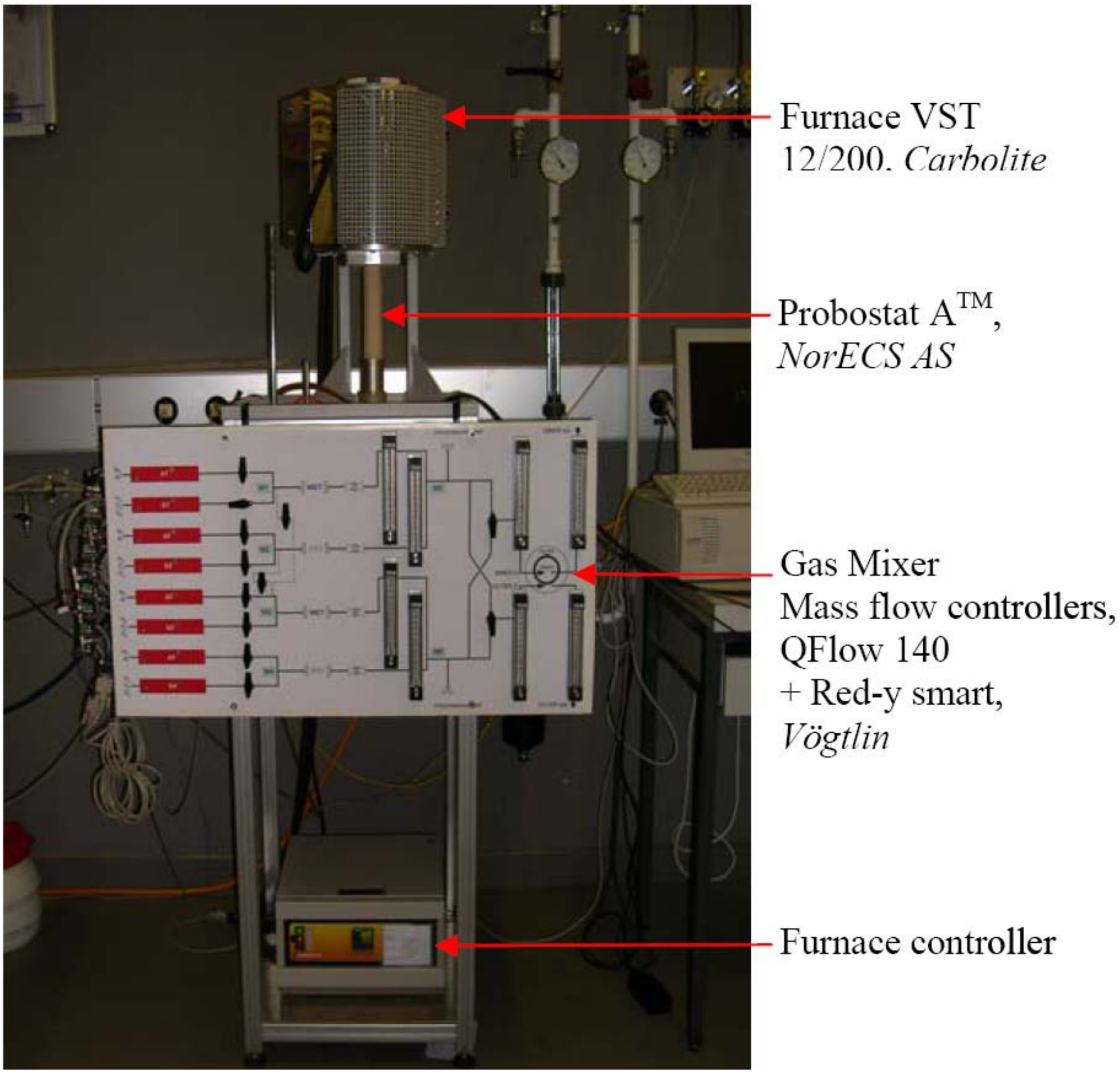

Figure 60: Impedance test rig including furnace, test cell housing (Probostat A^{TM}) and gas flow controllers.

The impedance spectra of symmetrical button cells were recorded as a function of the temperature at $p(O_2) = 0.2$ bar. The experimental setup with the mounted sample in the Probostat™, the frequency response analyser (QuanteQ, Newton4th Ltd., United Kingtom) and the Potentiostat (AMEL instruments Milano, Italy) is displayed in Figure 61.

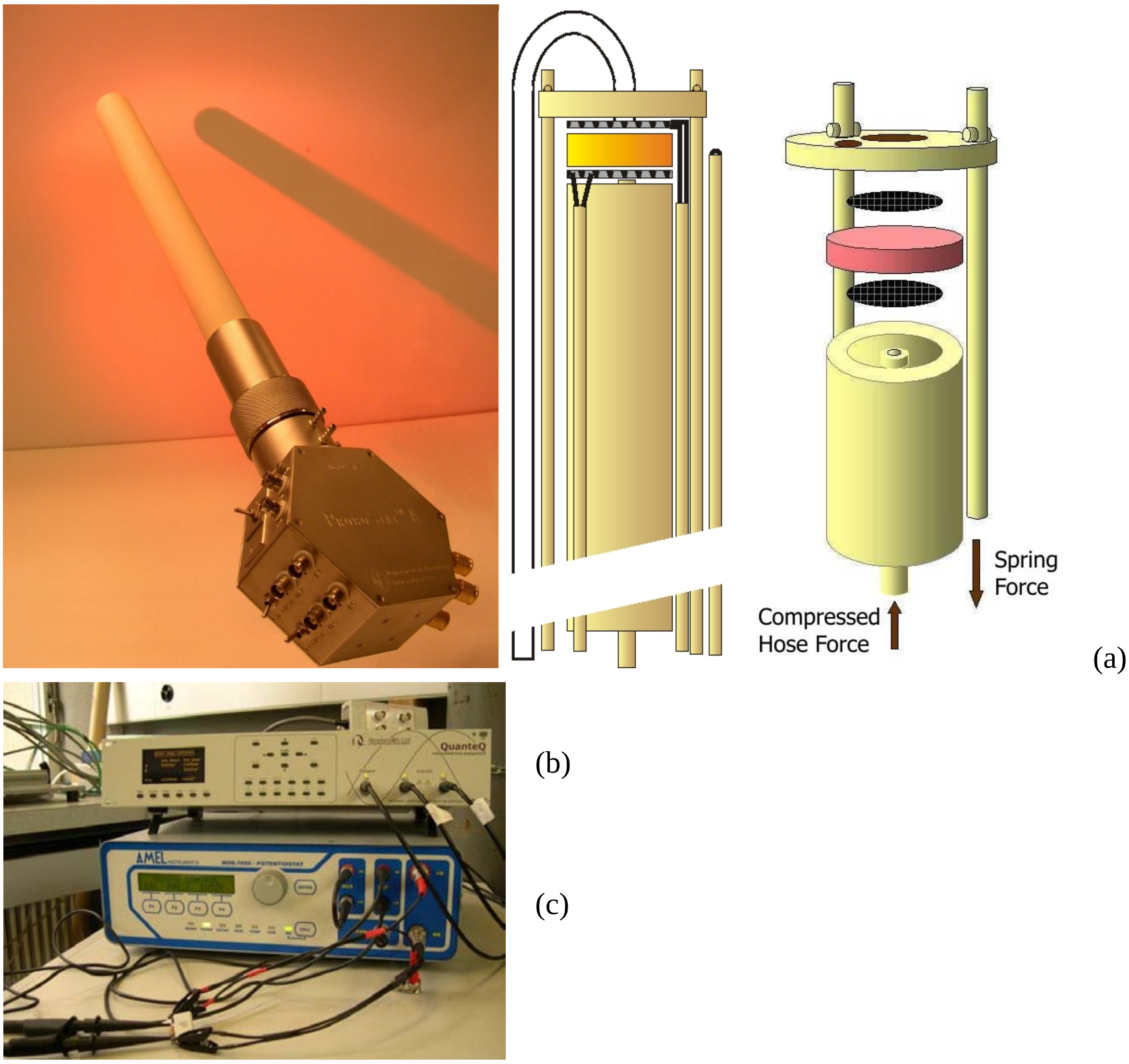

Figure 61: Experimental setup for the impedance measurement with the measuring cell ((a) mounting of the sample into Probostat^{TM}, figures from www.norecs.com), the frequency response analyser (b) QuanteQ Newtons4th Ltd. United Kingdom and (c) the potentiostat (AMEL7050, AMEL instruments Milano Italy).

The frequency response analyser is connected to the potentiostat. The impedance spectra of the samples were measured in a pseudo 4-point arrangement by connection of the counter electrode (CE) and the reference Hi with one Pt-current collector (A), and the working electrode (WE) and the reference Lo with the second Pt-current collector (B) of the potentiostat, respectively. Cathode layers were painted on both sides with Pt-paste (Metalor A4338A) and heat treated according to the recommendations of the provider (binder burn out at 200 °C, 1 h dwelling at 1000 °C). The symmetrical cell was mounted into the test rig between two Pt-grids that are pressed onto the sample with springs to ensure an appropriate electrical contact.

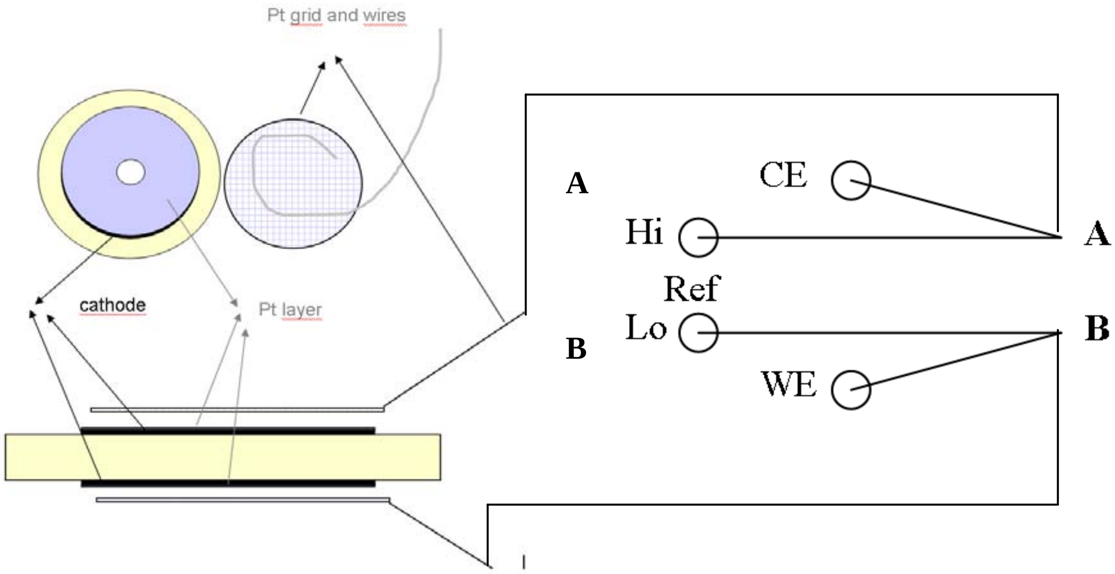

Figure 62: Connection of a LSCF//CGO//LSCF button cell to the AMEL™ Potentionstat (Ref(erence) Hi, Lo; CE = counter electrode, WE = working electrode).

The impedance response of the pure electrolyte was determined prior to the measurements on symmetrical cells samples with different thickness between 1 mm and 3.25 mm in the temperature range between 300 °C and 800 °C. The sample was painted with Pt paste and the results are further explained elsewhere [131].

5.3 Results: influence of the powder composition and the sintering temperature on the cathode microstructure

5.3.1 Influence of the powder composition

The influence of the precursor powders and mixtures on the sintering properties regarding the appearance of the surface and especially the grain size of the layers was studied. Figure 63 shows the comparison between layers produced from pure nano powders (N25) and layers with C11N22 and CNE46. The surface of the samples was investigated by light microscopy (LM) after 2 hours of sintering at 1000 °C. The white bar corresponds to 0.1 mm.

The LM picture of N25 shows cracks on the surface of the sample. The cracks appear slightly larger on the upper side of the sample than on the lower side that was in direct contact with the sintering bed. The samples with C11N22 and CNE46 don’t show cracks, neither on the upper nor on the lower surface.

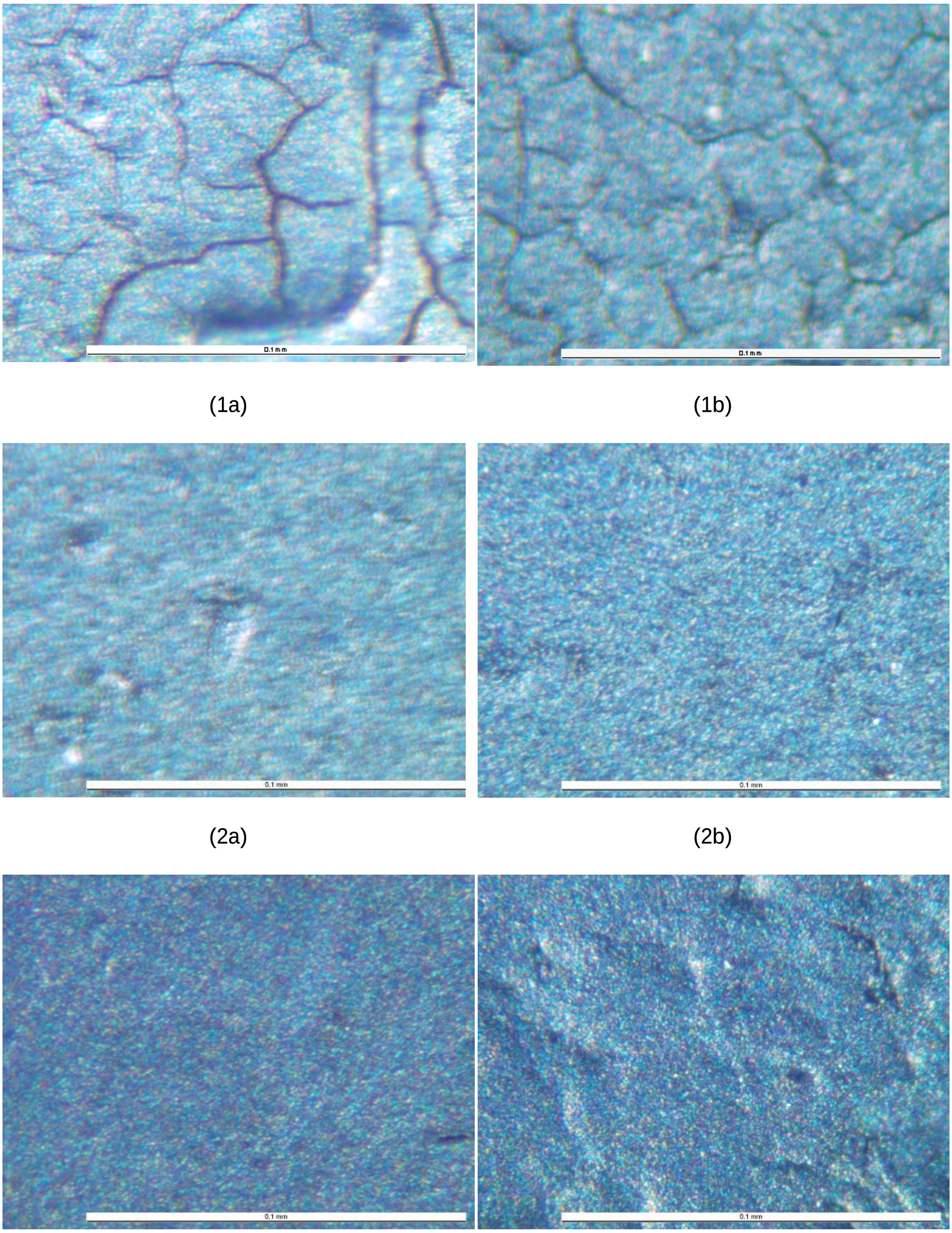

(1a) (1b)

(2a) (2b)

(3a) (3b)

Figure 63: Light microscope pictures of sintered layers printed of pastes N25 (1),C11N22 (2) and CNE46 (3) fired at 1000 °C showing the upper (a) and the lower surface (b).

5.3.2 Temperature dependence of the microstructure comparing N25 and C25

The SEM micrographs (Figure 64) show cross sections of symmetrical cells prepared with pastes containing coarse (sub-μ = C25) and nano powders (N25) both containing 25 vol% powder. The microstructures presented here were examined after optimized firing of the samples (Figure 59 with 900 °C, 1000 °C, 1100 °C and 1200 °C maximum temperature). The left part of the pictures shows the porous cathode layer und the right part is the dense electrolyte layer.

Firing sample C25 at a maximum temperature of 900 °C results in a rather dense microstructure with a higher porosity at the cathode/electrolyte interface or in other words no full coverage of the electrolyte by the cathode layer. A bonding between the grains exists and most of the small grains have a grain boundary with the neighbouring particles. The grain size of the primary particles ranges from 0.2-1 μm. Most grains are round and only a few square grains are visible.

Electrode N25 shows almost exclusively round particles in a similar range as the coarse powder. The porosity is estimated to 20 %, which is slightly higher for C25 estimated to 15 %. N25 shows rather individual grains (round shape) than connected particles. There is no visible difference in the density between the bulk of the cathode and the cathode/electrolyte interface.

The microstructure of electrode C25 does not show a significant difference after heat treatment at 900 °C or 1000 °C. N25 shows more densification at 1000 °C than at 900 °C and cracks (insert). The grain size is increased at higher firing temperatures. Several larger ball shaped particles and more grain boundaries than at 900 °C become visible. The visible intimate good contact between electrolyte and cathode indicates good bonding between the electrolyte and the cathode. Increasing the firing temperature to 1100 °C sample C25 results in an increased porosity (> 20 %) compared to the heat treatment at 900 °C and 1000 °C but no significant change of the grain size. The electrolyte is fully covered and the connection between the grains is visible.

Increasing the firing temperature for N25 to 1100 °C leads to increased densification (estimated porosity < 10%). The grains seem to be fully connected and the electrolyte is covered by the layer. An increase of the crack dimensions between 900 °C to 1100 °C was observed under the light microscope. This might indicate the increase of micro-structure failures despite the fact that no cracks were visible in the SEM image with higher resolution. The sample prepared from nano powder shows both, vertical cracks and delamination of the cathode from the electrolyte. The grains are almost sintered to a dense layer and show a grain size ≥ 0.5 μm.

Increasing the firing temperature to 1200 °C for pastes prepared from C25 shows an increase in grain size (0.5-2 μm) and a slightly lower porosity than the sample kept at 1100 °C. The bonding to the electrolyte is visible by grains connected directly to the electrolyte interface. The grains of the cathode layer appear to be bonded as well.

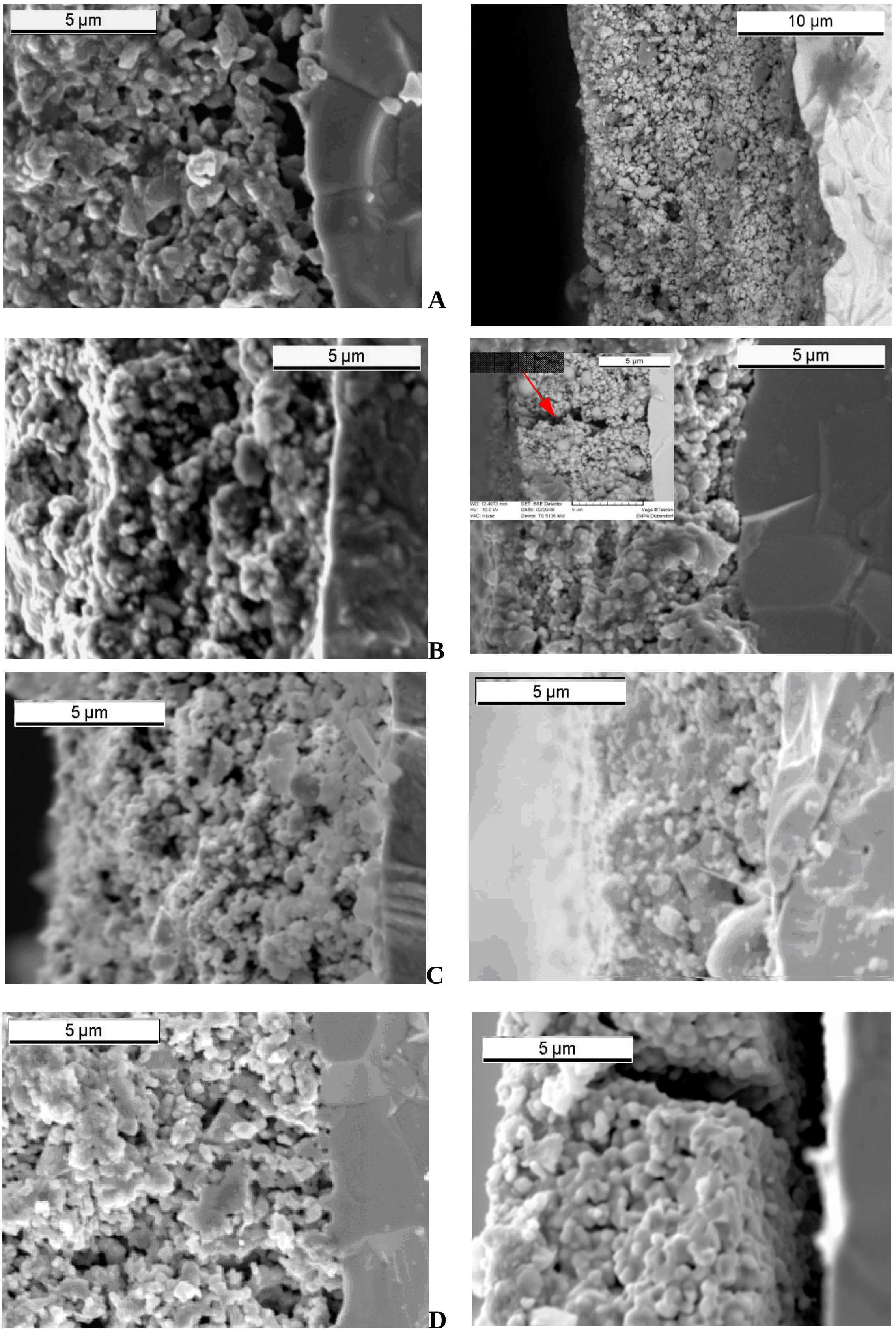

Figure 64: Cathode layers prepared from C25 (left) and N25 (right) after heat treatment at 900 °C (A), 1000 °C (B), 1100 °C (C) and 1200 °C (D); the red arrow shows a vertical crack.

5.3.3 Influence of the solid loading on the microstructure

Figure 65 shows a comparison of microstructures prepared from coarse and fine powders with solid loadings ranging from 20-40 vol% after heat treatment. Low solid loading of coarse powder (25 vol%) at 1050 °C results in a quite dense microstructure with grain sizes between 0.2 µm and 1 µm. The layer shows rather connected small grains than individual bigger particles. Low solid loading of nano powder at 1050 °C causes a much higher porosity. The grain size varies between 0.1-1.5 µm still having a lot of small grains around 100 nm but also several grains that reach a size ≥ 1 µm. High solid loading of coarse powder (40 vol%) at 1050 °C resulted in a more porous microstructure than low solid loading. The grain sizes seem to be slightly larger and areas with a dense microstructure in left bottom corner of Figure 65 (c) are visible. High solid loading of nano particles already leads at a heat treatment temperature of 1000 °C to the formation of large cracks. A lot of large round particles (up to 1 µm) are formed. In contest to the other layers, electrode N40 delaminated applying the tape test as described by Burnat [70].

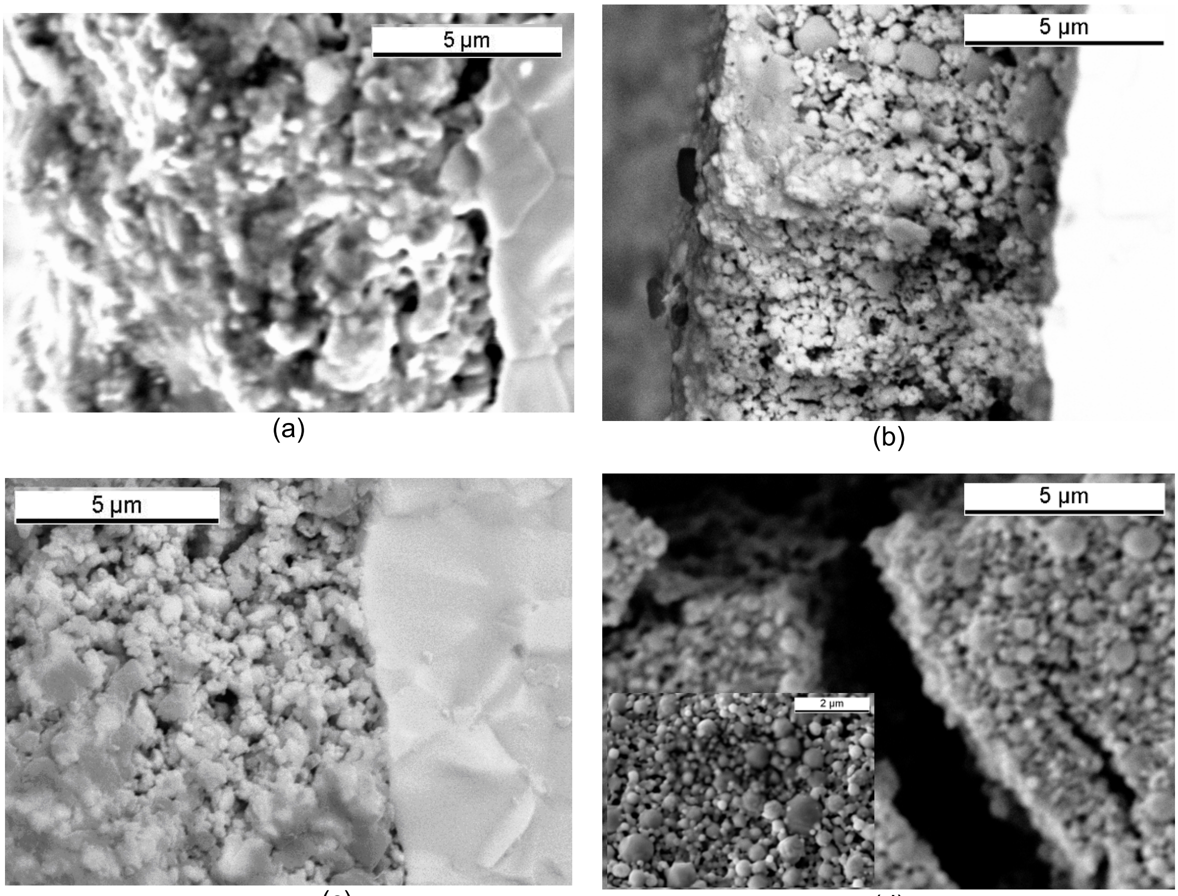

(a) (b)

(c) (d)

Figure 65: Influence of the solid loading (a) C25 = 25 vol%, (b) N20 = 20 vol%, (c) C40 = 40 vol% fired at 1050 °C, and (d) N40 = 40 vol% fired at 1000 °C on the microstructure of the cathode layers.

5.3.4 Temperature dependence of the microstructure comparing C11N22, CNE33 and CNE46

Figure 66 shows the SEM pictures of heat treated pastes containing powder mixtures after heat treatment at 950 °C and 1050 °C. C11N22 contains coarse and fine LSCF, CNE33 and CNE46 additionally CGO electrolyte powder. All 3 pastes contained totally 33 vol% powders and the heat treatment and the microstructures presented here correspond to an optimized firing programme (Figure 59, 950 °C, 1050 °C, with 1200 °C maximum temperature). The left part of the pictures shows the porous cathode layer und the right part is the dense electrolyte layer.

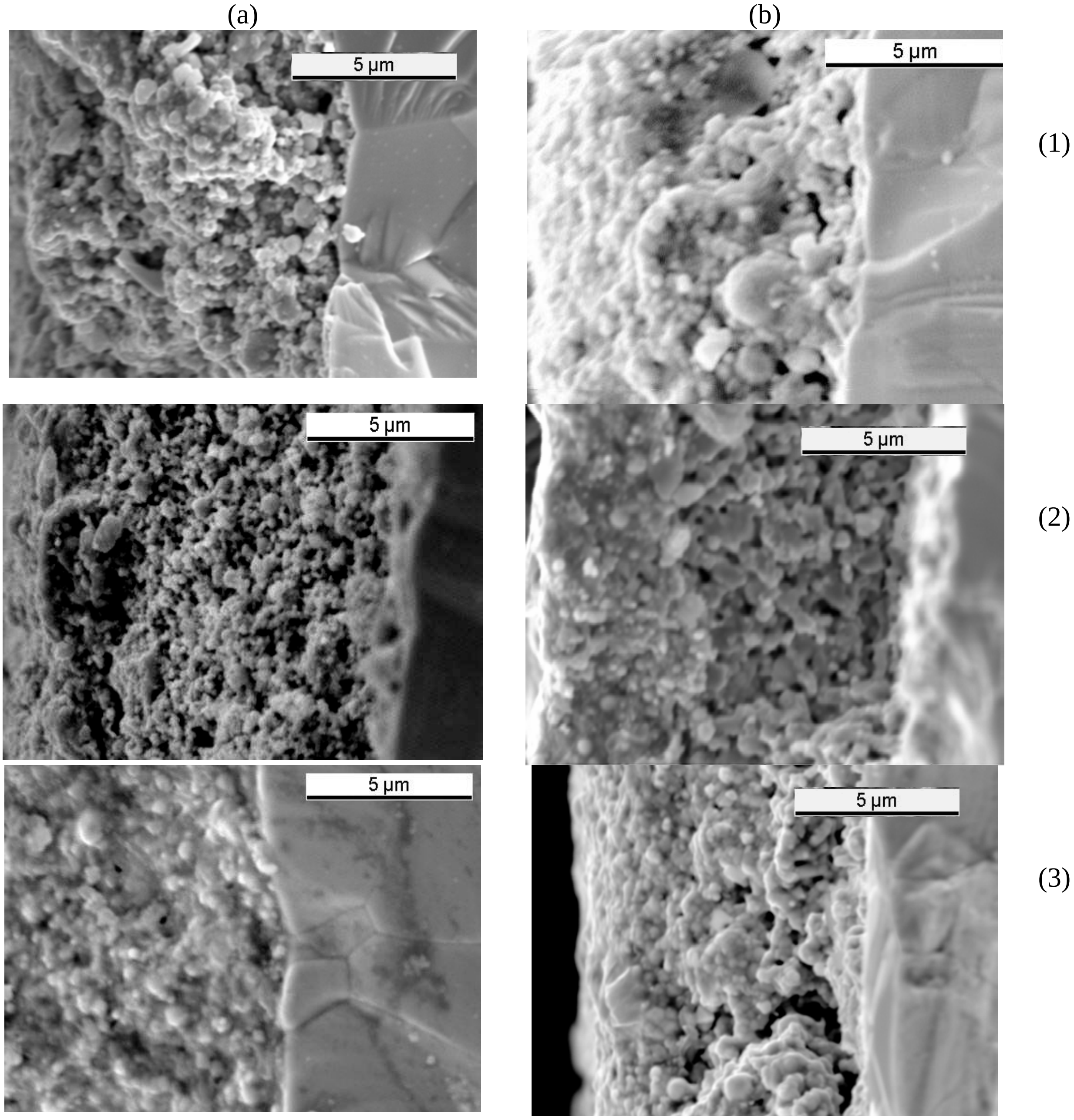

Figure 66: SEM pictures of cathodes from pastes made from powder mixtures C11N22 (1), and composite powders CNE33 (2), and CNE46 (3) after firing at 950 °C (a) and 1050 °C (b).

Heat treatment at 950 °C results in a porous microstructure with interconnected grains for C11N22. The grain size ranges from 0.1-1 µm. Next to the electrolyte especially small sized grains are visible. Cathode CNE33, containing 33 vol% electrolyte powder, shows a higher apparent porosity than C11N22 containing LSCF powder in coarse and nano-fraction. The grain size ranges from 0.1-1 µm and the grains are connected forming small sintering necks. Bigger grains of approximately 0.5 µm are equally distributed in the cathode bulk. The estimated porosity of cathode CNE46 is around 5 %. The visible grain size is between 0.2-1 µm. The adhesion to the electrolyte seems to be good and the LSCF grains are forming grain boundaries.

After heat treatment at 1050 °C the sample with the LSCF powder mixture (C11N22) has a microstructure with a low porosity, and partly bigger grains up to 1.5 µm are visible. However, smaller grains around 0.2 µm are still present. The grains are interconnected and the cathode seems to be bonded to the electrolyte. Cathode CNE33 shows a higher apparent porosity than the cathode C11N22 but the top layer of approximately 3 µm is almost dense. The grain size increased in comparison to the sample heat treated at 950 °C, and ranges from 0.2 µm mostly in the dense top layer to bigger grain sizes with interconnected grains between 0.5-1 µm. The apparent porosity of cathode CNE46 is estimated to 5-10 % and the grains seem to be connected. However, the porosity next to the interface with the electrolyte is higher than in the bulk of the material. The adhesion to the electrolyte is indicated by an intimate contact to the electrolyte.

The cathodes C11N22 and CNE46 after heat treatment at 1200 °C are displayed in Figure 67. The sample with the LSCF powder mixture (C11N22) has a microstructure with a low porosity. The grains are interconnected and the connection to the electrolyte is indicated by an intimate contact to the electrolyte layer. The grain sizes range between 0.5-1 µm connected by both sintering necks on the one hand and grain boundaries on the other hand. The sample containing 46 wt% CGO powder has a lower apparent porosity and an almost dense sintered microstructure. The grain size is hardly visible and estimated to ≥ 1 µm. No delamination is observed after heat treatment at 1200 °C.

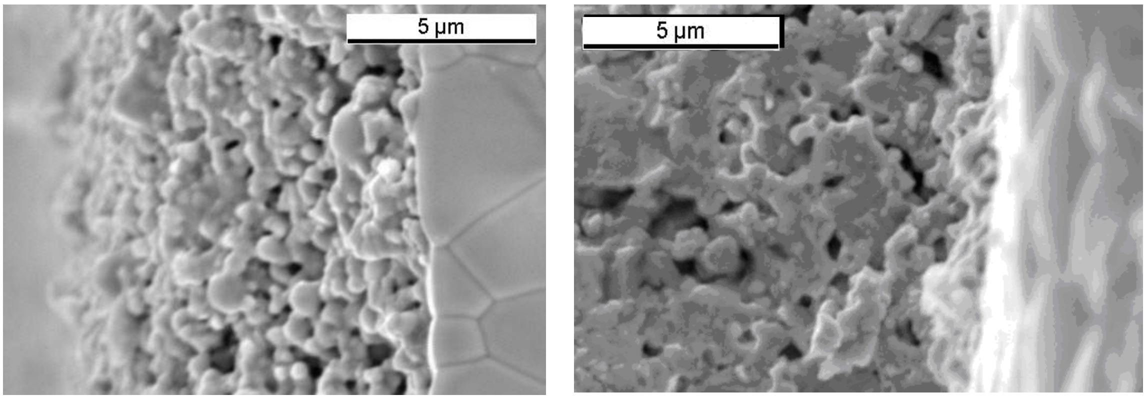

Figure 67: SEM microstructures of cathodes from pastes made from powder mixtures (C11N22, left) and composite powders (CNE46, right) after heat treatment at 1200 °C.

5.4 Discussion: influence of the starting powders and the solid loading on the microstructure

Cathode layers produced from pure nano powders (N20, N25 and N40), coarse powders (C25, C40) and powder mixtures (C11N22, CNE33, CNE46) including $Ce_{0.9}Gd_{0.1}O_{1.95}$ electrolyte (E) powder were compared at different sintering temperatures. Layers with pure nano powders show cracks (N20 and N25) or even delamination (N40) also with an optimized heat treatment. Layers from coarse powders show favourable sintering properties and resulted in porous, crack free layers. Powder mixtures including nano powders resulted also in crack free layers, but show quite low porosity. The cathodes C25, N25, C11N22 and CNE46 were further investigated by impedance spectroscopy.

The general trend of cathodes produced from nano powder is the formation of larger, spherical particles (≤ 1 μm), which seem to grow at the cost of smaller ones (≤ 0.2 μm). This kind of ripening seems to be favoured compared to the formation of sintering necks between individual grains. Cathodes from coarse powders seem to form connections between the grains and show grains of different shape. The connections between the grains in the cathode layer and between the cathode and the electrolyte seem to be established at temperatures around 900 °C with no delamination after tape test was observed. At lower sintering temperatures 800-850 °C the layers delaminated most probably due to insufficient bonding.

Microstructures clearly change upon a high or low solid loading of coarse and nano powder. Oswald ripening might be an explanation for grains of approximately 1 μm size growing at the expense of the nano particles. This effect might occur due to larger primary grains in the precursor powder and/or incomplete dispersion of the nano powders. The cathode prepared from N40 seems to have a more pronounced shrinkage than N25 visible by the formation of larger cracks. This derives possibly from a more intimate contact between the nano grains.

The reason of the higher porosity of electrode C40 than C25 might be that with a high solid loading no rearrangement of the particles during drying of the paste occurs. Both effects, a ripening of the particles and the formation of grain boundaries, occur.

The amount of cracks could be reduced by an adaption of the heat treatment for the pastes N25 and the layer delamination after sintering was eliminated. However, as visible in Figure 63 the upper surface (a) and the lower surface (b) of the sample exhibit a slightly different sintering behaviour and crack propagation. The slightly and lower number and smaller cracks at the lower surface might come from the direct contact to the sintering bed. This side of the sample most probably adapts slower to temperature changes in the furnace than the upper surface that is exposed to the air. Therefore, the mechanical stress deriving from temperature changes during heat treatment might be lower for the lower surface compared to the upper surface.

C11N22 and CNE46 show relatively smooth layers without cracks and delamination after the heat treatment. These results indicate clearly the advantages of the powder mixtures with the applied temperature profile. Cracks are supposed to be microstructure failures that might indicate already a beginning delamination of the cathode layer from the electrolyte. Furthermore, they are supposed to increase the lateral electrical resistance of the cathode under fuel cell operating conditions, which may result in a decrease the cathode performance.

Regarding the expected electrochemical performance, layers with a good apparent adhesion to the electrolyte, interconnected grains and high porosity are favoured to show low cathode polarization. The cathodes from C25 sintered at 1000 °C and 1100 °C, C11N22 sintered at 950 °C and CNE33 sintered at 950 °C show those microstructures (see SEM-pictures of Figure 65 and 67.

The SEM micrographs show only a small part (10 μm out of 10 mm cathode diameter) of the entire cathode. General trends like the packing of the grains, the connection between the grains can be observed. However, the SEM section might not be representative for the entire cathode layer. Especially cracks, delaminated areas and further defects (e.g. agglomerates) might not be observed.

The processing of coarse powders did not require special modification of the firing program in order to obtain crack free layers. The observed microstructures with coarse powder and powder mixtures show similar grain sizes but apparently lower porosity compared to the literature [27, 46, 135]. Cathodes prepared by spray pyrolysis and pulse laser deposition show a finer microstructure [51] with grains in the range of 40-50 nm and an apparent very narrow grains size distribution and an apparent bonding between the grains and the cathode layer and the electrolyte. The porosity of the cathode is apparently similar to the screen printed layers prepared in this study. The layers produced from pure nano powder in this study show crack formation which could be reduced by the adaption of the sintering program. Nano powders could be applied successfully as a mixture with coarse and electrolyte powder without cracks after firing.

The heat treatment of cathodes made from nano powders seems rather to result in a growth of round grains than to a bonding between them. The processing of the nano powders as well as the dispersion and the heat treatment might need further adaption in order to overcome the present problems. The application of a thin dense layer of LSCF between the cathode and the electrolyte e.g. might help to overcome contact problems between cathode and electrolyte.

5.5 Results: Impedance Response of LSCF//CGO//LSCF cells

5.5.1 Temperature dependence of impedance response

A Bode plot for a symmetrical cell is displayed in Figure 68 as an example. The frequency of the maxima shifts to higher values when increasing the temperature of the sample. The corresponding maximum frequencies are displayed in the spectra. The frequency of one apparent process increases from 3.16 Hz at 485 °C to 20 Hz at 591 °C, 79.5 Hz at 696 °C and 159 Hz at 800 °C. A second apparent process shows maxima at 20 kHz at 485 °C and 79.4 kHz at 591 °C. A third process appears at approximately 1.58 Hz at 696 °C and 2 Hz at 800 °C that seems to be fairly independent of the temperature.

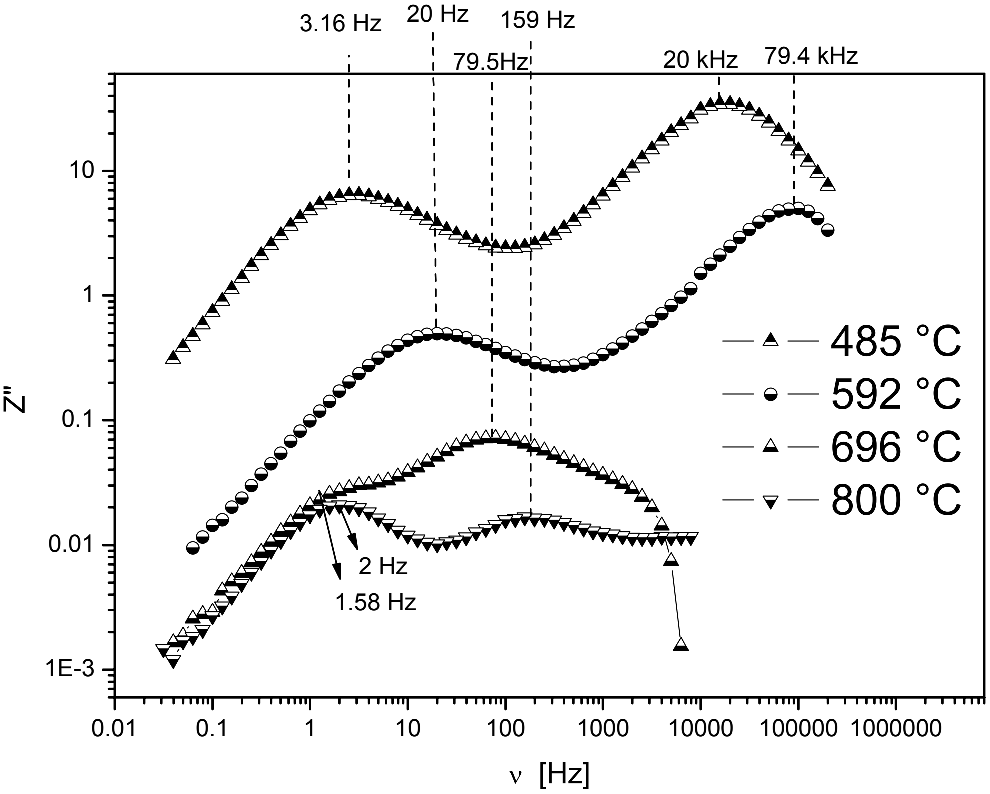

Figure 68: Bode plot: Z“ as a function of the frequency of a symmetrical cell (sample C11N22, 1000 °C firing temperature) measured at different temperatures (485, 592, 696 and 800 °C) with indication of the maxima.

5.5.2 Partial pressure dependence of the impedance response

The following two spectra (Figure 69) were recorded in different gas atmospheres, firstly from the sample in a mixed gas flow containing 80 % nitrogen and 20 % oxygen and secondly in pure oxygen at 485 °C. The Nyquist plot shows clearly a change in the impedance response for the two different oxygen partial pressures. While the first dominating semicircle is hardly changing, the small depressed semicircle is becoming smaller when the p(O_2) is increased from 0.2 bars to 1 bar. The Bode (imaginary part) remains unaffected in the high frequency maximum. The maximum in the low frequency range is shifting to higher frequencies at p(O_2) = 1 bar.

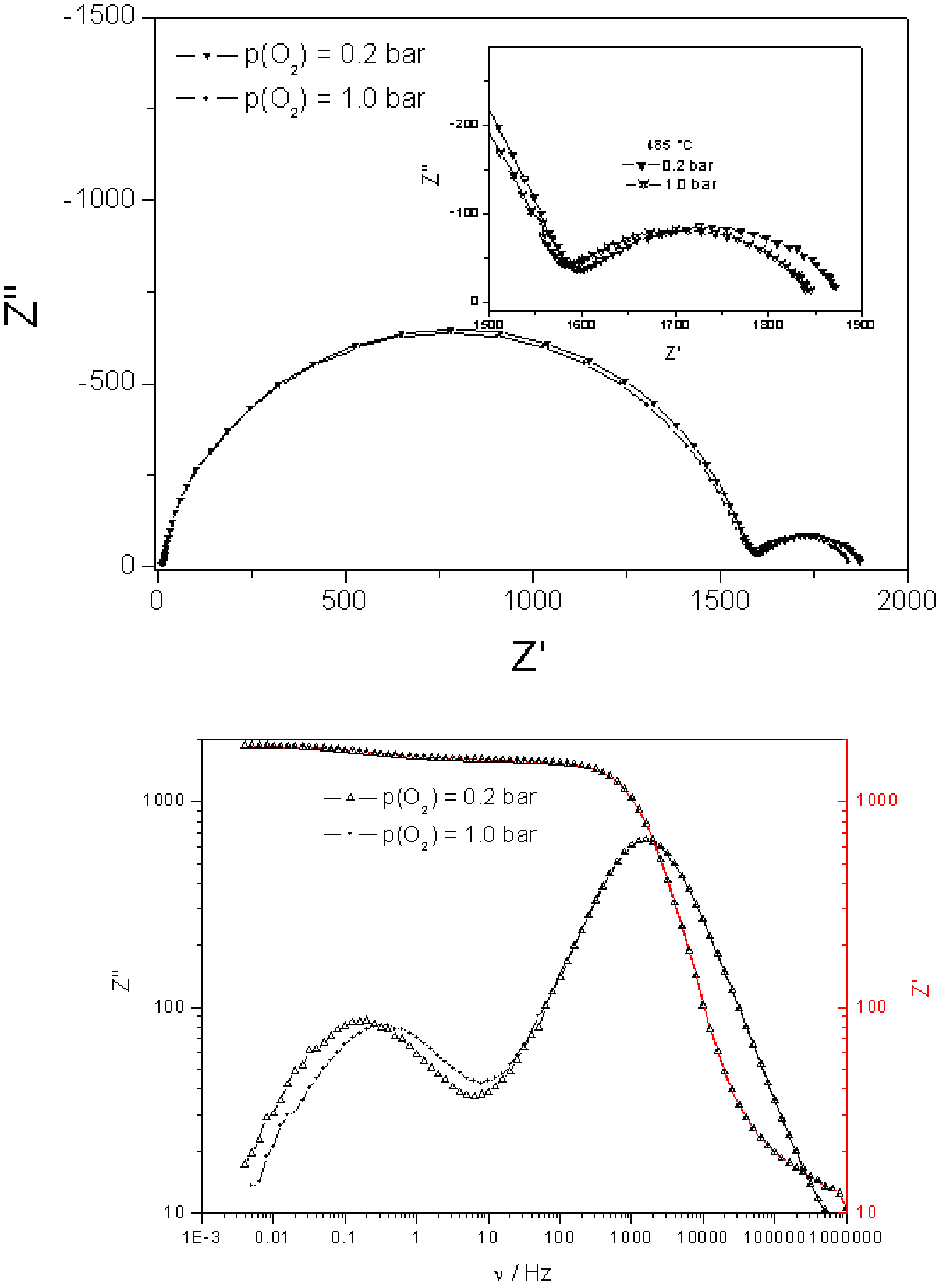

Figure 69: Impedance spectra (Nyquist plot on top and Bode plots on the bottom; red = real part, black = imaginary part) of symmetrical cells (N25, 1050 °C firing temperature) recorded at 485 °C in air and in oxygen atmosphere.

5.5.3 Influence of paste composition on the impedance

The influence of the paste composition on the appearance of the impedance spectra is exemplified in Figure 70. The second semicircle shows only a small overlap for cathodes from paste C25, whereas the overlap becomes more pronounced for N25 (b) and C11N22 (c, shows only the overlapping part). The size of the first semicircle is changing also as function of the applied paste, while the semicircle of sample C25 has only a diameter of 29, Ω the semicircle of sample C11N22 shows 71 Ω diameter, and 190 Ω are present for sample N25.

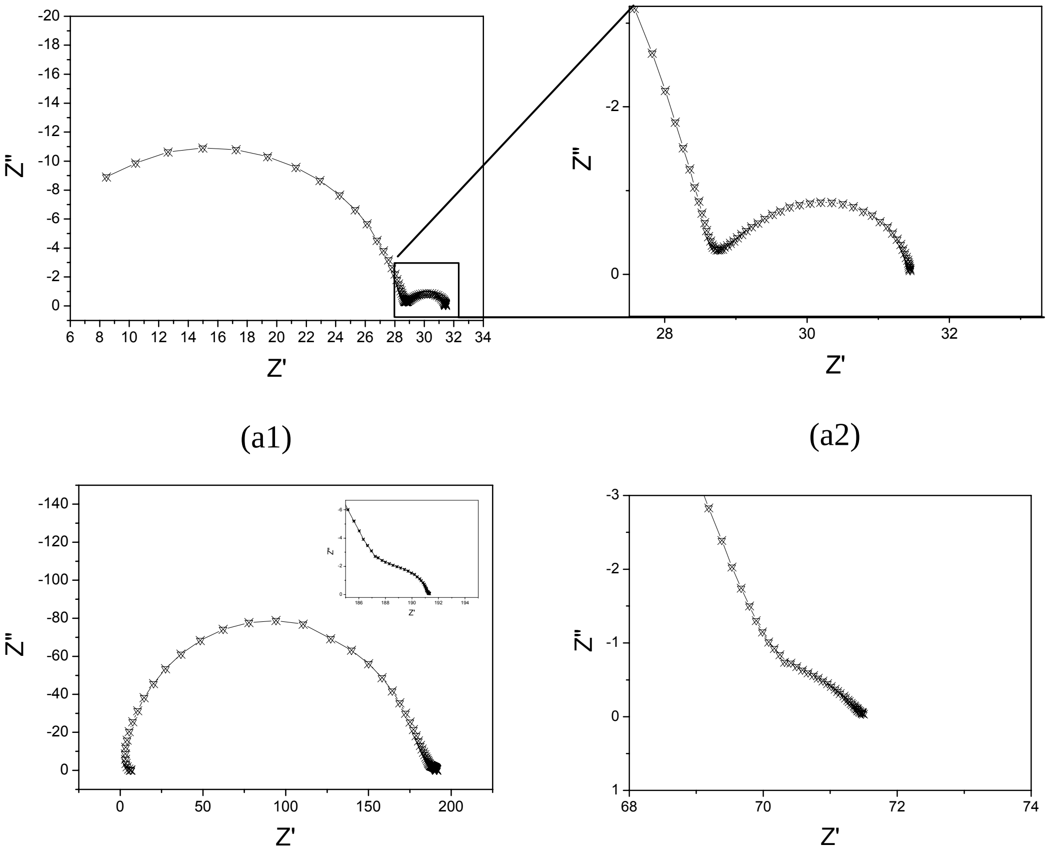

(a1) (a2)

(b) (c)

Figure 70: The Nyquist representation of (a) C25 fired at 900 °C (with entire spectrum (a1) and zoomed cathode contribution (a2)), (b) N25 fired at 1050 °C (insert is showing the cathode part), and (c) C11N22 (cathode part) fired at 950 °C, all measured at 591 °C.

5.6 Discussion : Oxygen partial pressure dependence of the impedance response

Looking at the kinetic parameters of LSCF leads to the assumption, that at a constant temperature the polarization resistance of a cathode will change when the atmosphere is changed. The conductivity of the material, as well as the chemical diffusion coefficient remain relatively constant, but the surface exchange coefficient is increasing, when the $p(O_2)$ is changed from 0.2 bars to 1 bar. Adler et al. , Søgaard et al. and Rüger et al. [31-33] show this by modelling the cathode resistance as a function of the microstructure and the kinetic parameter. The polarization resistance of an LSCF cathode is supposed to decrease when changing the atmosphere from air to pure oxygen. This might indicate a faster process due to the increased oxygen partial pressure. The conductivity of the $Ce_{0.9}Gd_{0.1}O_{1.95}$ electrolyte should not change significantly between 1 bar $< p(O_2) < 0.2$ bar.

Figure 69 shows that the left (high frequency) semicircle is independent on the $p(O_2)$, while the second semicircle (low frequency) becomes smaller with increasing the oxygen partial pressure from 0.2 bars to 1 bar. Using a platinum electrode as direct contact to the CGO electrolyte substrate, the diameter of the first semicircle becomes proportional to the thickness of the pellet (Figure 71). Both approaches lead to the conclusion, that the first semicircle can clearly be attributed to the electrolyte. Subtracting the electrolyte contribution the remaining spectrum can be attributed to the cathode polarization. This approach is in line with the literature [46, 51] were the high frequency part could be also identified as the electrolyte.

The commercially available program ZView ® (Scribner Associates, Inc.) was used for the analysis of the impedance spectra. The polarization resistance of the cathode was evaluated after subtracting the electrolyte contribution from the spectra. Figure 71 shows the procedure beginning with the entire spectrum of a symmetrical cell (a), the depressed semicircle after subtraction of the electrolyte contribution (b) and the residual (c) when subtracting the fit corresponding to the equivalent circuit (d) from (b). The polarization resistance is obtained by the sum(R1-3) divided by 2, because the symmetrical cell consists of two identical cathodes.

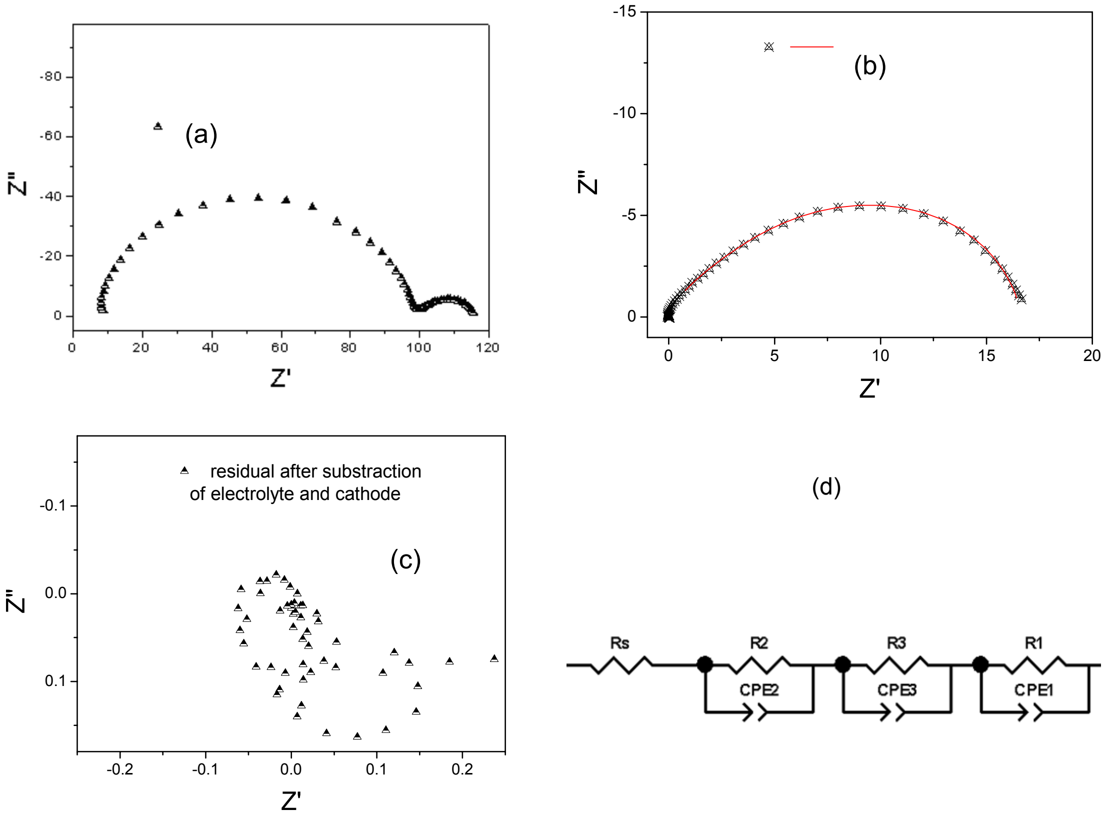

Figure 71: Evaluation of R_{pol} with (a) the entire spectrum, C25 cathode contribution ((b), electrolyte subtracted) with corresponding fit, (c) the residual after subtracting the electrolyte and the cathode contribution and the equivalent circuit with 3 R-Q elements in series (d), that served to fit the impedance spectra of the cathode contribution.

.

The polarisation resistance (R_{pol}) from EIS measurements was used in order to evaluate the quality of the differently prepared cathodes. The spectra generally consist of a large semicircle attributed to the electrolyte material, and a smaller depressed (often "mouse-shaped") semicircle, that is attributed to the electrochemical processes in the cathode. Subsequently the temperature dependence of R_{pol} is displayed for different cathodes and the influence of the different screen printing pastes is discussed.

In this analysis simply the polarization resistance of the cathode measured at 591 °C is taken into account to compare the different cathodes. The spectra show an overlap of the cathode and the electrolyte processes. All spectra could be fitted with a combination of 3 parallel RQ elements in series as displayed in Figure 71 after subtraction of the electrolyte.

The sum of (R2 + R3)/2 was taken as the polarization resistance (R_{pol}) for one cathode. The spectra of C25 heat treated between 900 °C and 1000 °C show a depressed semicircle with a 45 % angle at the left side and a subsequent part of a semicircle. These spectra could alternatively be fitted by a Warburg element (or a Gerischer representation) indicating diffusion processes responsible for the cathode resistance. Supposing that the gas diffusion to the cathode surface is fast this representation can be attributed to the diffusion "resistance" in the bulk of the cathode. This is in line with the literature e.g. from Adler et al. [31, 34] who suggests that gas diffusion has a negligible contribution to the polarization resistance at oxygen partial pressures as high as 0.2 bar.

5.7 Results: Influence of the paste composition on the cathode polarization resistance

5.7.1 Influence of the sintering temperature on the polarisation resistance of cathodes produced from C25 and N25

The temperature dependence of the polarization resistance (R_{pol}) of the cathodes is shown in Figure 72 comparing pastes with 25 vol% coarse particles (C25, sub micro) and 25 vol% nano powders (N25). The cathode layers were heat treated between 900 °C and 1100 °C.

C25 cathodes prepared at a firing temperature of 1100 °C exhibit a polarization resistance that is about a factor of 5 higher compared to the other cathodes fired at lower temperatures. Firing temperatures between 900 °C and 1000 °C lead to similar values of the polarization resistance; especially at 696 °C and 800 °C they are independent of the sintering temperature. At 591 °C and 485 °C the cathode sintered at 1000 °C shows significantly lower values. Between 485 °C and 800 °C R_{pol} shows a linear relation in the Arrhenius representation. Cathodes prepared with N25 show a significant dependence of R_{pol} between 485 °C and 800 °C on the firing temperature. R_{pol} is becoming lower with increasing sintering temperature from 950 °C to 1050 °C. The temperature dependence of R_{pol} in the Arrhenius representation shows a linear relation between 485 °C and 696 °C and between 696 °C and 800 °C.

The more pronounced temperature dependence between 696 °C and 800 °C indicates that a process with higher activation energy is dominating the cathode reactions than in the low temperature region. In the temperature range between 485 °C and 696 °C N25 cathodes show 3-5 times higher values of the polarization resistance than C25 cathodes (except C25 fired at 1100 °C). At 591 °C e.g. R_{pol} of N25 cathodes lies in between 3.3 and 9.8 Ωcm^2 while it is reduced to 0.87 and 1.46 Ωcm^2 for C25 cathodes. However, at 800 °C R_{pol} is similar for N25 and C25 sintered between 900 °C and 1050 °C. The best performing N25 cathode (1050 °C firing temperature) shows similar R_{pol} values like C25 sintered at 1100 °C.

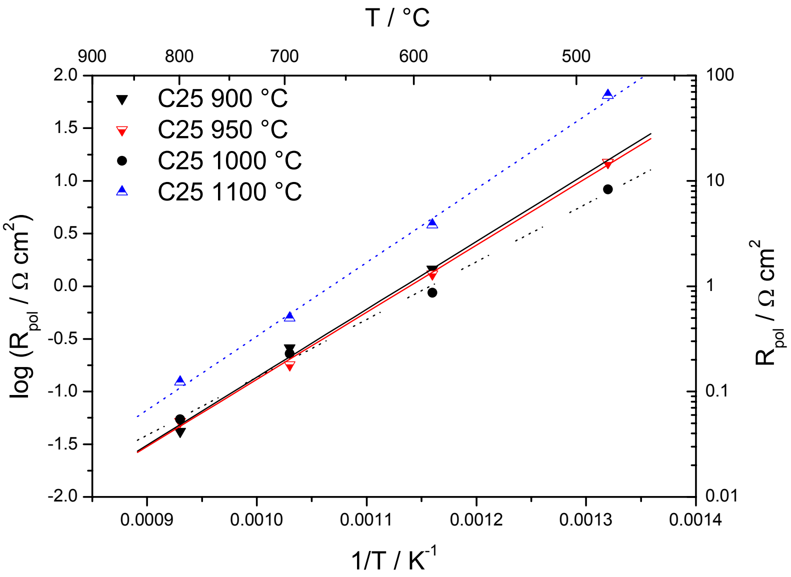

(a)

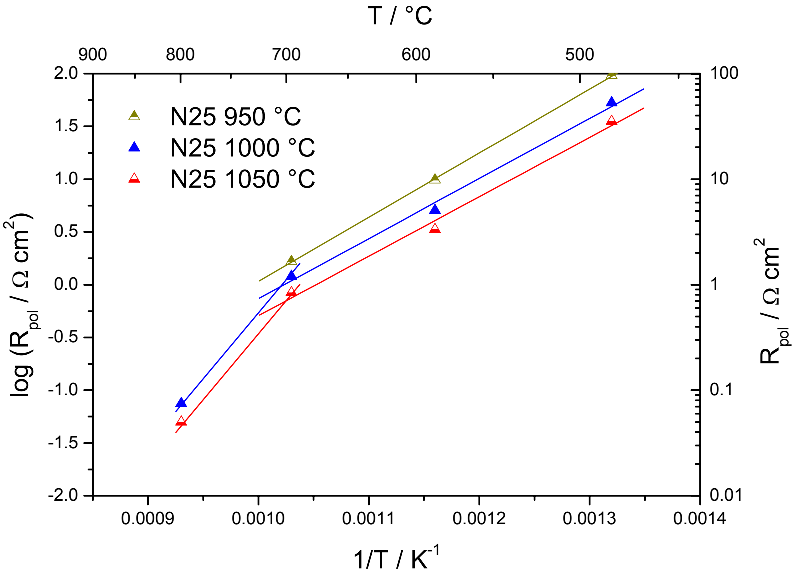

(b)

Figure 72: The temperature dependence of the polarization resistance of cathodes prepared with pastes C25 (a) 25 vol% solid loading 8% binder content relative to the weight of the powder Heat treatment: 900-1100 °C and N25 (b) nano powder 25 vol% solid loading no binder addition, heat treatment: 950-1050 °C.

The activation energy was calculated from the slopes of the logarithmic plots. The apparent activation energy for the layers prepared with C25 lies in between 1.1-1.3 eV. The slope for the layers sintered at 900 °C, 950 °C and 1100 °C corresponds to 1.3 eV while for 1000 °C heat treatment temperature the activation energy is apparently smaller (1.1 eV). The slope of the N25 layers calculated between 485 and 696 °C is 1.2 eV for heat treatment temperatures of 950 °C, 1000 °C, and 1050 °C. However, taking the data points at 796 °C and 800 °C the layers, heat treated at 1000 °C and 1050 °C show apparent activation energy of 2.4 eV.

5.7.2 Influence of the sintering temperature on single and multi phase cathodes

The temperature dependence of the cathode polarization resistance is shown in Figure 73 comparing pastes with 33 vol% loading of particles; i.e. an LSCF coarse/nano mixture (C11N22), a composite of the LSCF coarse/nano mixture with 46 vol% $Gd_{0.1}Ce_{0.9}O_{1.95}$ electrolyte powder (CNE46) and a composite mixture between LSCF nano powder and electrolyte powder (NE46).

The cathode layers were heat treated at temperatures between 950 °C and 1200 °C and the activation energy was calculated from the linear regions of the logarithmic plots. R_{pol} of C11N22, NE46 and CNE46 cathode layers heat treated at 1000 °C shows similar values between 0.76 and 0.96 Ωcm^2 at 591 °C. The activation energy for all layers lies in between 1.1 and 1.3 eV. The polarization resistance of C11N22 heat treated at 950 °C and 1000 °C shows significant difference in the temperature range between 485 °C and 800 °C. The C11N22 layers sintered at 1200 °C show the highest values in the polarization resistance (2.5 Ωcm^2) at 591 °C of all measured samples. The layer CNE46 heat treated at 950 °C shows a higher polarization resistance between 696 °C and 800 °C as the same composition heat treated at 1000 °C. The slope of R_{pol} between 485 °C and 696 °C of CNE46 heat treated at 1000 °C results in activation energy as low as 1 eV. The slopes of CNE46 sintered at 950 °C and 1000 °C evaluated between the 2 data points at 696 °C and 800 °C show apparent activation energy of 1.4 eV similarly to the nano powders.

A similar behaviour can be observed also with layers prepared from N25 with a more pronounced change in the activation energy from 1.2 eV between 485 °C and 696 °C and 2.4 eV between 696 °C and 800 °C. The composite cathodes (NE46 and CNE46) show similar values in the polarization resistance compared to the LSCF cathodes made from C11N22 and C25.

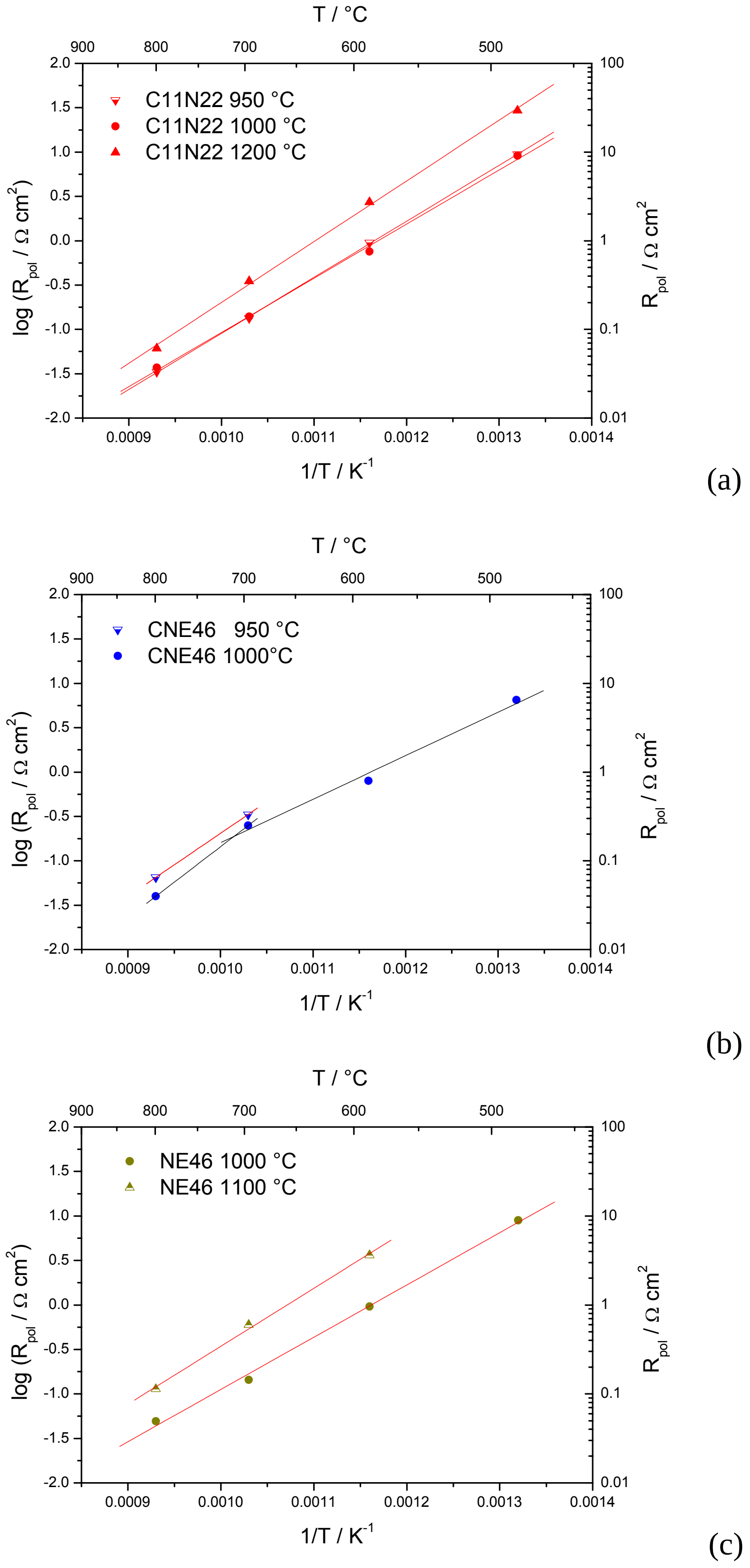

Figure 73: The temperature dependence of the polarization resistance of cathodes prepared with pastes of powder mixtures of C11N22 (a) 11 vol% coarse / 22 vol% nano powder, 950-1200 °C; CNE46 (b) 18 wt% coarse and 36 wt% nano LSCF, 46 wt% CGO, 950-1000 °C; NE46 (c) 54 wt% nano LSCF, 46 wt% CGO, 1000-1100 °C (powder loading of 33 vol%, no binder).

5.7.3 Influence of the layer thickness on the polarisation resistance of C25 cathodes

The cathodes presented before consist only of one printed cathode layer with a thickness is between 10-15 μm. Subsequent printing of 3 layers results in cathodes with a thickness between 30 and 40 μm. The temperature dependence of the polarization resistance is displayed in Figure 74.

The variation of the layer thickness and heat treatment at 950 °C apparently leads only to a minor change in R_{pol} (within the uncertainty of the measurement). After heat treatment at 1000 °C three subsequently printed C25 layers show R_{pol} approximately by the factor 1.4 higher than only one layer of about 10 μm thickness.

The slope of the Arrhenius plot is constant for one or three subsequently printed layers but changes with the heat treatment temperature. At 950 °C the slope of the plot corresponds to the activation energy of 1.3 eV while at 1000 °C heat treatment temperature the activation energy of 1.1 eV is slightly lower. The activation energy is not dependent on the layer thickness, but changes with the sintering temperature.

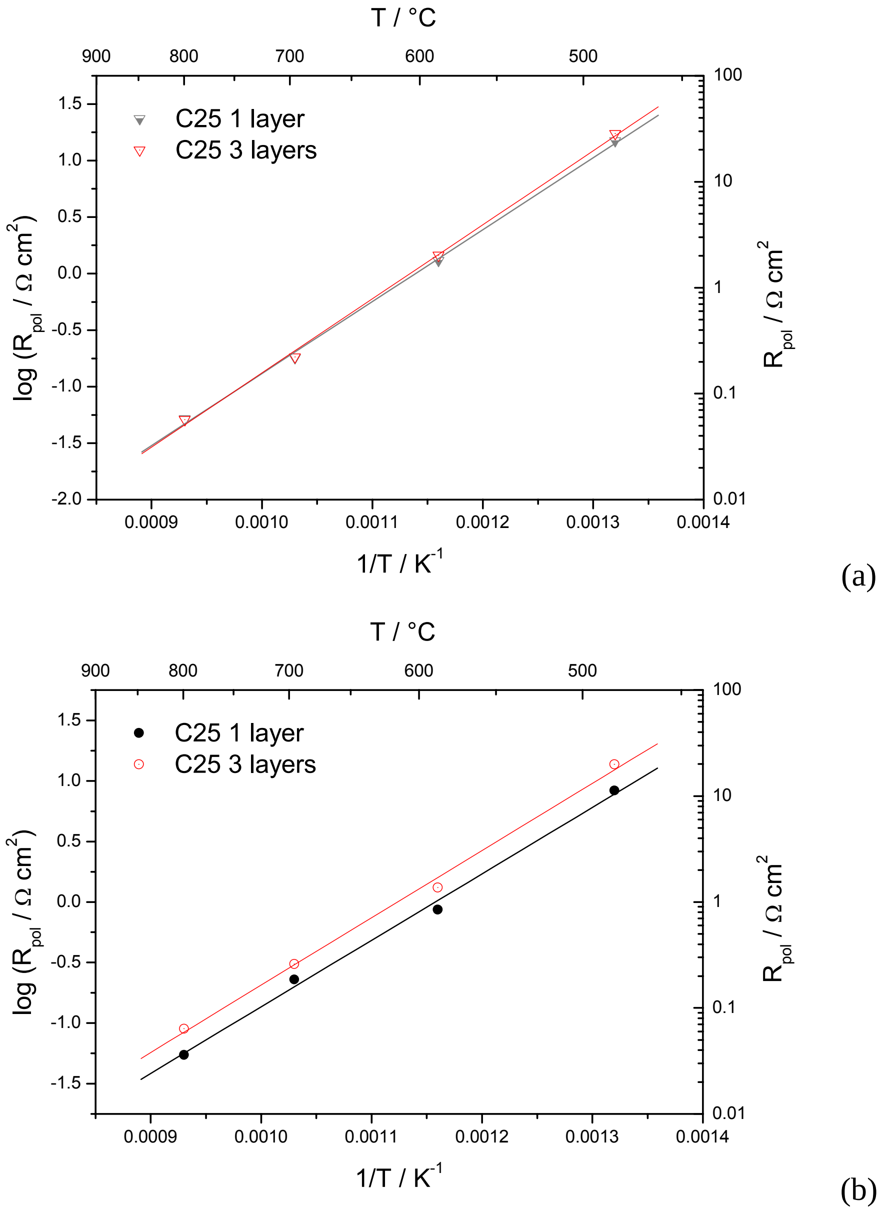

Figure 74: The temperature dependence of the polarization resistance of cathodes prepared with C25 paste (1 layer = 10-15 µm and 3 layers = 30-40 µm thickness) at (a) 950 °C and (b) 1000 °C firing temperature.

5.8 Discussion: Comparison of lowest measured polarization resistances for all starting powders

5.8.1 Microstructure and cathode polarization resistance – influence of the layer thickness and the grain size applying C25 and N25

Applying C25 and N25 as screen printing pastes with the same powder loading as cathode layers on the CGO electrolyte substrate, both layers show significant differences in the microstructure and the R_{pol}. The coarse powders show grains with both ball like and squared shape and apparently the grains are connected. The cathode layer seems to have good electrical contact to the electrolyte. The resulting values of R_{pol} are between 0.95-1.56 Ωcm^2 for 10-15 µm thick cathodes at 592 °C. They are about the factor 1.4 higher for 30-40 µm thick cathodes heat treated at 1000 °C and measured at 592 °C. The layers prepared from nano powders especially with a heat treatment below 1000 °C show mainly ball shaped grains that grow presumably due to Oswald ripening [136]. Layers of N25 show small cracks after heat treatment and are almost dense at $T \geq 1100$ °C but show visible delamination of the layer at 1200 °C. Both the R_{pol} (factor 5 – 20 higher then the lowest R_{pol}) and R_{tot} (factor 10 higher then lowest values) are among the highest values for all cathodes.

One big difference between C25 and N25 is the apparent resistance of the electrolyte. Values between 17.5-55 Ωcm^2 have been measured for the coarse powder at 592 °C, while the samples prepared with nano powder show values between 185 and 300 Ωcm^2 as illustrated in Table X. The overlap between the higher frequency region of the cathode contribution and the lower frequency region of the electrolyte contribution of the impedance becomes more pronounced when the electrolyte resistance (R_{el}) increases. This makes sense, because the time constant of the electrolyte contribution ($\tau = R_{el}C$) becomes higher at higher R_{el}, accordingly the frequencies attributed to the electrolyte become lower and so overlap more with the cathode.

Table X: Polarization resistances of different cathodes made from C25 and N25 evaluated with respect to their microstructure.

Composition electrolyte thickness total thickness	E_a/eV	ln(A)	591 °C R_{pol} Ωcm^2	R_{el} Ωcm^2	R_{tot} Ωcm^2	Micro structural properties
C25 at 900 °C						Microstructure dense, grain size 0.2-1 μm, apparently good adhesion to the electrolyte
0.53 mm	1.3	23.5	1.46	28.8	31.5	
0.58 mm						
C25 at 950 °C						dense microstructure, still small grains (0.2-1 μm), apparently good adhesion to the electrolyte
0.40 mm	1.3	23.3	1.31	49.9	52.5	
0.43 mm						
C25 3 layers 950 °C						No SEM
3 layers	1.3	23.7	1.45	65.8	68.7	
0.46 mm						
0.57 mm						
C25: at 1000 °C						coarser grains around 0.5 μm, more pores compared to 900 °C and 950 °C good adhesion
0.61 mm	1.1		0.866	17.6	19.3	
0.65 mm						
C25: at 1000 °C						No SEM
3 layers	1.1	21	1.32	16.4	18	
0.57 mm						
0.64 mm						
C25: at 1100 °C						No SEM
0.52 mm	1.2	17.2	3.82	47.4	55	
0.55 mm						
N25 @ 950 °C						Grains between 0.1-1μm, porous microstructure
0.85 mm	1.2*	20.6	9.82	288	308	
0.89 mm	* Ea between 485 °C and 696 °C					
N25 @ 1000 °C						grains growth from 900 °C to 1000 °C (0.2- 1.5 μm), porous , more and larger cracks than 950 °C, partly delamination
0.85 mm	1.1*	23.6	5.05	300	310	
0.88 mm						
N25 @ 1050 °C						Grains (0.2- 1.5 μm), dense layer, contact to electrolyte ok, cracks larger than 1000 °C
0.89 mm	1.1*	23.9	3.32	185	191	
0.93 mm						

Generally a temperature around 1000 °C seems to be adequate for the heat treatment of well performing layers. The different powder mixtures and the coarse powder show similar values in the polarization resistance but slightly different slopes in the temperature dependent plot (Figure 75) and the corresponding activation energies. The range of the slopes in the temperature interval between 485 °C and 696 °C corresponds to activation energies (E_a) between 1.09 and 1.25 eV. The nano powders show much higher values both in the R_{pol} and also in the total resistance of the symmetrical cell but also a slope corresponding to an E_a of 1.2 eV.

The differences between cathodes prepared from coarse powder and that with the powder mixtures are relatively small. The firing temperature possibly is already too high and the grain sizes become similar using coarse and fine powders. A higher catalytic activity (and lower R_{pol}) therefore probably is not obtained because it is usually attributed to smaller grain sizes and higher surface areas. The cathode made from paste N25 with pure nano powders shows significantly higher polarization resistance than the other pastes. This might be attributed to the different sintering properties of the nano powder forming rather individual spherical grains than grain boundaries.

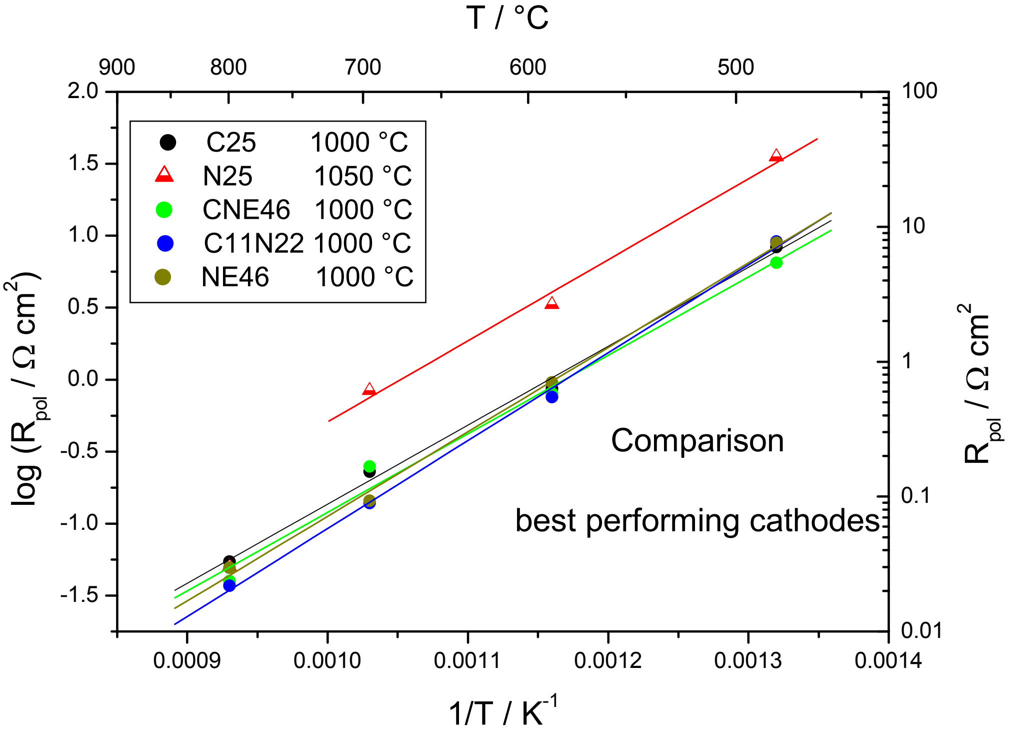

Figure 75: The temperature dependence of the polarization resistance of cathodes with the lowest values in the R_{pol} prepared with C25, N25, CNE46, C11N22 and NE46.

5.8.2 Comparison of cathodes prepared with the highest heat treatment temperatures

In the following the polarization resistance of N25 heat treated at 1050 °C resulting in the best performance of the pastes produced from pure nano powders is compared with C11N22 heat treated at 1200 °C, C25 and NE46 heat treated at 1100 °C. These four different cathode layers result in similar values for R_{pol} and total resistances measured at 591 °C. The activation energies represent the slopes of the temperature dependent plots between 485 °C and 696 °C show slight differences. C11N22 was fired at 1200 °C (the highest sintering temperature in this study) showing an activation energy of 1.3 eV and R_{pol} = 2.5 Ω cm^2, NE46 fired at 1100 °C has similar a slope evaluated between 585 °C and 800 °C corresponding to 1.2 eV equal to C25 fired at 1100 °C. The relatively high polarization resistance in comparison to the cathodes with lower R_{pol} might be explained by inactive (=isolated) cathode areas with no contact between current collector – cathode – electrolyte. Cracks and delamination due to the thermal stress are the most probable reasons although not visible in the SEM.

The values of the polarization resistance are comparable to values of approximately 1 Ω cm^2 obtained by Beckel et al. [51] for thin cathode layers at 650 °C and an activation energy of 1.18 eV corresponding to roughly 2.5 Ω cm^2 at 585 °C. The low thickness of the cathode might be the reason for slightly higher values in the polarization resistance assuming a penetration depth close to the cathode thickness. This might be similar in this work for the cathodes layers fired at higher temperatures, because the larger grains obtained in the cathode layer result in an increasing penetration depth.

The microstructure of cathode N25 fired at 1050 °C show a vertical crack and additionally delamination, when fired at 1200 °C. The vertical cracks in combination with delamination might be the reason for larger isolated areas that cause an enhanced charge transfer resistance between cathode and electrolyte. Most probably this effect occurs already at temperatures around 1050 °C for the cathodes prepared from N25. The lower E_a for N25 (1.0 eV between 485 °C and 696 °C) might be attributed to a good adhesion of the active areas on the electrolyte due to a higher sintering activity of the smaller particles. Despite higher firing temperatures (1100 °C and 1200 °C) the SEM pictures of all other cathodes do not show clearly an indication for horizontal or vertical cracks.

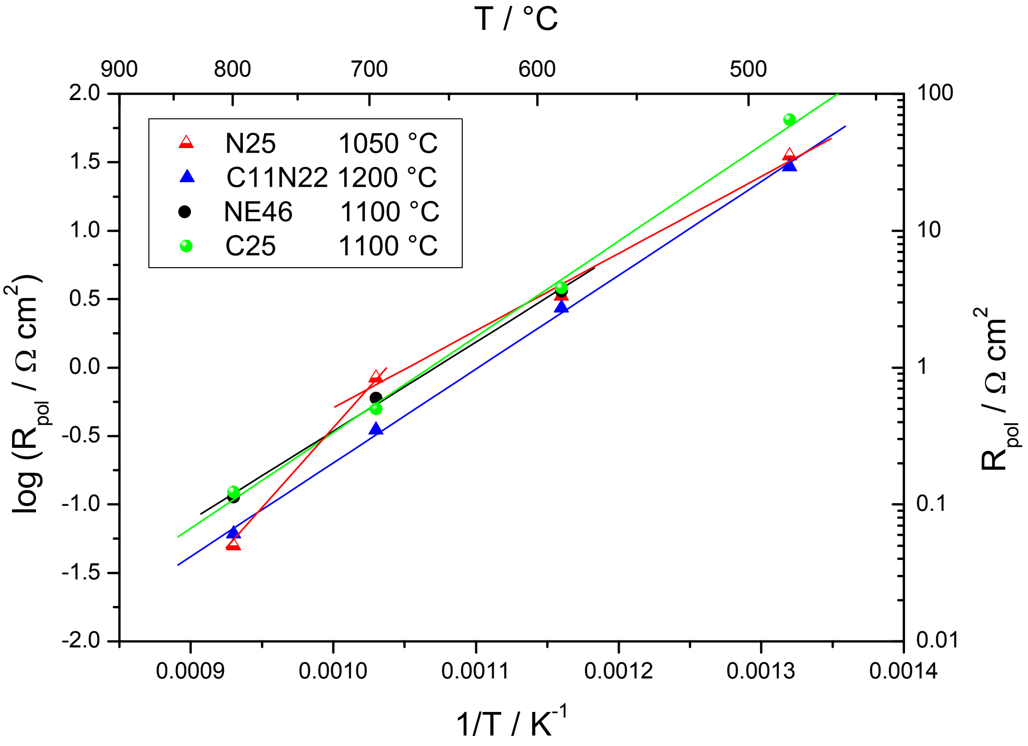

Figure 76: The temperature dependence of cathode layers heat treated at the highest temperatures.

5.8.3 Microstructure and cathode polarization resistance – influence of the grain size on R_{pol} applying C11N22 and NE46 and CNE46

The results of the SEM and EIS investigations are summarized in Table XI. The microstructures of cathodes made from C11N22 show relatively low porosity and moderate grain growth between 900 °C and 1100 °C, a significantly coarsened but still porous microstructure is present at 1200 °C. The polarization resistance at 591 °C is decreasing to 0.755 Ωcm^2 when the sintering temperature is increased from 950 °C to 1000 °C, being the lowest value among the cathodes. At 1200 °C R_{pol} is increased and above all R_{tot} increases to 2.5 Ωcm^2, similarly high as the N25 cathodes fired at 1050°C.

Cathodes made from CNE46 show similar values of R_{pol} as C11N22. However, R_{tot} is significantly higher indicating that the contact to the electrolyte might be worse. As the microstructure shows no major differences the high R_{tot} might be caused by contact problems between the cathode and the electrolyte.

NE46 as cathode material shows both, similar low R_{pol} and R_{tot} as C11N22 at 1000 °C heat treatment. Good adhesion of the cathode layer to the electrolyte and the current collector as well as an increased surface area of the cathode for the oxygen reduction can be supposed to be present.

At 1100 °C both R_{pol} and R_{tot} become higher by a factor of approximately 4 indicating that a coarsening of the microstructure especially for composite powders decreases the electrical performance of the cathode considerably. Some differences in the microstructure are visible but they are less significant than comparing the cathodes made from pure coarse (C25) and nano powders (N25). Parameters, like the triple phase boundary length or the inner surface area couldn’t be estimated from the SEM micrographs. The porosity was difficult to estimate, because of the rough surface of the broken samples.

Table XI: Polarization resistances of different cathodes made from C11N22, NE46 and CNE46 evaluated in the light of the microstructure.

Composition electrolyte thickness total thickness	E_a/eV	ln(A)	591 °C R_{pol} Ωcm^2	R_{el} Ωcm^2	R_{tot} Ωcm^2	Micro structural properties
C11N22 @ 950 °C						Grains between 0.1 and 1 µm, good adhesion to electrolyte, more pores than at 850 °C.
0.48 mm	1.2	24.25	0.95	69.7	71.6	
0.52 mm						
C11N22 @ 1000 °C						
0.58 mm	1.2	23.53	0.755	15.5	17	Grains between 0.2-1 µm, good apparent adhesion, low porosity (higher at interface to electrolyte).
0.61 mm						
						Coarse grains (0.5-2 µm), low remaining porosity, partly delamination from electrolyte.
1200 °C(C11N22)						
0.41 mm	1.3	20.75	2.500	202	207	
0.45 mm						
CNE46 @ 950 °C						Grains 0.2-1µm, dense layer, adhesion ok.
0.42 mm	no EIS below 696 °C!					
0.47 mm						
CNE46 @ 1000 °C						
0.54 mm	1.1	21.31	0.799	73.2	74	No SEM at 1000 °C; grains 0.2-1 µm at 1050°C, structure dense (top), sintering between several grains, higher porosity at interface to the electrolyte.
0.58 mm						
NE46 @ 1000 °C	1.2	22.34	0.958	72.4	73.4	-
NE46 @ 1100 °C	1.3	22.70	3.61	186	193	
						-

The implementation of nano powders was supposed to decrease the polarization resistance significantly. However, the cathodes with pure nano powder show even higher values of R_{pol} than all other prepared cathodes. This is attributed to problems in the processing, due to increased sintering activity causing cracks and subsequently delamination of the layers. The large values of the cathode polarization resistance are attributed in part of that cathode area, that is not electrically contacting the electrolyte and to increased lateral resistance caused by the cracks.

These drawbacks most likely were overcome by powder mixtures containing nano powders and a coarse fraction of powder (CGO electrolyte powder or LSCF sub-μ). Sintering temperatures around 1000 °C were necessary to ensure good performance and stability of the layers. This reflects the same temperature that was necessary for the heat treatment of layers from pure sub-μ powder.

Values for the polarization resistance (R_{pol}) compared to the literature

Beckel et al. [51] compare literature values of R_{pol} for different LSCF cathodes at 650 °C. The values amount to 0.47-6.2 Ωcm^2. The lowest value corresponds to the lowest values achieved in course of the present study.

However, Steele et al. [40] and Bae et al. [137] after etching of the electrolyte reached values as low as 0.5 Ωcm^2 at 520 °C with double layer LSCF cathodes using a dense LSCF interlayer. These values correspond approximately to 0.2 Ωcm^2 at 600 °C or less than 0.1 Ωcm^2 at 650 °C. The double layer cathodes without etching of the electrolyte correspond to a polarization resistance of approximately 0.8 Ωcm^2 at 600 °C. These results point out the importance of an intimate contact between the electrolyte and cathode.

5.9 Assessment of the obtained results

5.9.1 Assessment of processing, thermal treatment and obtained polarization resistance at 600 °C

The presented results show a difference in the polarization resistance between the samples produced from pure coarse (C25) and pure nano powder (N25). The still high values for N25 show that there are still problems in the processing and/or thermal treatment of pastes containing pure nano powder. Similarly, low R_{pol} was achieved for layers produced from paste C11N22 (containing LSCF coarse and nano powder), C25 and the composite pastes NE46 and CNE46 after firing at 1000 °C. The similar values and the SEM indicate that the effect of the nano powders (higher surface and catalytic activity) is most probably no more present at these firing temperatures. However, such temperatures are needed to ensure good adhesion between electrolyte and cathode. Furthermore, the cathode grains have to be well connected to ensure electronic and ionic transport through the cathode. The low activation energies and relatively low values of R_{pol} indicate that electrochemically active layers for operating temperatures around 650 °C have been produced.

Cathodes for 600 °C operating temperature would need a further improvement by a factor of about 2. Chapter 5.10 discusses different factors in the cathode microstructures that might need improvement and possible values of R_{pol} that might be reached by further optimization. The comparison with literature values, as discussed before, indicates that especially the contact between electrolyte and cathode might have a potential to be further optimized.

5.9.2 Assessment of the polarization resistance at 600 °C and 800 °C with modelled values

The comparison with ASR values, calculated by Rüger et al. [33] for 800 °C, shows that the measured values are within the modelled range (between 38 and 389 $\text{m}\Omega\ \text{cm}^2$). The cathodes (regardless the composition, with a layer thickness around 10 μm) that show the lowest polarization resistance at 800 °C show also values as low as 35 mΩcm^2 at 800 °C. Cathodes sintered at higher temperatures (≥ 1050 °C) show higher cathode polarization up to 180 mΩ cm^2. The model predicts this increase of the ASR due to an increase of the particle size and resulting increase of the penetration depth. These cathodes might require a higher thickness of the cathode layer to lower the polarization.

The cathodes, made from pure nano powder, having a high polarization resistance at 592 °C show polarization resistances as low as 50–75 mΩcm^2 at 800 °C. There are two possible reasons: first the cathode contribution might not fully be visible in the impedance spectra and leads to underestimation of $R_{pol,nano}$. Alternatively it can be assumed, that the nano powder leads to an enhanced catalytic activity at 800 °C at the cathode/electrolyte interface, and a higher thermal activation, compared to the temperature range between 485 °C and 696 °C, occurs. The influence of the layer thickness on the polarization resistance of cathodes is present after heat treatment at 1000 °C for the cathode produced from C25, but not after heat treatment at 950 °C. However, the model predicts lower or equal R_{pol} for cathodes of increased thicknesses, while the measured values for R_{pol} increased with increasing thickness of the cathode. The reason might be that the particle sizes in the cathode layer are still small, resulting in penetration depths far below 10 μm.

The measured polarization resistance of composite cathodes with 46 wt% CGO exhibit similar values as compared to the model of Søgaard et al. [32] for large particles sizes of both the cathode and the electrolyte powder (≤ 1 Ωcm^2 at 600 °C and ≤ 50 mΩcm^2 at 800 °C). Lower particles sizes in a composite were shown to result into R_{pol} as low as 0.2 Ω cm^2. Despite the low (<< 30 %) porosity of the cathodes and a slight difference in the amount of CGO (Søgaard et al. [32] used 50 wt% CGO) these results might indicate high particle sizes after firing and/or insufficient percolation of the MIEC and the CGO. The difficulty in the assessment of the polarization resistance in comparison to the models from Søgaard et al. [32] and Rüger et al. [33] is that porosity and particle sizes can hardly be estimated from the SEM micrographs.

However, the magnitude of R_{pol} can be regarded to fit to the modelled values by Rüger et al. [33], obtained for LSCF for cathode thicknesses of 12 µm. The lowest R_{pol} of composite cathodes correspond to the values modelled by Søgaard et al. [32] for larger particles sizes of both the LSCF and the CGO powder.

5.10 Discussion: correction of the polarization resistance

Regarding the electrolyte resistance of different symmetrical cells in this study, one can observe that two different cells with the same thickness of the electrolyte often show large differences in the electrolyte resistance. Assuming an equally good contact between cathode and the electrolyte, the area specific electrolyte resistance should result in equal values in agreement to the specific conductivity of the electrolyte. Higher values of the electrolyte resistance may indicate that only a small part of the cathode area has a proper connection to the electrolyte and therefore, the ohmic charge transfer resistance of the interface electrode/electrolyte adds on the electrolyte resistance. The varying and higher electrolyte resistances observed in this study are hardly attributed to different specific conductivities, but might rather result from imperfect contact. In order to account for this the following is proposed: Corrected values for the polarization resistances were calculated, taking the electrolyte resistance (R_{el}) and the thickness of the electrolyte (d_{el}) into account (Equation 34).

$$R_{pol,corr} = R_{pol,x} \frac{R_{el,best}}{R_{el,x}} \frac{d_{el,x}}{d_{el,best}} = R_{pol,x} . A_{conn,rel} \qquad \text{Equation 34}$$

The polarization resistance of the sample x ($R_{pol,x}$) was corrected multiplying by the relative area of the cathode that is assumed to be connected ($A_{conn,rel}$) to the electrolyte. The symmetrical cell with the lowest electrolyte resistance (C11N22 fired at 1000 °C, $R_{el,best}$) was taken as a reference. The indices “x” denote the values for the particular samples and “best” the values for the reference sample. The corrected polarization resistances are displayed in Table XII.

The lowest calculated value of $R_{pol,corr}$ for the cathodes made from coarse powders is 0.28 Ωcm^2. This value might indicate a potential to improve the cathode polarization with the addition of nano powders by a factor of about 2.

The lowest calculated value of $R_{pol,corr}$ for the cathodes made from pure nano powders is 0.38 Ωcm^2. This value is about the factor 3 higher than the lowest corrected values obtained from cathodes layers produced from powder mixtures including nano powder. The apparently low connectivity between the spherical grains might be the reason. The cathode C11N22 fired at 1000 °C

Table XII: Measured polarization resistances and corrected values of LSCF cathodes.

Sample	$R_{pol,x}$	$R_{el,x}$	$R_{pol, corr}$
d_{el} / mm	Ωcm^2	Ωcm^2	Ωcm^2
C11N22 at 950 °C			
0.48	0.95	69.7	0.17
C11N22 at 1000 °C			
0.58	0.755	15.5	0.76
C11N22 at 1200 °C			
0.41	2.5	202	0.14
CNE46 at 1000 °C			
0.54	0.799	73.2	0.16
NE46 at 1000 °C			
0.5	0.958	72.4	0.18
NE46 at 1100 °C			
0.5	3.61	186	0.26
C25 at 900 °C			
0.53	1.46	28.8	0.72
C25 at 950 °C			
0.4	1.31	49.9	0.28
C25 at 950 °C	3 layers		
0.46	1.45	65.8	0.27
C25: at 1000 °C			
0.61	0.866	17.6	0.80
C25: at 1000 °C	3 layers		
0.57	1.32	16.4	1.23
C25/1100°C			
0.52	3.82	47.4	1.12
N25 at 950 °C			
0.85	9.82	288	0.77
N25 at 1000 °C			
0.85	5.05	300	0.38
N25 at 1050 °C			
0.89	3.32	185	0.43

Figure 77 shows the trend of the cathode polarization resistance at 591 °C depending on the heat treatment temperature. The comparison between cathodes produced from powder mixtures, nano powders and coarse powders is shown. The original values measured at 591 °C are displayed by black squares, the calculated ones by red ones. The black lines are put to 0.5 Ωcm^2 as the target value aimed to be reached at 600 °C and 0.2 Ωcm^2 for the best values found in the literature [137].

The lowest corrected values of R_{pol} were obtained equally for cathodes sintered between 950 °C and 1000 °C maximum temperature, compared to the original values (black symbols).

Cathodes made from powder mixtures show a minimum in the corrected polarization resistance at a firing temperature of 1000 °C. Exceptions are cathode C11N22 sintered at 1000 °C which was used as a reference and therefore, the values are not corrected, and cathode C11 N22 fired at 1200 °C that shows the lowest value among all cathodes. The lowest values are in between 0.14 Ωcm^2 0.18 Ωcm^2 and correspond to measured values that were presented by Mogensen et al. [138]. These low values are attributed to a so called “nano-effect”. These values might indicate the lowest possible cathode polarization resistance that could be reached with LSCF as cathode material for the particular microstructure without failures.

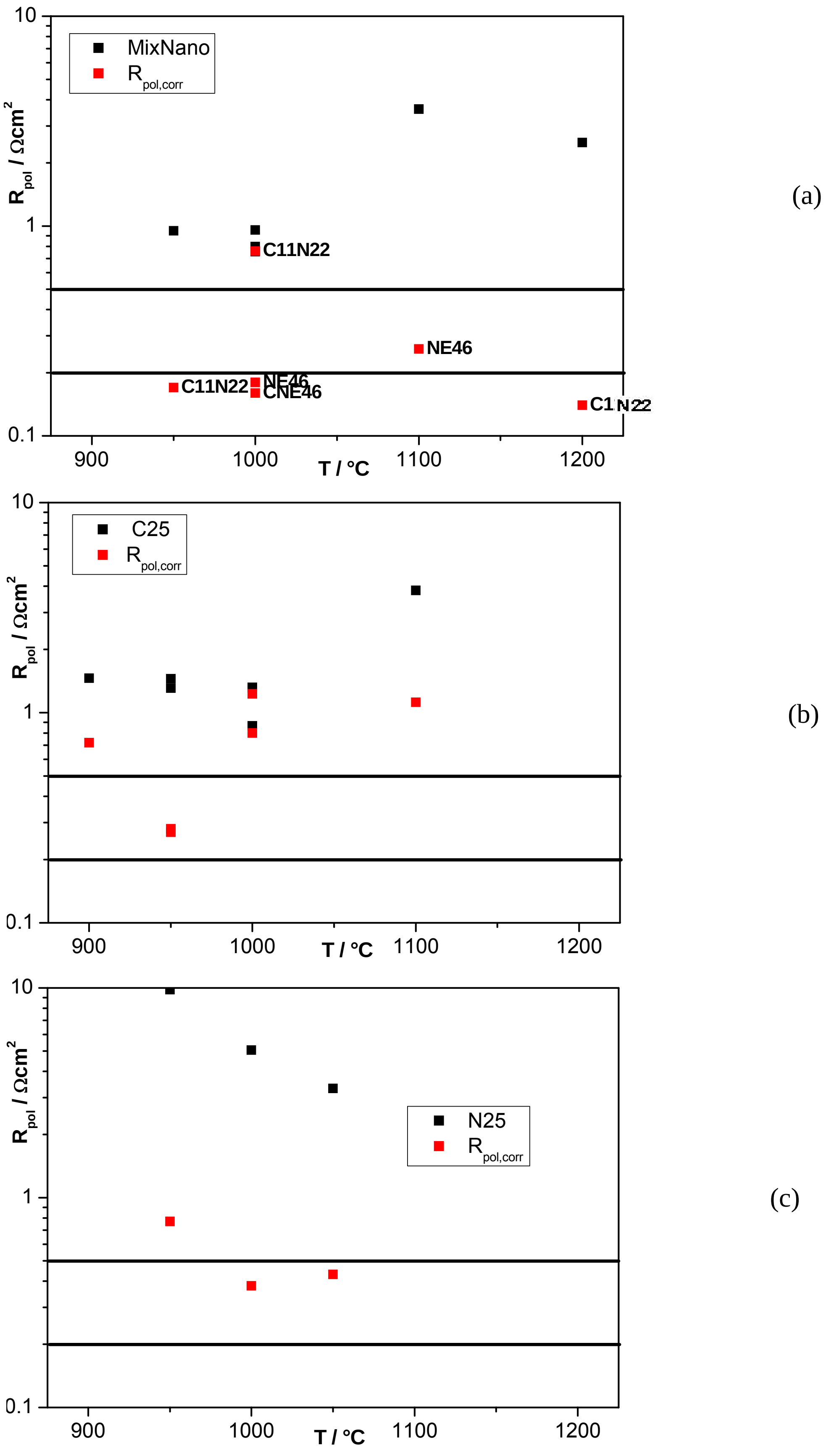

Figure 77: Dependence of R_{pol} and $R_{pol,corr}$ at 592 °C on the heat treatment temperature for powder mixtures (MixNano), coarse (C25) and nano powder (N25).

The cathodes can be divided into different categories regarding the microstructure and/or contact failures (Figure 78). Some of these microstructure or contact failures could be observed by SEM, others were assumed to be the most probable reasons causing high values of the total cell resistance.

a) Contact between the grains and the electrolyte and low formation of grain boundaries: N25, 950-1050 °C - ball like shape of the grains indicating rather grain growth by Oswald ripening; C25 at 900 °C firing temperature might be too low to form sufficient connection between the grains.

b) Delamination of the layer and „mud cracks“: all samples prepared from N25.

c) Partial delamination without formation of surface cracks: cathodes sintered at $T \geq 1100$ °C (CNE46 and C25 at 1100 °C, C11N22 at 1200 °C).

d) Grain coarsening: decrease of the active surface area and the length of the triple phase boundary line; (cathodes C11N22 fired at 1200 °C, CNE46 fired at 1100 °C, C25 fired at 1100 °C).

e) Insufficient contact of the Pt-current collecting layer: C25 900 °C because of lower burning temperature (850 °C), C11N22 fired at 1000 °C; C25 fired at 1000 °C doesn’t influence the electrolyte resistance and leads to apparently higher values of $R_{pol,corr}$.

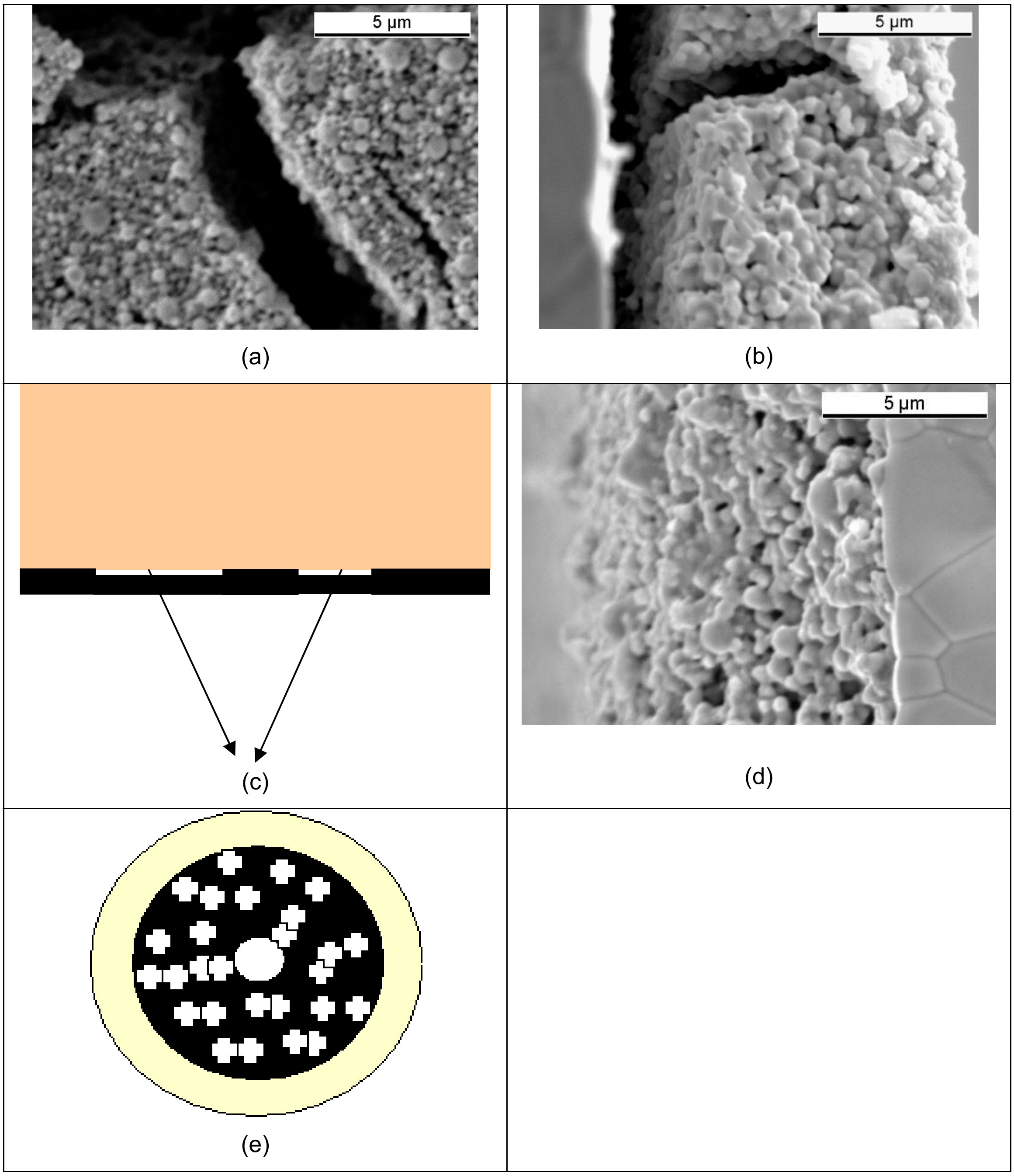

(a)

(b)

(c)

(d)

(e)

Figure 78: Possible reasons for high electrolyte resistance (a) round particle shape, less grain boundaries (as ✙40: 1000 °C), (b) Delamination of the layer (as N25 1200 °C), (c) cathodes areas not connected to the electrolyte, no cracks on the surface, (d) Grain coarsening: decreased active area and triple phase boundary (as C11N22: 1200 °C), e) Pt contact: The white spots indicate areas, where the Pt forms a contact to the cathode layer.

5.11 Conclusions regarding the corrected values of the polarization resistance

The polarization resistance of cathodes produced from pure coarse powder might be reduced by a factor of about 2 by the addition of LSCF nano powder to a coarse powder fraction. The lowest values for the measured polarization resistance in this study might have the potential to be further decreased by a factor of about 4.

The corrected R_{pol} values of cathodes made from pure nano powders are by a factor of 3 higher than the lowest values obtained with powder mixtures. Round grain shape and apparently weak or no connection between the grains might be the reason for higher polarization resistances.

The results of $R_{pol,corr}$ indicate that cathodes made from powder mixtures and pure nano powders might need a slightly higher heat treatment temperature than the cathodes made from pure coarse powder. The different sintering behaviour of the nano powder that seems to form rather spherical shaped particles than grain boundaries might be the origin of this effect.

Exceeding the optimum sintering temperature grain coarsening is most probably the reason for the increase in the polarization resistance due to lower active surface and triple phase boundary length.

6 Final Discussion and Conclusions

In order to develop SOFC cathodes for the operation at 600 °C four materials namely $La_{0.6}Sr_{0.4}FeO_{3-\delta}$ (LSF64), $(La_{0.8}Sr_{0.2})_{0.95}FeO_{3-\delta}$ (LSF82), $La_{0.6}Sr_{0.4}Co_{0.2}Fe_{0.8}O_{3-\delta}$ (LSCF), and $Ba_{0.5}Sr_{0.5}Co_{0.8}Fe_{0.2}O_{3-\delta}$ (BSCF) were synthesized by spray pyrolysis and characterized by XRD, ICP-OES, dilatometer and conductivity relaxation. Especially the obtained electrical conductivity, the chemical diffusion and surface exchange coefficients were taken into account to select one out of the four materials. The phase purity of the nano powder, produced in one step by flame spray synthesis, was a further important criterion. LSCF turned out to be a good compromise regarding the materials properties and was selected to produce screen printing slurries for the application as cathode.

The selection of suitable cathode materials is a compromise between several factors. LSCF finally was selected because it has the

- highest electrical conductivity among tested materials
- considerably high chemical surface exchange coefficient at SOFC relevant conditions
- a chemical diffusion coefficient with low dependence on the $p(O_2)$,
- and a one-step-synthesis of 1 kg batches of phase pure LSCF nano powder by flame spray synthesis was possible.

BSCF as a further interesting material for the production of nano powders had to be ruled out, because the formation of carbonates during production didn’t allow the synthesis of a phase pure nano powders in one step and might cause problems in the long term operation as well.

The optimization of the cathode for operation at 600 °C is essential to reduce the parasitic losses and to be able to produce highly efficient SOFCs with an enhanced life time. The approach to use nano powders in this study was expected have a potential to reduce the polarization resistance to meet these requirements.

LSCF cathodes have been prepared from slurries containing pure coarse and nano powders with and without the addition of electrolyte material. The layer quality was characterized by light microscopy, scanning electron microscopy and electrochemical impedance spectroscopy.

The dispersion of nano powders and application by screen printing were possible, but pastes with pure nano powders (d_{50} around 30 nm) allow only lower solid loading compared to coarser powders (sub micro particles). Pure nano powders applied by screen printing caused cracks after firing, and the cathode layers show relatively high polarization resistances from 3.3 and 9.8 Ωcm^2 at 600 °C. In addition the electrolyte contribution was higher than expected and scattered between 185 and 300 Ωcm^2. Both, the cracks and the higher electrolyte contributions point to contact problems between cathode and electrolyte being the most probable reasons for these high polarization resistances of cathodes from nano powders. Cracks and partial delamination are the most probable cause for this, which need to be overcome by optimizing the cathode layer processing further.

In order to overcome these problems, the sintering program could be further optimized. A lower heating rate e.g. in the temperature range between 600 °C and 800°C might additionally improve the layer properties. Another open question is whether nano powder agglomerates could be dispersed sufficiently.

The use of nano powders turned out to be only useful, when mixed with coarser fractions of $La_{0.6}Sr_{0.4}Co_{0.2}Fe_{0.8}O_{3-\delta}$ (LSCF) and/or $Gd_{0.1}Ce_{0.9}O_{3-\delta}$ (CGO) electrolyte powder. Nano powders mixed with coarser grain fractions show favourable properties and no cracks and delamination occurring after firing. Generally mixtures with a total solid loading of 33 vol% showed the most favourable properties for screen printing and the layer quality after heat treatment. The polarisation resistances for these layers range from 0.76 Ωcm^2 to 3.6 Ωcm^2. The lowest value is close to the target (0.5 Ωcm^2), but still a scatter in the electrolyte contributions is observed, indicating remaining electrode areas, which are not electrochemically active.

A model to correct the polarization resistance from cathodes areas that are not connected to the electrolyte was applied. The corrected polarization resistance was lower than 0.2 Ω cm^2 for cathodes produced with powder mixtures of coarse and nano powder of LSCF and LSCF/CGO composites. These results indicate that a further optimization of the cathode/electrolyte interface could potentially decrease the resistivity by a factor of about 3-4 compared to the best values (0.76 Ω cm^2) measured in this study. Among the produced cathodes the potentially best cathodes result from powder mixtures and composites after correction of the polarization resistance.

To better understand this result, the relationship between micro structure and performance has to be established more in detail e. g. by applying an appropriate electrode model as presented by Rüger or Adler involving the kinetic parameters determined in this study. However, the SEM microstructures do not allow a serious estimation of the porosity, triple phase boundary length and internal surface area. A modelling of the polarization resistance could therefore not be applied. A comparison to literature values modelled for cathodes at 600 °C and 800 °C shows that the measured values are in the range of values modelled from the kinetic parameter of LSCF for different cathode thicknesses and microstructures.

To apply this approach to the presented data would require favourable sample cross sections prepared by embedding the sample in a resin with subsequent cutting and polishing steps. In order to observe nano particles with a size ≤ 30 nm higher magnifications are necessary that require a different instrumentation with high magnification is recommended. The microstructure has to be examined with sufficient magnification to visualise nano grains, and other nano-scaled structures. SEM pictures with higher magnification and three dimensional imaging techniques should allow quantification of the porosity, triple phase boundary length and the internal surface area in order to be able to model precisely the cathode polarization resistance together with the values of the electrical conductivity, the chemical diffusion and surface exchange coefficients.

7 Summary

The current solid oxide fuel cell technology suffers from high degradation of the cell components due to high operating temperatures in the range between 800 °C and 1000 °C and high material costs. Chromium containing interconnects as a major reason can be replaced by ferritic steel at lower operating temperatures. The cell materials as $(La,Sr)MnO_{3-\delta}$, yttria stabilized zirconia (YSZ) and Ni-YSZ need adjustment or substitution by other materials in order fulfil the requirements of the lower temperature operation. Especially cathodes have a major contribution to the cell resistance and therefore, the development of SOFC cathodes for the operating range 550-650 °C was the aim of the present work in order to increase the life time of future cells to become commercially competitive.

Four different cathode materials, namely $La_{0.6}Sr_{0.4}Co_{0.2}Fe_{0.8}O_{3-\delta}$, $Ba_{0.5}Sr_{0.5}Co_{0.8}Fe_{0.2}O_{3-\delta}$, $La_{0.6}Sr_{0.4}Fe_{0.8}O_{3-\delta}$ and $(La_{0.8}Sr_{0.2})_{0.95}Fe_{0.8}O_{3-\delta}$, for the required temperature range were selected in order to compare the relevant properties for fuel cell operation at 600 °C. The materials were synthesised by spray pyrolysis and flame spray synthesis and characterized by XRD regarding phase purity. Furthermore, the particle size distribution, the specific surface area of the powders, the sintering behaviour, the coefficient of thermal expansion, the chemical composition of the products, and the compatibility with electrolyte materials were evaluated. Conductivity and oxygen exchange kinetics were evaluated on dense samples - properties that have a significant impact on the catalytic activity of the cathode.

Phase pure powders of all materials could be obtained after spray pyrolysis and subsequent calcination. Nano powders with a single phase could be only produced from $La_{0.6}Sr_{0.4}Co_{0.2}Fe_{0.8}O_{3-\delta}$ by flame spray synthesis. $La_{0.6}Sr_{0.4}Co_{0.2}Fe_{0.8}O_{3-\delta}$ sub-µ and nano powders additionally show a better compatibility to $Gd_{0.1}Ce_{0.9}O_{1.95}$ (CGO) than $Ba_{0.5}Sr_{0.5}Co_{0.8}Fe_{0.2}O_{3-\delta}$. The evaluated CTE at 600 °C for LSCF and BSCF are 16.2 ppm/K and 27.3 ppm/K, respectively.

The conductivity of the four materials in air at 600 °C lies in between 48 Scm^{-1} ($Ba_{0.5}Sr_{0.5}Co_{0.8}Fe_{0.2}O_{3-\delta}$) and 411 Scm^{-1} for $La_{0.6}Sr_{0.4}Co_{0.2}Fe_{0.8}O_{3-\delta}$. The values of the chemical surface exchange coefficient were compared at 700 °C and show similar values (> 10^{-3} cm s^{-1}) for all four evaluated materials at SOFC relevant oxygen partial pressure of 0.2 bars. $La_{0.6}Sr_{0.4}Co_{0.2}Fe_{0.8}O_{3-\delta}$ shows a lower chemical diffusion coefficient (< 10^{-5} cm^2 s^{-1}) than the three other materials at 700 °C and 0.2 bars. However, the diffusion coefficient of $La_{0.6}Sr_{0.4}Co_{0.2}Fe_{0.8}O_{3-\delta}$ in contrast to the other materials shows only a little decrease when lowering the oxygen partial pressure that may virtually shift towards lower values under high cathode polarization.

Assessing the results from above, finally $La_{0.6}Sr_{0.4}Co_{0.2}Fe_{0.8}O_{3-\delta}$ (LSCF) was selected for the application as cathode layers. Screen printing pastes containing sub-μ and nano powders were developed and applied on $Gd_{0.1}Ce_{0.9}O_{1.95}$ (CGO) pellets as electrolyte substrates. The microstructures obtained after heat treatment were examined by light microscopy and scanning electron microscopy. The polarization resistance as a fingerprint for the electrochemical performance was evaluated.

The surface of cathode layers produced from pure nano powders show surface cracks attributed to the high sintering activity. Layers produced with the conventional sub-μ powder and powder mixtures showed no cracks in the LM pictures. Grain sizes between 0.1 and 2 μm could be observed in the different cathode layers with increasing average grain sizes with increasing firing temperature. Layers produced from pure nano powders show rather separated spheres than grains forming sintering necks as observed for sub-μ powder and powder mixtures. The electron micrographs for layers produced from nano powder indicate delamination of layers especially at firing temperatures ≥ 1050 °C.

Polarization resistances as low as 0.76 Ωcm^2 measured at 585 °C were obtained. These values are close to the defined target of 0.5 Ωcm^2 at 600 °C and justify the selection of LSCF as cathode materials for the targeted temperature range according to the evaluated bulk properties.

Comparing with the lowest measured values an optimization of the cathode polarization by a factor 2 by additional application of nano powders with respect to the conventional approach with sub-μ powders seems to be possible. The next optimization steps should concern the cathode/electrolyte interface, because contact problems between cathode and electrolyte are supposed to be one of the main sources of higher values of the area specific resistance of the cathode.

REFERENCES:

1. High Temperature Solid Oxide Fuel Cells: Fundamentals, Design and Applications, In: S.C. Singhal and K. Kendall, Editors, Elsevier Advanced Technology, Kidlington Oxford (2003).
2. W. Nernst, *Z. Elektrochem.* **6** (1899), p. 41.
3. E. Baur and H. Preis, *Z. Elektrochem.* **43** (1937), p. 727.
4. H.-H. Möbius, *Journal of Solid State Electrochemistry* **1** (1997) (1), p. 2.
5. P. Holtappels and U. Stimming, In: W. Vielstich, A. Lamm and H.A. Gasteiger, Editors, *Handbook of Fuel Cells - Fundamentals, Technology and Appications*, John Wiley & Sons, Ltd, Chichester (2003), pp. 335-354.
6. G. Buchinger, P. Hinterreiter, T. Raab, S. Griesser, R. Claassen, D.P. Claassen, W. Sitte and D. Meissner, *Journal of Fuel Cell Science and Technology* **3** (2006) (3), p. 280.
7. S.C. Singhal, Advances in Tubular Solid Oxide Fuel Cell Technology, In: M. Dokiya, O. Yamamoto, H. Tagawa and S.C. Singhal, Editors, *in: "Proceedings of the 4th international symposium on Solid Oxide Fuel Cells", Hrsg.: S.C. Singhal*, The Electrochemical Society (1995), pp. 195-207.
8. S.C. Sinhal, *MRS Bulletin* (2000), p. 16.
9. S.P.S. Badwal, R. Bolden and K. Föger, In: P. Stevens, Editor, *3rd European SOFC Forum*, Bossel, Ulf., Oberrohrdorf, Switzerland, Lucerne (1998), p. 105.
10. C.F.C. Limited, Fuel Cell Systems, (2008).
11. H.P. Buchkremer, U. Diekmann, L.G.J. de Haart, H. Kabs, U. Stimming and D. Stöver, In: U. Stimming, S.C. Singhal, H. Tagawa and W. Lehnert, Editors, *Solid Oxide Fuel Cells, (SOFC V)*, The Electrochemical Society, Pennington, NJ (1997), p. 160.
12. http://www.topsoefuelcell.com/.
13. D. Stamm, Crofer 22 APU: new material for fuel cells, *IAA Passenger Cars 2003* (2003).
14. Q.M. Nguyen, *Journal of the American Ceramic Society* **76** (1993) (3), p. 563.
15. J. Molenda, K. Swierczek and W. Zajac, *Journal of Power Sources* **173** (2007) (2), p. 657.
16. F.S. Baumann, J. Fleig, M. Konuma, U. Starke, H.-U. Habermeier and J. Maier, *Journal of The Electrochemical Society* **152** (2005) (10), p. A2074.
17. S.J. Skinner and J.A. Kilner, *Solid State Ionics* **135** (2000) (1-4), p. 709.
18. L.W. Tai, M.M. Nasrallah, H.U. Anderson, D.M. Sparlin and S.R. Sehlin, *Solid State Ionics* **76** (1995) (3-4), p. 273.
19. J.E. ten Elshof, M.H.R. Lankhorst and H.J.M. Bouwmeester, *Solid State Ionics* **99** (1997) (1-2), p. 15.
20. V.V. Vashook, N.E. Trofimenko, H. Ullmann and L.V. Makhnach, *Solid State Ionics* **131** (2000) (3), p. 329.

21. J. Vente, S. McIntosh, W. Haije and H. Bouwmeester, *Journal of Solid State Electrochemistry* **10** (2006) (8), p. 581.

22. S. Wang, M. Katsuki, M. Dokiya and T. Hashimoto, *Solid State Ionics* **159** (2003) (1-2), p. 71.

23. W. Zajac, K. Swierczek and J. Molenda, *Journal of Power Sources* **173** (2007) (2), p. 675.

24. W. Zhou, Z. Shao, R. Ran, H. Gu, W. Jin and N. Xu, *Journal of the American Ceramic Society* **91** (2008) (4), p. 1155.

25. L. Kindermann and K. Hilpert, Chemical compatibility of LaFeO3 based perovskites with Yttria stabilized zirconia, *5th International Symposium on Solid Oxide Fuel Cells (SOFC-V)*, The Electrochemical Society, Pennington, NJ (1997), pp. 773-782.

26. Z. Qingshan, J. Tongan and W. Yong, *Solid State Ionics* **177** (2006) (13-14), p. 1199.

27. L. Ronghui, D. Qingshan, M. Wenhui, W. Hua, Y. Bin, D. Yongnian and M. Xueju, *Journal of Rare Earths* **24** (2006) (1, Supplement 1), p. 98.

28. E. Tsipis and V. Kharton, *Journal of Solid State Electrochemistry* **12** (2008) (9), p. 1039.

29. A. Petric, P. Huang and F. Tietz, *Solid State Ionics* **135** (2000) (1-4), p. 719.

30. M. Søgaard, T.Z. Sholklapper, M. Wandel, L.C.D. Jonghe and M. Mogensen, Infiltration of SOFC Cathodes, *8th EUROPEAN SOLID OXIDE FUEL CELL FORUM*, Ulf Bossel, European Fuel Cell Forum, Oberrohrdorf/Switzerland, Lucerne (2008).

31. w.B. Adler, J.A. Lane and B.C.H. Steele, *Journal of The Electrochemical Society* **143** (1996) (11), p. 3554.

32. M. Søgaard, P.V. Hendriksen, T. Jacobsen and M. Mogensen, Modelling of the Polarization Resistance from Surface Exchange and Diffusion Coefficient Data, *7th EUROPEAN SOLID OXIDE FUEL CELL FORUM*, Ulf Bossel, European Fuel Cell Forum, Oberrohrdorf/Switzerland, Lucerne (2006).

33. B. Rüger, A. Weber and E. Ivers-Tiffée, 3D-Modelling and Performance Evaluation of Mixed Conducting (MIEC) Cathodes, *Solid Oxide Fuel Cells 10 (SOFC X)*, The Electrochemical Society, Nara, Japan (2007), p. 2065.

34. S.B. Adler, *Chemical Reviews* **104** (2004) (10).

35. M. Prestat, J.-F. Koenig and L. Gauckler, *Journal of Electroceramics* **18** (2007) (1), p. 87.

36. M. Prestat, A. Infortuna, S. Korrodi, S. Rey-Mermet, P. Muralt and L. Gauckler, *Journal of Electroceramics* **18** (2007) (1), p. 111.

37. L.W. Tai, M.M. Nasrallah, H.U. Anderson, D.M. Sparlin and S.R. Sehlin, *Solid State Ionics* **76** (1995) (3-4), p. 259.

38. M. Liu and Z. Wu, *Solid State Ionics* **107** (1998) (1-2), p. 105.

39. J.D. Sirman, J.A. Lane and J.A. Kilner, *Electrochemical Society proceedings* **97-24** (1997), p. 57.

40. B.C.H. Steele and J.-M. Bae, *Solid State Ionics* **106** (1998), p. 255.

41. A. Esquirol, N.P. Brandon, J.A. Kilner and M. Mogensen, *Journal of The Electrochemical Society* **151** (2004) (11), p. A1847.

42. W. Sitte, surface exchange and diffusion coefficients of LSCF6428, *Personal communication* (2007).

43. S.P. Jiang, *Solid State Ionics* **146** (2002) (1-2), p. 1.

44. Z. Lei, Q. Zhu and L. Zhao, *Journal of Power Sources* **161** (2006) (2), p. 1169.

45. H. Zhao, L. Huo, L. Sun, L. Yu, S. Gao and J. Zhao, *Materials Chemistry and Physics* **88** (2004) (1), p. 160.

46. V. Dusastre and J.A. Kilner, *Solid State Ionics* **126** (1999) (1-2), p. 163.

47. H.J. Hwang, J.-W. Moon, S. Lee and E.A. Lee, *Journal of Power Sources* **145** (2005) (2), p. 243.

48. E. Perry Murray, M.J. Sever and S.A. Barnett, *Solid State Ionics* **148** (2002) (1-2), p. 27.

49. A. Mai, V.A.C. Haanappel, S. Uhlenbruck, F. Tietz and D. Stover, *Solid State Ionics* **176** (2005) (15-16), p. 1341.

50. F.S. Baumann, J. Fleig, G. Cristiani, B. Stuhlhofer, H.U. Habermeier and J. Maier, *Journal of The Electrochemical Society* **154** (2007) (9), p. B931.

51. D. Beckel, U.P. Muecke, T. Gyger, G. Florey, A. Infortuna and L.J. Gauckler, *Solid State Ionics* **178** (2007) (5-6), p. 407.

52. H. Ullmann, N. Trofimenko, F. Tietz, D. Sto?ver and A. Ahmad-Khanlou, *Solid State Ionics* **138** (2000) (1-2), p. 79.

53. B. Wei, Z. Lu, X. Huang, J. Miao, X. Sha, X. Xin and W. Su, *Journal of the European Ceramic Society* **26** (2006) (13), p. 2827.

54. S. Li, Z. Lü, X. Huang, B. Wei and W. Su, *Journal of Physics and Chemistry of Solids* **68** (2007) (9), p. 1707.

55. Q.L. Liu, K.A. Khor and S.H. Chan, *Journal of Power Sources* **161** (2006) (1), p. 123.

56. V.V. Vashook, M.A. Daroukh and H. Ullmann, *Ionics* **7** (2001) (1-2), p. 59.

57. Z. Shao, G. Xiong, H. Dong, W. Yang and L. Lin, *Separation and Purification Technology* **25** (2001) (1-3), p. 97.

58. Z. Shao and S.M. Haile, *Nature* **431** (2004) (7005), p. 170.

59. B. Wei, Z. Lu, X. Huang, J. Miao, X. Sha, X. Xin and W. Su, *Journal of the European Ceramic Society* **26** (2006) (13), p. 2827.

60. H.J.M. Bouwmester, M.W. Den Otter and B.A. Boukamp, *Journal of Solid State Electrochemistry* **8** (2004), p. 599.

61. M. Petitjean, G. Caboche, E. Siebert, L. Dessemond and L.C. Dufour, *Journal of the European Ceramic Society* **25** (2005) (12), p. 2651.

62. S.P. Simner, J.P. Shelton, M.D. Anderson and J.W. Stevenson, *Solid State Ionics* **161** (2003) (1-2), p. 11.

63. M.V. Patrakeev, J.A. Bahteeva, E.B. Mitberg, I.A. Leonidov, V.L. Kozhevnikov and K.R. Poeppelmeier, *Journal of Solid State Chemistry* **172** (2003) (1), p. 219.

64. G.C. Kostogloudis, G. Tsiniarakis and C. Ftikos, *Solid State Ionics* **135** (2000), p. 529.

65. L. Qiu, T. Ichikawa, A. Hirano, N. Imanishi and Y. Takeda, *Solid State Ionics* **158** (2003) (1-2), p. 55.

66. B.C.H. Steele, K.M. Hori and S. Uchino, *Solid State Ionics* **135** (2000) (1-4), p. 445.

67. K. Murata, T. Fukui, H. Abe, M. Naito and K. Nogi, *Journal of Power Sources* **145** (2005) (2), p. 257.

68. M. Mogensen, M. Søgaard, P. Blennow and K.K. Hansen, The Action of Nano-Particles in SOFC Electrodes, *8th EUROPEAN SOLID OXIDE FUEL CELL FORUM*, Ulf Bossel, European Fuel Cell Forum, Oberrohrdorf/Switzerland, Lucerne (2008).

69. P. Ried, D. Burnat, W. Sitte, P. Holtappels and T. Graule, Stabilization of Nanopowders in Organic Suspensions and Their Application as SOFC Cathode Layers by Screen Printing, *Proceedings of the 8th European SOFC Forum, Luzern, Switzerland* (2008), p. B610.

70. D. Burnat, Screen Printing of Micro - Structured Cathodes for Solid Oxide Fuel Cells, AGH - University of Science and Technology, Cracow (2008), p. 141.

71. P. Holtappels, U. Vogt and T. Graule, *Advanced Engineering Materials* **7** (2005) (5), p. 292.

72. A. Heel, P. Holtappels and T. Graule, Nanoscale Perovskite Powders for SOFC Cathodes by Means of Flame Spray Synthesis, In: R. Steinberger-Wilckens, Editor, *in Proceedings of the 8th European SOFC Forum, Luzern, Switzerland*, Ulf Bossel, Lucern, Switzerland (2008), p. B502.

73. A. Heel, Flame spray synthesis, *Personal communication* (2008).

74. A. Heel, A. Vital, P. Holtappels and T. Graule, *Journal of Electroceramics* (2008).

75. A. Wichser and A. Ulrich, ICP-OES conditions, *Personal communication* (2008).

76. K. Xie, R. Yan, D. Dong, S. Wang, X. Chen, T. Jiang, B. Lin, M. Wei, X. Liu and G. Meng, *Journal of Power Sources* **179** (2008) (2), p. 576.

77. E. Tsipis and V. Kharton, *Journal of Solid State Electrochemistry* **12** (2008) (11), p. 1367.

78. E. Bucher, G.B. Caraman and W. Sitte, Applicability of BSCF as IT-SOFC Cathode in CO2-Containing Atmospheres, *in Proceedings of the 7th European SOFC Forum, Luzern, Switzerland* (2008), p. B603.

79. A. Heel, BSCF by flame spray synthesis, In: P. Ried, Editor, Dübendorf (2007).

80. B. Wei, Z. Lü, X. Huang, J. Miao, X. Sha, X. Xin and W. Su, *Journal of the European Ceramic Society* **26** (2006) (13), p. 2827.

81. E. Bucher, A. Egger, P. Ried, W. Sitte and P. Holtappels, *Solid State Ionics* **179** (2008) (21-26), p. 1032.

82. Y. Wang, S. Wang, Z. Wang, T. Wen and Z. Wen, *Journal of Alloys and Compounds* **428** (2007) (1-2), p. 286.

83. E. Bucher, W. Jantscher, A. Benisek, W. Sitte, W. Preis, I. Rom and F. Hofer, *Solid State Ionics* **141** (2001), p. 375.

84. W. Sitte, E. Bucher, A. Benisek and W. Preis, *Spectrochimica Acta Part A: Molecular and Biomolecular Spectroscopy* **57** (2001) (10), p. 2071.

85. E. Bucher, W. Sitte, I. Rom, I. Papst, W. Grogger and F. Hofer, *Solid State Ionics* **152** (2002), p. 417.

86. W. Sitte, E. Bucher and W. Preis, *Solid State Ionics* **154-155** (2002), p. 517.

87. E. Bucher and W. Sitte, *Solid State Ionics* **173** (2004) (1-4), p. 23.

88. E. Bucher and W. Sitte, *Journal of Electroceramics* **13** (2004) (1), p. 779.

89. E. Bucher, G.B. Caraman, A. Egger and W. Sitte, Oxygen Exchange Kinetics and Transport Properties of La0.58Sr0.4Co0.2Fe0.8O3-δ for IT-SOFC Cathodes, *Proceedings of the 8th European SOFC Forum, Luzern, Switzerland* (2008), p. A0406.

90. M.H.R. Lankhorst, H.J.M. Bouwmeester and H. Verweij, *Journal of the American Ceramic Society* **80** (1997) (9), p. 2175.

91. A.N. Petrov, O.F. Kononchuk, A.V. Andreev, V.A. Cherepanov and P. Kofstad, *Solid State Ionics* **80** (1995) (3-4), p. 189.

92. E.B. Mitberg, M.V. Patrakeev, I.A. Leonidov, V.L. Kozhevnikov and K.R. Poeppelmeier, *Solid State Ionics* **130** (2000) (3-4), p. 325.

93. J. Maier, J. Jamnik and M. Leonhardt, *Solid State Ionics* **129** (2000) (1-4), p. 25.

94. D. Grientschnig and W. Sitte, *Journal of Physics and Chemistry of Solids* **52** (1991) (6), p. 805.

95. W. Sitte, *Journal De Chimie Physique Et De Physico-Chimie Biologique* **90** (1993) (2), p. 269.

96. W. Preis and W. Sitte, *Solid State Ionics* **76** (1995) (1-2), p. 5.

97. J.O. Besenhard, M. Wachtler, M. Winter, R. Andreaus, I. Rom and W. Sitte, *Journal of Power Sources* **82** (1999), p. 268.

98. Y.L. Yang, C.L. Chen, S.Y. Chen, C.W. Chu and A.J. Jacobson, *Journal of The Electrochemical Society* **147** (2000) (11), p. 4001.

99. W. Preis and W. Sitte, *Journal of the Electrochemical Society* **145** (1998) (6), p. 2179.

100. W. Preis, E. Bucher and W. Sitte, *Solid State Ionics* **175** (2004) (1-4), p. 393.

101. E. Bucher, A. Benisek and W. Sitte, *Solid State Ionics* **157** (2003) (1-4), p. 39.

102. A. Berenov, A. Atkinson, J. Kilner, E. Bucher and W. Sitte, Oxygen tracer diffusion in Ba0.5Sr0.5Co0.8Fe0.2O3-d, *Proceedings of the 8th European SOFC Forum, Luzern, Switzerland* (2008), p. A0307.

103. M. Katsuki, S. Wang, K. Yasumoto and M. Dokiya, *Solid State Ionics* **154-155** (2002), p. 589.

104. J. Maier, P. Murugaraj and G. Pfundtner, *Solid State Ionics* **40-41** (1990) (Part 2), p. 802.

105. J. E. ten Elshof, M. H. R. Lankhorst and a.H.J.M. Bouwmeester, *J. Electrochem. Soc.,* **144** (1997) (3), p. 1060.

106. J.A. Lane, S.J. Benson, D. Waller and J.A. Kilner, *Solid State Ionics* **121** (1999) (1-4), p. 201.

107. I. Rom, W. Jantscher and W. Sitte, *Solid State Ionics* **135** (2000) (1-4), p. 731.

108. L. M. van der Haar, M. W. den Otter, M. Morskate, H. J. M. Bouwmeester and a.H. Verweij, *Journal of The Electrochemical Society* **149** (2002) (3), p. 41.

109. W. Preis, M. Holzinger and W. Sitte, *Monatshefte für Chemie / Chemical Monthly* **V132** (2001) (4), p. 499.

110. W. Preis and W. Sitte, *Solid State Ionics* **179** (2008) (21-26), p. 765.

111. J. Crank, *The mathematics of diffusion*, Claredon Press, Oxford (1998).

112. W. Preis, Analysis of conductivity relaxation curves, *Personal communication* (2008).

113. W. Preis, E. Bucher and W. Sitte, *Journal of Power Sources* **106** (2002) (1-2), p. 116.

114. L.J. van der Pauw, *Philips Research Reports* **13** (1958), p. 1.

115. D. Grientschnig and W. Sitte, *Zeitschrift Fur Physikalische Chemie Neue Folge* **168** (1990), p. 143.

116. L.M. van der Haar, M.W. den Otter, M. Morskate, H.J.M. Bouwmeester and H. Verweij, *Journal of The Electrochemical Society* **149** (2002) (3), p. J41.

117. E. Bucher, Conductivity relaxation experiments, *Personal communication* (2006).

118. M.W. den Otter, H.J.M. Bouwmeester, B.A. Boukamp and H. Verweij, *Journal of The Electrochemical Society* **148** (2001) (2), p. J1.

119. J. Mizusaki, *Solid State Ionics* **52** (1992) (1-3), p. 79.

120. M. Mosleh, N. Prydsa and P.V. Hendriksen, *Materials Science and Engineering: B* **144** (2007) (1-3), p. 38.

121. P. Ried, E. Bucher, W. Preis, W. Sitte and P. Holtappels, *Electrochemical Society Transactions* **7** (2007), p. 1217.

122. R. Merkle and J. Maier, *Physical Chemistry Chemical Physics* **4** (2002), p. 4140.

123. M. Sahibzada, W. Morton, A. Hartley, D. Mantzavinos and I.S. Metcalfe, *Solid State Ionics* **136-137** (2000), p. 991.

124. M. Søgaard, P. Vang Hendriksen and M. Mogensen, *Journal of Solid State Chemistry* **180** (2007) (4), p. 1489.

125. X. Chen, S. Wang, Y.L. Yang, L. Smith, N.J. Wu, B.I. Kim, S.S. Perry, A.J. Jacobson and A. Ignatiev, *Solid State Ionics* **146** (2002) (3-4), p. 405.

126. S. Kim, S. Wang, X. Chen, Y.L. Yang, N. Wu, A. Ignatiev, A.J. Jacobson and B. Abeles, *Journal of The Electrochemical Society* **147** (2000) (6), p. 2398.

127. S. Wang, A. Verma, Y.L. Yang, A.J. Jacobson and B. Abeles, *Solid State Ionics* **140** (2001) (1-2), p. 125.

128. D. Mantzavinos, A. Hartley, I.S. Metcalfe and M. Sahibzada, *Solid State Ionics* **134** (2000) (1-2), p. 103.

129. K. Swierczek, *Solid State Ionics* **179** (2008) (1-6), p. 126.

130. S. McIntosh, J.F. Vente, W.G. Haije, D.H.A. Blank and H.J.M. Bouwmeester, *Solid State Ionics* **177** (2006) (19-25), p. 1737.

131. P. Ried, EMPA, Swiss Federal Laboratories, Dübendorf, CH (2008).

132. P. Ried, C. Lorenz, A. Bronstrup, T. Graule, N.H. Menzler, W. Sitte and P. Holtappels, *Journal of the European Ceramic Society* **28** (2008) (9), p. 1801.

133. S. Zuercher and T. Graule, *Journal of the European Ceramic Society* **25** (2005) (6), p. 863.

134. J. Divisek, L.G.J. de Haart, P. Holtappels, T. Lennartz, W. Mallener, U. Stimming and K. Wippermann, *Journal of Power Sources* **49** (1994) (1-3), p. 257.

135. Y. Zhang, J. Liu, X. Huang, Z. Lu and W. Su, *Solid State Ionics* **179** (2008) (7-8), p. 250.

136. W. Oswald, *Lehrbuch der Allgemeinen Chemie*, Leipzig, Germany (1896).

137. J.-M. Bae and B.C.H. Steele, *Solid State Ionics* **106** (1998) (3-4), p. 247.

138. M. Mogensen, M. Sogaard, P. Blennow and K.K. Hansen, The Action of Nano-Particles in SOFC Electrodes, *8th European SOFC Forum*, Lucerne (2008), p. A0402.